The Fabrication and Analysis of the Magnetic and Crystallographic Properties of Fe-rich (Fe_xGa_{1-x}) Galfenol Alloys.

Christopher John Quinn

Physics and Materials Research Centre,

College of Computing, Science and Engineering,

University of Salford

Greater Manchester

United Kingdom.

Submitted in partial fulfilment of the requirements of the degree of Doctor of Philosophy, November, 2012

Dedicated to my Mum & Dad.

Without your support this work would not be possible.

Contents

Declaration

All of the work contained in this thesis has been undertaken in this thesis is the sole work of the author with the exceptions that are presented within this declaration.

The melt-spun Galfenol ribbons were manufactured for the University of Salford by Nicoleta Lupu and Horia Chiriac at the National Institute of Research and Development for Technical Physics, Iasi 700050, Romania.

Mössbauer experimentation and analysis was performed by Prof. S.H. Kilcoyne, Dr. L. Simmons and Dr. X. Zhao, as presented in chapter 4 and also in Appendix V. Neutron experimentation and analysis was performed by the author with the assistance of Prof. N. Mellors, Dr. X. Zhao and Dr. P. Henry.

Scanning electron microscopy, energy dispersive spectroscopy and X-ray diffraction experiments were performed by the author at the laboratories of Salford Analytical Services with the assistance of both Dr. G. Parr and Mr. J. McMahon.

All work that has been based on or taken from any other literature has been referenced accordingly to the rightful author(s) and any copyright owners or publishers who have rights to that material.

Abstract

Understanding the fundamental physics and properties of smart materials is a very important area of research for nano and micro mechanical systems especially in the applications of sensing and actuation, such as SONAR.

This thesis is focused on the investigations of Galfenol solid solutions and the associated magnetic properties, crystal structures and the influence that additional Ga has upon a Fe-rich Galfenol system. This has been achieved by using a variety of compositions of $Fe_{1-x}Ga_x$ melt-spun alloy ribbons and then characterised using a number of measurement techniques including; x-ray diffraction, neutron diffraction, Mössbauer interaction, differential scanning calorimetry, vibrating sample magnetometry and electron microscopy.

By identifying the various crystallographic phases and their relevant magnetic properties a clearer picture has been established to enable further research to build upon the results published in this thesis. After fabrication several standard measurements were taken to evaluate the crystalline phases within and the proposed site occupancy of the atomic structure. Compositional analysis was performed in order to clarify the specific atomic weight percentages produced. Magnetic and thermal magnetic measurements were then undertaken to measure magnetic saturation values and relevant Curie temperatures.

Further thermal measurements were taken in order to explain some of the anomalous thermo-magnetic results in the two most dilute compositions. These results were directly compared to ascertain both the structural and magnetic changes that were instigated by the thermal treatment of the alloys. Finally, some rapid annealing and quenching and also a slow cooling treatment was applied to the most dilute composition in order to capture the structural transformation caused by the thermal treatment and these resulting phases identified and the results discussed.

List of Figures and Tables

Acknowledgements

There are many individuals I would like to thank in regard to this thesis and for all their support, advice and help in my time at the University of Salford and more specifically the Joule Physics Laboratory and the Functional Materials Department.

Firstly, my thanks go to my supervisor, Professor Nigel Mellors who allowed me to undertake this research, had the belief in my research abilities and also for his help and support throughout this project.

Special thanks go to Professor Phil Grundy who has been a great inspiration and whose knowledge of material science was an invaluable resource throughout this project. He has always helped me with regard to experimentation, data analysis and the in-depth discussions that resulted have greatly impacted on this work.

I must also thank my partner, Miss Jennifer Warburton, who has managed to put up with me throughout my PhD research and has been a great companion throughout our relationship together.

Respect and thanks go to Professor Roger Ford for employing me regularly over the first few years of my research in order to broaden my research area, enhancing my other key skills. He has been a great influence and a great colleague.

Mr. Geoff Parr and Mr. Joe McMahon are also accredited for their great help when using the XRD, SEM and EDX systems.

A mention must also go to Dr. Daniel Bull, for undertaking the role as my second supervisor and always providing a light-hearted, relaxed atmosphere in the office.

Many thanks to both Professor Sue Kilcoyne and Dr. Lisa Simmons for their valuable contributions regarding the Mössbauer experiments and analysis.

Thank you to Dr. Chester Faunce for initially helping with the early thin film SEM work.

Thank you to Dr. Grenville Jones, who always would contribute to discussions regarding the various experiments that were performed and for also allowing me to attend some of his advanced magnetism lectures.

Thanks also go to Dr. Xeugen Zhao, who is now no longer at Salford, but played a crucial role in the neutron diffraction experiments undertaken at the ILL.

Thanks to Professor Jaap Van den Berg who has also provided his advice, support and has always been involved in the running of the PhD office.

To all of my fellow PhD students who have helped me in any way, Dr. Robert Moorehead, Mr. Christopher Pawley and Dr. Rhiannon Mitchell-Thomas to name but a few.

Mr. Bruce Lewis should also be given a mention here, apart from being a great colleague; he would also always find me the relevant parts to repair my computer whenever it was broken.

Finally, I would like to thank my brother, Mr. Martin Quinn, without whom, this research would have never been accomplished. Thank you for ordering me back to University to study Physics; it has been the greatest thing I have ever done.

Chapter 1: Introduction

1.1 FeGa Alloys and Galfenol

This thesis is concerned with the study of the crystallographic and magnetic characterisation of FeGa alloys (also termed Galfenol by the patent holders at the Etrema Laboratory, USA) which displays remarkable giant magnetostrictive properties; these have been extremely well documented **[1.1.1.4] [1.1.1.5]** since the first relevant investigation of this phenomena of Galfenol in 1998 **[1.1.1.1].** However, it is the crystallographic properties of the Galfenol alloy which determines both the magnetic and magnetostrictive properties. Galfenol undergoes physical changes in shape when influenced by an external magnetic field known as *Joule magnetostriction* and also creates an external magnetic field when external physical forces are applied to the material known as the *Villari effect* **[1.1.1.1].**

Magnetostriction is the term used to describe a deformation or change in shape of a ferromagnetic material when magnetised, this change can be induced by either applying an external magnetic field or an external stress. This effect was first experimentally discovered by James Prescott Joule in 1842 when undertaking a series of laboratory experiments on various samples of Nickel, Iron and a variety of ferrous steels **[1.1.1.2]**. It was not until the early 1970s that Clark et al. found that by alloying Iron with certain rare earth elements that the direct effect of giant magnetostriction with strain values in excess of 2000ppm could be achieved with an alloy of iron, terbium and dysprosium known as Terfenol-D. **[1.1.1.3]**

The amount of this change is governed by the strength of the magnetic field or external force but underpinning this effect is the crystallographic state or phase of the material. The tuneable nature (directly affected by the crystallography) of such functional materials enables them to be operated not only in different dynamic conditions but also over a larger resonance range than most conventional piezoelectric devices **[1.1.1.3].** Thus the ability to have a

magnetic device which is both a sensor and an actuator in a single design is a potential engineering breakthrough.

The data presented in this work focuses mainly on melt-spun Galfenol thin, rapidly solidified ribbons of various compositions, and also, very briefly on DC sputtered thin Galfenol films grown on silicon substrates. Galfenol, somewhat a primitive binary alloy, has a complex phase diagram as discussed in section 3.1, where many different types of lattice structure can potentially co-exist. The resulting alloyed compositions will be denoted $Fe_{100-x}\,Ga_x$, where x is the amount of Ga content in atomic percent. Concentrations below Ga at.20% are termed *solid solutions* as the Ga atoms substitute directly onto the Fe sites and not interstitially, here it is assumed only short-range ordering (SRO) occurs. For higher concentrations of Ga at.>20% there is potential of both short-range ordering (SRO) and long-range ordering (LRO) as other larger structures co-exist within the parent lattice and potential interstitial substitutions are probable **[1.1.1.4].** The structures identified in this work will be compared to that of the existing research that has been presented, along with the impact that Ga addition has by changing the ferromagnetic and physical properties of the material that have been investigated.

The advantage of Galfenol compared to the aforementioned Terfenol-D is the fact that this alloy does not contain any rare earth elements such as Terbium or Dysprosium and therefore is relatively cheap to produce. It also has other beneficial properties such that Galfenol is easily machinable, unlike Terfenol-D and more importantly has the potential to be used under *tensional* forces where Terfenol-D or piezoelectric materials cannot be used due to their frailty. Terfenol however displays a linear magnetostriction of approximately ~2000ppm (parts per million) compared to ~300ppm for Galfenol (where pure iron is approximately 60ppm). **[1.1.1.5]**

A typical Terfenol bar of one metre length when magnetically saturated would give rise to a length expansion of 0.002 metres (2mm).

This research is part of a continual development of so-named *smart materials* within the Nanomaterials Laboratory at the University of Salford, jointly funded by the Engineering and Physical Sciences Research Council (EPSRC), the Doctoral Training Account (DTA) and the Graduate Teaching Assistantship (GTA) schemes.

1.2 Ferromagnetic Smart Materials

Smart materials can be exploited for use in many mechanical systems and can provide an important role in the development of energy harvesting systems, remote sensors, actuators and transducers **[1.2.1.3] [1.2.1.4].** Smart materials are either naturally available elements and compounds or engineered alloys and compounds which transform one form of energy to another. The energy transformation is manifested as a change in shape or as a physical property change within the material. It has been proposed that if these materials could be fabricated into elaborate shapes and exploited in the nanoscale using for example, the Glancing Angle Deposition Technique (GLAD) for structured thin films developed and patented by Brett et al **[1.2.1.1],** then the possibility for miniaturisation of magnetic sensor and actuation designs could be achieved. Thus far this has not been achieved using Galfenol or any other functional material on a reproducible basis. If this engineering step were made possible, the development of complex nano-electrical-mechanical-systems (NEMS) would open up an exciting area of research.

The applications of these materials are varied, but Galfenol shows high potential when compared to other similar materials such as Terfenol-D. Although Galfenol shows widely reported experimental magnetostrictive strains of ~300 ppm **[1.2.1.3]** it remains one of the primary choices for a magnetostrictive material as it does not contain any of the much more

expensive lanthanide elements. Other metals such as aluminium, boron, indium and thallium have also been alloyed with iron to try to establish other subtle alternatives, but Galfenol shows the greatest deformation thus far. Current applications under development include linear actuators and sensors especially useful in remote scenarios, linear motors, acoustic sensors, micro cantilevers and vibrational sensors; not dissimilar to the applications that current piezoelectric materials are employed for. **[1.2.1.4, 1.2.1.5]**

The characterisation of the different crystallographic phases of Galfenol films and ribbons is thus of great importance in order to optimise the material for specific applications and to ensure the material is in the optimum phase to be suitable for each individual application. The specific crystal phase that the material is in will directly impact upon the physical characteristics and behaviour of the material and some of the desired working properties could potentially be reduced if a certain ordered or disordered phase is present. It is important to observe if the relationship between the magnetic properties, the Ga concentration, the crystallographic state, the magnetostrictive properties and any thermal treatment of the alloy can be ascertained and how this is affected by the stoichiometry of the sample.

Galfenol melt-spun ribbon and thin-film samples grown on Si have been investigated as a function of Gallium concentration. These are polycrystalline by nature due to the fact that the cooling rate for the composition of the samples investigated is not high enough to form the amorphous state. Additionally, the phase diagram shows no eutectic from the liquidus state, thus this confirms by previous investigations that cooling rate of the ribbon is not significantly high enough for it to retain an amorphous form **[1.2.1.2].** The amorphous phase has only been reported once in the literature by Seguin et al when thin FeGa films were grown on $PMN_{0.69}Pt_{0.31}$ (which is a Ferroelectric material with a Perovskite type structure composed of Lead, Manganese, Niobium, Oxygen and Platinum) at temperatures less than

600 Celsius, where it was assumed that the Galfenol-substrate interface was the influencing factor on the state of the resulting film **[1.2.1.2].**

1.3 Contents of this Thesis

This thesis has been divided into several chapters each of which aims to present an in-depth description of the research and analysis undertaken. Chapter 1 gives a brief overview of the various topics such as smart materials and what Galfenol alloys are employed for.

Chapter 2 is dedicated to the phenomenon of magnetism, including its origins, the various types of magnetism, how magnetism is quantified and how various outside influences can affect the magnetic behaviour of a particular material. Here the relevant crystal structures of Galfenol are discussed along with the various phase diagrams that have been studied and used as a basis for this work.

Chapter 3 presents a brief literature review of the research of Galfenol and similar alloys both past and present. Due to Galfenol's current popularity as an exploitable resource, a large proportion of this research has been performed parallel to the work in the thesis. A much greater amount of relevant literature is presented in each results section where the results in this work are compared and contrasted to that of other publications.

Chapter 4 focuses upon the making of the Galfenol ribbons, investigations using neutron diffraction, Mössbauer analysis and X-Ray diffraction are presented, discussed and compared to other work of this nature. A brief overview of the theory of each experiment is given with a practical description of the relevant equipment.

Chapter 5 focuses directly on the study of employing scanning electron microscopy (SEM) and energy dispersive spectroscopy (EDX). A brief explanation of the equipment used is

given and a basic overview on the theory of the experiment. Several images and compositional results are presented and relevant discussion of these results put forth.

Chapter 6 presents the final set of experimental results using vibrating scanning magnetometry (VSM), differential scanning calorimetry (DSC), focussing only on the two most dilute compositions. Then a second experiment is performed on the most dilute composition regarding x-ray diffraction, due to the anomalous magnetic results. These are presented in full along with relevant comparisons to similar publications and arguments for the validity of results in this work.

Chapter 7 suggests proposals for further work and other experimental investigations that should be effectuated in order to confirm the results in Chapter 6. Additionally, any publications that have been attributed to the author of this work or have been contributed to by the author and any other publications that are currently in preparation.

Appendix I contains the brief amount of research carried out on the fabrication, growth and results from Galfenol thin films and the repeated attempts to fabricate nanostructures from Galfenol and presents the relevant findings.

Appendix II contains the generated x-ray diffraction patterns that are currently known to exist in Galfenol alloys along with a table with relevant details regarding the journals and authors who have discovered them; these have been generated using ICSD data from the International Crystallographic Database, currently managed and updated at the Daresbury laboratory in Cheshire.

Appendix III lists all of the reports generated by the Crystal Match! software used in the analysis of the X-ray diffraction experiments carried out in this work.

Appendix IV contains a magnetism conversion table between the units used in this thesis and other units used elsewhere.

Appendix V displays a copy of the recently published journal paper regarding the neutron and Mössbauer work undertaken.

1.4 Chapter 1 References

[1.1.1.1] Engdahl, G., Handbook of Magnetostrictive Materials, Academic Press Inc, 1999. ISBN:9780122386404

[1.1.1.2] Joule, J.P., On the Effects of Magnetism upon the Dimensions of Iron and Steel Bars, The London, Edinburgh and Dublin philosophical magazine and journal of science **30**, Third Series: 76–87, 225–241, 1847.

[1.1.1.3] Clark A.E., Cullen J.E., McMasters O.D., Callen E.B., AIP Conf. Prof. **29 192,** 1976.

[1.1.1.4] Buschow, K.H.J., Handbook of Magnetic Materials Volume 20, Elsevier Science & Technology, North-Holland, 2012. ISBN:978044456374

[1.1.1.5] Clark A.E., Savage H.T., and Spano M.L., Effect of stress on the magnetostriction and magnetization of single crystal Tb.27Dy.73Fe2, IEEE Transactions on Magnetics, **20(5)**, pp 1443-1445, 1984.

[1.2.1.1] J.C. Sit, D. Vick, K. Robbie, and M.J. Brett, Thin Film Microstructural Control Using Glancing Angle Deposition by Sputtering, Journal of Materials Research **14**, 1197-1199. 1999.

[1.2.1.2] Seguin, D., Moran, P., Demonstration of Epitaxial $Fe_{0.8}Ga_{0.2}$ Films on Single-Crystal $Pb[Mg_{1/3}Nb_{2/3}]_{0.69}[PbTiO_3]_{0.31}$ Substrates, Journal of Crystal Growth, **311**, **12**, pp 3235-3238, 2009.

[1.2.1.3] Clark A.E., Wun-Fogle M., Restroff J.B., Ross T.A. Schlagel D.L., Proceedings of the 7th International Conference on New Actuators, edited by H. Borgmann, Messe Breman GmbH, Bremen, Germany, p.111-115 2000.

[1.2.1.4] Ueno T., Summers E., Higuchi T., Machining of Iron-Gallium for Microactuator, Proceedings of SPIE Smart Structures and Materials, Vol. **6170**, 2006.

[1.2.1.5] Staley M.E., Flatau A.B., Characterization of Energy Harvesting Potential of Terfenol-D and Galfenol, Proc. of SPIE Vol. 5764, **05**, **16.** 2005

Chapter 2: Magnetism

2.1 Magnetism: History, Origins, Types and Atomic Theory.

Magnetism was thought to be first discovered around 1000 BC. References by the Greek philosopher known as Pliny reported that the herdsman Magnes saw magnetic interaction when the iron tip of his staff broke off and struck a rock. The staff's tip stuck to this rock, which we now call lodestone. It is thought that the Earth's magnetic field could not possibly magnetise lodestone due to its low intensity. The only other possibility at this particular time would be that if the rock had been struck by lightning, which would have been of ample current to magnetically saturate the magnetite within the lodestone. Apparently, after the tip of the staff had stuck to the lodestone Magnes was then also stuck fast to the rock by his iron hobnail boots. **[2.1.1.1]**

Many years later (around 380BC), Aristotle tried to explain magnetic effects by taking a more scientific approach. He determined that there must be some unseen carrying force for the explanation of this action at a distance. These views then didn't change for a substantial period of time until William Gilbert in the 16th century, he was the first to discover that the Earth itself was a weak magnet. He published what is thought to be the first fundamental book called *De Magnete* **[2.1.1.2]** and, to some scientists, Gilbert has become known as the founding father of magnetism and electricity.

One of his quotes is as follows:

"In former times when philosophy, still rude and uncultured, was involved in the murkiness of errors and ignorances, a few of the virtues and properties were, it is true, known and understood...when, by the genius and labors of many workers, certain things needful for man's use and welfare were brought to light and made known to others,...then did mankind

begin to search the forests, the plains, the mountains,...the innermost bowels of earth, and to investigate all things. And by good luck at last the loadstone was found, as seems probable, by iron-smelters or by miners in veins of iron ore. On being treated by the metallurgists, it quickly exhibited that strong powerful attraction of iron -- no latent nor obscure property, but one easily seen of all... then many ancient philosophers and physicians discoursed of it, and briefly (but briefly only) made it matter of record..."

Gilbert W., ***De Magnete, Magneticisque Corporibus, et de Magno Magnete Tellure*** (*On the Magnet and Magnetic Bodies, and on That Great Magnet the Earth*) c.1600. **[2.1.1.2]**

The modern day theories of magnetism have changed somewhat over time and, in the last century, readily exploited and used in all electrical equipment. Both experimental and theoretical scientists have contributed widely to understanding magnetism, such as Faraday, Curie, Joule, Gauss, Neél, Bloch and Maxwell to name but a few. The subject of magnetism is now enveloped by the complex world of quantum mechanics to try to understand how the intrinsic exchanges between the nuclear interactions, collective atomic orbitals and individual electron spins give rise to the large macroscopic effects that are observed.

All solid state matter can be divided into two main types of magnetic material, these being diamagnetic and paramagnetic; the paramagnetic materials can then in some situations (which are temperature dependent as discussed later) be subdivided again into another three types, these being antiferromagnetic, ferrimagnetic and ferromagnetic. A basic schematic diagram of this can be seen in Figure 2.1.1.1.

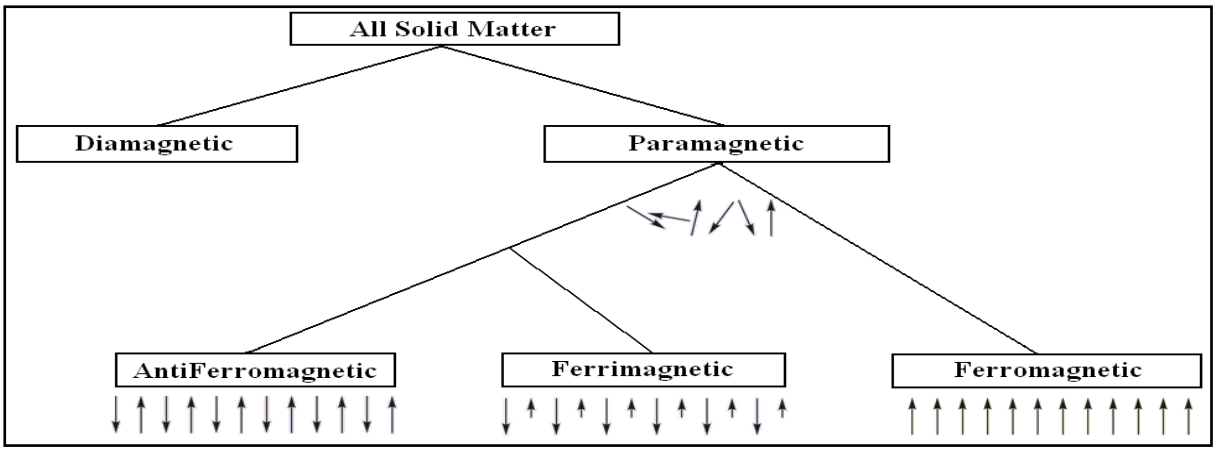

Figure 2.1.1.1 - Schematic Diagram of the Various Types of Magnetism [2.1.1.3]

In general, diamagnetic materials weakly oppose a magnetic field, paramagnetic materials weakly accept an external magnetic field, ferromagnetics strongly accept an external magnetic field and antiferromagnetics have antiparallel spins and weakly accept a magnetic field. In diamagnetic materials such as copper and gold, all electrons are paired so that the magnetic moments associated with the electronic spins are compensated and a net magnetic moment only arises from the orbital moment. When an external magnetic field is applied to such a material, the angular momentum associated with the orbit precesses around the direction of the applied field with an angular velocity directly proportional to the applied magnetic field. The magnetic moment associated with the orbital precession is induced in a direction opposite to the applied field as can be seen in Figure 2.1.1.2 below.

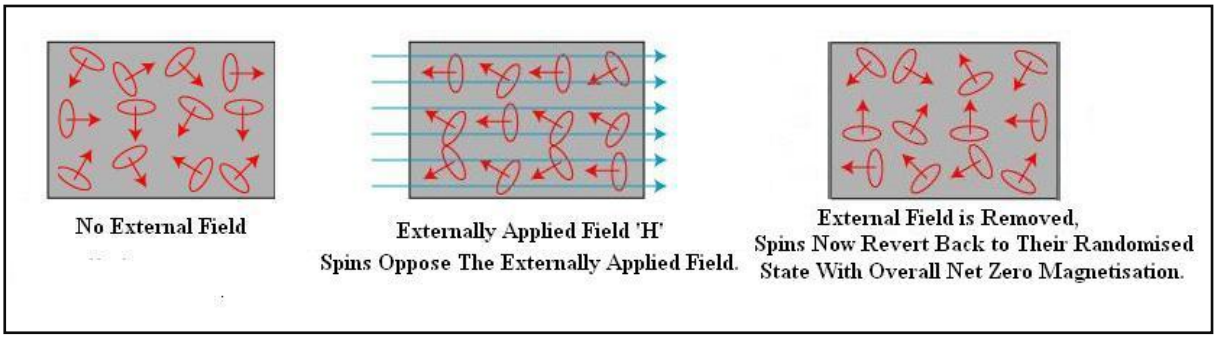

Figure 2.1.1.2 – The exaggerated effect of the diamagnetic spin behaviour. [2.1.1.4]

Paramagnetism exists in materials such as palladium and magnesium, where the atoms have unpaired electron spins. The magnetic moment per atom has a net non-zero value and as a result a net magnetic moment arises in the material when an external magnetic field is applied. This net magnetization is in the field direction and will remain until the applied field is removed, when the material then reverts back to the original state where the electron spins are randomised in a way in which they once again cancel each other, to give a net zero magnetic moment as is illustrated in Figure 2.1.1.3.

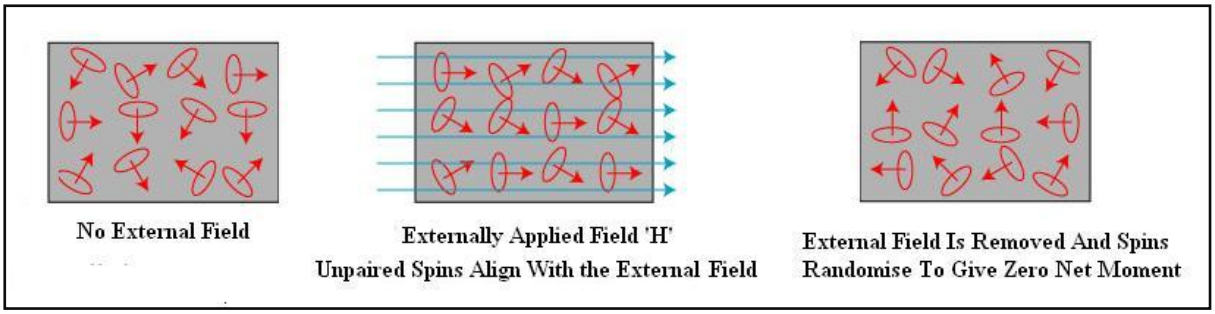

Figure 2.1.1.3 – The exaggerated effect of a paramagnetic material behaviour in an external magnetic field. [2.1.1.4]

Ferromagnetic materials, not dissimilar to paramagnetic materials, have uncompensated spins, the adjacent atomic moments interact, which produces an internal magnetization without applying an external field. If the distance between neighbouring atoms is small enough, the atomic orbital levels will overlap giving rise to a combinatorial effect. In the simplest case of an electron pair interaction, the energy of the system is not the sum of the energy of the individual electrons but also contains a term, the *exchange energy,* which is of quantum mechanical nature. This term is a result of the interaction between neighbouring magnetic moments and is minimised by alignment of atomic moments leading to a spontaneous magnetisation in the absence of an external magnetic field. It is the coupling of the unbalanced electron spins that gives rise to the large macroscopic effect of ferromagnetism. The phenomenon of magnetocrystalline anisotropy as discussed in section 2.2. Ferromagnetism is of the greatest importance to material scientists and engineers. Due to

this strong macroscopic force emanating from these atomic level interactions; these materials have the ability to retain these internal magnetic fields even when the external field is removed. This is providing that they have been *magnetically saturated*, as will be discussed in much greater detail in section 2.3. In Figure 2.1.1.4 the image shows briefly how an external field can be used to instil remanent magnetisation in a ferromagnetic material providing the external field is of large enough magnitude, here it is the unbalanced spins that align with the field. The discussion of how the atomic orbitals and unbalanced electron spins couple together to form magnetic domains is covered in chapter 2.4.

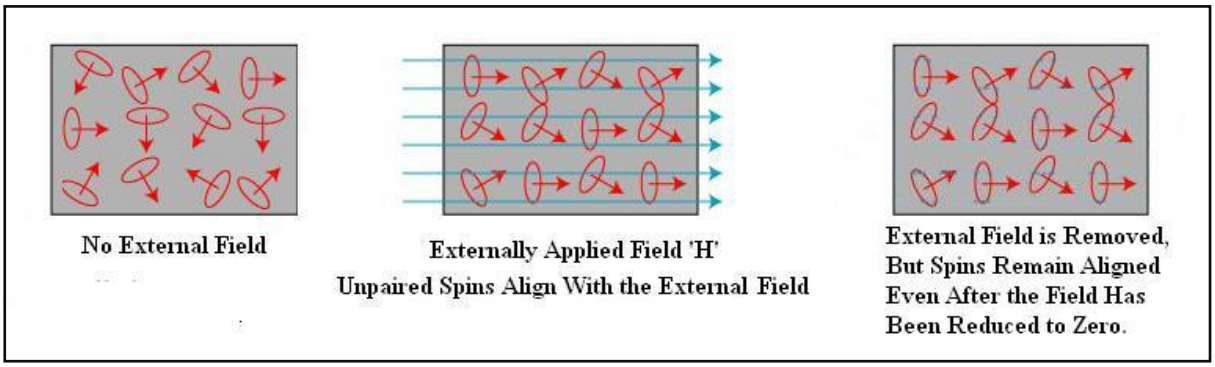

Figure 2.1.1.4 - Typical ferromagnetic behaviour after saturation in an external magnetic field [2.1.1.4]

Only three pure metals and metallic alloys of these elements exhibit true ferromagnetic behaviour; these are namely Iron, Cobalt and Nickel. In the case of oxidised materials, such as Magnetite or Haematite, are termed ferrimagnetic. The additional oxygen atoms provide an atomic link between nearest-neighbour atoms, which are otherwise too far apart for a direct exchange. The overlap of the of transition metals orbitals with the oxygen orbitals results in the spin vectors being *coupled*, sometimes parallel to each other, sometimes antiparallel which gives rise to an overall *net* magnetic moment. The exchange energy contribution here is much less than that of a ferromagnetic material although it is still possible to have remanent magnetisation if the material has been saturated. The strength of this magnetisation is considered very weak compared to that of a saturated ferromagnet. All ferromagnets,

ferrimagnets and antiferromagnets show a property known as magnetic hysteresis which shall also be discussed for the case of ferromagnetism in section 2.3.

Magnetic fields are generated whenever there is movement of charge, whether this is in the microscopic atomic world when electrons orbit the nucleus of an atom, the electron itself can be thought of as spinning on its own axis (which is analogous to the Earth orbiting the Sun, whilst spinning on its own axis) or macroscopically in a current carrying conductor. The rudimentary form of the electron orbiting the atomic nucleus and the electron spinning on its axis can be found in figure 2.1.1.5.

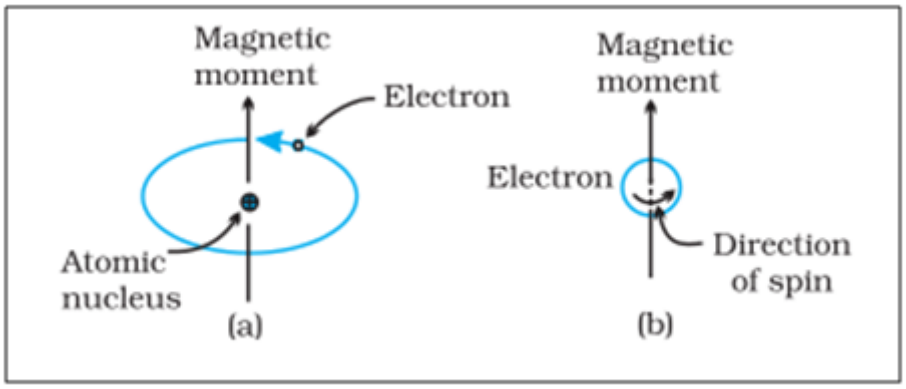

Figure 2.1.1.5 - The Two Examples of Atomic Current Loops (a) an electron orbiting the atomic nucleus and (b) an electron spinning on its own axis. [2.1.1.6]

When a magnetic field, denoted *H*, is produced in a volume of empty space, a magnetic field gradient is developed within this specific volume, inducing a force upon any electrical charges (such as electrons, protons or ions), current-carrying conductors, and magnetic dipoles within this volume **[2.1.1.5].** The Biot-Savart law as denoted in Equation 2.1.1.1 The Biot–Savart law is used to compute the resultant magnetic induction, ***B*,** at position **r** generated by a steady current *I*. The law is a physical example of a line integral evaluated over the path *C* in which the electric currents flow.

$$B = \frac{\mu_0}{4\pi} \int \frac{Idl \times \hat{r}}{|r^2|} \qquad \textbf{(2.1.1.1)}$$

Where: B is the magnetic induction due to the current element increment of Idl, $\hat{r}$ is the unit vector of r from the current position to the point to be measured, I is the current, l is the total length of the conductor and μ_0 is the magnetic permeability of free space. **[2.1.1.5]**

To increase the amount of magnetic flux within a given volume, the conductors are usually manipulated to form solenoidal or toroidal arrangements. The magnetic field strength calculated using Ampere's law at the centre of one of these long thin solenoids (in order to make the length much greater than the diameter, thus $l >> d$) in air is given in Equation 2.1.1.2 **[2.1.1.5].**

This is equivalent to the Biot-Savart law in Equation 2.1.1.1 as shown in equation 2.1.1.3:

$$H = \frac{Ni}{l} \qquad \textbf{(2.1.1.2)}$$

Where: Ni is the number of current turns on the conductor and l is the length of the conductor. The next thing to consider is the total magnetic induction, denoted B, defined as the total amount of magnetic flux through a surface of area A. The flux ϕ is considered as a scalar quantity and is defined as the net number of magnetic field lines per unit surface area. The relationship between the magnetic flux per unit area and the magnetic field is given in Equation 2.1.1.3:

$$\phi = \int B.dA = \mu H = \mu_0 \mu_r H \qquad \textbf{(2.1.1.3)}$$

Where A is the area, μ is the total permeability, μ_0 is the permeability of free space (4×10^{-7} NA^{-2} in SI units), and μ_r is the relative permeability. Relative permeability is a material property that is dimensionless and is equal to unity in free space. It is nearly constant over large ranges of H for paramagnetic and diamagnetic materials, and is nonlinear for ferromagnetic materials such as iron and cobalt.

Here *A* relates to the area of the loop. For this, the magnetic dipole moment, *m* can be defined using Equation (2.1.1.4)**:**

$$m = \pi r^2 i = Ai \qquad \textbf{(2.1.1.4)}$$

$$M = \frac{m}{V} \qquad \textbf{(2.1.1.5)}$$

As *m* is a vector product, no magnetisation occurs when the conductor is parallel to the applied field similar to the Lorentz force. The total magnetisation, *M*, is now be defined as the number of dipole moments per unit volume; orientated in a non-parallel direction to the magnetic dipole moment as in Equation 2.1.1.5 **[2.1.1.5].**

As the magnetic induction applies a torque force upon the magnetic dipoles, a relationship can be derived to relate the magnetic induction *B* to that of the magnetisation *M* as in Equation 2.1.1.6 **[2.1.1.5]:**

$$B = \mu_0 M \qquad \textbf{(2.1.1.6)}$$

The magnetic flux density can either be induced by either electric currents within a conductor (i.e. an internal magnetic field) or by a collection of dipole moments (i.e. by magnetisation effects). The total magnetic induction *B* is the result of the addition of these two factors; the resulting total magnetic induction is given in Equation 2.1.1.7**:**

$$B = \mu_0(H+M) \qquad \textbf{(2.1.1.7)}$$

Here *B* is given the SI unit of the Tesla, *H* in Amperes per metre and *M* in Amperes per metre squared.

The magnetic moment per atom is the vector sum of all of the electronic moments, therefore the magnetisation is defined as the total magnetic moment per unit volume and is termed the

Bohr magneton, denoted μ_B and is the atomic magnetic moment and is expressed in relation to the permeability μ_0 and is given in equation 2.1.1.8.

$$\mu_B = \mu_0 \frac{e\hbar}{2m} \qquad \textbf{(2.1.1.8)}$$

Where e is the electronic charge, m is the electronic mass, $\hbar$ is the Planck constant divided by 2π. The Avogadro constant is simply the number of constituent atoms per mole of material and if this number is divided by the (material density/atomic mass number), then this gives the number of iron atoms in the sample. In a cubic centimetre of iron, there are 6.02 x 10^{23}(7.86/55.85) iron atoms. The magnetic moment per atom is found by dividing the total moment by the number of atoms, or 2.23 * 10^{-20} emu (9.274 * 10^{-24} JT^{-1} in SI units). This equates to 2.218 $\boldsymbol{\mu_B}$, so it appears that in Fe just over two unpaired electrons contribute from each atom **[2.1.1.7].** The saturation magnetization of iron at 0K is 2.2 Tesla in SI units (or 22,000 Oersteds, 1714 emu cm^{-3} and 218 emu g^{-1} in other units).

There are other magnetic parameters that we need to consider for materials and one of the most important is the magnetic susceptibility; which is the ratio of the induced magnetisation with the applied magnetic field. This is defined as χ and is given by the relationship in equation 2.1.1.9 which is dimensionless**:**

$$\chi = \frac{M}{H} \qquad \textbf{(2.1.1.9)}$$

The majority of magnetic materials are characterised by their susceptibility value and some typical values for the three main types of magnetic materials are presented in the following examples.

Material Type	Magnetic Susceptibility	
Diamagnetic	~ -10^{-5}	
Paramagnetic or Antiferromagnetic	~ 10^{-3} to 10^{-5}	
Ferromagnetic	~ 50 to 10,000	**[2.1.1.5]**

2.2 Magnetic Anisotropy and Demagnetisation Fields

Anisotropy is a contribution of energy to the orientation of the atoms within the internal structure of the material. Anisotropy contributions eventually come to equilibrium in order for the material to achieve the lowest possible energy state at any given time. There are several different types of anisotropy that may contribute in magnetic materials. For the majority of cases it is a combination of several of these effects whether it is magnetic, crystallographic, shape or physical deformation (external stress) of such a material. In this section only the effect of anisotropy in ferromagnetic materials is assessed. Magnetocrystalline anisotropy is an intrinsic property of a ferromagnetic crystal and is independent of the crystal size and shape. This property can be most easily seen by measuring magnetization curves along different crystal directions; these materials arrange themselves so that a *hard* and an *easy* axis of magnetisation can be experimentally observed, hence there is a preferred crystallographic and magnetic orientation which are not necessarily the same.

Figure 2.2.1.1 shows a Galfenol atom of body centred cubic (BCC or A2) structure which is typical for compositions of Galfenol from 0 to 15 at. % Ga with each atomic position shown as in an [x,y,z] co-ordinate system with respect to an origin of [000], here the Ga atom is positioned in the middle of the structure, but in the A2 disordered lattice the Ga can substitute for any one of Fe atoms in the lattice, hence the term *disordered*. The easy axes for the Galfenol BCC structure are the <001> family of directions and the hard axes are the <111> directions.

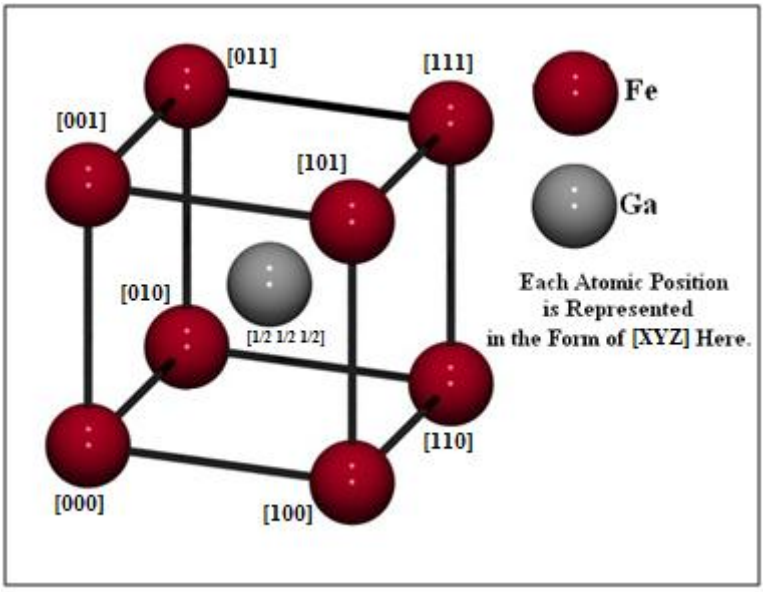

Figure 2.2.1.1 - A Galfenol Atom of body centred cubic (BCC) ordered structure. [2.2.1.1]

(Diagram Created Using CrystalMaker Software, then Adapted using CorelDraw)

The magnetocrystalline anisotropy energy is the energy necessary to deflect the magnetic moment in a sample from the easy to the hard direction. These easy and hard orientations arise from the interaction of the spin magnetic moment coupling to the crystal lattice; this is sometimes called spin-orbit lattice coupling.

In cubic crystals, like Galfenol, the magnetocrystalline anisotropy energy is calculated by a mathematical series in the terms of the angle between the direction of the applied magnetisation field and the axes of the cubic structure as shown by Akulov in 1929 **[2.2.1.2]** It is widely accepted that the anisotropy energy in any arbitrary direction can be described by just the first two variable terms in this series expansion, as the successive terms become more and more negligible. For a cubic crystal the anisotropy energy density is expressed as:

$$Ek = K_0 + K_1 (\alpha_1^2 \alpha_2^2 + \alpha_2^2 a_3^2 + \alpha_1^2 a_3^2) + K_2 (\alpha_1^2 \alpha_2^2 \alpha_3^2) + \ldots\ldots\ldots \quad \textbf{(2.2.1.1) [2.2.1.2]}$$

Where K_0, K_1 and K_2 are known as the anisotropy constants, K_0 is ignored as it is independent of the angle between the magnetisation and the easy axes. α1, α2 and α3 are the direction cosines between the magnetisation and the crystal axes. For the case of Galfenol, K_1 is

positive and K_2 is negative (and K_1 is of greater magnitude by a factor of ~50) meaning the total anisotropy energy E_k is substantially higher for the <111> directions as opposed to the <100> directions, hence the direction with the lowest associated anisotropy energy is termed the easy axes.

In addition to magnetocrystalline anisotropy, there is another contributing effect that is directly related to the long range spin-orbit lattice coupling. This is called magnetostriction, which manifests itself as stored magnetoelastic energy. This effect is produced from the strain dependence of the anisotropy constants. When the material experiences the magnetisation force from the applied external field, a virgin or unmagnetised crystal experiences a resultant strain that can be measured as a function of applied field along a chosen crystallographic axis. A ferromagnetic material physically changes its dimensions when undergoing magnetisation i.e. magnetostriction. The inverse effect with an applied stress also takes place. A uniaxial stress can produce an easy axis of magnetisation but only if the applied stress is sufficient to overpower all of the other combined anisotropy forces such as the shape and magnetic anisotropies. The magnitude of the stress anisotropy is described by two empirical constants known as the magnetostriction constants, one in the easy direction, λ_{100} and one in the hard direction $\lambda_{111.}$ These constants are determined by using the magnetoelastic energy equation; which is the coupling between all of the mechanical and magnetic terms.

Within a cubic crystal system using the directions *(λ_{100} and λ_{111})* as previously mentioned, but additionally, the magnitude (σ) and direction cosines (β_{1s}, β_{2s}, β_{3s}) of the applied stress as well as the orientation of the internal magnetic moments termed (α_1, α_2, α_3) gives:

$$E_{magnetoelastic} = \gamma_\sigma \left[-\frac{3}{2}\lambda_{100}\left(\alpha_1^2\beta_{1s}^2 + \alpha_2^2\beta_{2s}^2 + \alpha_3^2\beta_{3s}^2\right) - 3\lambda_{111}\sigma\left(\alpha_1\alpha_2\beta_{1s}\beta_{2s} + \alpha_2\alpha_3\beta_{2s}\beta_{3s} + \alpha_3\alpha_1\beta_{3s}\beta_{1s}\right)\right]$$

(2.2.1.2) [2.2.1.3]

Here γ_σ is a scaling term in order to scale the magnetoelastic energy so that it is *relative* to the other anisotropy contributions. A physical basis for this term has not as yet been established; but it is best described as an empirical scaling factor that allows for the effect of magnetoelastic energy within the system. This allows for an accurate calculation of the effect of applying an external stress on the material and observing the resultant magnetomechanical behaviour or applying a field to the sample and observing the resultant deformation of the lattice. **[2.2.1.3]**

Another type of anisotropy is due to the physical shape or dimensions of the material. A magnetised object produces external magnetic poles on the surface of the material. This surface charge distribution is itself another source of a magnetic field known as the demagnetising field. This field acts in opposition to the externally applied magnetic field that produces it. For a long thin object such as a ribbon or thin film, the demagnetising field along the long axis is weak because the poles are well separated. For magnetisation induced across a relatively thin object the demagnetising field is large because the induced poles are much closer together. The demagnetising field causes a shearing effect or distortion on the initial magnetisation curve **[2.2.1.5].**

To calculate the demagnetising field within a ferromagnetic material, the pole density on the surface of that object must be determined. If the particular material has a susceptibility χ, the demagnetising field is represented by the demagnetisation factor, N_d. The only currently known analytical solution for N_d relates to solid ellipsoid shapes; theoretical solutions have been formulated for cylinders and other shaped objects but there seems to be no standardised solutions as yet for hollow objects and shapes, therefore these must be modelled individually to acquire the correct demagnetisation factor **[2.2.1.4].** A visual example of the demagnetising field and how it directly opposes the externally applied field can be seen in

figure 2.2.1.2; where the image also shows how the demagnetising field affects the initial part of the B-H magnetisation curve.

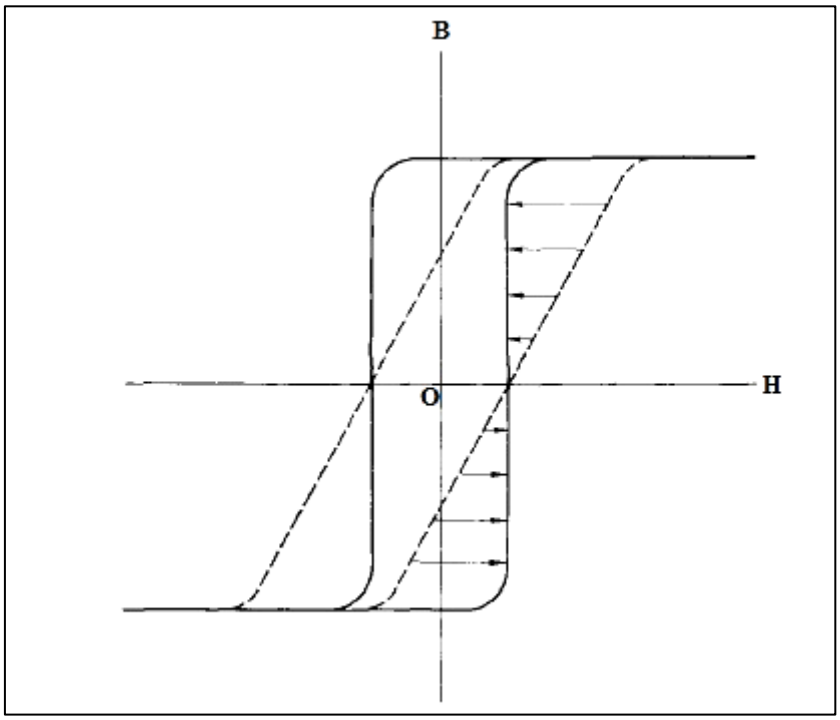

Figure 2.2.1.2 - The Demagnetising Field and the Impact on the B-H Curve (True curve is solid line) Demagnetisation affected curve is the sheared curve (Represented by the dashed line). [2.2.1.5]

In order to quantify this shape anisotropy effect, it is considered to directly oppose the force to the externally applied magnetic field. Equation 2.2.1.3 is revisited and recalculated to include the demagnetising field, H_d.

Quantitively we start with the total magnetic induction equation:

$$B = \mu_0(\Delta H + M) \qquad \textbf{(2.2.1.3)}$$

For a non-closed magnetic circuit such as for a flat thin film or long ribbon, this can be expanded to give:

$$B = \mu_0(H - H_d + M)) \qquad \textbf{(2.2.1.4)}$$

The demagnetising field within the material is defined as:

$$H_d = -N_d M \qquad \textbf{(2.2.1.5)}$$

Including H_d and rearranging:

$$B - \mu_0 H = \mu_0 (1 - N_d) M \qquad \textbf{(2.2.1.6)}$$

Now utilising Equation 2.1.1.9 and substituting, we can rearrange to give:

$$M = \chi_{eff} H = \frac{(B - \mu_0 H)}{\mu_0 (1 - N_d)} \qquad \textbf{(2.2.1.7)}$$

Here χ_{eff} is the *effective* susceptibility of the material [2.2.1.5]. This is distinct from the standard material susceptibility that would be measured in the case where there were no demagnetising fields. (This effective susceptibility is a combined function of both χ and N_d.)

2.3 Magnetic Hysteresis and Curie Temperature

Ferromagnetic materials exhibit magnetic hysteresis which is an intrinsic dependence on the history of externally applied magnetic fields. A ferromagnet can thus be described as exhibiting a memory of its previous magnetic states. Ferromagnetic materials are comprised of atomic *domains*, which are literally microscopic regions in which the atomic moments are locally aligned. When in an unmagnetised state, these domains are randomly oriented but even so, each domain is spontaneously magnetised to saturation. The direction of magnetisation is also randomised from domain to domain which means that the overall effect is to produce a total magnetisation of near zero. When an external magnetic field is applied to the material the domain boundaries begin to move and eventually the magnetisation begins to rotate in the direction of the magnetic field. Magnetic domain theory was first developed by French physicist Weiss who in 1906 **[2.3.1.1]** postulated the existence

of a large scale type of ordering within ferromagnetic materials. These large so-called ordering units he called magnetic domains. Weiss still had to explain the reason for this spontaneous alignment of atomic moments within a ferromagnetic material and formulated the Weiss molecular field theory **[2.3.1.1].** As the field is increased certain domains that are aligned to the field would expand at the expense of the smaller unaligned domains until such a point is reached where only a single aligned domain exists and the field at which this point is reached is known as the *Magnetic Saturation Point* denoted M_s **[2.3.1.1].**

The Weiss theory then encapsulates two distinct criteria; the overall magnetisation of the ferromagnetic material is a combinatorial effect of both the paramagnetic and ferromagnetic moments which involves both short and long range ordering. It is a property of all ferromagnetic materials that some domains remain aligned even after the external field has been removed. In order to look at this further and visualise this concept, the typical hysteresis loop of a ferromagnetic material in Figure 2.3.1.1 will be used.

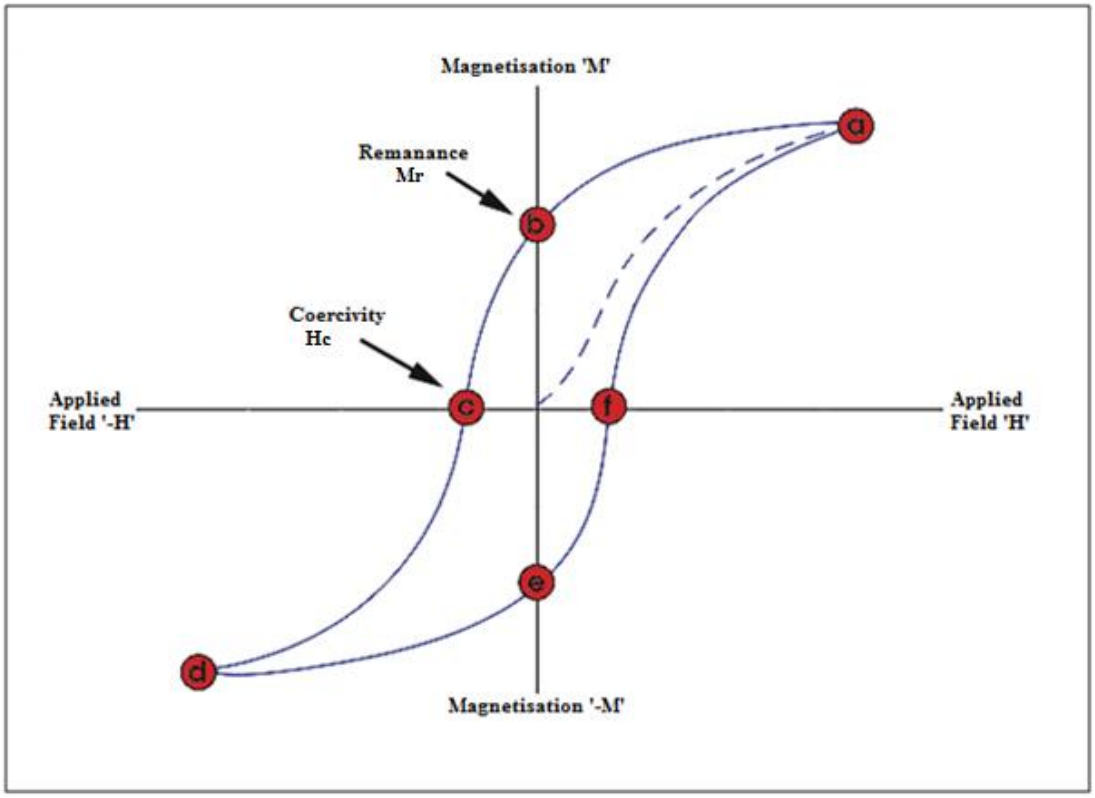

Figure 2.3.1.1 - Typical M-H Hysteresis Loop for a Ferromagnetic Material. [2.3.1.2]

The hysteresis loop is generated by measuring the resultant magnetisation of a ferromagnetic material while the applied magnetising force is changed. A ferromagnetic material that has never been previously magnetised, or what is termed to be in its virgin state, will trace the dashed line as the first externally applied field is increased. As the line demonstrates, the greater the amount of magnetic field that is introduced, the larger the magnetic field within the sample. At point ***a*** almost all of the magnetic domains are effectively aligned into one domain and any additional increase in the magnetising force results in almost no change in the amount of magnetisation within the ferromagnetic sample, hence the material has reached the point of magnetic saturation, M_s. Fe has the highest saturation magnetisation of the single elements at room temperature, typically 1714 emu cm^{-3} or 218 emu g^{-1}. When the external field is gradually reduced to zero, the curve will move steadily from point *a* to point *b*. At this position, it can be observed that the magnetic flux within the material is non-zero even though the external field is. This is referred to as the point of *remanence*, M_r, and indicates the amount of residual (or retained amount of) magnetism in the material. This indicates that some of the domains have remained aligned with the (now-zero) field, but other domains have now lost their alignment and have randomised. As the external field is reversed, the curve moves to the point *c*, this is where the remanent flux has now been reduced to zero as the external field has now managed to rotate enough of the magnetic domains so that the net flux within the material is now zero, this is denoted the *coercivity*, H_c.

As the external field is increased further in the negative direction, the material will again become magnetically saturated but in the opposite direction *d*. By reducing the external field to zero once again, the curve now approaches point *e*. It theoretically will possess the same value of residual magnetism that was measured in the other direction (although experimentally this is not always the case). Increasing the external field again, in the positive direction, will return the ferromagnetic samples magnetic flux to zero. The curve does not

return to the initial origin of the graph because a force is required to remove the residual magnetism. The curve will take a different path from point ***f*** back to the saturation point where it then completes the overall loop.

In this thesis the preferred units of saturation magnetisation, M_s, are given in emu g^{-1} as the ribbons are not of exact uniform thickness and therefore it is easier and more accurate to work with the mass of the ribbon as opposed to the volume and due to the compositions of the ribbon varying, the density of the material also varied due to the differences between Fe and Ga in atomic mass.

The anisotropy of the material changes the shape of the hysteresis loop dependent upon the material orientation and this was documented in great detail by the Stoner and Wohlfarth in their published paper, ***A Mechanism of Magnetic Hysteresis in Heterogenous Alloys***, published in 1948 **[2.3.1.3];** the main points of which will now be covered to evaluate the main conclusions of this theory. The Stoner-Wohlfarth model firstly assumes that a particular individual single domain particle is ellipsoid in shape and that the magnetisation is aligned with the magnetocrystalline *easy* axis. It assumes that as the magnetisation rotates the magnitude remains constant. Because the assumption that the particle is uniformly magnetised, its exchange energy is deemed to be zero. As the magnetisation of the particle is rotated, the internal demagnetising field changes in magnitude as the demagnetising energy has to alter because the demagnetising factors along the different axes of the particle are different due to the shape anisotropy. The magnetisation will be oriented in such a way that the total energy due to the combinatorial effects of all the anisotropies are *minimised*. We will assume that a field is applied horizontally to a particle whose long axis makes an angle β with it, as shown in Figure 2.3.1.2. All of the angles are measured in the anticlockwise direction, so that θ, the angle the magnetisation makes with respect to the particle's long axis is therefore always negative.

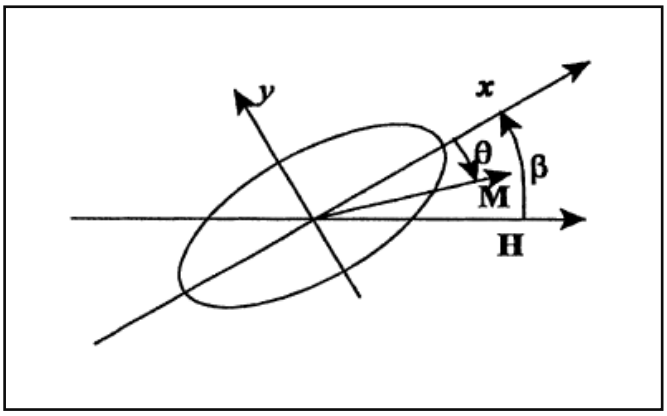

Figure 2.3.1.2 - Stoner-Wohlfarth Description of a Spheroidal Particle. [2.3.1.3]

It can be seen that if the applied field is zero the magnetisation will be positioned along the easy axis of the particle due to the overall anisotropy. However it could be oriented in either direction along that axis implicating that the anisotropy energy must be doubly periodic as the magnetisation of the particle rotates. The applied field energy is unidirectional and therefore is a single periodic function in this particular case. **[2.3.1.3]**

If the body remains uniformly magnetised, then the exchange energy within the system remains constant. Since the magnetocrystalline anisotropy has the same spatial variation as the demagnetising field, if their easy axes coincide then these two variables can be coupled together into a single mathematical term. The effective demagnetising factor must be increased by a specific amount depending on the ratio of the long axis to the short axis of the particle. If the long particle axis does not line up with the magnetocrystalline axis, an *effective* easy axis between the two components must be selected **[2.3.1.3].** The demagnetising factor determined for the long:short aspect ratio for a spheroidal particle can be obtained from the graph shown in Figure 2.3.1.3.

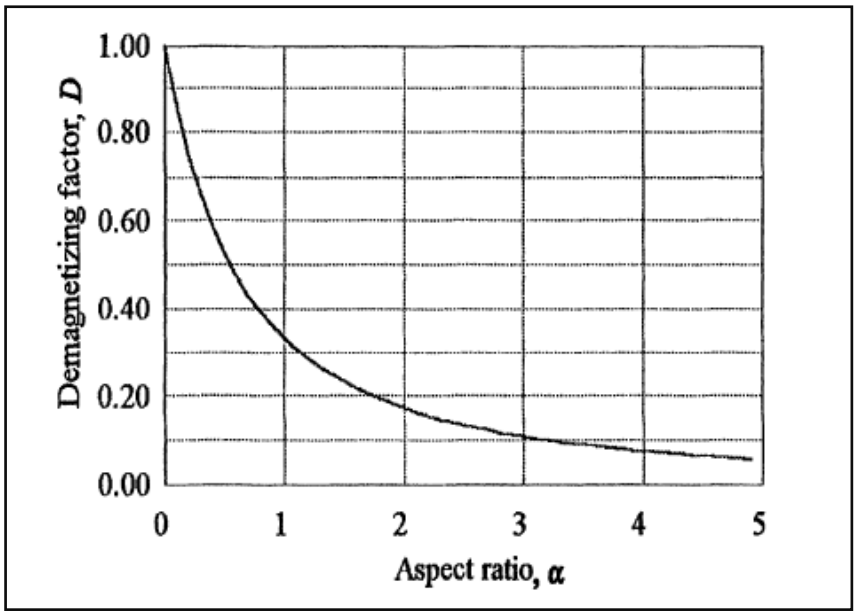

Figure 2.3.1.3 - The Demagnetising Factor for a Spheroidally Shaped Particle [2.3.1.3]

By plotting the component of the magnetisation vector parallel to the externally applied fields axis, hence $M_s \cos(\theta + \beta)$, as a function of the externally applied field gives the resulting theoretical hysteresis loops shown in Figure 2.3.1.4 for three given values of β, here they are 5, 25 and 45 degrees respectively.

These hysteresis loops show that for particles in a negatively magnetised state when the applied field reaches a critical field value named H_k the particle quickly switches to align in a positive state. If the magnetisation was still negative before this switching field was applied, then this must also be equal to the coercivity value. Conversely, if the magnetisation was already positive, H_k must be of greater value than that of the coercivity. The largest value of β for which H_k is equal to the coercivity is at 45°. All hysteresis loops have two critical fields that are the same in magnitude but opposite in sign; hence that magnetic hysteresis is a function of the extreme fields of a sample and in ferromagnetic materials is non-linear. **[2.3.1.3]**

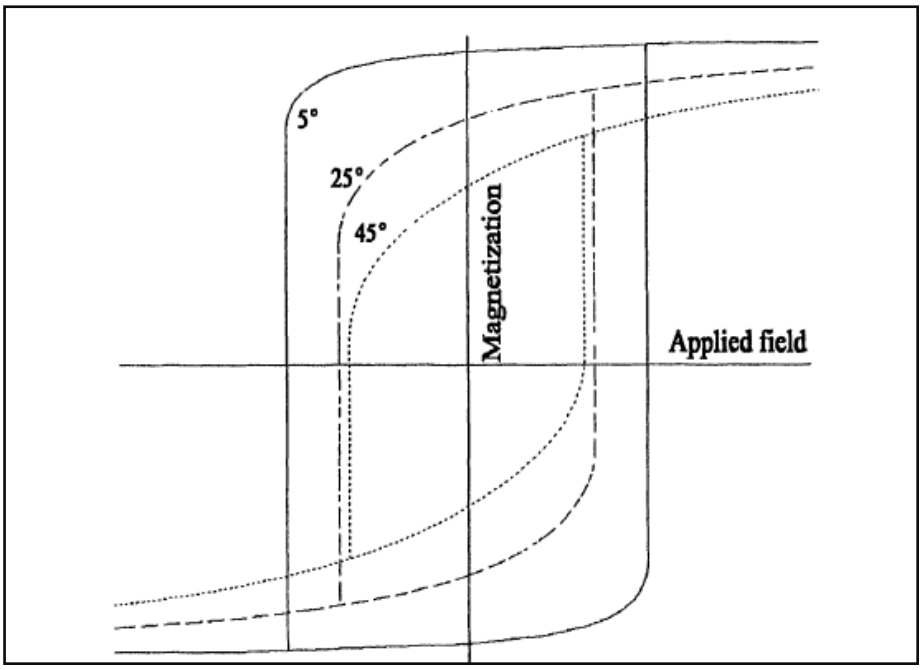

Figure 2.3.1.4 - Stoner-Wohlfarth particle hysteresis loops for β = 5°, 25°, and 45°. [2.3.1.3]

In order for the material to once again follow the initial dashed magnetisation curve on the hysteresis curve in Figure 2.3.1.1 it must be completely demagnetised. There are several ways of doing this but the two main methods are that of using alternating fields and the more familiar method of taking the material past the Curie temperature, T_c, which is also a fundamental property of all ferromagnetic materials as is briefly discussed below.

Ferromagnetism appears only below a certain temperature, which is known as the *ferromagnetic transition temperature* or more simply as the *Curie temperature*. This temperature depends on the specific substance, but its order of magnitude is 1043°K (770°C) for pure Fe. Alternative materials have much lower Curie temperatures for example it is 631°K (358°C) for pure Ni. Thus the ferromagnetic range often includes the whole of the usual temperature region. Above the Curie temperature, the magnetic moments become oriented randomly resulting in a near-zero net magnetisation. Above the Curie temperature the substance is paramagnetic, and its susceptibility is given by the equation:

$$\chi = \frac{C}{T\text{-}T_c} \qquad \textbf{(2.3.1.1)}$$

Where, C is the Curie constant, T is the absolute temperature and T_c is the Curie temperature. This is known as the Curie-Weiss law **[2.2.1.5].** The Curie-Weiss law can be derived using the arguments proposed by Weiss as mentioned earlier at the start of chapter 2.3. In ferromagnetic materials the moments are magnetised spontaneously, which implies the presence of an internal magnetic field that produces this effect. Weiss assumed that this field is directly proportional to the magnetisation such that it is possible to formulate equation 2.3.1.2:

$$H_e = \lambda M \qquad \textbf{(2.3.1.2)}$$

Here λ is the *Weiss constant.* Weiss called H_e the molecular field and thought that this field arises from a contribution from all of the atoms within the sample and is considered to be a very strong internal magnetic field. The origin of this field is accepted to be the exchange interaction and is considered to be the combination of Pauli's exclusion principle and the Coulomb interaction between electrons. Consider the system of two electrons; there are only two possible arrangements for the spins of the electrons: either parallel or antiparallel. If they are parallel, the exclusion principle requires the electrons must remain far apart, if they are antiparallel the electrons may come closer together and their wave functions overlap resulting in a much greater interaction. These two arrangements have different energies because when the electrons are close together the total energy dramatically increases as a result of the large Coulomb repulsion. As we see from the following example the electrostatic energy of an electron system depends on the relative orientation of the intrinsic spins. The difference in this energy defines the exchange energy and is given by equation 2.3.1.3:

$$E_{EX} = -2J_{EX}S_iS_j\cos\theta \qquad \textbf{(2.3.1.3)}$$

Here J_{EX} is the exchange integral, S_i and S_j are the spins of the *i* and *j* atoms respectively and θ is the angle between them. When $J_{EX} > 0$ then the exchange energy is minimised if S_i and S_j are parallel, hence $\cos\theta=1$, also J_{EX} is also minimised if *Si* and *Sj* are antiparallel, thus $\cos(180°)=-1$. This allows for the ferromagnetic configurations to be explained.

The exchange interaction is only of very short range and only nearest neighbour atoms are responsible for producing the Weiss or molecular field. The magnitude of the exchange field is very large; approximately 10^3 T. Weiss's logic was to consider the paramagnetic phase: an applied magnetic field H_0 causes a finite magnetisation, resulting in a finite exchange field H_e. If χ_p is the paramagnetic susceptibility then the induced magnetization is given by equation 2.3.1.4:

$$M = \chi_p(H_0+H_e)= \chi_p(H_0+ \lambda M) \qquad \textbf{(2.3.1.4)}$$

The main assumption here is that the material sample is in the paramagnetic phase. This equation can now be solved for the magnitude of magnetisation to give equation 2.3.1.7:

$$M = \chi_p(H_0+ \lambda M) \qquad \textbf{(2.3.1.5)}$$

$$M - \chi_p\lambda M= \chi_p H_0 \qquad \textbf{(2.3.1.6)}$$

$$M = \frac{\chi_p H_0}{1-\chi_p\lambda} \qquad \textbf{(2.3.1.7) [2.3.1.4]}$$

This formulation can be used to demonstrate how the magnetisation of a ferromagnetic material varies with temperature.

The classical Langevin theory of Paramagnetism assumes that the behaviour of elementary magnets subject to thermal gradients may have any orientation to the applied field and they are also too far apart to have any effect on each other. Quantum concepts alter these assumptions somewhat and limit the number of possible orientations, in the simplest case to only two.

Also it introduces interactions between the magnets themselves i.e. intrinsic spins, which are in equivalence to the internal molecular field. The Langevin equation **[2.3.1.5]** reduces to:

$$\frac{M}{M_s} = tanh\frac{\mu_a H}{kT} \qquad \textbf{(2.3.1.8)}$$

Where $M/Ms = M'$ is the relative magnetisation and μ_a is the atomic magnetic moment. When the molecular field is introduced, then we have equation 2.3.1.9.

$$M' = tanh\frac{\mu_a(H+\lambda M)}{kT} \qquad \textbf{(2.3.1.9)}$$

If it is assumed that in this case $H << \lambda M$, which is reasonable. Then we have equation 2.3.1.10:

$$M' = tanh\frac{\mu_a \lambda M}{kT} \qquad \textbf{(2.3.1.10)}$$

Letting the Curie point, $T_c = \mu_0 \lambda M_s / k$ gives:

$$M' = tanh\frac{MT_c}{M_s T} = tan\frac{M'}{T'} \qquad \textbf{(2.3.1.11)}$$

Where $T' = T / T_c$.

Equations 2.3.1.10 and 2.3.1.11 can be utilised to plot the graphs shown in figures 2.3.1.5a and 2.3.1.5b. The intersections of the linear equation *M' vs M'* with the *tanh M'/T'* curve in figure 2.3.1.5a, which gives the resultant *M' vs Reduced Temperature* curve in 2.3.1.5b.

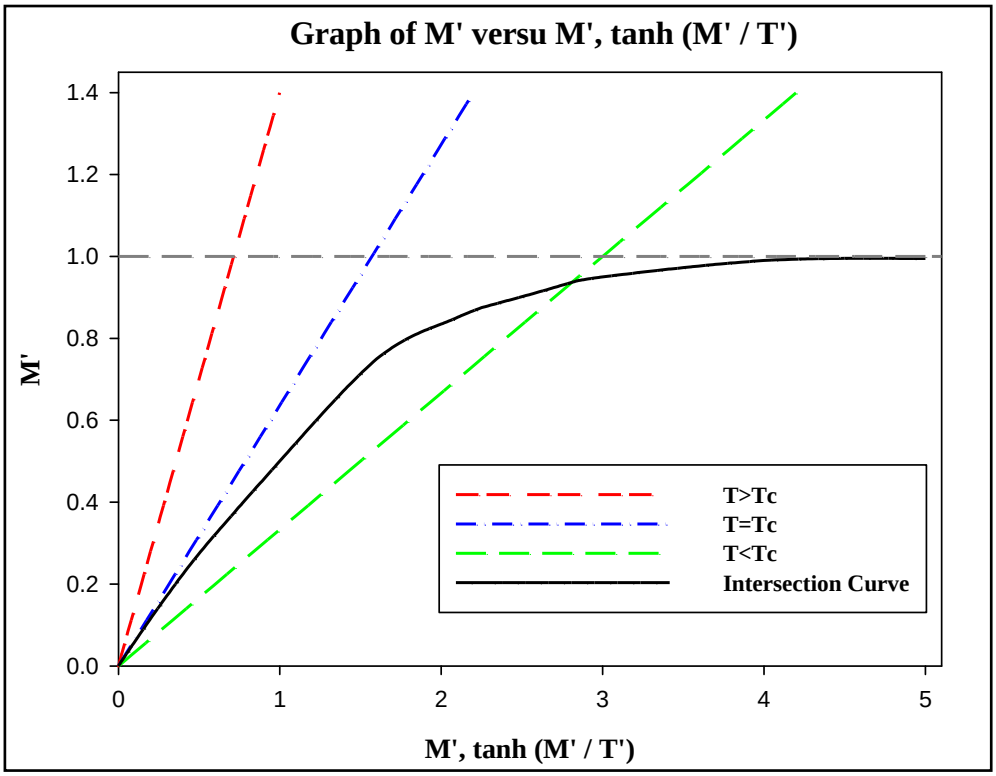

Figure 2.3.1.5a Graph of M' vs M', tanh (M'/T')

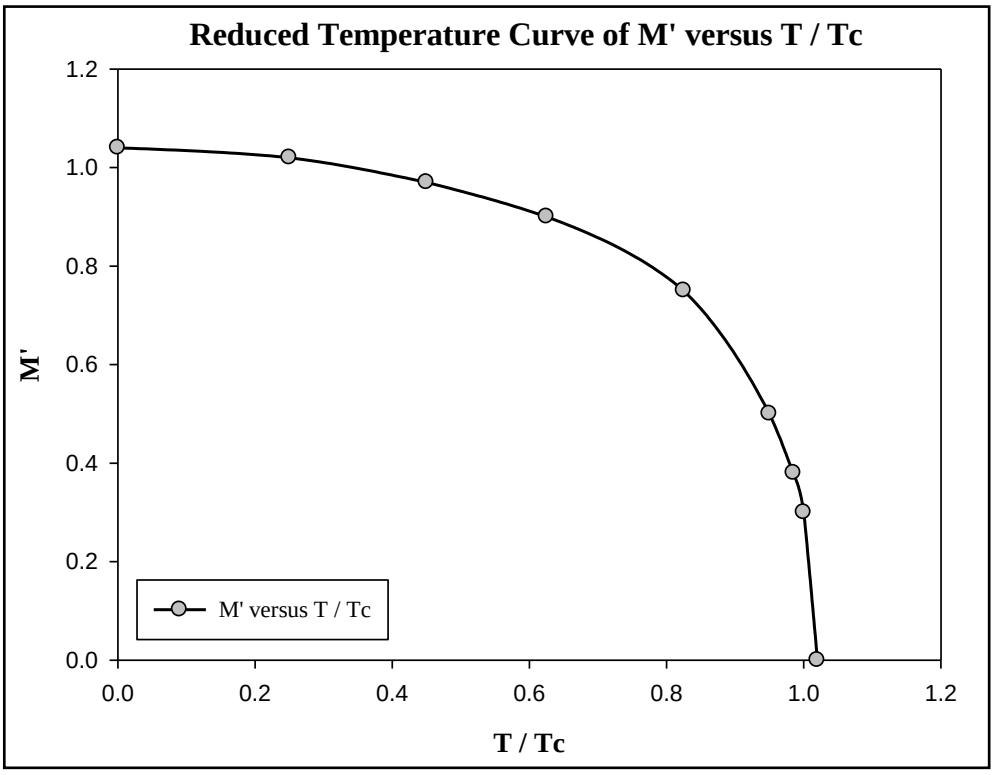

Figure 2.3.1.5b – Reduced Temperature Curve of M' vs T/T_c

Data points based on the curves from Craik [2.3.1.5]

2.4 Magnetic Domains and Domain Wall Formation

Magnetic domains are formed for the purpose of reducing the magnetostatic energy of any magnetic system. If a ferromagnetic material is a single domain then a certain amount of free magnetic poles will be present on the surface due to certain discontinuities in the normal component of the magnetisation at the surface as in Figure 2.4.1.1a. These magnetic poles can also exist inside the material if the magnetisation is non-uniform and these free poles cause the demagnetisation effect as described earlier. This magnetostatic energy and can be expressed by the formula 2.4.1.1:

$$E_m = \int \frac{H^2}{8\pi} dv \qquad \textbf{(2.4.1.1)}$$

Where H is the net-field produced by all of the existing free poles from both the surface and inside the ferromagnetic material. The single domain may first separate into two new domains of equal but opposite orientation as in Figure 2.4.1.1b ,which reduces the overall magnetostatic energy. The system may continue to divide in to more and more domains similar to Figure 2.4.1.1c in order to keep reducing the magnetostatic energy until this reaches a finite limit. This is when an equilibrium point where the magnetostatic energy is negated by the energy required in domain wall formation. In the case of a 180° domain wall where the magnetisation rotates 180° between two domains, if the magnetisation rotates once then the spins adjacent to each side of the wall would be antiparallel resulting in a colossal increase in the exchange energy of the material. This exchange energy can be reduced if the change in the spin direction is more gradual as can be seen in Figure 2.4.1.1d which justifies the necessity of a finite domain wall thickness; hence the reversal of the magnetisation through a domain wall is done *'at a distance'*. The exchange energy prefers the domain walls to be as thick as possible in by making the rotation angle between the spins a minimum, but counteracting this the anisotropy energy is the magnetic anisotropy attempting to make the

wall thin to decrease the number of spins pointing towards non-easy directions. The result is a wall of finite thickness with a specific energy per unit area of wall. Since the spins are not parallel to each other and also are not parallel with the easy axis, the domain wall thickness can be given by equation 2.4.1.2.

$$\delta = \sqrt{\frac{JS^2\pi^2}{Ka_0}} \qquad \textbf{(2.4.1.2)}$$

Where J is the exchange integral, S is the spin, a_0 is the lattice constant and K is the anisotropy constant. The total wall energy is given by: $\gamma_w = 2K\delta$. Using the above equation the average thickness of domain walls can be calculated for soft magnetic materials such as Galfenol. The domain wall thickness was calculated to be of the order of 0.2μm with small non-zero in-plane anisotropy. These calculations are based on the fact that domain walls exist in bulk ferromagnetic materials and the first to study this theoretically was Bloch in 1932 **[2.4.1.1]** and the domain walls described here of this 180°-type are known as Bloch walls. There is another known type of domain wall known as Néel walls, but these are limited to existing only in thin films or materials of thickness of 120nm or less and therefore are not considered in this work. **[2.4.1.2]**

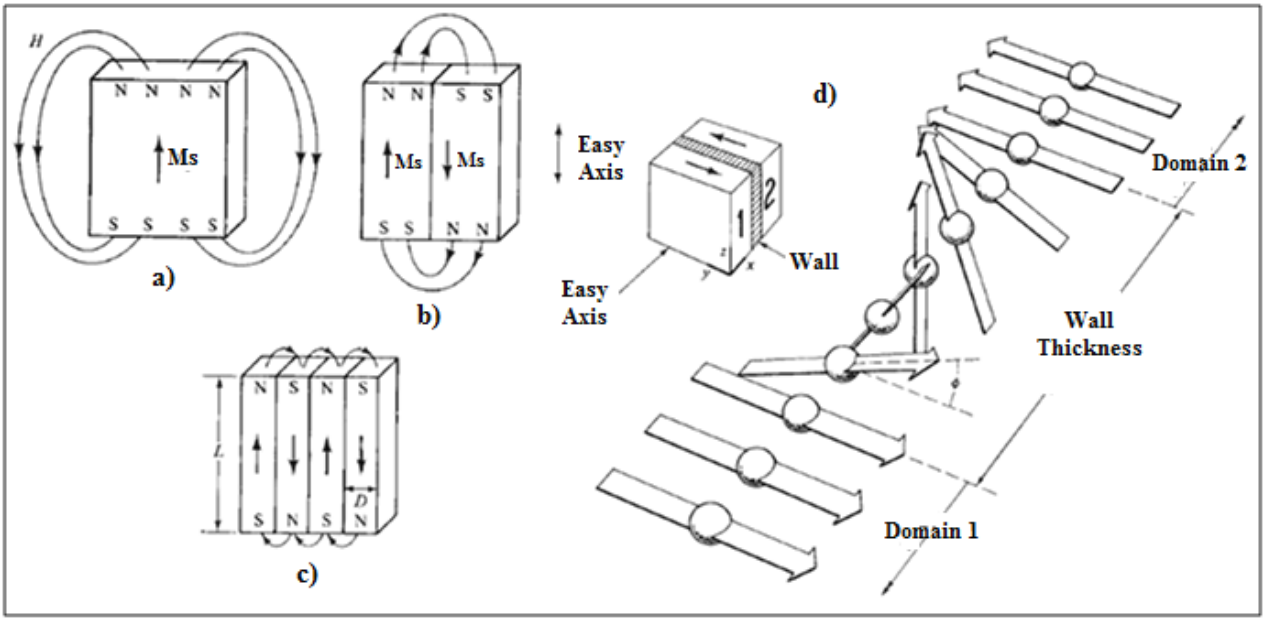

Figure 2.4.1.1 - Domain Formation a) to c) division of Domains and d) structure of a 180 degree wall. [2.4.1.3]

2.5 Crystal Structures: The Bravais Lattice, Space Groups and Reflections

The systematic work of describing and identifying the space lattices was done initially by Frankenheim in 1835. He proposed that there were fifteen unique types of lattice in total. Upon inspection, Bravais noticed that two of these lattices were in fact identical and that there were actually a total of 14 unique lattices. These lattices were not accredited to him for his work and became known as the Bravais lattices in 1848. **[2.5.1.1]** The 14 different lattices are depicted in Figure 2.5.1.1.

The different shapes and sizes of these cells may be described in terms of three cell edge lengths or axial distances, *a*, *b*, *c*, or lattice vectors **a, b, c** and the angles between them, α, β, γ , where α is the angle between **b** and **c**, β the angle between **a** and **c**, and γ the angle between **a** and **b**.

The axial distances and angles are measured from any one corner deemed to be the origin to the point in question. Usually the origin is taken as the back left-hand corner of the cell (from convention), the *a*-axis pointing forward, the *b*-axis towards the right and the *c*-axis upwards.

The, *a*, *b* and *c* axes are analogous to *x*, *y* and *z* in a standard Cartesian coordinate system. This also gives a right-handed axial system. If any one of the axes is reversed (e.g. the *b*-axis towards the left instead of the right), then it results in a left-handed axial system.

This defines that the system is like a mirror image of the other and cannot be confused by rotation of the coordinate system. The unit cells simply represent arbitrary ways of connecting up specific lattice points.

Consider the three basic cubic lattices; *Primitive* (SC), denoted *P*, which contains one lattice point per cell, i.e. the eight lattice points at the corners of the cell contribute $1/8^{th}$ of an atom each. *Body-centred cubic* (BCC), denoted *I*, meaning *Innenzentrierte*', German for "*body-centered*"; which contains the contribution of $1/8^{th}$ from each of the eight corner lattice points plus an extra full lattice point at the centre of the unit cell, resulting in a total contribution of two lattice points per cell. Finally *Face-centered cubic* (FCC), denoted *F*, which has the eight corner lattice points and six lattice points at the centers of each face of the cell (the body centre point now removed), which gives four lattice points per cell, an $1/8^{th}$ from each of the eight corner points and ½ from each of the three face centred points giving a total of four lattice points contributing to the unit cell **[2.5.1.2].**

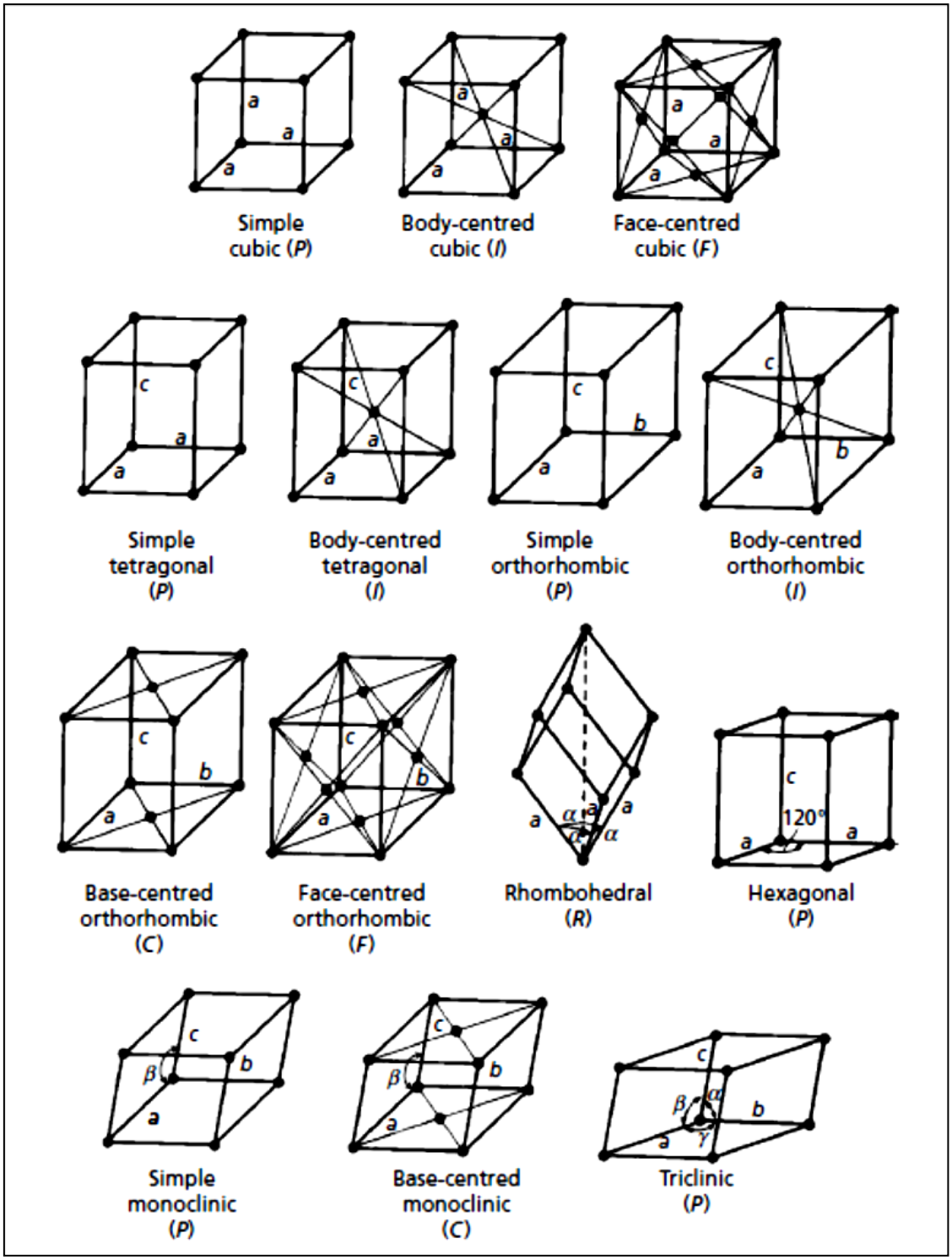

Figure 2.5.1.1 - The 14 Individual Bravais Lattices [2.5.1.2]

The drawings of the unit cells of the Bravais lattices in Figure 2.5.1.1 can be slightly misleading because it is the *pattern* of lattice points or lattice reflections which allows each lattice to be identified.

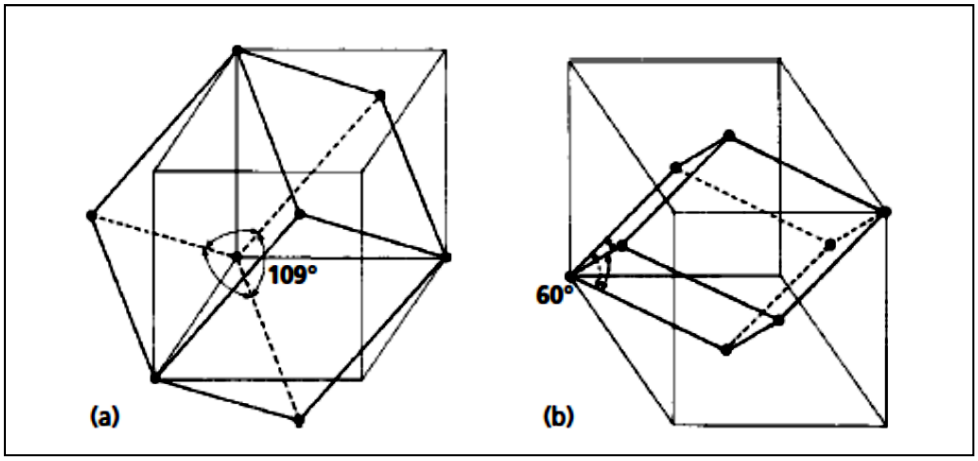

Figure 2.5.1.2 - (a) The Cubic *I* and (b) the cubic *F* lattices with the primitive Rhombohedral, *R*, Cells – showing the Interior Angles. [2.5.1.2]

It is possible to outline alternative primitive cells for the cubic *I* and cubic *F* lattices, this time just using the corner lattice points of the primitive unit cell as is shown in Figure 2.5.1.2. These primitive cells are not often used due to the interior angles not being perpendicular and because they do not clearly show the high symmetry of the cubic *I* (BCC) and cubic *F* (FCC) lattices. Similar rules can be applied to the use of primitive cells to represent all the other centred lattices. It can be observed that the unit cells of two of the lattices are centred on the top and bottom faces, these are so-called base-centered because these faces are intersected by the *c*-axis.

The Bravais lattices can be considered as being constructed by stacking layers of the five plane lattices on top of one another. The cubic and tetragonal lattices are based on the stacking of square lattice layers due to their symmetry; the orthorhombic *P* and *I* lattices on the stacking of rectangular shaped layers; the orthorhombic *C* and *F* lattices on the stacking of rectangular centred layers; the rhombohedral and hexagonal lattice represented by stacking of hexagonal layers and the monoclinic and triclinic lattices on the stacking of asymmetrical layers **[2.5.1.1].** These relationships between the plane and the Bravais lattices are easy to visualise excluding the rhombohedral lattice. The rhombohedral unit cell has axes of equal length and equal angles α between the axes. The layers of lattice points perpendicular to the

vertical direction in figure 2.5.1.3a form triangular or hexagonal layers. The hexagonal and rhombohedral lattices differ in the ways in which the hexagonal layers are stacked. In figure 2.5.1.3 the hexagonal lattice can be seen to be stacked directly one on top of the other and in the rhombohedral lattice they are stacked such that the next two layers of points lie above the tetrahedral shaped gaps from the lattice point layer below; resulting in a three layer repeating pattern as can be seen in figure 2.5.1.3b. It can be seen that for the hexagonal lattice, the repetitive stacking sequence is simply A..A..A..etc; yet for the rhombohedral lattice it is slightly more complex being A..B..C..A..B..C as the pattern rotates around the axis.

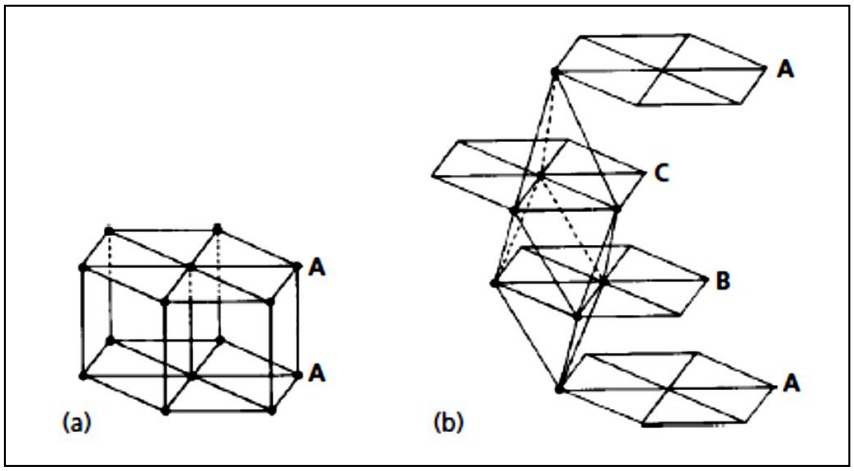

Figure 2.5.1.3 - Stacking of hexagonal layers of lattice points in (a) the hexagonal lattice and (b) the rhombohedral lattice [2.5.1.2]

The *primitive* cells of the cubic *I* and cubic *F* lattices seen in figure 2.5.1.2 are rhombohedral and the axes are of equal length and the angles $\boldsymbol{\alpha}$ between them are equal.

As in the two-dimensional situations the distinguishing feature that separates the cubic lattices from the rhombohedral is their overall symmetry. When the angle α is 90° a cubic *P* (sc) lattice is formed, when it is 60° a cubic *F* (fcc) lattice and when it is 109.47° a cubic *I* (bcc) lattice. When the hexagonal layers of lattice points from a rhombohedral lattice are orientated so that the angle α is 90°, 60° or 109.47° then a cubic type lattice symmetry is formed.

For completeness, the seven different types of lattice are shown in Table 2.5.1.1, but the work in this thesis uses the crystal structures formed in the Fe-rich portion of the Galfenol system (0<x<30% at. % Ga) which is limited to the following shaped lattices:

- A2 disordered bcc
- B2 ordered bcc
- L_{12} ordered fcc
- DO_{19} hcp
- Superlattice D03; which is an ordered combination of sc and bcc.

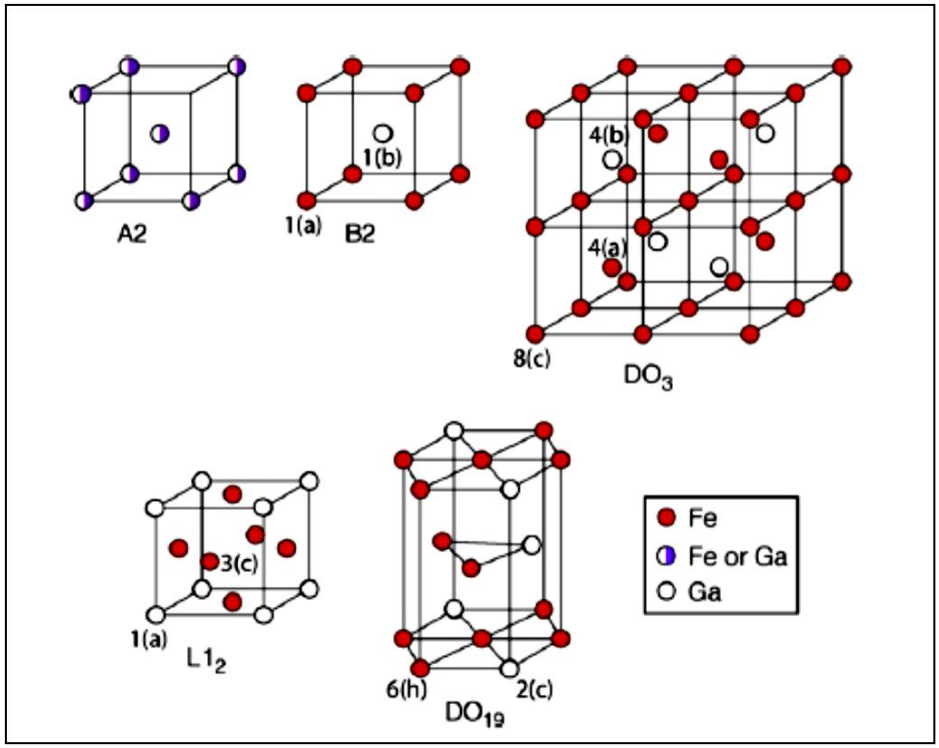

Figure 2.5.1.4 - Long range ordered structures of Galfenol. [2.5.1.3]

The B2 is similar to CsCl structure and the D03 similar to the Fe_3Al ordered structure are simple binary ordered systems that are coherent with the parent A2 cubic structure. The formation of the other lattices L_{12} and DO_{19} which have incoherent interfaces are limited by phase transformation kinetics. All of these structures can be seen in figure 2.5.1.4.

The B2 structure is equivalent to the CsCl ionic structure and consists of simple cubic Fe and Ga sublattices with a body-centred interpenetration. The B2 structure corresponds to the simple cubic space group *Pm3m* (No. 221) with two basis atoms. The Fe atoms sit on the 1(a) (corner) position and the Ga atoms sit on the 1(b) (body-centered) position. The identification of the B2 phase by diffraction techniques therefore corresponds to the observation of an extra set of H + K + L odd superlattice reflections, such as (1,0,0). The ideal stable stoichiometry for the B2 ordered phase is $Fe_{100-x}Ga_x$ (where x=50) but the B2 phase is stable over a wide range of compositions at high temperatures, even for Ga compositions as low as x =22. For Ga-deficient compositions with x < 50 the B2 structure can still be thought of as consisting of two sublattices. The 1(a) sublattice is entirely occupied by iron, while the 1(b) consists of a random distribution of Ga and the remaining Fe atoms. The D03 (or Fe3Al) structure appears in both the equilibrium and metastable phase diagrams of Galfenol. The ideal D03 structure occurs with the stoichiometry $Fe3_{100-x}$ Ga_x (x=25). Similar to the B2 structure, it consists of a simple cubic sublattice of Fe atoms, this time located at the 8(c) site of the *Fm3m* (No. 225) space group. The body centered sublattice is then split equally between 4(a) and 4(b) sites that are occupied by Fe and Ga, resulting in a doubled cell with a primitive FCC symmetry. Due to the symmetry of each lattice the occurrence of A2, B2 or D03 long-range ordering can be identified by the allowed reflections from the respective lattices.

The L_{12} (similar to $AuCu_3$) structure with space group *Pm3m* (No. 221) consists of a simple cubic lattice of Ga atoms with the centers of the faces of the Ga cube (at the 1(a) position) occupied by Fe atoms (the 3(c) position). Unlike the B2 and D03 binary structures which are coherent with the A2 structure, a bcc to fcc structural transformation to the L12 structure within the A2 matrix requires a large lattice strain to be induced along the [110] direction in the a-Fe cell. Due to the large elastic energy barrier required for such a transformation into the L12 structure, the kinetics of the phase transformation should allegedly be very slow.

[2.5.1.6]. The D019 structure can occur in stoichiometric Fe_3Ga and has the hexagonal space group *P63/mmc* (like the Ni_3Sn structure). The Fe atoms are located at the 6(h) position and the Ga at the 2(c) position.

There are certain *allowed* reflections when diffraction experiments are performed that can be identified in bcc, fcc and hcp systems. There are certain reflections that are not allowed, this is due to the symmetry of certain types of lattice and these can be ascertained by a full Fourier analysis of the symmetry, which will not be covered here but can be found in the book of Practical Electron Microscopy and Databases **[2.5.1.7].**

System	Bravais lattices	Axial lengths and angles	Characteristic (minimum) symmetry	Non-centrosymmetric point groups		Centrosymmetric point groups[a]
				Enantiomorphous[b]	Non-enantiomorphous[c]	Non-enantiomorphous[c]
Cubic	*PIF*	$a = b = c$ $\alpha = \beta = \gamma = 90°$	4 triads equally inclined at 109.47°	23, 432	$\bar{4}3m$	$m\bar{3}$, $m\bar{3}m$
Tetragonal	*PI*	$a = b \neq c$ $\alpha = \beta = \gamma = 90°$	1 rotation tetrad or inversion Tetrad	4^P, 422	$\bar{4}$, $4mm^P$, $\bar{4}2m$	$4/m$, $4/mmm$
Orthorhombic	*PICF*	$a \neq b \neq c$ $\alpha = \beta = \gamma = 90°$	3 diads equally inclined at 90°	222	$mm2^P$	mmm
Trigonal	*PR*	$a = b = c$ $\alpha = \beta = \gamma \neq 90°$	1 rotation triad or inversion triad (= triad + centre of symmetry)	3^P, 32	$3m^P$	$\bar{3}$, $\bar{3}m$
Hexagonal	*P*	$a = b \neq c$ $\alpha = \beta = 90°, \gamma = 120°$	1 rotation hexad or inversion hexad (= triad + perp. mirror plane)	6^P, 622	$\bar{6}$, $6mm^P$, $\bar{6}m2$	$6/m$, $6/mmm$
Monoclinic	*PC*	$a \neq b \neq c$ $\alpha = \gamma = 90° \neq \beta \geq 90°$	1 rotation diad or inversion diad (= perp. mirror plane)	2^P	m^P	$2/m$
Triclinic	*P*	$a \neq b \neq c$ $\alpha \neq \beta \neq \gamma = 90°$	None	1^P		$\bar{1}$

[a] All the crystals which possess a centre of symmetry and/or a mirror plane are non-enantiomorphous.
[b] The eleven enantiomorphous point groups are those which do not possess a plane or a centre of symmetry. Hence enantiomorphous crystals can exist in right- or left-handed forms.
[c] Eleven of the twenty-one non-enantiomorphous point groups are centrosymmetric. Crystals which have a centre of symmetry do not exhibit certain properties, e.g. the piezoelectric effect.
The ten polar point (non-centrosymmetric) groups (indicated by a superscript P) possess a unique axis not related by symmetry. They are equally divided between the enantiomorphous point groups (1, 2, 3, 4, 6) and non-enantiomorphous point groups (m, $mm2$, $3m$, $4mm$, $6mm$).
Trigonal crystals are divided into those which are represented by the hexagonal *P* lattice and those which are represented by the rhombohedral *R* lattice.

Table 2.5.1.1 - The seven crystal systems, their corresponding Bravais lattices and symmetries [2.5.1.4]

The table 2.5.1.2 is also taken from this book which denotes the allowed reflections from each crystal structure.

Bravais Lattice	Forbidden reflections	Allowed reflections
Primitive Cubic	None	Any h, k, l
fcc	h, k, l are mixed odd and even	h, k, l are all odd or all even
bcc	h + k + l is odd	h + k + l is even
Primitive Hexagonal	h + 2k = 3m and l is odd	All other cases
fcc	h, k, l are mixed odd and even	h, k, l are all odd or all even
	h + k + l is odd	
fcc	h, k, l are mixed odd and even; or, all even and h + k + l ? 4n	As fcc, but if all even and h + k + l ? 4n, then absent (n is integer)

Table 2.5.1.2 - Conditions of forbidden and allowed reflections (h k l) of common crystal structures [2.5.1.7].

Each structure also has a corresponding method in which to calculate the lattice parameters, namely **a**, **b** and **c** from each reflection and how it relates to the d-spacing between the lattice planes; here the selection is limited to the crystal structures that are dealt with in this thesis and these are shown in figure 2.5.1.6.

System	d_{hkl}
Cubic	$\left[\frac{1}{a^2}(h^2 + k^2 + l^2)\right]^{-1/2}$
Tetragonal	$\left[\frac{h^2 + k^2}{a^2} + \frac{l^2}{c^2}\right]^{-1/2}$
Orthorhombic	$\left[\frac{h^2}{a^2} + \frac{k^2}{b^2} + \frac{l^2}{c^2}\right]^{-1/2}$
Hexagonal	$\left[\frac{4}{3a^2}(h^2 + hk + k^2) + \frac{l^2}{c^2}\right]^{-1/2}$ hexagonal indexing
	$\left[\frac{1}{a^2}\frac{(h^2 + k^2 + l^2)\sin^2\alpha + 2(hk + kl + lh)(\cos^2\alpha - \cos\alpha)}{1 - 2\cos^3\alpha + 3\cos^2\alpha}\right]^{-1/2}$ rhombohedral indexing

Figure 2.5.1.6 - d-spacing for cubic, tetragonal, orthorhombic and hexagonal systems [2.5.1.5]

In order to now complete the setting for the Galfenol alloy, the following phase diagrams are presented in order to identify where each crystal structure resides. In figure 2.5.1.7 on the left is the current equilibrium phase diagram indicating the A2, B2, DO3, DO_{19} and L_{12} structures respectively; on the right is the *metastable* phase diagram which has been formed by a variety of methods including diffusion couple (DC), scanning electron microscopy (SEM), concentrated gradient method (CGM) and differential scanning Calorimetry (DSC) experiments.

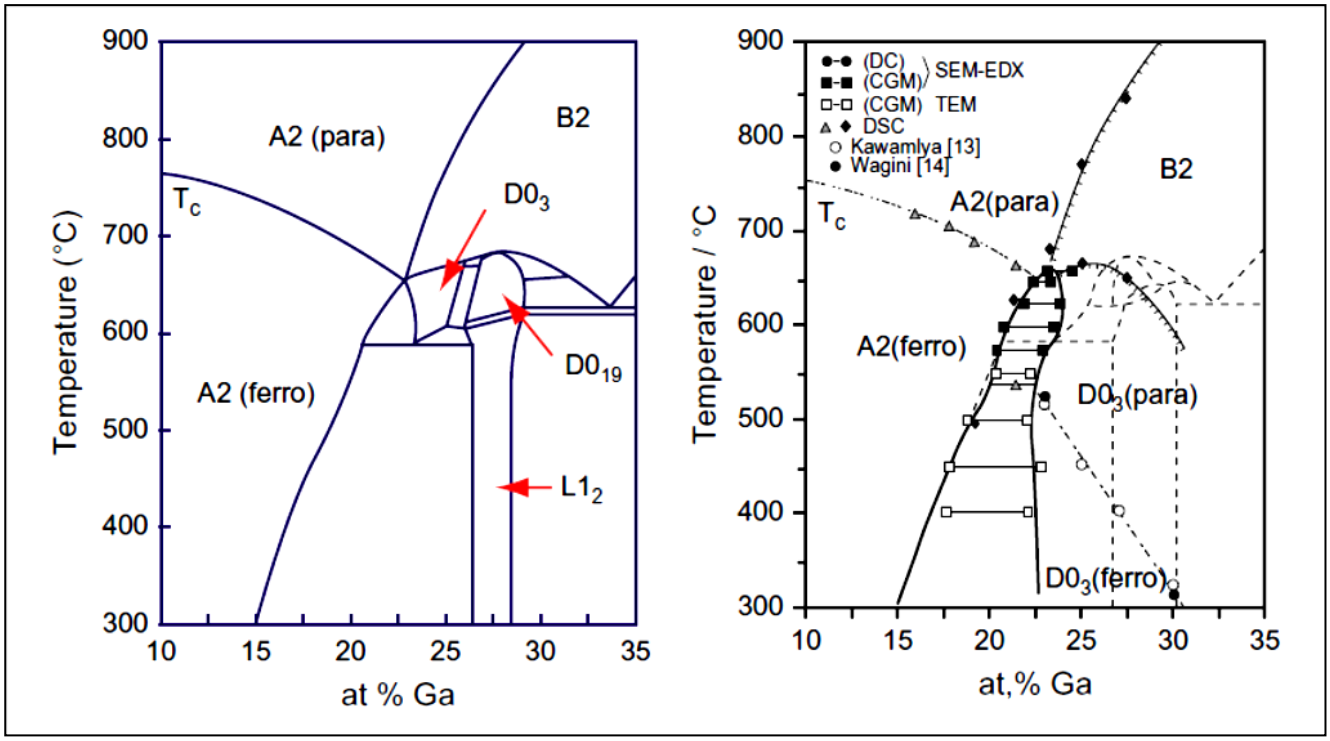

Figure 2.5.1.7 - Equilibrium phase diagram for Galfenol (left) and metastable and magnetic phase diagram (right) [2.5.1.6]

2.6 Chapter 2 References

[2.1.1.1] Nozedar, A., Element Encyclopedia of Secret Signs and Symbols: The Ultimate A-Z Guide from Alchemy to the Zodiac, Harper Element 2008. ISBN:9780007264452

[2.1.1.2] Gilbert, W., De Magnete, Dover Publications Inc. 1991. ISBN:048626761X

[2.1.1.3] Buschow, K.H.J, Handbook of Magnetic Materials, Volume 11, Page 309, Elsevier Science B.V. 1998. ISBN:9780444889522

[2.1.1.4] Earnshaw, S., On the Nature of the Molecular Forces which Regulate the Constitution of the Luminiferous Ether, Trans. Camb. Phil. Soc. **7**, 97-112. 1842. Images taken from: http://skullsinthestars.com/2009/04/13/levitation-and diamagnetism-or-leave-earnshaw-alone/

[2.1.1.5] Mahajan, A.S., Rangwala, A.A., Electricity and Magnetism, Tata McGraw-Hill Education, 1988. ISBN:9780074516393

[2.1.1.6] Image taken from: *AccessScience from McGraw-Hill*. [New York, N.Y.], McGraw-Hill Companies. 2000. http://www.accessscience.com/. ISSN:10978542

[2.1.1.7] Kittel, C., Introduction to Solid State Physics, 5th ed. Chapter 15, New York: John Wiley & Sons, 1976. ISBN:0471490245

[2.2.1.1] Image produced with CrystalMaker made by CrystalMaker Software Ltd. http://crystalmaker.com/crystalmaker/index.html

[2.2.1.2] Cullity, B.D., Introduction to Magnetic Materials 2nd Edition, John Wiley & Sons, Inc. 2008. ISBN:9780471477419

[2.2.1.3] Buschow, K.H.J., Handbook of Magnetic Materials Volume 20, Elsevier Science & Technology, North-Holland. 2012. ISBN:978044456374

[2.2.1.4] Aharoni, A., Introduction to the Theory of Ferromagnetism. Clarendon Press, 1996. ISBN:0198517912

[2.2.1.5] Chikazumi, S., Physics of Ferromagnetism Second Edition, Oxford University Press 2005. ISBN:9780199564811

[2.3.1.1] Smart, J.S., Effective Field Theories of Magnetism, Saunders, Philadelphia, 1966. ISBN:B0006BN9T2

[2.3.1.2] Image of a Typical Hysteresis Curve: http://www.ndted.org/EducationResources/CommunityCollege/MagParticle/Physics/HysteresisLoop.htm

[2.3.1.3] Stoner, E.C., Wohlfarth, E.P., Phil. Trans. Roy. Soc. **A240**:599–642. 1948.

[2.3.1.4] Spaldin, N.A., Magnetic Materials: Fundamentals and Device Applications, Cambridge University Press, 2003. ISBN:9780521016582

[2.3.1.5] Craik, D., Magnetism Principles and Applications, Pg 83-84, John Wiley & Sons, 1995. ISBN:9780471929598

[2.4.1.1] F.Bloch, Z. Physik **74, 295,** 1932.

[2.4.1.2] A. Hubert, Magnetic Domains: The Analysis of Magnetic Microstructures, Springer, 1998. ISBN:3540641084

[2.4.1.3] Cullity, B.D., Introduction to Magnetic Materials 2nd Edition, John Wiley & Sons, Inc. 2008. ISBN:9780471477419

[2.5.1.1] Hammond, C., The Basics of Crystallography and Diffraction 3rd Edition, Oxford University Press, 2009. ISBN:9780199546459

[2.5.1.2] The Fourteen Bravais lattices: Cullity, B.D., Elements of X-Ray Diffraction 2nd edition, Addison-Wesley, 1978. ISBN:9780201011746

[2.5.1.3] Buschow, K.H.J., Handbook of Magnetic Materials Volume 20, Magnetoelasticity of bcc Fe–Ga Alloys, Chapter 3, Pg 144. Elsevier Science B.V 2012. ISBN:978044456374

[2.5.1.4] Phillips, F.C., Introduction to Crystallography 3rd edition, Longmans. 1963. ISBN:0582441846

[2.5.1.5] Nuffield, A., Brooker, E., A General X-Ray Method for Orienting a Crystal, Acta Crysta, **20**, **496** 1966.

[2.5.1.6] Phase Diagrams: Ikeda, O., Kainuma, R., Ohnuma, I., Fukamichi, K., Ishida, K., J. Alloys Comp. **347, 198.** 2002.

[2.5.1.7] Liao, Y., Practical Electron Microscopy and Online Database, pp 4832, 2006. http://www.globalsino.com/EM/4832.htm

Chapter 3: Concise Literature Review of Galfenol Alloys

3.1 Early research of Galfenol

The first substantial results emerging from early research on Galfenol alloys performed by Dasarathy and Hume-Rothery back in 1965 **[3.1.1.1]** was the phase diagram for the Fe-Ga system as pictured in figure 3.1.1.1. Work had already been carried out on Cu-Al and Cu-Ga alloys and the similarities between the systems ascertained. Dasarathy noticed there was no known existing phase diagram for alloys of iron and gallium and set about work on examining the many compositions. In the diagram, the upright triangles represent the heating curve and the inverted triangles the cooling curve respectively.

The magnetostrictive properties of iron-gallium alloys at this time however were still unknown, so the focus of research in the 1960s and 1970s was purely of a structural nature, with several main contributors. Schubert and Meissner, along with Dasarathy, being the most prevalent, whom discovered a multitude of the crystal structures including the A2, B2, D019 and L12 phases within the iron-rich region; this was whilst working on a variety of metallic binary alloys all containing gallium **[3.1.1.3-3.1.1.4]**.

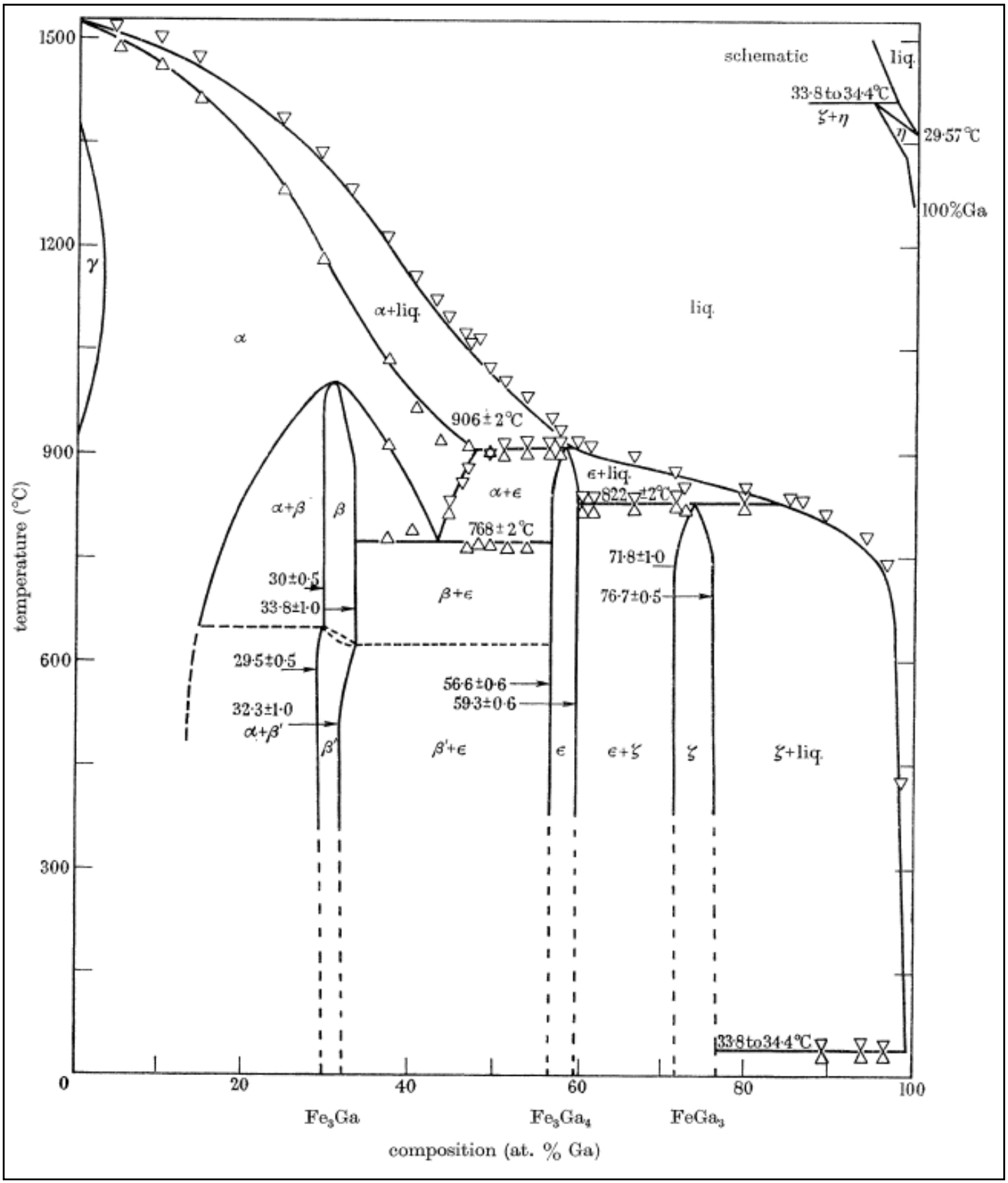

Figure 3.1.1.1 - Iron-Gallium equilibrium phase diagram, 1965 [3.1.1.1]

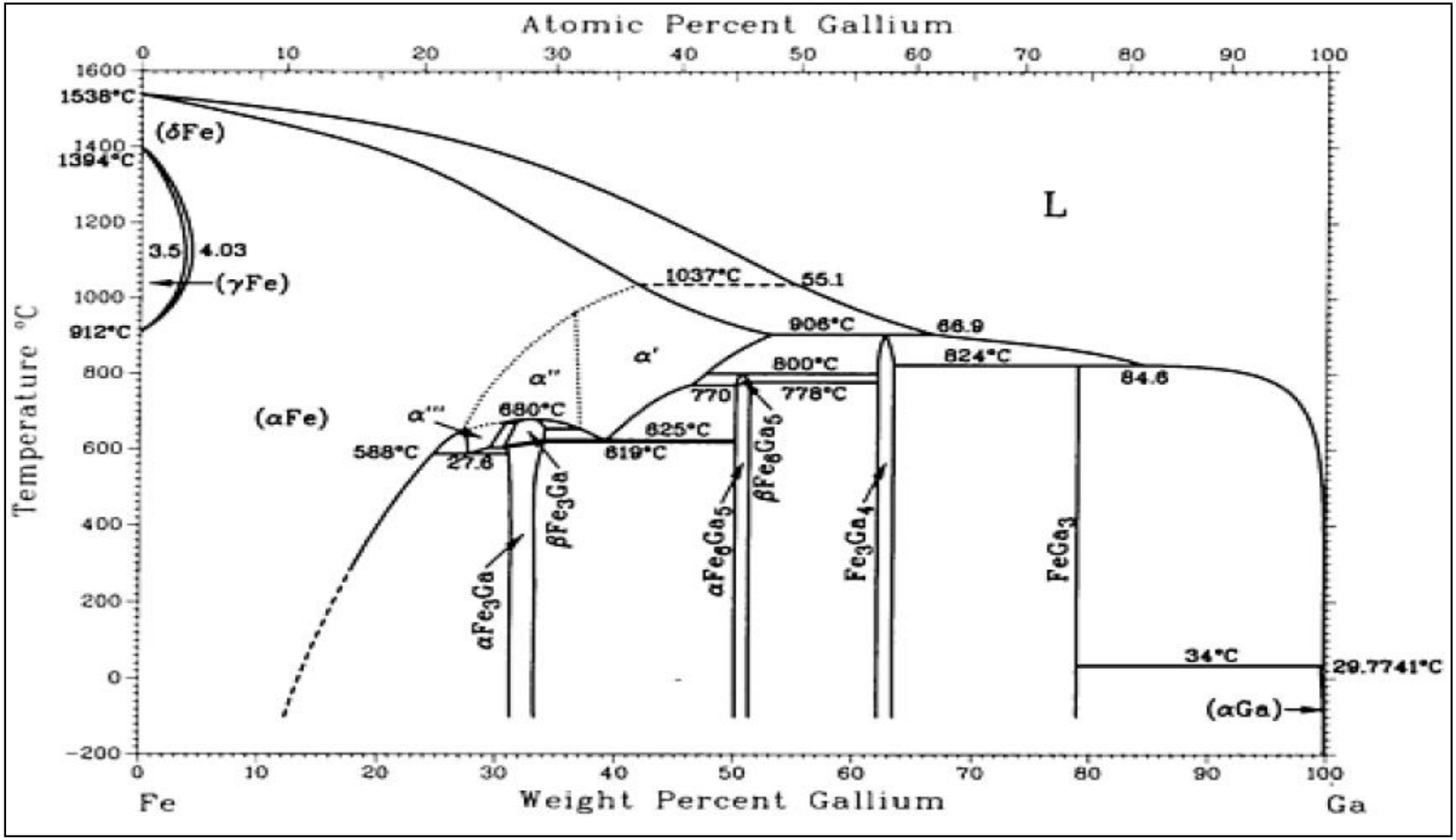

Figure 3.1.1.2 - Updated Iron-Gallium phase diagram by Okamoto [3.1.1.2]

The phase diagram has not been greatly modified since its creation, but has had additional exotic phases added in the 20 to 30 at. % Ga region by Okamoto in 1990. These extra regions in the composition range mentioned are at around the 600°C temperature region and were described by authors such as Suzuki, T.; et al and Buschow, K.H.J. et al and Kawamiya, N. who confirmed the more complex structures within the Galfenol system during the 1970-80s. **[3.1.1.5-3.1.1.7]**. The extra metastable diagram was also created (as seen in Chapter 2) so that the magnetic structure could also be added**;** the updated Okamoto diagram can be seen in figure 3.1.1.2.

Much of the work completed by these early researchers is still used today in the ASM book of binary alloy phase diagrams. It was then not until the 1990s that the material again became of any interest due to the need for giant magnetostrictive materials.

3.2 Discussion of Recently Published Literature

The giant magnetostrictive properties were not realised until the late 1990s, where Clark, whom was already working with the material Terfenol-D identified that some non-rare earth intermetallics could potentially be used as cheaper and more robust alternative to the brittle Terfenol-D. Several materials were considered all alloys of iron with metalloids and post-transition metals such as aluminium, silicon, germanium, indium and zinc. It was the iron-gallium alloy that became the primary material of focus **[3.2.1.1]**, as it displayed far greater magnetostrictive properties than any of the others tested. The commercial producer of Galfenol is Etrema Products Inc. based in Ames, Iowa, USA. Since it has regained popularity with researchers, the magnetostrictive properties have been heavily and thoroughly documented. Figure 3.2.1.1 shows the generally accepted magnetostriction curve versus composition for Galfenol alloys up to 40 at. % Ga; which appears in almost every publication relating to magnetostriction in Galfenol alloys. The two maxima

correspond to the values at ~19.5 and 27.5 at. % Ga for peaks in the magnetostrictive values respectively.

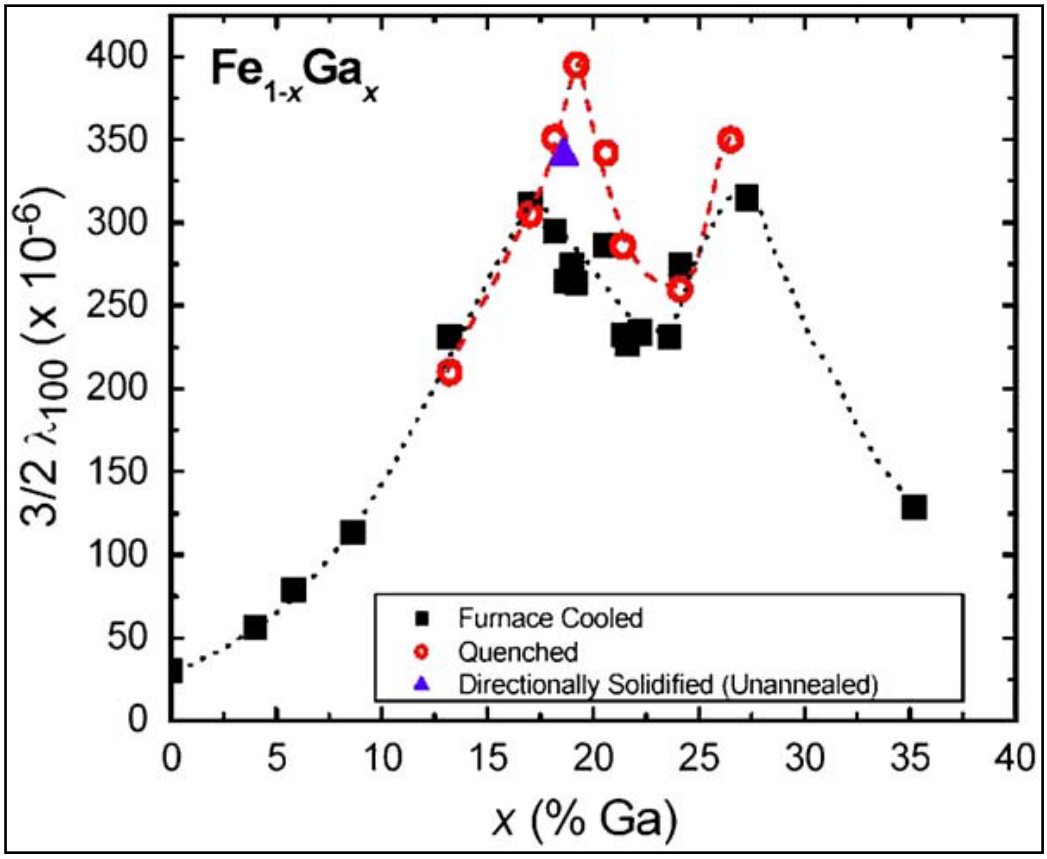

Figure 3.2.1.1 - Magnetostriction curve for Galfenol at. 0 to 40 % Ga (with relevant heat treatments) [3.2.1.11]

The peak at 19.5 at. % Ga has been characterised as a magnetostrictive maximum due to only the A2 disordered phase existing within the material or in some cases a very small amount of D03 phase, this causes internal strain and thus the material retains a high saturation magnetisation due to it being fe-rich and the magnetostrictive properties are caused by local interactions as the Ga atoms are far enough apart. Density functional theory (DFT), which is computationally complex, uses functions of another function, known as functional, to calculate the spatially dependant electron density in the ground state and the corresponding electron wavefunctions. These theoretical modelling calculations have been performed more recently by Paduani et al, and give good agreement with the experimental results for compositions of less than 20 at. % Ga **[3.2.1.12]**. As for the compositions above 20 at. % Ga,

it is generally accepted that a mixed phase alloy exists, but this can be suppressed by annealing-quenching techniques. There is much debate regarding which particular phases exist in this region and due to the lower compositions being accepted as understood, it has been these anomalous compositions of 20 to 35 at. % Ga that has been the focus of several research groups in the last few years **[3.2.1.2-3.2.1.5]**. The main arguments regarding the magnetostrictive behaviour are orientated on the Ga movement and distribution within the lattice. These properties are also dependant on the method used of producing the material, whether it is sputtered into a thin-film, melt-spun into a thin ribbon or grown as a single crystal. Some research groups are in favour of Ga-Ga pairing in the <110> directions in order to induce the strain **[3.2.1.6]**, whilst some others predict that nanoclusters of Ga atoms are randomly distributed in a larger matrix of A2 or B2 structures, the D03 structure inducing strain into the larger matrix **[3.2.1.7]**. The other alternative theory is that the lattice changes structurally from cubic-cubic to cubic-tetragonal with thermal treatment and thus alters the lattice parameters and internal strain of the structure. This manifests itself in the resultant x-ray diffraction scans which show both additional peaks and peak shifts from the original scan and as such, induces strain in the lattice. This additional strain induces the magnetostrictive maximum in the 27.5 at. % Ga composition **[3.2.1.8]**. Conclusive evidence proving any of these arguments beyond reasonable doubt has not been published as far as can be ascertained and all three arguments have their own points of merit. The main issue is that not everybody's experimental results agree and the theoretical DFT calculations are constrained as the use of larger unit cells are necessary to model the disordered distribution patterns, in particular for multiple-phase structures. Simulations with large unit cells are needed to provide meaningful statistics and a better understanding of geometric and magnetostrictive properties of binary or ternary Fe–Ga alloys with high at. % Ga content.

Experimental techniques also have their limitations, for example, when performing magnetic measurements, x-ray diffraction and neutron diffraction or thermal measurements using DSC, the material is examined as a whole; yet when examined by microscopy techniques such as SEM or TEM, then only a very small area is analysed. Therefore when studying Galfenol and similar intermetallics alloys, combinatorial *in-situ* experiments are the best method of examination. If any changes that occur can be observed on both macroscopic and microscopic scales then this provides the information required on how to understand these complex systems.

Other materials directly related to Galfenol have recently also become of interest due to Galfenol having a tendency to become brittle after slow cooling, such materials like Galfenol steels (Fe-Ga-Al-C) are being researched to produce viable and cheaper alternatives to Galfenol alone and has as such been patented in 2008 by the same owner as the original Galfenol patent **[3.2.1.9]**. Another advantage of these steels is that unlike the majority of giant magnetostrictive materials they do not require a pre-stress to achieve maximum magnetostriction after magnetic annealing treatment **[3.2.1.10]**.

Much more of the literature has been discussed further in chapters 4, 5 and 6 when comparing and contrasting the results presented in this work with the theoretical and experimental work in journals that have already been published.

3.3 Chapter 3 References

[3.1.1.1] Dasarathy C., Hume-Rothery W., The System Iron-Gallium, Proceedings of the Royal Society of London. Series A, Mathematical and Physical Sciences, Vol.**286**, No. **1405**, pp.141-157. 1965.

[3.1.1.2] Okamoto, H., The Fe-Ga (Iron-Gallium) system, Bulletin of Alloy Phase Diagrams, Volume **11**, Issue **6**, pp 576-581. 1990.

[3.1.1.3] Schubert, K., Bhan, S., Burkhardt, W., Gohle, R., Meissner, H.G., Pötzschke, M., and Stolz, E., Einige strukturelle Ergebnisse an metallischen Phasen (5), Naturwissenschaften, Volume 47, Number **13**, **303**, 1960.

[3.1.1.4] Meissner, H.G., Schubert, K., Zum Aufbau einiger zu T^5-Ga homologer und quasihomologer Systeme. I. Die Systeme Vanadium-Gallium, Niob-Gallium und Tantal-Gallium und die Struktur von Ti_6Sn_5(h), Z. Metallkd., Vol. **56**, p 475-484, 1965.

[3.1.1.5] Buschow, K.H.J., van Engen, P.G., Jongebreur, R. Magneto-optical properties of metallic ferromagnetic materials, Journal of Magnetism and Magnetic Materials, Volume **38**, Issue **1**, Pages 1-22, 1983.

[3.1.1.6] Suzuki, T., Oya, Y., Ochiai, S., The mechanical behaviour of non-stoichiometric compounds Ni_3Si, Ni_3Ge, and Fe_3Ga. Metallurgical and materials transactions A, Volume 15, Number 1, pp173-181, 1984.

[3.1.1.7] Nishino, Y., Matsuo, M., Asano, S., Kawamiya, N., Stability of the DO3 phase in $(Fe_{1-x}M_x)_3Ga$ (M=3d transition metal). Scripta Metallurgica et Materialia, **25**, 2291-2296, 1991.

[3.2.1.1] Kellogg, R.A., Flatau, A., Clark, A.E., Wun-Fogle, M., Lograsso, T.A., Temperature and Stress Dependencies of the Magnetic and Magnetostrictive Properties of $Fe_{81}Ga_{19}$, Journal of Applied Physics, vol.**91**, No.**10**, pp.7821, 2002.

[3.2.1.2] McClure, A., Li, H., Idzerda, Y.U., J. Appl. Physics, **107,** 09A924, 2010.

[3.2.1.3] Wang, Z.B., Liu, J.H., Jiang, C.B., Chin. Phys. B **19** 117504, 2010.

[3.2.1.4] Wu, R.Q., J. Appl. Physics **91** 7358, 2002.

[3.2.1.5] Grössinger, R., Sato-Turtelli, R., Mehmood, N., Heiss, S., Müller, H., Bormio-Nunes, C., Giant magnetostriction in rapidly quenched Fe–Ga?, Journal of Magnetism and Magnetic Materials, Volume **320**, Issue **20**, Pages 2457-2465, 2008.

[3.2.1.6] J. Cullen, P. Zhao, and M. Wuttig, Anisotropy of crystalline ferromagnets with defects, J. Appl. Phys. **101**, 123922, 2007.

[3.2.1.7] Wu, R., Origin of large magnetostriction in FeGa alloys J. Appl. Phys. **91**, 7358 2002

[3.2.1.8] Wang, H., Zhang, Y. N., Yang, T., Zhang, Z. D., Sun, L. Z., Wu, R. Q. , Ab initio studies of the effect of nanoclusters on magnetostriction of $Fe_{1-x}Ga_x$ alloys, Appl. Phys. Lett. **97**, 262505, 2010

[3.2.1.9] Clark, A.E. et al, United States patent application, US2008/0011390A1, 2008.

[3.2.1.10] Borrego, J.M., Blazquez, J.S., Conde, C.F., Conde, A., Roth,S., Intermetallics **15** 193, 2007.

[3.2.1.11] Brooks, M., Summers, E., Restorff, J. B., Wun-Fogle, M., Behaviour of magnetic field–annealed Galfenol steel, J. Appl. Phys. **111**, 07A907, 2012.

[3.2.1.12] Paduani, C., and Bormio-Nunes, C., Density functional theory study of Fe_3Ga, J. Appl. Phys. **109**, 033705, 2011.

Chapter 4: Neutron Diffraction, Mössbauer and X-Ray Diffraction Studies.

4.1 Physical Compositions of Iron-Gallium Ribbons

The ribbons were produced for the University of Salford by Nicoleta Lupu and Horia Chiriac at the National Institute of Research and Development for Technical Physics, Romania. Ingots of $Fe_{100-x}Ga_x$ with x = 12.8, 17.5, 19.5, 22.5 and 27.5 at. % Ga were prepared by co-melting the appropriate amounts of high purity (99.9%) constituent elements in an argon arc furnace and then melt-spun as shown in figure 4.1.1.1.

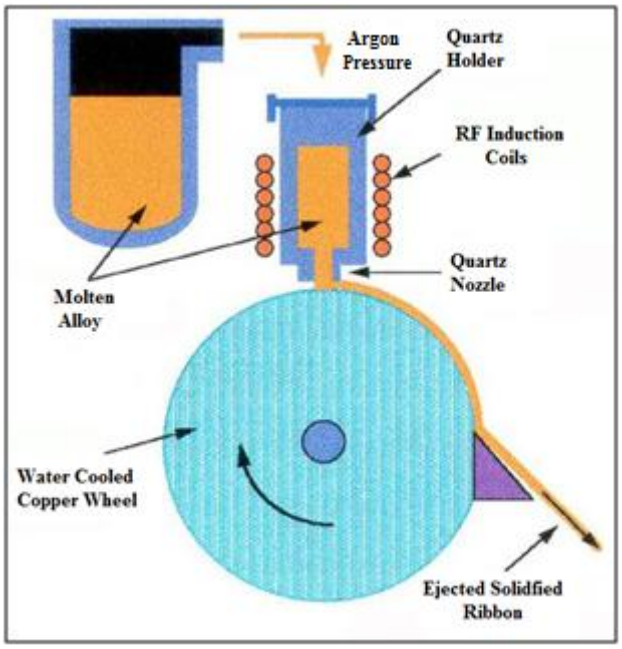

Figure 4.1.1.1 - Schematic of the melt-spinning process [4.1.1.1]

When the induction coils are activated, a jet of molten alloy is ejected from the quartz nozzle due to the Argon gas pressure from above. The molten metal is subject to rapid solidification upon landing onto the fast rotating water cooled copper wheel. The resulting alloy formed can be amorphous or polycrystalline depending upon the cooling rate. For the case of Galfenol alloys, they are polycrystalline in nature. The wheel had a tangential speed of ~35ms^{-1}.

The as-spun ribbons showed varying ductility, the 12.8, 17.5 and 19.5 at% Ga all of which displayed good workability and pliability. The 22.5 and 27.5at% Ga were slightly more brittle than the previous compositions but still showed potential for use in physical applications.

Some of the samples were annealed using an argon vacuum furnace and were heated to 1000°C for 24 hours before being quenched into ice cold water. The annealed ribbons displayed much more brittle characteristics with reduced ductility, the 19.5 and 27.5 at. % Ga particularly so; these had in some cases due to the annealing process formed into tightly packed folded ribbon arrangements which when attempted to be separated would easily turn into small flakes or even a rough powder-like substance.

4.2 Neutron and Mossbauer Analysis

4.2.1 The Institute Laue-Langevin Neutron Source in Grenoble, France.

The neutron experiments performed in this work were carried out at the Institute Laue-Langevin (ILL) in Grenoble, France as can be seen in figure 4.2.1.1.

The reactor core is comprised of a single highly enriched 10 kilogram uranium fuel element that is cooled by deuterium oxide (D_20 or heavy water). The reactor produces the most intense and continuous neutron flux in the world, a maximum of 1.5 x 10^{15} neutrons cm^{-2} s^{-1}. The reactor has a maximum thermal output power of 58 Megawatts.

Figure 2.2.1.1 - The Institute Laue-Langevin in Grenoble, France. [4.2.1.1]

The thermal output is not reused and the excess heat is removed by a secondary cooling system supplied with water from the nearby river Drac. The heavy water vessel that contains

the nuclear core is situated in a pool filled with demineralised water which provides shielding from the neutron and gamma radiation produced by the core. The reactor is controlled by means of a neutron-absorbing rod made of boron, which is gradually withdrawn from the core as the uranium is gradually used up in order to maintain criticality. There are also five safety rods, all with high neutron absorbing attributes; these are automatically controlled by a sophisticated detection system and are inserted into the core to shut down the reactor in the event of an emergency without the requirement of electrical power. **[4.2.1.1]**

4.2.2 The D2B Diffractometer

The instrument used in the neutron research presented here was the D2B powder diffractometer situated within the ILL. D2B is designed as a very high-resolution instrument and is limited only by powder particle size. It also has an alternative high flux mode providing a much higher intensity of neutrons whilst still maintaining good resolution. The D2B is characterised by the very high take-off angle (135°) for the monochromator, which has a relatively large spread of 20' to compensate for the corresponding neutron intensity ($\Delta l / l$) losses. It is 300 mm high, focusing vertically onto about 50 mm. This large incident vertical divergence is matched by using 200 mm high detectors and collimators, a schematic diagram of the D2B instrument can be seen in figure 4.2.2.1. A complete diffraction pattern is obtained after about 25 steps of 0.05° in 2θ, since there are 128 individual ^{3}He detectors spaced at 1.25° intervals. A normal single scan takes typically 30 minutes; they are often repeated several times to improve statistics or allowed to run over much longer periods. The D2B is particularly well suited for the Rietveld refinement of relatively large complex structures; as Rietveld requires sharp diffraction peaks and the D2B provides this as the neutrons diffract off the nuclei of atoms (rather than off the electron cloud as with X-ray diffraction) and the D2B helium detectors are highly sensitive to the diffracted neutrons and thus give a very accurate diffraction pattern.

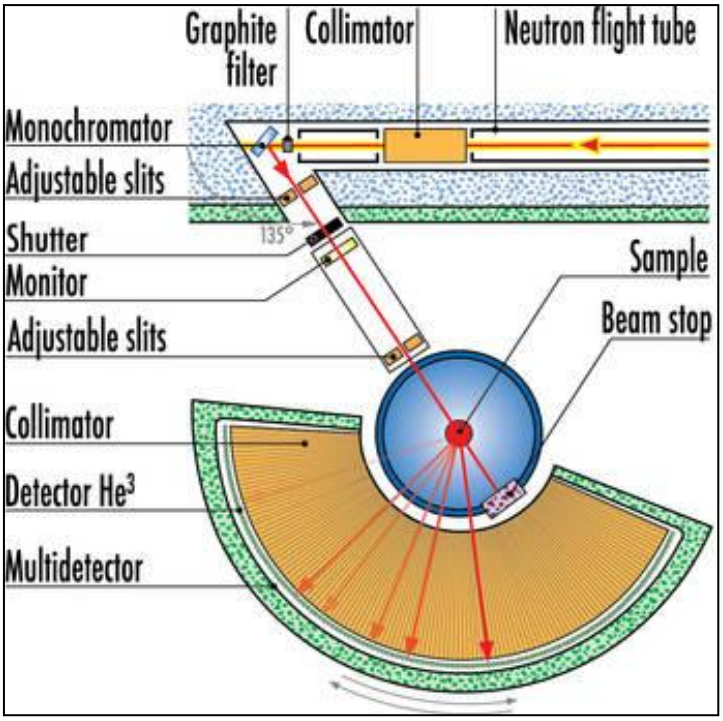

Figure 4.2.2.1 - Schematic Diagram of the D2B Powder Diffractometer at the ILL in Grenoble. [4.2.2.1]

The efficiency of D2B was increased in April 2008 by an order of magnitude making it now possible to measure small samples of about 200 mg. D2B was also designed for work on magnetic samples and for the high resolution scanning of materials with large d-spacings when using wavelengths of between 2.4 Å and 6 Å. Wavelengths can easily be changed under computer control, since they are all obtained by the simple rotation of a germanium crystal. A large graphite filter can be switched on to provide a very clean beam at 2.4 Å and a cold Be-filter can be used if longer wavelengths are required. The optimum wavelength for the instrument is 1.594 Å and for high resolution scans a flux of 10^6 neutrons c m^{-2} s^{-1} is used and for high intensity scans a flux of 10^7 neutrons c m^{-2} s^{-1} is selected. In the case of the work carried out here, typical scans were of the time period of 7 to 8 hours each, in order to achieve a higher average data count per scan. **[4.2.2.2]**

4.2.3 Principles of Neutron Diffraction

In general all the nuclei of atoms consist of protons and neutrons. The proton being positively charged, the neutron having zero net charge. The neutron though does have a magnetic moment and a half spin component both of which can be exploited to be used in experiments with their own merit. Neutrons are beneficial as unlike X-Rays they do not permanently damage inorganic matter and most samples, apart from being *hot* for a period of time later are reusable. When using neutrons in diffraction experiments, it is taken into account that neutrons also possess wave-like properties in addition to their particle like nature; this is described by using the De Broglie relationship given in equation 4.2.3.1.

$$\lambda = \frac{h}{p} = \frac{h}{mv} \qquad \textbf{(4.2.3.1)}$$

Where λ is the De Broglie wavelength of the neutron, h is the Planck constant, p is the momentum, v is the velocity of the neutron and m is the particle rest mass which is given as 1.67495×10^{-27} kg for the neutron. Also here we define the wavevector k which is defined as $2\pi/\lambda$. It is possible therefore to change the perceived wavelength of the neutron by altering its velocity, for example to achieve a de Broglie wavelength of 1 Å, then a neutron velocity of 4000 ms^{-1} is required or we can formulate an equation for the required energy, E, of the scattering experiment as shown in equation 4.2.3.2.

$$E = \frac{h^2}{(2m\lambda^2)} = \frac{\hbar^2 k^2}{2m} \qquad \textbf{(4.2.3.2)}$$

Where (h-bar) $\hbar = h/2\pi$. On the basis of the amount of energy they possess, neutrons are classified (in increasing energy) as ultra-cold, very cold, cold, thermal, epithermal and fast. In the case of thermal neutrons as are used in the diffraction experiments carried out in this thesis, the energy per neutron is ~0.0322 eV (32meV), which equated to a mean velocity of 2482 ms^{-1} or a de Broglie wavelength of ~1.594Å, this corresponded to a neutron temperature of 290 K which was calculated by the temperature of the moderator used for the experiment. **[4.2.3.1]**

The neutrons start off as *fast* neutrons from the core of the reactor but are then moderated by a series of materials, for the D2B machine, this is D_2O (Heavy water), H_2O (light water) and then graphite respectively.

Neutrons are a useful tool in the probing of materials as they can interact in different ways with the target lattice. A target nucleus gives rise to a nuclear scattering event, but also there can be interaction via a dipole-dipole interaction which is considered a magnetic scattering event (although this usually requires polarised or spin-flipped neutrons). In this work the diffraction studies undertaken just take into account what is termed *Bragg scattering*, which is not dissimilar to a Young's slit experiment but utilising a much smaller wavelength of photon (or wave-like properties of a particle). In order for constructive interference to be achieved, the interfering beams must be an integer number of wavelengths different in order to be parallel, coherent and collimated and the scattering is considered elastic.

The Bragg-Law for a scattering event from a neutron colliding with a nucleus is not dissimilar to that of X-Ray diffraction (XRD) or transmission electron diffraction from a crystal and as such the Bragg equation is given in equation 4.2.3.2 and a simple schematic of this can be found in figure 4.2.3.1.

$$n\lambda = 2d \sin\theta \qquad \textbf{(4.2.3.2)}$$

Here $\boldsymbol{\lambda}$ is the wavelength (or de Broglie wavelength) d is the interplanar spacing and θ is the angle of incidence the incoming wave makes with the lattice alternatively known as the grazing angle, n is a constant relating to an integer value of 1, 2, 3 etc which is the *order* of the diffraction. There are other forms of scattering such as small-angle, wide-angle, inelastic and diffuse but with this particular experimental work the elastic scattering was of main importance. The Bragg diffraction angle will give all orders of refraction up to the finite limit which is when $n\lambda = 2d$.

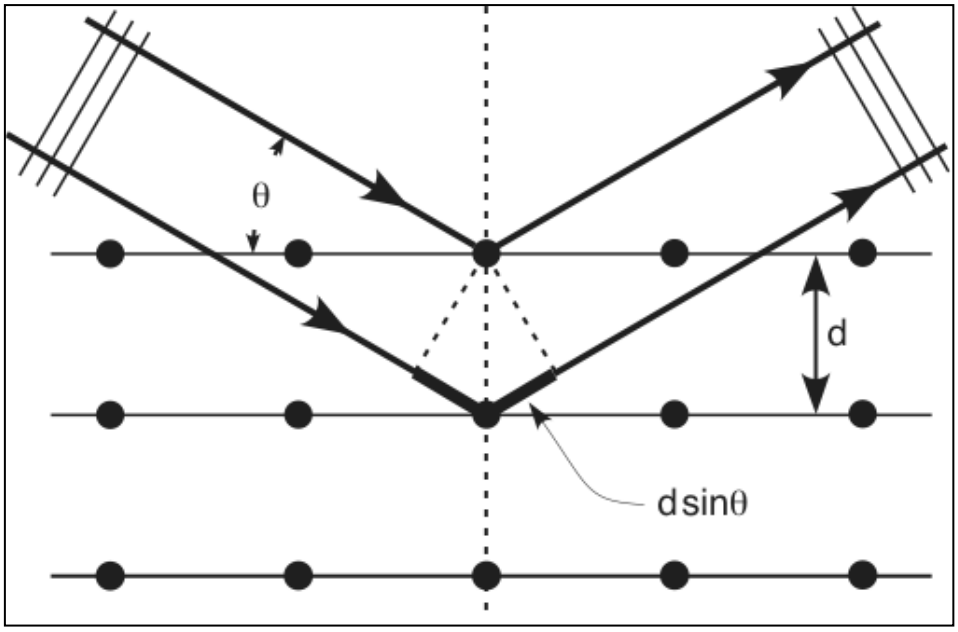

Figure 4.2.3.1 - Schematic of the Bragg Diffraction Diagram [4.2.3.2]

The uniform repetitive pattern of a crystal lattice allows for certain values of the relevant miller indices termed [hkl], in 3d-space to either be constructive or destructive which gives the relevant diffraction pattern, but the limits of this must be ascertained.

If there is an NaCl crystal with the [111] reflection peak, then the [222], [333] and [444] will also be allowed all having different angles of 2θ; yet the value of d must be the same for all of these reflections as the spacing is a constant and the order value n increasing. The concept implicated here is that not all lattice planes will produce a measurable diffraction and that as higher numbered planes are reached, it is much harder to represent these in normal 3-d space, even if using vectors removes some dimensional effects, for example a plane with the index [257] would be extremely difficult to represent due to the density of vectors representing the other planes within a diagram. Here, the reciprocal lattice (also called reciprocal space) is used alongside a concept known as the Ewald Sphere designed by P.P. Ewald **[4.2.3.3]** and makes use of the reciprocal of d_{hkl} to allow a 3-dimensional geometrical construction of the data set and serves as a good visual representation of understanding the diffraction results. Ewald suggested that by using a sphere of radius $1/\lambda$ and instead of drawing the d_{hkl} vectors in

real-space; that plotting the reciprocal lattice of these points would greatly help; as this would allow for the relevant indices to be plotted as a simple lattice, this equation is given in 4.2.3.3.

$$d^*_{hkl} = \frac{1}{d_{hkl}} \qquad (4.2.3.3)$$

This allows for figure 4.2.3.2 to be drawn representing a 2-d lattice of reflections in one particular plane. The [hk0] plane is used in this example as the ***l***-plane has been set to zero for simplicity. It is now possible to say that from the origin point of [000] it is possible to get to any other point by addition or subtraction of vectors by moving ***h*** in steps of ***a****, ***k*** in steps of ***b**** and ***l*** in steps of ***k****. This gives the vector addition equation given in 4.2.3.4.

$$d^* = ha^* + kb^* + lc^* \qquad (4.2.3.4)$$

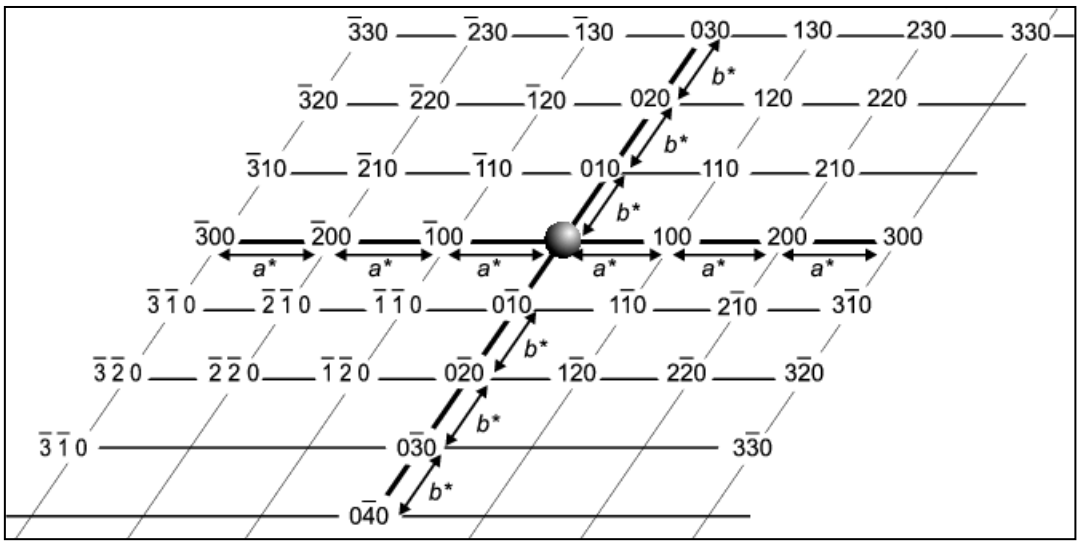

Figure 4.2.3.2 - Reciprocal 2D Lattice of d_{hkl} showing the h and k planes. [4.2.3.3]

The reciprocal lattice here is simply the allowed geometric reflections from the Ewald sphere. Any rotation of the sample studied will also rotate the real-space lattice; hence the reciprocal lattice will also be affected by this rotation due to the way it has been defined. Figure 4.2.3.3 shows how the Ewald sphere acts at a specific time, here the (230) point is the one of interest.

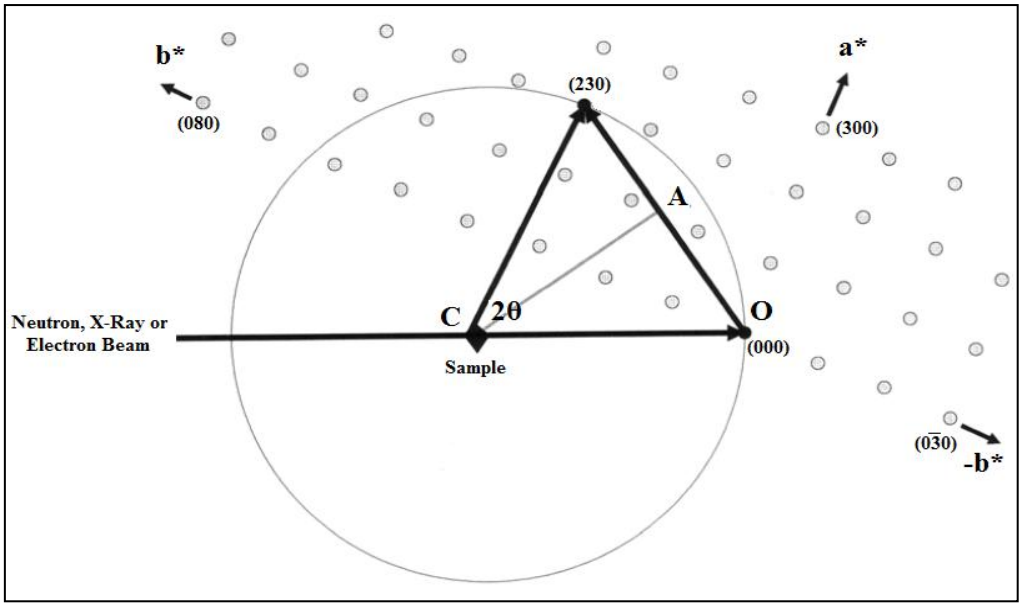

Figure 4.2.3.3 - Ewald Sphere Projection onto the point (230). [4.2.3.3]

Here the reciprocal lattice point of focus $\boldsymbol{d^*_{(230)}}$ so it is possible to equate the diagram mathematically using simple geometry. Here it shows that distance CO is the radius of the sphere, thus $CO = \frac{1}{\lambda}$ and that also $OA = \frac{d^*_{(230)}}{2}$ and using these two components equation 4.2.3.5 is easily formed.

$$sin\theta = \frac{OA}{CO} = \frac{\frac{d^*_{(230)}}{2}}{\frac{1}{\lambda}} \text{ which simplifies to: } \lambda = \frac{2\,sin\theta}{d^*_{(230)}} \qquad (4.2.3.5)$$

From the reciprocal definition of the reciprocal lattice vector to that of the real-space lattice, we get $d_{(230)} = \frac{1}{d^*_{(230)}}$ and thus finally arrive back to the original real-space Bragg diffraction equation $(\lambda = 2d\,sin\theta)$ as given previously in equation 4.2.3.2.

This particular theory applies to three of the different elements within this thesis, namely, neutron diffraction, x-ray diffraction and electron diffraction, so this section will be referred back to for the basic principles of the mathematics of the reciprocal lattice, real-lattice and resultant diffraction pattern(s) as it is the same for all three diciplines. Any more complex

interactions regarding the differences between the three disciplines will be mentioned within each individual section.

4.2.4 Principles of Mossbauer Analysis

Mössbauer spectrometry utilises a quantum-mechanical effect and provides a crucial link between nuclear and solid state physics. In essence this effect measures the spectrum of energies in which the nucleus of one atom emits and another absorbs γ-rays. In order for this effect to take place the two atoms must in some way be bonded together within a solid, similar to that of a coupled harmonic oscillator. This was first observed by Rudolf Mössbauer using ^{191}Ir in 1958 **[4.2.4.1]** based on the earlier work performed using neutron resonant scattering as undertaken by W. E. Lamb in 1939. **[4.2.4.1]** There are several potential sources that can be used in this type of spectrometry, the ones now primarily used being ^{57}Fe, ^{119}Sn, ^{151}Eu, ^{121}Sb and ^{161}Dy. The main principle involved here are the *hyperfine interactions* in which the electrons surrounding a nucleus occupy the various discreet quantum nuclear states, these interactions with the nucleus cause small perturbations or changes in the transmitted and detected energies of the γ-rays. These discreet energy changes can be observed with a relatively inexpensive Mössbauer spectrometer. The perturbation energies are of the order 10^{-9} to 10^{-7} electron volts compared to the energies of the γ-rays themselves which are of much higher, typically 10^{4} to 10^{5} electron volts.

There are four measurable quantities using the Mössbauer approach which are the *recoil-free fraction* and the hyperfine interactions, which are divided into three separate quantitive elements known as, *isomer shift*, *electric quadrupole splitting* and the *hyperfine magnetic field*. **[4.2.4.2]**

The peaks in the resultant Mössbauer spectrum undergo observable energy shifts when the Mössbauer atom is within different materials. These shifts arise from the hyperfine interactions of the nucleus and the inner electrons, these are termed *isomer shifts*. There are

two concepts that describe the origins of these shifts, the first being the allowance of the electron wavefunctions that interact directly with the wavefunction of the nucleus and secondly, the nuclear radius changes in size depending on whether it is in the ground (R_g) or excited state (R_e). In ^{57}Fe, the nuclear radius is actually smaller in the excited state. Therefore if there is a constant charge density coupled with an overlap of a finite nucleus size, the total electrostatic attraction is increased when the nucleus is reduced in size (for Fe). This energy shift manifests itself as a shift in the position of the absorption peak of the observed spectrum and is given by equation 4.2.4.1.

$$\Delta E_{is} = C\,Z\,e^2\left(R_e^{\,2} - R_g^{\,2}\right)\left|\Psi_{sample} - \Psi_{source}\right|^2 \qquad (4.2.4.1)$$ **[4.2.4.3]**

Here *C* is a factor which is shape dependant on the charge distribution. If there is an increase in the s-electron density near the nucleus the spectral peaks will be shifted to more negative velocities. This isomer shift is source dependant, as with a ^{119}Sn nucleus the opposite to that of ^{57}Fe occurs, in an excited state its nucleus actually increases in size so the peaks would be shifted positively in this case. **[4.2.4.4]**

The isomer shift, though, is not simply a case of the s-orbital densities within the atom. In Fe it is well documented how the *3d* electrons act as a barrier to the nuclear charge for the *4s* electrons, thus if the *3d* band is more densely populated the screening effect is greater; thus reducing the perceived *4s* electron density in turn causing a positive isomer shift in the observed spectrum. Although this has been proven for most metallic compounds, it has been documented and accepted that in Fe-alloys the isomer shift does not depend on the *3d*-density but on the charge transfer of the *4s* electrons resulting in an isomer shift value of -3.55×10^{-32} mm s^{-1}**. [4.2.4.4]**

The isomer shift is a result of an electric monopole interaction as there is no *static* dipole moment of a nucleus, thus the *electric quadrupole splitting interaction* depends upon the shape of the nucleus. The spin of the nucleus determines its asymmetric shape and its shape

will change in the event of a transition from a ground to excited state or vice-versa which in effect also changes its spin characteristic. In an electric field gradient there are different energies relating to different alignments of the quadrupole moment. The electric field gradient must change depending upon the components of the electric field vector. An ^{57}Fe nucleus has an excited state spin of I = 3/2 and a ground state spin of I = 1/2; the shape of the excited state being that of a prolate spheroid. If the nucleus interacts with an electric field gradient then it would point along the z-axis of the field gradient when $I_z = \pm 3/2$, the excited state energy is separated into two distinct levels, yet the ground state is not separated. The electric quadrupole moment for the excited state is defined as *Q*, the energy level splitting is given in equation 4.2.4.2.

$$\Delta E_q = \frac{\pm 1}{4} eQV_{zz} \left(1 + \frac{\beta^2}{3}\right)^{\frac{1}{2}} \qquad (4.2.4.2)\ \textbf{[4.2.4.5]}$$

β is related to the relevant field gradients, V_{zz} is the larger gradient along the z-axis of the field. The corresponding energy level diagram can be found in figure 4.2.4.1, where the isomer shift and electric field gradients are shown. The electric field gradient is zero when the Mössbauer isotope has a cubic symmetry, so when the ^{57}Fe atom has a 3d-electronic structure V_{zz} becomes very large. The quadrupole splitting is sensitive to local environments and the high spin Fe differences can be identified using this method.

Hyperfine magnetic field splitting is associated with the nuclear magnetic dipole moment and the corresponding spin when experiencing a magnetic field environment. Depending upon the magnetic field, the spins can be orientated with different directions within the field, thus the transitions are more complex when a nucleus encounters a magnetic field. The hyperfine magnetic field (HMF) is analogous to the Zeeman Effect where there is a splitting of the energy levels of the electrons when they experience a magnetic field. The HMF allows for all the degeneracies of the spins for the nucleus which results in six separate transitions that can be observed within Mössbauer spectra.

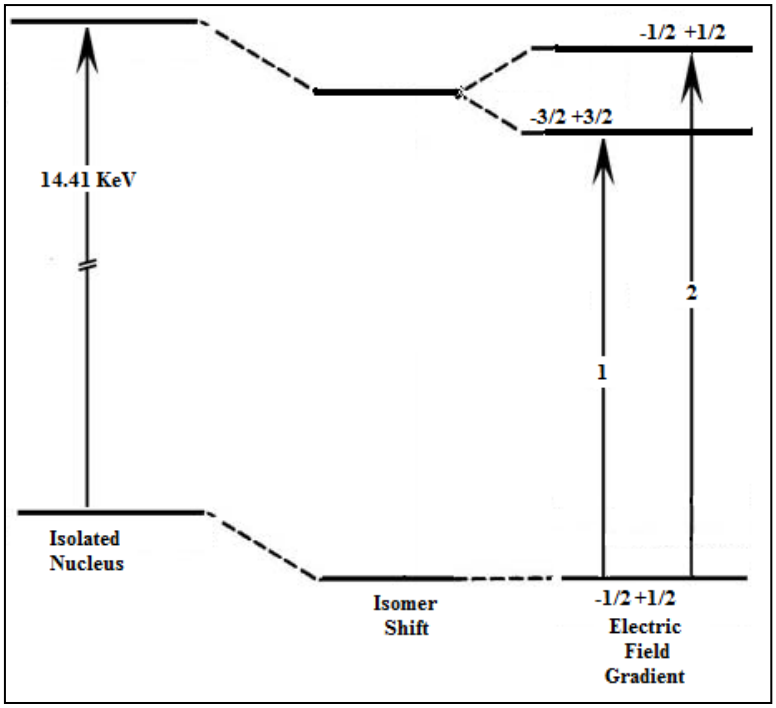

Figure 4.2.4.1 - Energy Level Diagram for ^{57}Fe in an Electric Field Gradient.

The $\boldsymbol{I_z}$ can now cover all of the states from $\boldsymbol{-I}$ to $\boldsymbol{+I}$ using all of the combinations of excited states and ground states, these being (+3/2, +1/2, -1/2 and +1/2) for the excited state and (+1/2 and -1/2) for the ground state. The allowed transitions are governed by selection rules given by M1 magnetic dipole radiation. For the ^{57}Fe atom, the following hyperfine field transitions are allowed:

(-1/2 → -3/2) (-1/2 → -1/2) (-1/2 → +1/2) (+1/2 → -1/2) (+1/2 → +1/2) (+1/2 → +3/2) **[4.2.4.6]**

These six allowed transitions are shown in figure 4.2.4.2.

In ^{57}Fe at room temperature, the magnetic flux density of the nucleus is observed to be 33.0 Tesla **[4.2.4.6].** This extremely large value indicates that the cause of this cannot be described by the traditional theories of magnetism. There is an additional reduction in magnetic splitting in the Mössbauer spectra when an external magnetic field is applied. This suggests that the HMF of the nucleus has an opposite sign to that of the crystal lattice in which it resides, thus the HMF is given as -33.0 Tesla. The classical contributions to the HMF are termed H_{mag}, H_{dip} and $H_{orb,}$ and here they are briefly discussed as to the impact each has on the overall HMF.

H_{mag} is the contribution from the lattice magnetisation, M which equates to $4\pi M/3$. Additionally, the contribution from any additional fields applied externally must be considered and any demagnetisation effects subtracted. H_{mag} has a value of ~0.7 Tesla or less. **[4.2.4.5]** H_{dip} is the classical dipole moment addition to the field caused by the atoms within the vicinity of the Mössbauer nucleus. In pure iron, this term is neglected due to cubic symmetry but within alloys of iron such as with Ga, small contributions are possible as the addition of non-magnetic atoms can alter the symmetry and cause a net moment, although the value of this is given as ~0.1 Tesla. **[4.2.4.5]** H_{orb} results from the orbital magnetic moment of the Mössbauer atom that is not removed by the interaction with the crystal lattice; this contributes ~2 Tesla **[4.2.4.5]** and can possibly change quite dramatically with the addition of nonmagnetic atoms to the metal. Here, with simple addition it is clear that only around 3 Tesla has been accounted for and there must be a much larger contributor to the HMF than any of the above three.

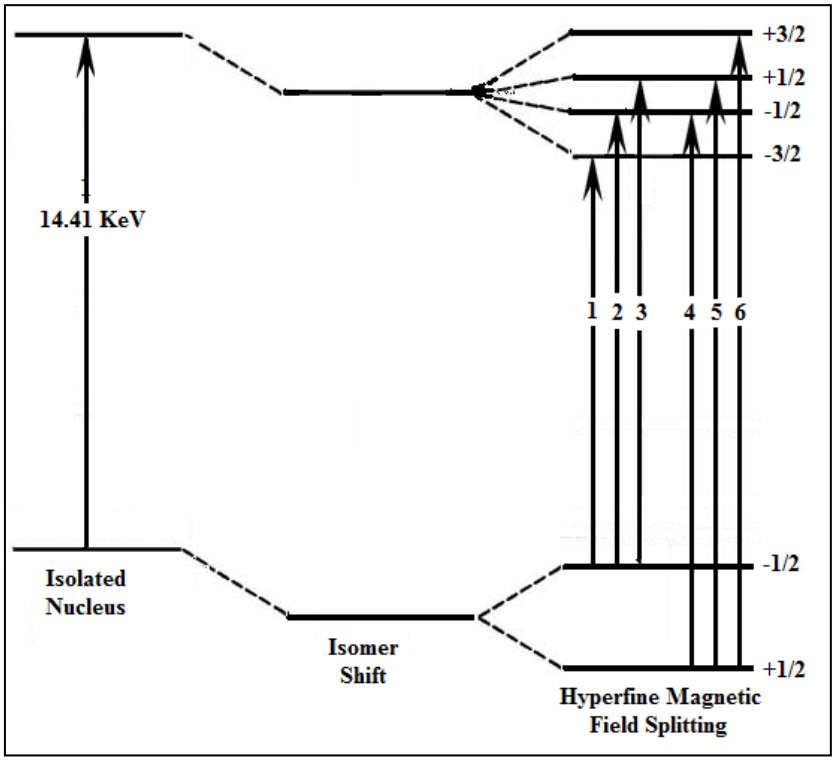

Figure 4.2.4.2 - Energy Levels for a Magnetic Hyperfine Field (Transition Energy Increases from 1 through 6)

The additional large field is supplied by what is termed the *Fermi contact interaction*, H_{FC} which is an additional term for the interaction of a nucleus and an electron. The Dirac equation is given in equation 4.2.4.4 where Serge and Fermi **[4.2.4.7]** realised that a new term was required which allows for the interaction of the spin operators.

$$H_{FC} = -\frac{8\pi}{3} g_e g_n \mu_e \mu_n \boldsymbol{I}\cdot\boldsymbol{S}\, \delta(r) \qquad (4.2.4.4)\ \textbf{[4.2.4.7]}$$

Termed $\boldsymbol{I}$ and $\boldsymbol{S}$, these operate upon both the nuclear and electron wavefunctions. μ_e and μ_n are the nuclear and electron magnetons respectively and the $\delta(r)$ term means that this is a function of distance from the nucleus and ensures that the electron wavefunction is quantified at the nucleus. g_e and g_n are the electron and nuclear gyromagnetic ratios, which give the ratio of the nuclear spin to the nuclear magnetic moment. Nuclear ground and excited states differ from that of electrons, where the nucleus does not have the same value for g_n. In ^{57}Fe, the nuclear magnetic moment differs by a factor of -1.7145 due to the fact the nucleus decreases in size when transforming from the excited state to the ground state. It is now possible to define the Fermi contact energy by placing the nuclear magnetic moment within a magnetic field, H_{eff}, this is defined in equation 4.2.4.5.

$$H_{eff} = \frac{8\pi}{3} g_e \mu_e S\, |\Psi(0)|^2 \qquad (4.2.4.5)\ \textbf{[4.2.4.7]}$$

The electron spin is still either ±1/2 and the $|\Psi(0)|^2$ term gives the total electron density contribution at the nucleus. To have a large overall HMF, there must be an imbalance of electron pairs near the nucleus, as electrons with equal charge and opposite spin will just negate each other. As ferromagnetism arises due to the imbalance in the 3d-electron orbits, this has a marked effect on the 2s electrons. There are more 3d-spin up electrons than spin down, thus in the lower 2s shells there is now a greater number of 2s-spin down electrons than spin up, these contribute greatly (also with the inner 1s shell) so that the HMF is opposite in magnitude to that of the lattice, which is dominated by the unbalanced 3d spin up electrons. **[4.2.4.7]**

A simple schematic of the Mössbauer experimental set up can be seen in figure 4.2.4.3

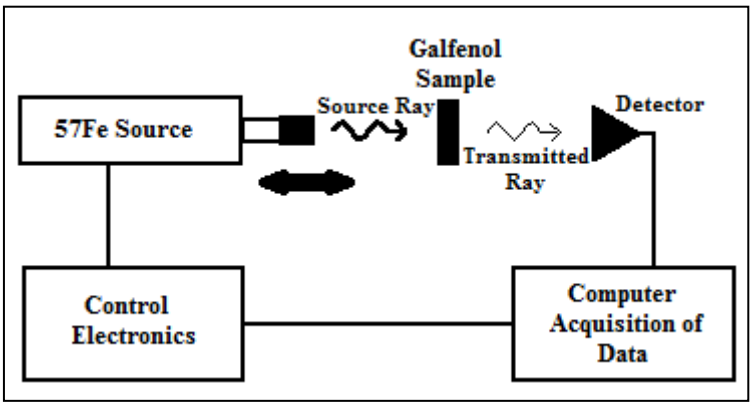

Figure 4.2.4.3 - Schematic of the Mössbauer Spectrometer.

The sample is vibrated back and forth in order to Doppler shift the emitted gamma rays, as the scanned energies of the gamma rays are also scanned by Doppler shifting thus the detector records the frequencies of the gamma rays absorbed by the sample and thus the corresponding energy changes calculated.

4.2.5 Neutron Diffraction and Mossbauer Analysis of FeGa Ribbons

Neutron diffraction experiments were carried out on both as-spun and annealed ribbons on the D2B diffractometer at the ILL Grenoble, France. Approximately 2g of the 12.8, 17.5, 19.5 and 22.5 at% Ga ribbons were packed into 8mm diameter vanadium cans. Here the 12.8 at. % Ga sample has been named the 15% at. % Ga, due to the fact that this sample was supposed to be made as a 15% Ga sample, but it was not until this experiment was complete that the samples were tested by EDX – the 15% at. % Ga was actually found to be on average 12.8 at. % Ga as can be seen in the SEM/EDX results in chapter 5. Blank vanadium cans were first run at ambient temperatures in order to record the background diffraction patterns from each blank can. The same experiments were then repeated for the cans containing the Galfenol ribbons. Diffraction patterns were collected from 0 deg to 158 deg at ambient temperature by using the high-resolution mode with a scanning step size of 0.051 deg. The neutron diffraction patterns from both as-spun (as-quenched) and annealed ribbons are shown in Fig. 4.2.5.1

The experiment here was focussing upon the crystallography of the highest magnetostrictive compositions of the Galfenol alloy and therefore due to reduced experimental time due to problems with the stability of the neutron beam, it was decided that the 27.5 at% Ga. was of least interest and would not be experimentally tested.

The six strong intensity diffraction peaks can be easily identified as arising from the bcc A2 disordered structure or the corresponding reflections from the ordered bcc D03 structure. Diffraction patterns from the ribbons with x=19.5 and 22.5 at% Ga are emphasised in Fig.4.2.5.2, in which the portion between 2θ = 20 deg and 110 deg has been enlarged and shows the existence of small additional peaks in both patterns.

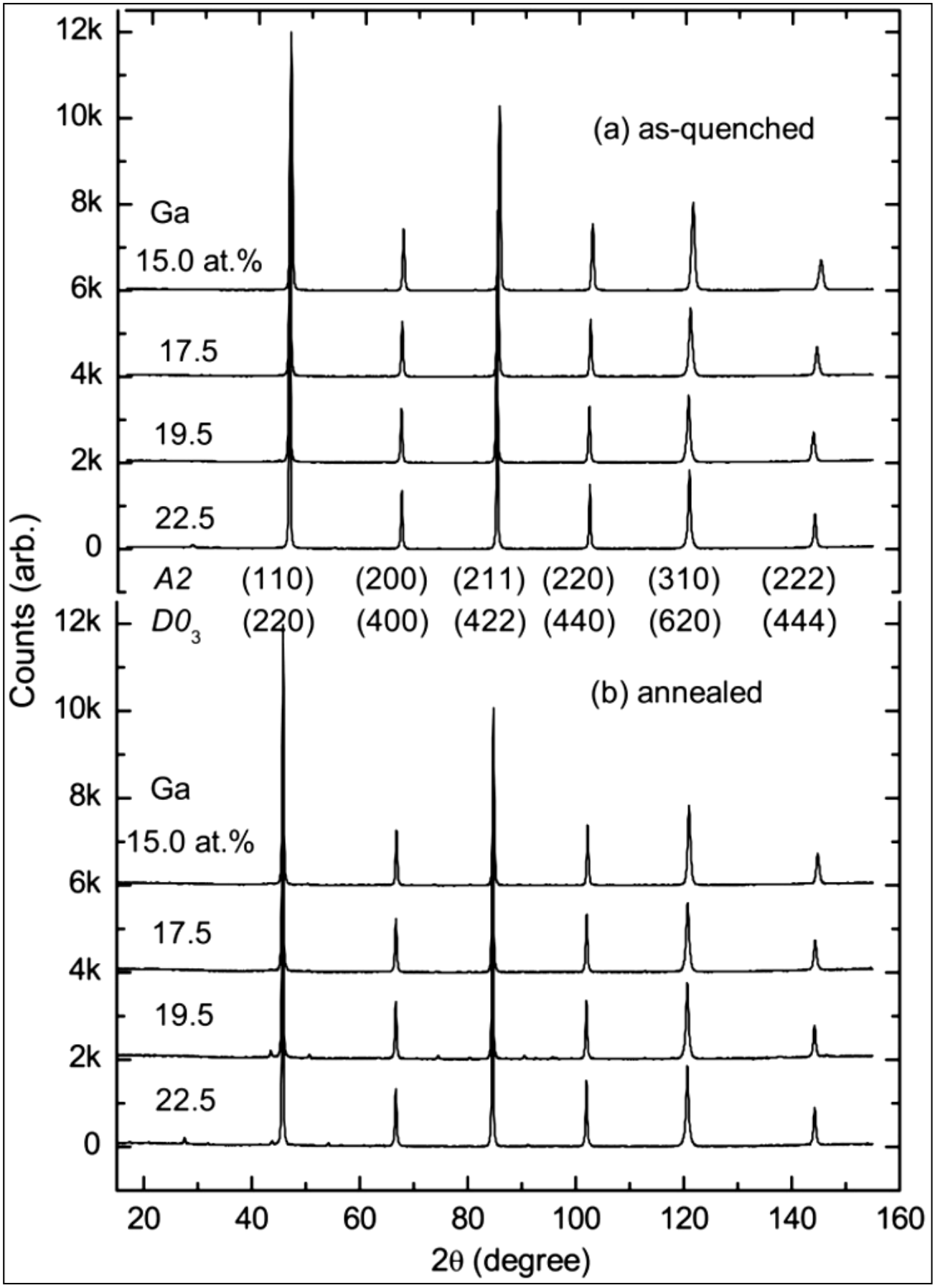

Figure 4.2.5.1 - Room temperature neutron diffraction patterns of as-spun and annealed $Fe_{100-x}Ga_x$ ribbons with x = 15, 17.5, 19.5, and 22.5 at% Ga.

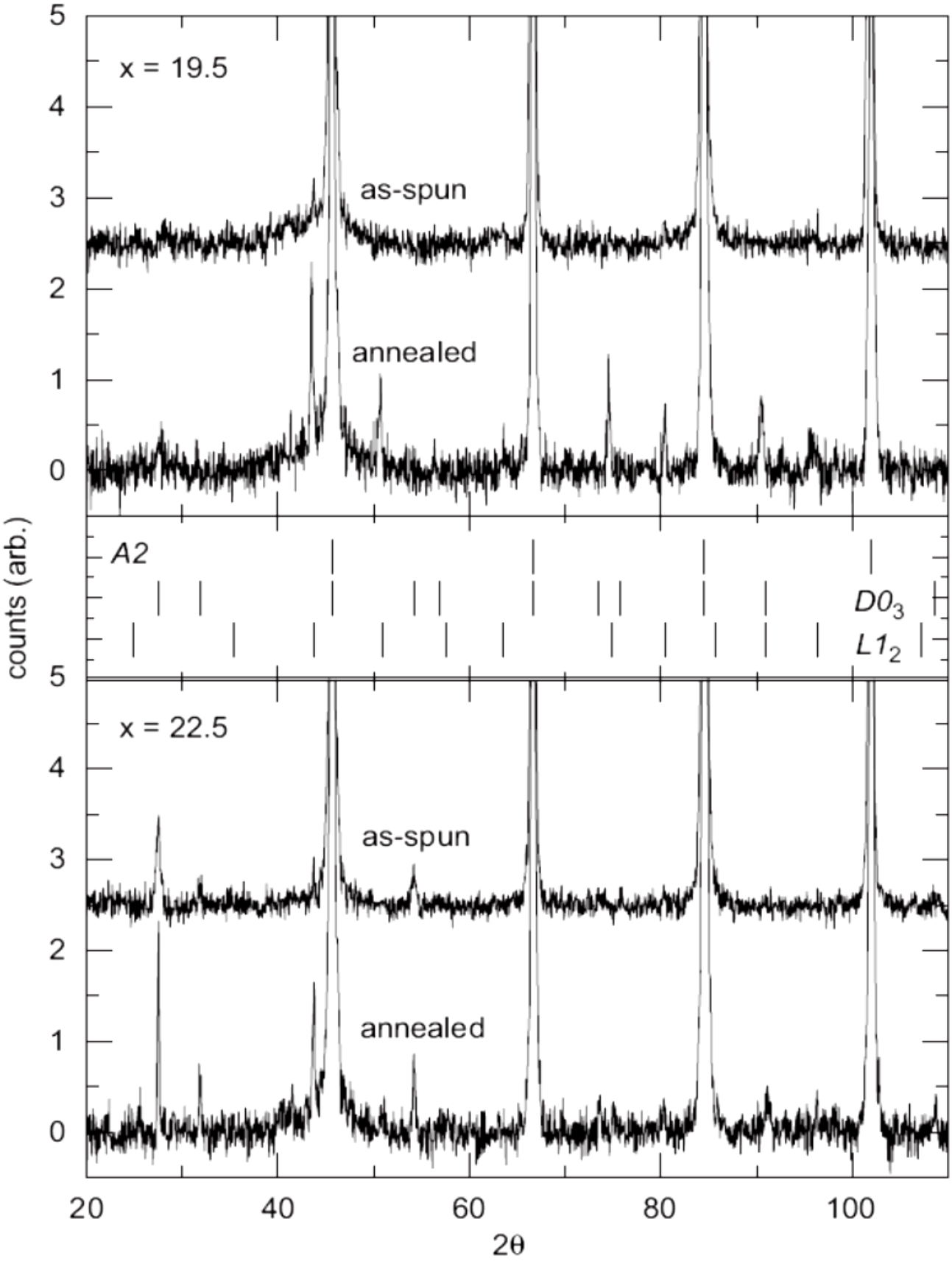

Figure 4.2.5.2 - Expanded room temperature neutron diffraction pattern of as-spun and annealed x=19.5 and x=22.5 $Fe_{100-x}Ga_x$ alloy ribbons. Tick marks for the A2, D03 and L12 phases are shown in the central panel.

One group of peaks belongs to the vanadium can used in experiment. Vanadium has a bcc structure with a lattice parameter of 3.0297 Å, and gives rise to diffraction peaks which appear to the left of the A2 peaks due to the larger lattice parameter. One such peak is clearly seen at $2\theta = 41°$ in all the patterns. Additional reflections were observed in the patterns from both the annealed and the as-spun ribbons, and are particularly obvious in the x=19.5 at.% Ga pattern. These new peaks have been indexed and are associated with the Fe_3Ga L12 fcc ordered structure. This was unexpected, as it is generally believed that the L12 phase is very difficult to form and this structure has not been observed in annealed Galfenol bulk samples with similar composition(s) unless given lengthy and extensive thermal treatment as proved by Kawamiya **[4.2.5.1].** It is clear that a significant volume of the D03 phase has not formed in the x=19.5 at. % Ga ribbon as no obvious Bragg peaks from D03 reflections can be seen even in the low intensity part of the diffraction pattern. This suggests a direct structural transformation from A2 to the L12, rather than from D03 to L12 during the annealing process. When the Ga content is increased to 22.5 at. % Ga, extra reflections arising from what is thought to be the ordered Fe_3Ga D03 bcc structure are observed. There is some agreement between these results and those of Zhang et al **[4.2.5.2, 4.2.5.3]**. In this study the melt spun ribbons of $Fe_{100-x}\,Ga_x$ with x=17 and 19.5 at. % Ga both compositions exhibit the distorted bcc (A2) structure. This A2 phase remains in the x=19.5 at. % Ga sample after annealing but is also accompanied by a very small percentage (~1%) of the D03 phase which is not seen in the annealed x=17.5 at.% Ga sample. The lattice parameters for all eight samples were determined using the diffraction fitting software package GSAS **[4.2.5.4]**. There is good agreement between these lattice parameters and those determined by Dunlap et al. **[4.2.5.5],** where ribbons of $Fe_{100-x}\,Ga_x$ with x=8.3, 17.9, 20.5 and 23.3 were also shown to form in the A2 structure when quenched. The results of this work together with the results of Dunlap et al. **[4.2.5.5]** and Luo **[4.2.5.6]** are shown in Fig. 4.2.5.3, where it can be seen that in

all three systems the lattice parameter increases approximately linearly as the Ga concentration increases at a rate of $1.9*10^{-4}$ nm at. $\%^{-1}$.

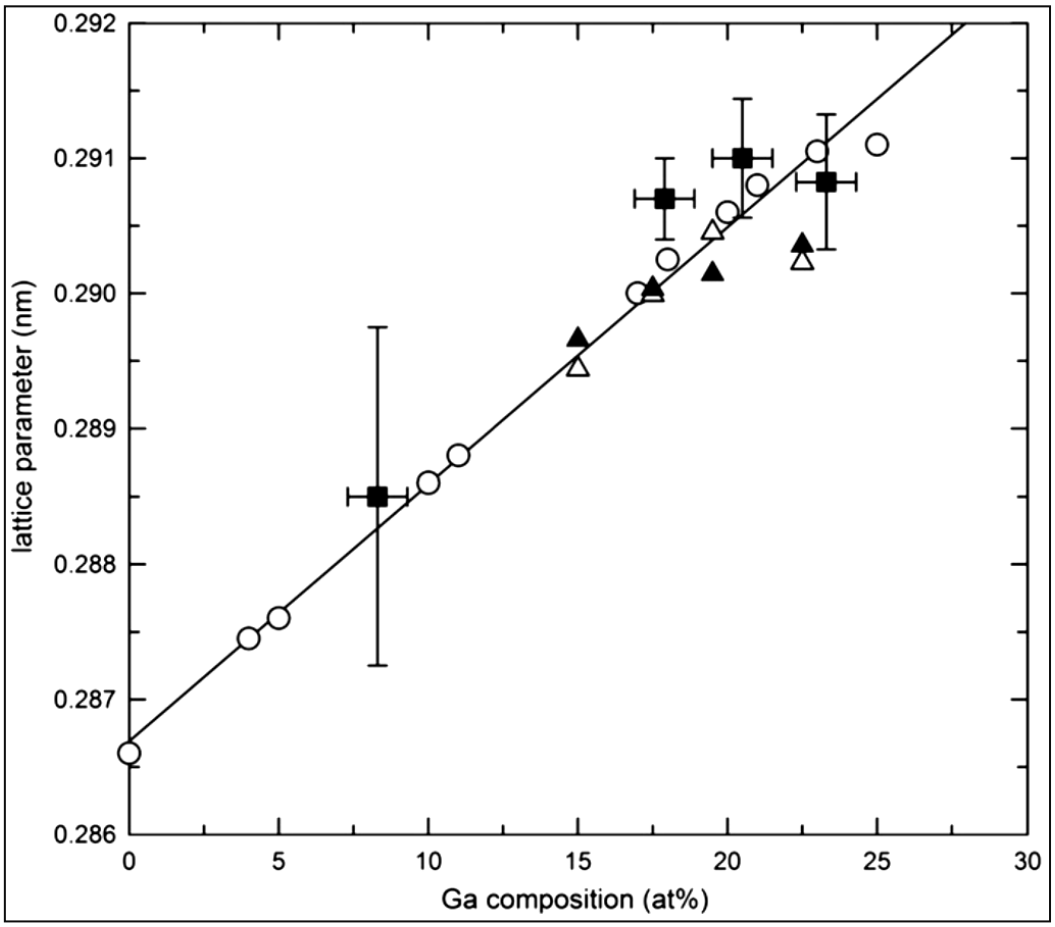

Figure 4.2.5.3 - Room temperature lattice parameter of the bcc phase as a function of Ga content. The values are taken from Luo (open circles) [4.2.5.6], Dunlap et al. (solid squares) [4.2.5.5] and this study (open and solid triangles).

A more detailed discussion of the neutron diffraction data is presented in an earlier paper by Zhao et al. **[4.2.5.7]** and in summary describes the high-resolution neutron diffraction spectra shown in Figs. 4.2.5.1 and 4.2.5.2 indicating that only diffraction peaks arising from the disordered bcc A2 phase are present in as-spun x=15, 17.5 and 19.5 at. % Ga ribbons, without any trace of satellite peaks, peak splitting or shouldered peaks. Post-annealing L12 reflections appeared, and are most prominent in the x=19.5 at. % Ga alloy. In contrast, the as-quenched 22.5 at. % Ga ribbons contain traces of both the A2 and D03 phases; furthermore, upon annealing it is noted that very small fractions of the A2 phase are transformed into the D03 phase.

The Room-temperature ^{57}Fe Mossbauer effect spectra were collected in transmission geometry using a standard Rh(^{57}Co) source and a Wissel System Mossbauer spectrometer operating in the sinusoidal mode. The ɣ-ray was orientated perpendicular to the ribbon plane and the sample size was typically an area of $20mm^2$. All spectra were referenced to a room-temperature standard α-Fe pattern. The intrinsic spectrometer line width is approximately $0.10mms^{-1}$ (FWHM). It is apparent that all samples are ferromagnetically ordered at room temperature as six line spectra are observed for all compositions. However there are some variations in the form of the magnetic order. The spectra from ribbons with x=15, and 17.5 at% Ga exhibit only broadened sextets while the spectra from x=19.5 samples start to show additional, sharper features. The x=22.5 spectra are noticeably different from those of alloys with lower Ga content, showing several resolvable sextets that suggest some fundamental structural changes and a much greater degree of short range ordering as the Ga content has increased as shown in Figure 4.5.2.4. Rancourt and Ping [**4.2.5.8]** and Lagarec and Rancourt [**4.2.5.9**] have shown that it is appropriate to model Mössbauer spectra from such materials as a combination of Gaussian-distributed Lorentzian sextets.

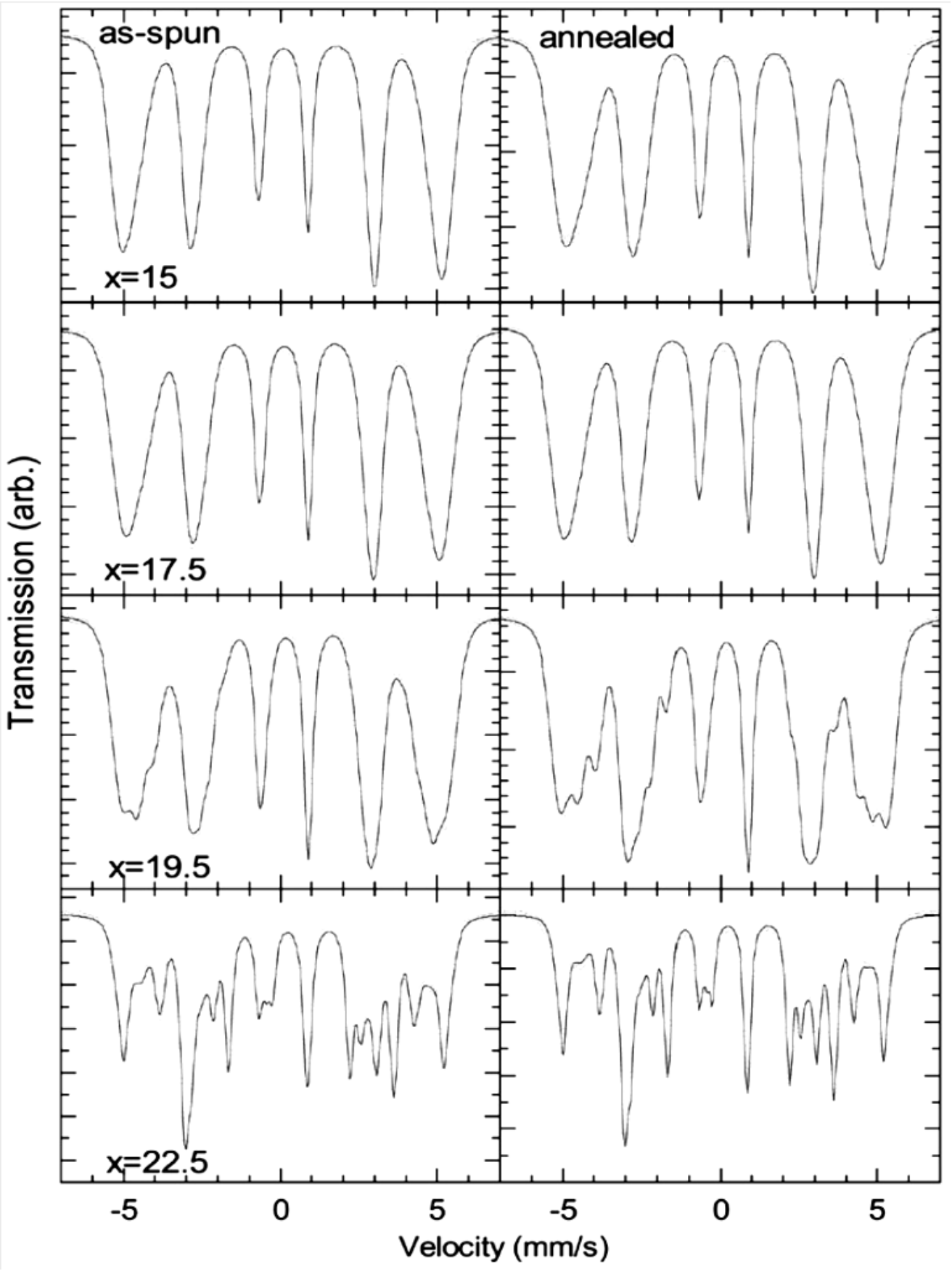

Figure 4.2.5.4 - Room-temperature ^{57}Fe Mössbauer spectra of $Fe_{100-x}Ga_x$ ribbons.

(The solid lines are the best profile fit.)

Each sextet was described using an isomer shift δ, a mean hyperfine field value $<H>$, a width, δH, and an area A. The quadrupole shift was assumed to be zero in all cases due to the cubic symmetry of the Mössbauer isotope used. The relative areas of the six spectral peaks were constrained to be **3:y:1:1:y:3** where **y** was determined during the fitting procedure. The resultant spectra from Galfenol ribbons of composition 15 and 17.5 at. % Ga were best fitted using two sextets respectively and the resulting hyperfine field distributions are illustrated in Figure 4.2.5.6

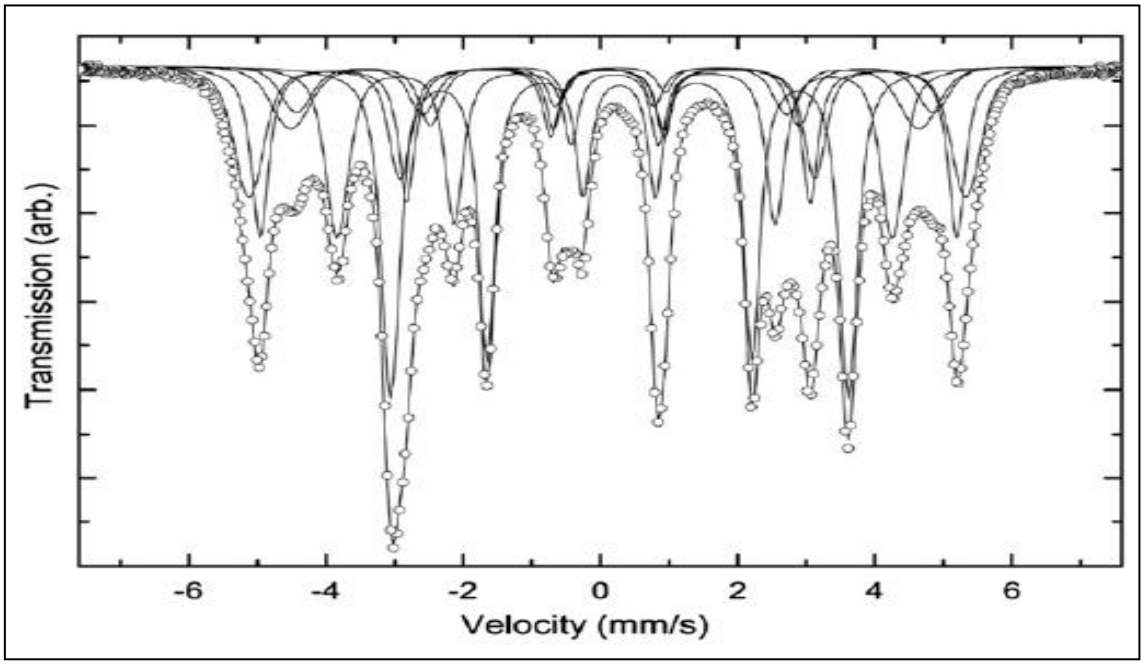

Figure 4.2.5.5 - Room-temperature ^{57}Fe Mössbauer spectra of as-spun 22.5 at. % ribbons. Open circles represent experimental data, the solid lines joining the circles are the best fit. The individual sub-spectra are shown as thin solid lines.

The mean values of the hyperfine fields decrease with the increase of Ga content. Annealing has little effect on the hyperfine field in these samples, except to reduce the hyperfine field of the 15 at% Ga sample slightly. The spectra from the 19.5 at. % Ga ribbons show more features than observed in the spectra from ribbons of 15 and 17.5 at. % Ga. In order to model these additional features four sextets are needed to fit the as-spun spectrum, while the spectrum from the annealed x=19.5 ribbon is best fitted using six sites. The parameters for the best fits for spectra from ribbons with x=15, 17.5 and 19.5 at. % Ga are shown in Table 4.2.5.1.

Site	$<H>$ (T)	σ_H (T)	δ (mm s^{-1})	A (%)	Site	$<H>$ (T)	σ_H (T)	δ (mm s^{-1})	A (%)
$x=15$ *as-spun*					$x=15$ *annealed*				
1	32.26	1.59	0.04	44.6	1	31.71	2.07	0.09	56.96
2	29.83	2.28	0.13	55.4	2	27.87	2.30	0.16	43.04
$x=17.5$ *as-spun*					$x=17.5$ *annealed*				
1	31.80	1.94	0.07	53.2	1	32.03	1.85	0.07	52.5
2	28.45	2.39	0.16	46.8	2	28.99	2.27	0.15	47.5
$x=19.5$ *as-spun*					$x=19.5$ *annealed*				
1	31.80	1.94	0.07	53.2	1	32.03	1.85	0.07	52.5
2	28.45	2.39	0.16	46.8	2	28.99	2.27	0.15	47.5
3	31.80	1.94	0.07	53.2	3	32.03	1.85	0.07	52.5
4	28.45	2.39	0.16	46.8	4	28.99	2.27	0.15	47.5
					5	32.03	1.85	0.07	52.5
					6	28.99	2.27	0.15	47.5

Table 4.2.5.1 - ^{57}Fe Mössbauer effect parameters for the sites obtained from the fits to the spectra from the ribbons with x=15, 17.5 and 19.5 as described in the text. The velocity scale is referenced to the a-Fe spectrum at room-temperature.

For x<20 the variation in mean hyperfine field value is approximately linear with Ga composition decreasing at a rate of 0.18T per at%. There have been several Mössbauer studies on FeGa alloys. For example Conversion Electron Mössbauer Spectroscopy (CEMS) was used to study thin film samples of Fe_{100-x} Ga_x with 10< x<35 **[4.2.5.10].**

Blachowskietal et al **[4.2.5.10]** carried out a Mössbauer study of $Fe_{100-x}Ga_x$ ingots with 10<x<29 at%. However as the structural examinations have shown, the phase-composition diagrams vary for different forms of the alloys and therefore it is really useful to compare the results of this study only with the results obtained from studies of rapidly quenched material. Newkirk and Tsuei **[4.2.5.11]** examined quenched $Fe_{100-x}Ga_x$ foils of 35mm thickness. For 0<x<20 at.% Ga the samples gave broad six line Mössbauer spectra, while the sample with x=25 at. % Ga gave a spectrum with sharper lines arising from several distinct magnetic sites.

Similarly Dunlap et al.'s **[4.2.5.5]** study of melt spun $Fe_{100-x}Ga_x$ ribbons showed broad six line Mössbauer spectra from samples with 8.3<x<20 at.% Ga, which were best fitted with a distribution of hyperfine fields.

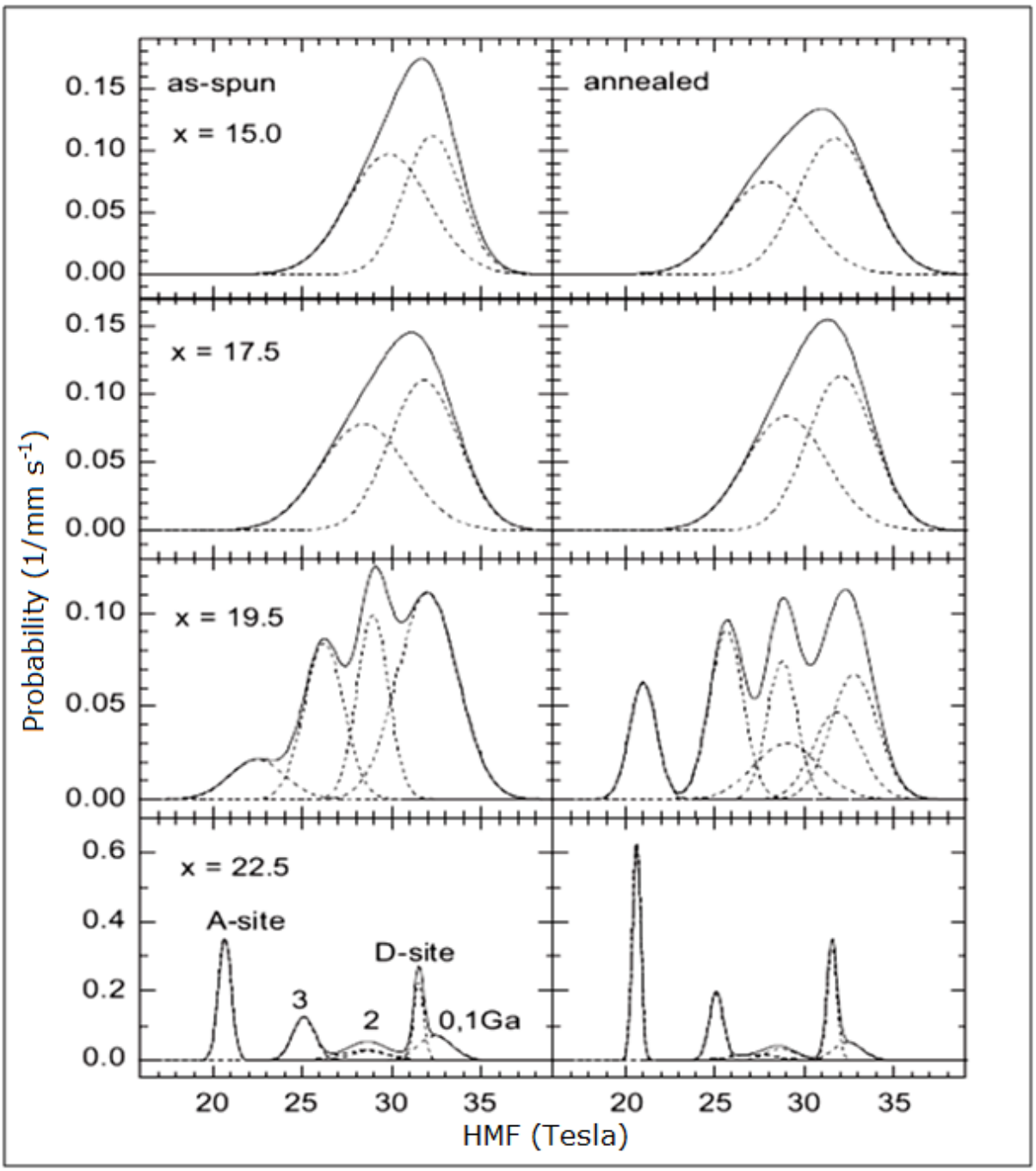

Figure 4.2.5.6 - Room-temperature Fe hyperfine field distributions in $Fe_{100-x}Ga_x$ ribbons. The distributions for the individual spectral components are shown by the broken lines and the total distribution is shown by the solid line.

When x was increased to 23.5% the spectrum became much sharper, showing three clearly resolved sextets. In both these studies the spectra were comparable to those obtained in this work from the as-spun samples (displayed on the left hand side of Figure 4.2.5.4). Neither

Newkirk and Tsuei nor Dunlap et al. examined annealed or thermally treated alloys. These results of the fits to the Mössbauer spectra from ribbons with 15<x<22.5 are shown in Figure 4.2.5.4, where the results of this work when compared with the results of Newkirk and Tsuei **[4.2.5.11]** and Dunlap et al. **[4.2.5.5]** are all in good agreement regarding the distributions of the spectra.

x=22.5 as-spun					
Site	$<H>$ (T)	σ_H (T)	δ (mm s^{-1})	A (%)	Description
1	32.42	0.94	0.10	16.9	< 6 Ga NNN
2	31.51	0.27	0.11	15.4	$D0_3$ D-site
3	28.78	1.00	0.21	7	2 Ga NN
4	28.42	1.36	0.06	9.2	2 Ga NN
5	25.10	0.62	0.21	19.3	3 Ga NN
6	20.70	0.36	0.28	32.1	$D0_3$ A-site
x=22.5 annealed					
Site	$<H>$ (T)	σ_H (T)	δ (mm s^{-1})	A (%)	Description
1	32.43	0.79	0.09	10.4	< 6 Ga NNN
2	31.55	0.28	0.11	22.5	$D0_3$ D-site
3	28.66	0.85	0.15	7.03	2 Ga NN
4	27.14	1.59	0.00	5.3	2 Ga NN
5	25.09	0.38	0.21	18.6	3 Ga NN
6	20.65	0.23	0.28	36.1	$D0_3$ A-site

Table 4.2.5.2 - ^{57}Fe Mössbauer effect parameters for the sites obtained from the fits to the spectra of ribbons with x=22.5 at.% as described in the text. The velocity scale is referenced to the a-Fe spectrum at room-temperature.

Visual inspection of the resolvable absorption peaks in the spectrum of as-spun x=22.5 at. % Ga ribbon implies the presence of at least four distinct sites; however, in practice six distinct sites are needed to obtain a good fit to this spectrum. The final fit is shown in Figure 4.2.5.5 with the resulting hyperfine field distribution in Figure 4.2.5.6. The mean hyperfine parameters for the six sites are summarised in Table 4.2.5.2. The values of *y* of the line intensity (not shown) from the fit to this spectrum are greater than 2, suggesting that a very small amount of in-plane magnetic anisotropy has been detected. It should be noted that this particular result is in complete contrast to the results of Dunlap et al. **[4.2.5.5]**, where the spectra from as-spun samples with 8.3<x<23.3 could be fitted with 1.95<y<2.09, indicating

that in his work there is no evidence for preferred magnetic orientation in those particular samples.

4.2.6 Discussion of Mossbauer and Neutron Results

For a random distribution of Ga on the A2 bcc α-Fe lattice, assuming a standard binomial distribution and that the eight nearest neighbours have the nominal composition, we expect the probability, P(n), of Fe sites with n Ga nearest neighbours to be expressed by equation 4.2.3.1.

$$P(n) = \frac{8!}{n!(8-n)}\left(\frac{x}{100}\right)^n \left(1-\frac{x}{100}\right)^{8-n} \qquad \textbf{(4.2.3.1) [4.2.6.1]}$$

For the x=15 and17.5 at.% Ga samples, the probability of Fe sites with 0 or 1 Ga nearest neighbours is calculated to be 0.66 and 0.58 respectively. However, it is found that the relative area of the sites at a higher hyperfine field is 45% and 53%, respectively, which is significantly less than the calculated value. This seems to indicate that the distribution of Ga in the bcc phase is not entirely random and that Ga prefers sites with a high number of Ga nearest neighbours. Initially this phenomenon was regarded as evidence of the enhancement of Ga–Ga pairing **[4.2.5.5].** However, the assumption above completely neglects the fact that the central position must be occupied by an Fe atom. When taking the central Fe atom and the eight nearest neighbours as a whole and assuming its Ga content is *x*, the Ga content in the nearest neighbours should be $\frac{9x}{8}$, instead of just *x*. With this new Ga content and Equation 4.2.3.1, the probability of sites with 0 or 1 Ga atom is recalculated to be 0.60 and 0.51 for x=15 and17.5 at.% Ga ribbons respectively, which is closer to the observed value. At least four sextets were needed to fit the spectrum from the as-quenched x=19.5 at% Ga ribbon, which corresponds to the sites with 0 or 1 Ga nearest neighbours and 2, 3, and 4 Ga nearest neighbours, respectively. The mean hyperfine fields and isomer shifts change approximately linearly with the number of Ga neighbours. The probabilities calculated from Equation 4.2.3.1 are 0.52, 0.29, 0.14 and 0.04 for the four sites mentioned above respectively. The

relative areas of sites at 32.0, 29.0, 26.2 and 22.5T are 46.7, 21.9, 23.3 and 8.2% respectively. Again this seems to indicate that the distribution of Ga in the A2 phase in these ribbons is not entirely random but that Ga prefers Ga nearest neighbours. However, the calculated probability of the site with two Ga nearest neighbours is higher than the observed 21.9%, suggesting no improvement in the Ga–Ga pairing; although the disordered A2 bcc Galfenol alloy of this composition demonstrates the highest magnetostriction. In contrast, the relative area of the site with four Ga nearest neighbours is double that predicted, indicating the formation of high Ga content clusters or more probable that there are short-range ordered D03 precipitates in the disordered bcc A2 matrix. It is possible these D03 precipitates might be responsible for the increase in magnetostriction of high Ga content Galfenol alloys, as predicted by Dunlap et al **[4.2.5.5].** The absorptions in the Mössbauer spectrum from the annealed ribbon with x=19.5 at% Ga occur at the hyperfine fields similar to those observed in the x=22.5 at% Ga spectrum. All three spectra were best fitted using six sextets. In the x=19.5 at.% Ga ribbon the absorption at around 21T is well separated from other peaks, and is believed to be attributed to Fe sites with four Ga nearest neighbours, similar to the A-sites of D03, indicating the formation of D03 phase after annealing treatment. However, the broader distribution of this site suggests that the formed D03 phase is probably only of short range order. This is confirmed experimentally by its neutron diffraction pattern, where no obvious superlattice diffractions peaks arise from the D03 phase. The relative area of this site fitted from the spectrum is 12%, which corresponds to a D03 volume of approximately 18% in this sample when assuming that the number of A-sites is twice that of D-sites.

In the spectrum from the as-quenched x=22.5 at% Ga ribbon the two sites with hyperfine fields of 20.7 and 31.5T and narrow field distributions correspond well to the values of the D03 phase reported by previous studies **[4.2.5.1]** and **[4.2.5.5],** with room-temperature Fe hyperfine field values of 20.5 and 31.2T for the D03 phase and 26.9T for the L12 phase in Fe3Ga samples **[4.2.5.1],** and 20.69 and 31.44T for the D03 phase and 25.30T for the L12

phase in x=23.3 at% Ga samples **[4.2.5.5].** The two fields for the D03 structure correspond to the so called A-sites with four Fe and four Ga nearest neighbours and six Fe next nearest neighbours (NNN), and D-sites with eight Fe nearest neighbours and six Ga next nearest neighbours. It is believed that the reasonable agreement of the hyperfine fields for those samples, suggests a conventional Ga–Ga pairing along <110> directions which occurs in the D03 structure. However, the site with a hyperfine field of 25.08T is expected to be an Fe site similar to A-sites of D03 but with only three Ga and five Fe nearest neighbours, rather than an L12 site as suggested previously **[4.2.5.5]**. It is reported that the Fe3Ga L12 phase has one hyperfine field at 26.9T with two quadrupole shifts **[4.2.5.11].** In this present work, there was no need to introduce any quadrupole shifts to obtain a better fit, suggesting no observable L12 absorptions in the samples. However, despite the fact that neutron diffraction patterns show no L12 phase in the as-quenched ribbons, they do reveal a trace of L12 phases in the annealed samples, most notably in the x=19.5 at. % Ga ribbons although the volume of such a phase is estimated to be less than 1%, which is not discernible in the Mössbauer spectra. In contrast, the relative area of absorption with a hyperfine field of 25.08T for x=22.5 at. % Ga. The two sites with a hyperfine field of around 28.6T are considered as Fe sites with two Ga and six Fe nearest neighbours; the difference in the isomer shift value potentially indicates a difference in the Ga pair arrangement, either along the <100>, <110> or <111> directions, but this would need to be confirmed experimentally. The site with a hyperfine field of 32.45T has an isomer shift value identical to that of D03 D-sites, suggesting that this site is similar to the D-sites but with fewer Ga atoms as its next nearest neighbours. As the absorption area is much larger than the site with two Ga nearest neighbours, it is very probable that the absorption with a hyperfine field of 32.45T has a contribution from the site having only one Ga nearest neighbour, as the sites with 0 or 1 Ga nearest neighbours in disordered A2 bcc phase are believed to have similar hyperfine fields **[4.2.3.4].** The occurrence of sites with hyperfine fields around 28.6T and 32.45T indicates the existence of disordered bcc A2 phase

in this sample. Comparing the hyperfine field distributions of the x=22.5 at% Ga ribbons pre- and post-annealing treatment (lower section of Figure 4.2.2.6), one can see that the hyperfine field distributions of A-sites and D-sites of these annealed samples become narrower, suggesting an improvement of chemical ordering in the D03 phase, and that the corresponding probabilities are also higher than those of as-quenched ribbons while the probabilities of bcc sites mentioned above become lower. The probability increases from 32.1% to 36.1% for A-sites and 15.4% to 22.5% for D-sites. This is consistent with the given neutron diffraction patterns, where the integrated intensities of D03 superlattice peaks at 2θ ~27.51 and ~57.21, normalised to the (220) peak, increases from 2.14% and 0.82% to 2.40% and 1.07% respectively after annealing, with an uncertainty of ±0.05%. The increases in both the peak intensities of neutron diffraction and the relative areas of Mössbauer spectrum and therefore indicate an increase in the volume of D03 phase after annealing, which in turn confirms that there is a vast majority of A2 bcc disordered phase in the as-quenched ribbons and a partial transformation from an A2 bcc phase into D03 bcc phase during the annealing process.

4.3 X-Ray Diffraction Analysis (XRD)

4.3.1 Principles of XRD

The principles of x-ray diffraction are very similar to that of neutron diffraction as discussed in section 4.2.1. The wavelengths of x-rays are similar to the atomic separation distances in solids and are also a useful tool to investigate crystals and structures. The main advantage of x-rays is that they do not require expensive equipment needed for neutron generation using either a continuous or pulsed neutron source. X-ray diffractometers are commonplace in research departments and are relatively compact pieces of equipment.

When electrons are accelerated and driven into a metal target, a proportion of their energy is converted into x-rays similar to that is described for the EDX measurements as described in

section 5.1. If an electron converts all of its kinetic energy into x-ray photons in one instance, the energy of this x-ray photon is given by equation 4.3.1.1.

$$E = eV = hv = \frac{hc}{\lambda} \qquad \textbf{(4.3.1.1.)}$$

Where, e is the charge on the electron, V is the applied voltage, h is the Plank constant, v is the frequency of the x-ray photon, c, the velocity of light and λ, the wavelength of the x-ray photon. If this beam of x-rays is directed at an absorbing crystal, the intensity of the beam is attenuated. The size and shape of each unit cell determines the positions of the diffracted x-ray beam whilst the total distribution of atoms determines the intensities of the diffracted peaks. X-rays are scattered by all the electrons of atoms within the material, the structure factor is the relationship governing the relative size of each scattering event and is given by equation 4.3.1.2.

$$F = \sum_j f_j \exp[2\pi i (hx_j + ky_j + lz_j)] \qquad \textbf{(4.3.1.2)}$$

Here, f_j is the scattering amplitude of the target atom j; x_j, y_j and z_j are the co-ordinates of the atoms j in a specific unit cell.

Again, the diffraction geometry is demonstrated using the Ewald sphere as described back in section 4.2.3. Unfortunately here, the structure factor is of limited use in the x-ray diffraction of Galfenol, as the structure factors of Fe and Ga are very similar; as they are very close to each other on the periodic table. The data gathered here gives good analysis of the size and shape of the unit cell, but it is difficult to ascertain the specific atomic distribution from the intensity of the peaks alone, this is why further neutron diffraction work is required as the structure factors of Fe and Ga when working with neutrons is somewhat different due to the scattering events occurring only from the target nuclei.

A simple schematic of the x-ray diffraction setup is shown in figure 4.3.1.1 and the actual Bruker D8-Diffractometer machine used in these experiments shown in figure 4.3.1.2.

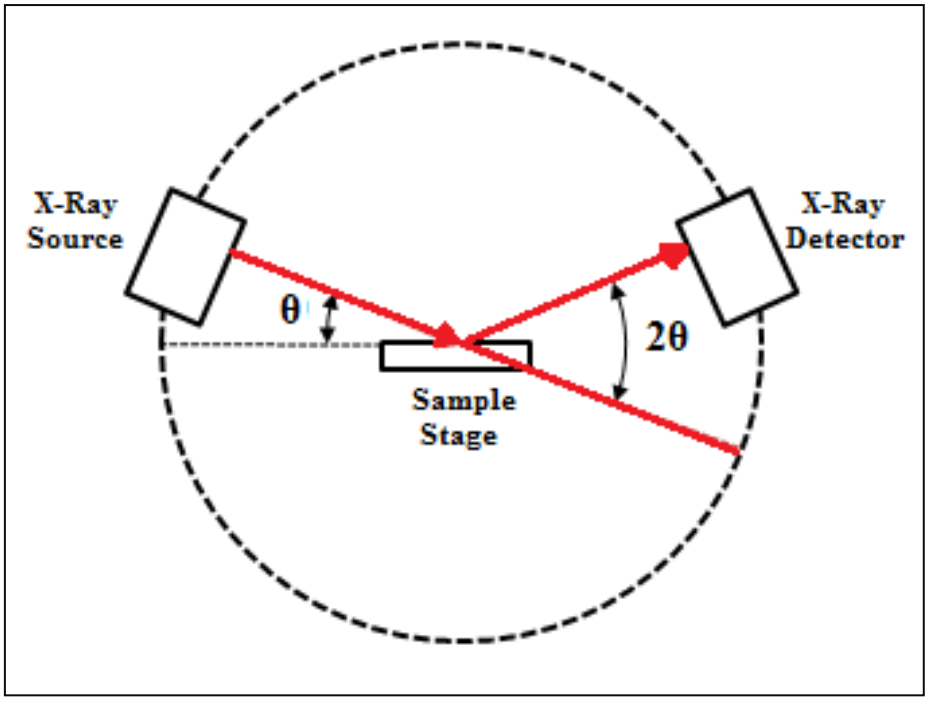

Figure 4.3.1.1 - Schematic of an x-ray diffraction experiment

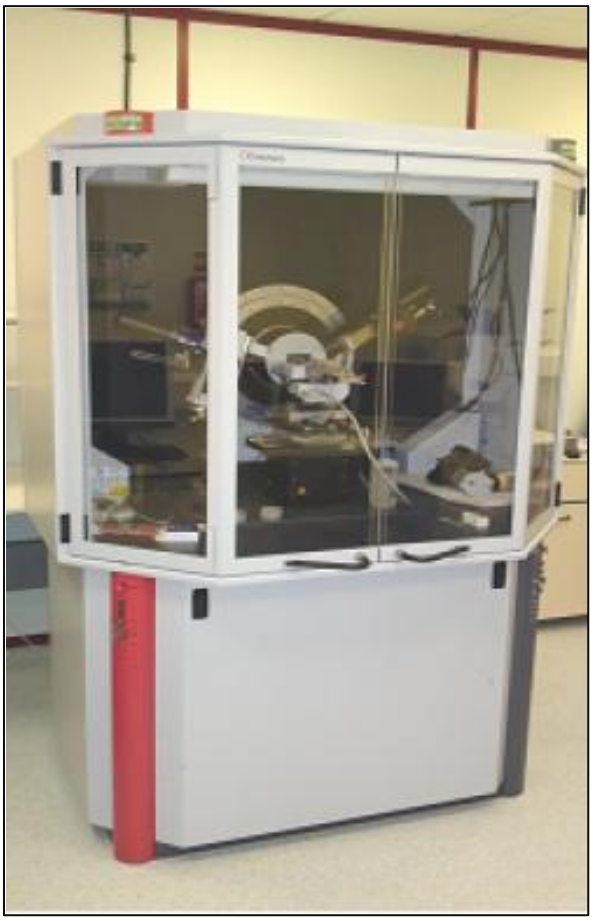

Figure 4.3.1.2 - The Bruker D8 diffractometer in Salford Analytical Services (SAS)

4.3.2 Initial XRD Results

The ribbon samples were cut or ground into as fine pieces as possible to carry out the powder type XRD experiments, here the ideal sample texture for XRD analysis is to have a finely ground powdered sample. This gives a random orientation of all the crystallites in the sample and eliminates the texturing effect that can be induced during any type of fabrication process. In this instance, as an additional measure to give the crystallites within the sample true random orientation, the sample holder was also rotated about the x-axis. The Galfenol ribbons of compositions 12.8, 17.5, 19.5, 22.5 and 27.5 at. % Ga were all scanned using the Salford in-house Bruker D8 Powder X-Ray Diffractometer; each sample was given a run time of approximately three hours over a range of angles from 0 to 90 degrees (2θ) with an angle step size of 0.04° to maintain high resolution and a step rate of 5 seconds per step. The machine was operated at a potential of 30kv and a current of 30mA and the x-ray radiation used was Cu-Kα of wavelength 1.5418 Å.

Here are presented the XRD scans from all the compositions of the as-spun Galfenol ribbons, the graphs have been imported into computer software called Crystal Match! By a company called Crystal Impact. To identify the XRD patterns for each alloy a database must be used containing the relevant patterns for the existing compositions of the Galfenol system. Here a combination of databases has been used, firstly the main database is the Powder Diffraction File-2 (known as the PDF-2) which is produced by the International Centre for Crystal Diffraction (ICCD). Individual Galfenol patterns were also obtained with thanks to the Chemical Database Service (CDS) who provide the Inorganic Crystal Structure Database (ICSD) which is an academic service for researchers funded by the Engineering and Physical Sciences Research Council (EPSRC) and maintained by the Science & Technology Facilities Council (STFC) at the Daresbury Laboratory; it allows access to experimental and computer generated diffraction patterns for all types and wavelengths of incident radiation.

The Galfenol 15 at. % Ga (which as is now known is actually 12.8 at. % Ga or 15 wt. % Ga from the EDX) alloy scan is shown in figure 4.3.2.1 and the diffraction pattern fitted using the databases previously described; the reports in Appendix III contain all of the information regarding the fitting procedure and the parameters used; this has been repeated for all of the other Galfenol compositions.

It can be seen in the figure that as well as trying to match the actual pattern with the reference pattern from the database, the software also tried to index each peak according the [hkl] miller indices. On the figure, the very broad peak that appears from 5° to 15° in the 2θ range is the background contribution from the amorphous grease which is used to hold the Galfenol to the amorphous Si sample holder. This reduced the background intensity count. No contributing peaks are expected at these low angles and can be ignored. Also to be noted on the figure are the small blue check marks underneath the pattern, these indicate the actual peak positions from the scan, the small red check marks underneath those represent the closest match from the reference database, additional check marks included on other patterns will be discussed when they are presented.

The pattern is also automatically normalised against the reference database, so gives a clear indication of the ratio of the peaks with respect to each other. Here it is also noticed that the three very dominant peaks have been identified as [101], [200] and [211] which is typical of a BCC cubic structure not dissimilar to α-Fe, but in this case the closest match is for $(Fe_4Ga)_{0.4}$; which is the same stoichiometry as $Fe_{80}Ga_{20}$ with the same peak positions but there is a subtle difference in the relative intensities of the two higher order reflections.

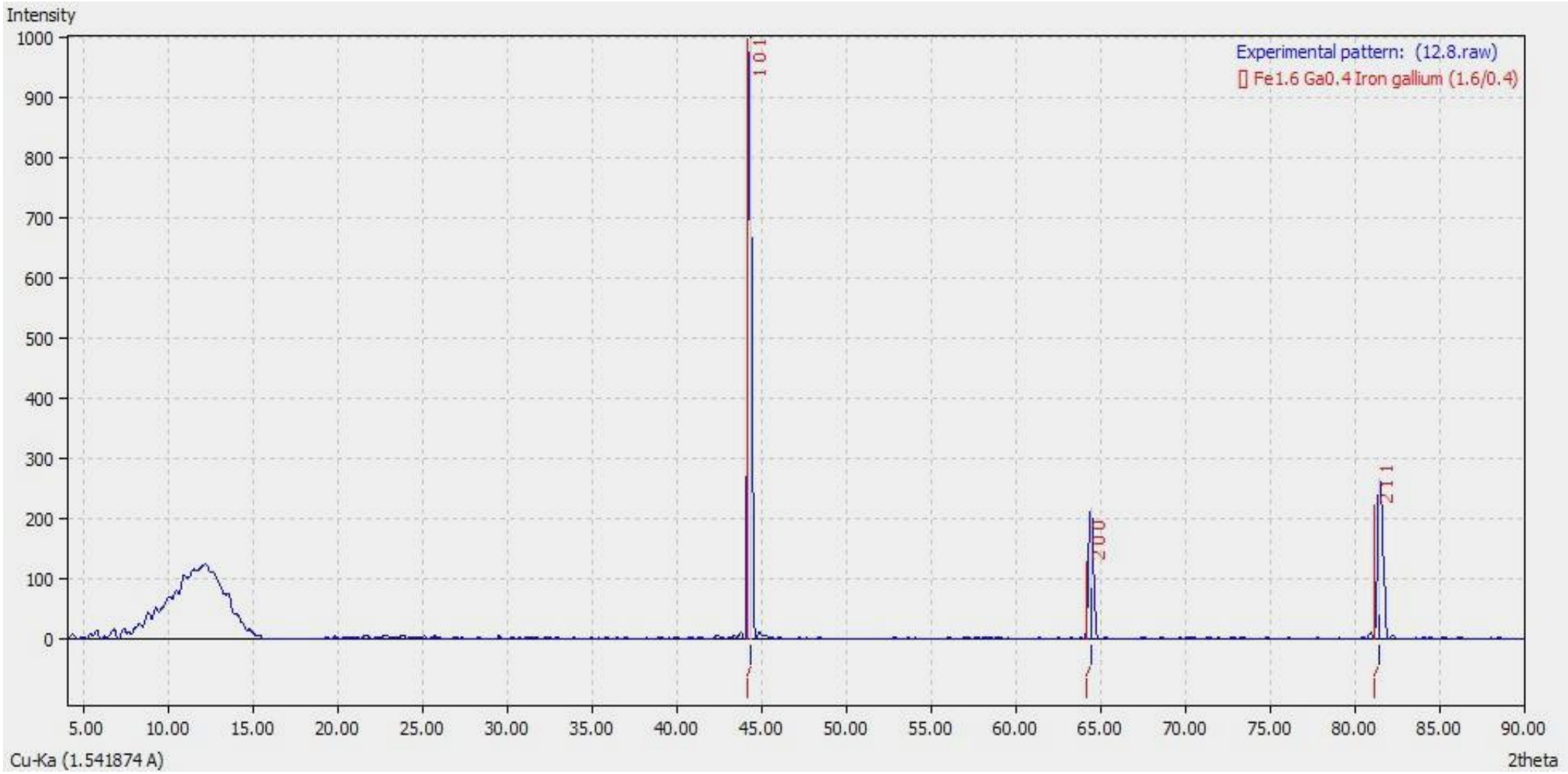

Figure 4.3.2.1 - Galfenol x-ray scan for the 12.8 at. % composition

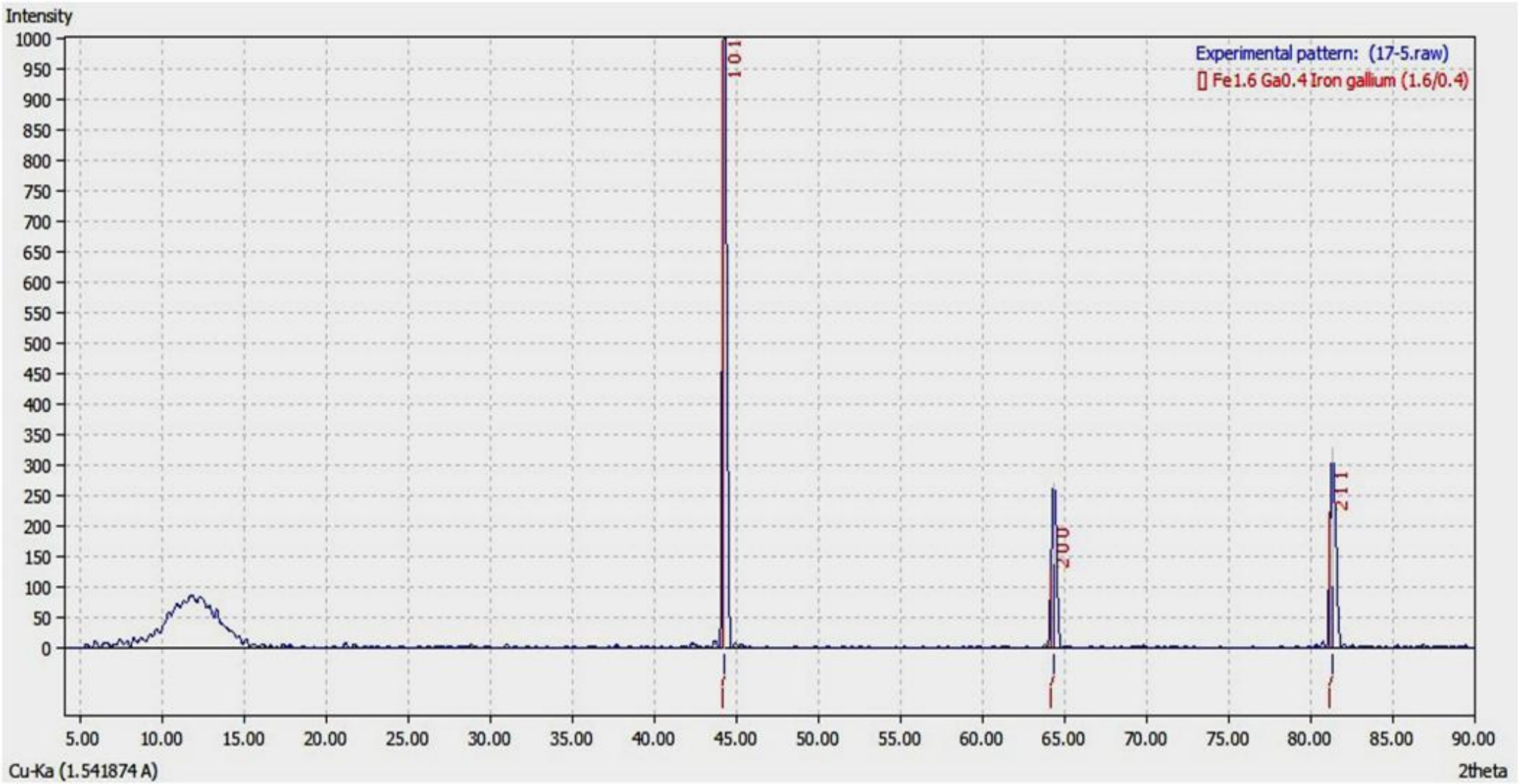

Figure 4.3.2.2 - X-ray scan for Galfenol 17.5 at. %

The Crystal Match! report for the 12.8 % at. Ga is presented as are all of the other compositions are in Appendix III. The rest of the compositions will now be presented in a similar fashion, the x-ray scan and the relevant report given in that order.

In figure 4.3.2.2 the x-ray scan for the Galfenol sample of 17.5 at. % is displayed, again the software has selected the $(Fe_4Ga)_{0.4}$ as the closest potential match, we can see though that in the report in Appendix III, the peaks here have shifted ever so slightly to the left. In a cubic system this indicates a small increase in the lattice parameter which is consistent with the addition of Ga atoms into a predominantly Fe lattice, the atomic radius of Ga is very similar to Fe but is ever so slightly larger. This is also why it should be noted in the report that in the "other candidates" section, the D03 structure has appeared, this is because this structure has exactly double the lattice parameter of the A2 bcc structure – the only way to differentiate the two is that the primitive lattice of the D03 is fcc, therefore there would be peaks for the primitive lattice at much lower angles around the $2\theta \sim 25°$ area for the [111] reflection; here it is obvious these are not present.

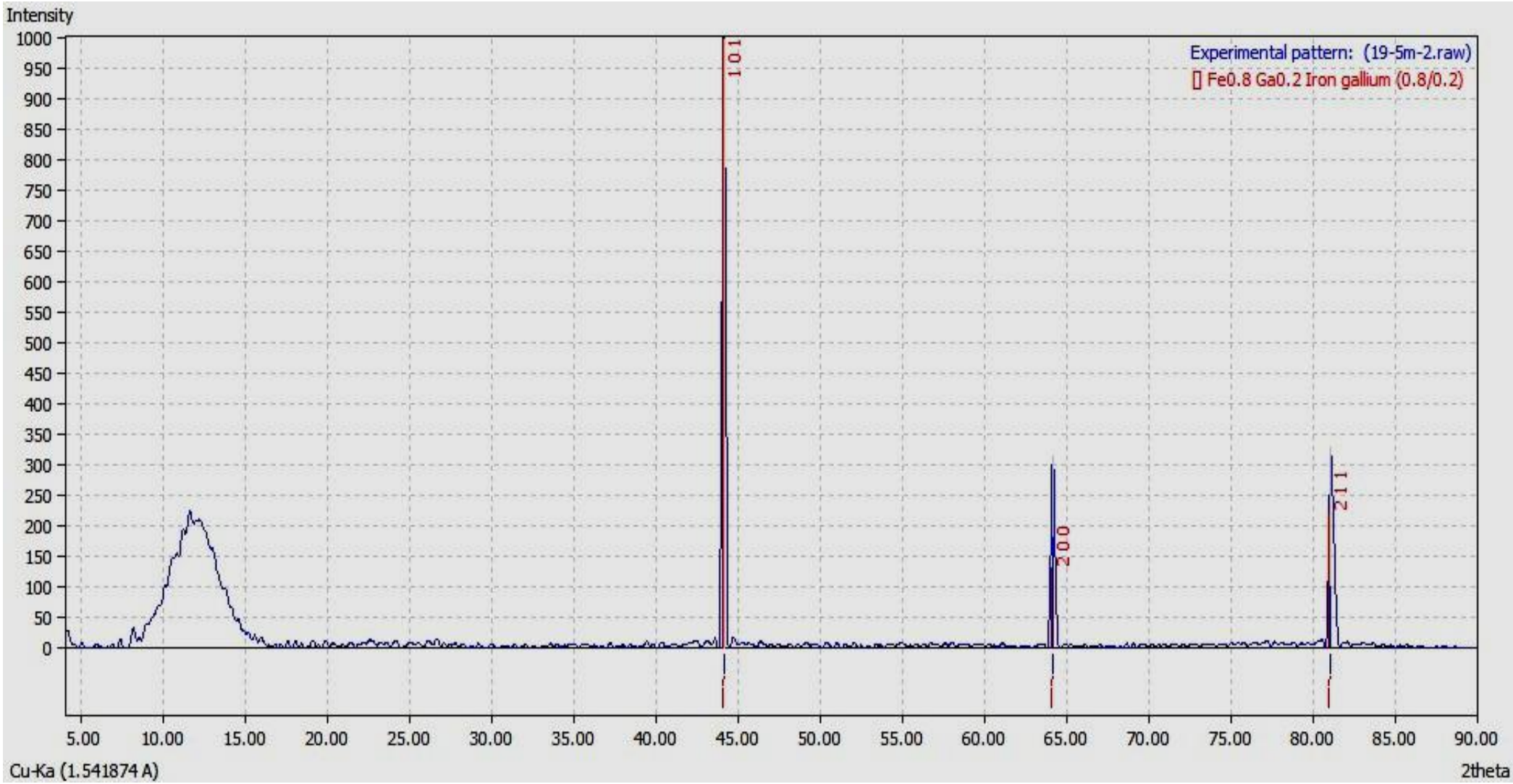

Figure 4.3.2.3 - X-ray scan of Galfenol 19.5 at.%

The scan here has decided that the best match in this case is the $Fe_{80}Ga_{20}$, there is subtle difference between the $(Fe_4Ga)_{0.4}$ and the $Fe_{80}Ga_{20}$ apart from a neglible difference in the intensity of the [211] peak which increases by around 4%. Again it can be observed that the peaks have again subtly moved to the left as can be seen from the d-spacing in the report.

Another difference in the 19.5 at. % pattern is also the FWHM of the peaks, it has decreased from 0.3200 to 0.2400, this suggests the crystallite or grain size has increased in accordance with the Scherrer equation, which states that the grain size is proportional to the wavelength of incident radiation divided by the FWHM, multiplied by the cosine of the peak position as given in equation 4.3.2.1.

$$L = \frac{K\lambda}{B\cos\theta} \qquad (4.3.2.1)$$

Where L is the crystallite or grain size, K is the Scherrer constant of 0.9, λ is the wavelength of incident radiation, B is the FWHM of the selected peak and θ, the angle of the centre of the selected peak. This should not be considered exact as there will be a distribution of crystallite sizes, yet the Crystal Match! software takes a Gaussian distribution for the average FWHM of the peak and thus this equation should be used with caution. In this work, these values are not calculated using this equation as it is thought that a more complex Lorentzian or Voigt function should be used, yet according to Suortti et al, even then it does not account for strain broadening and particle size simultaneously and this leads to contentious results. **[4.3.2.1]**

The reason for the increases in the lattice parameter is directly from strain broadening caused by the Ga addition **[4.3.2.2]**, thus it was reasoned that if crystallite size was calculated using this method it would not be accurate.

The next scan is the Galfenol 22.5 at. % sample, the best fit here has reverted back to the $(Fe_4Ga)_{0.4}$ as it can noticeably observed that both the [200] and [211] peak have reduced in intensity. This time the peaks have again shifted slightly to the left again indicating a further increase in lattice parameter. In this pattern though the match is absolutely perfect, there is no

difference between the actual scan pattern and the reference pattern, as could be noticed in the three earlier scans.

Finally, the x-ray scan for the Galfenol sample of 27.5 at. % Ga is in figure 4.3.2.5; this is the highest Ga content of any of the Galfenol alloys in this work and as will be seen became the focus of our further investigations when looking at thermal treatment of the alloys. Certain compositions will be revisited in order to determine the effects that thermal treatments have on these complex systems.

The software in this case has also identified the 27.5 at. % composition as the $(Fe_4Ga)_{0.4}$ structure; as reported by Dasarathy and Hume-Rothery in 1965 **[4.3.2.3]** which is also an A2 disordered phase. The peaks have again shifted to the left indicating a further increase in lattice parameter. All of the compositions show the A2 disordered BCC structure, implying that the cooling rate from the melt is such that none of the more exotic structures of Galfenol alloy have had the chance to form; not even the ordered D03 phase which one would think should appear for Galfenol compositions ~25 at. %. The texture in the [200] peak continues to be further reduced with the addition of Ga at higher compositions suggesting preferred crystallographic orientation for the [110] direction due to the high relative intensity of the peak.

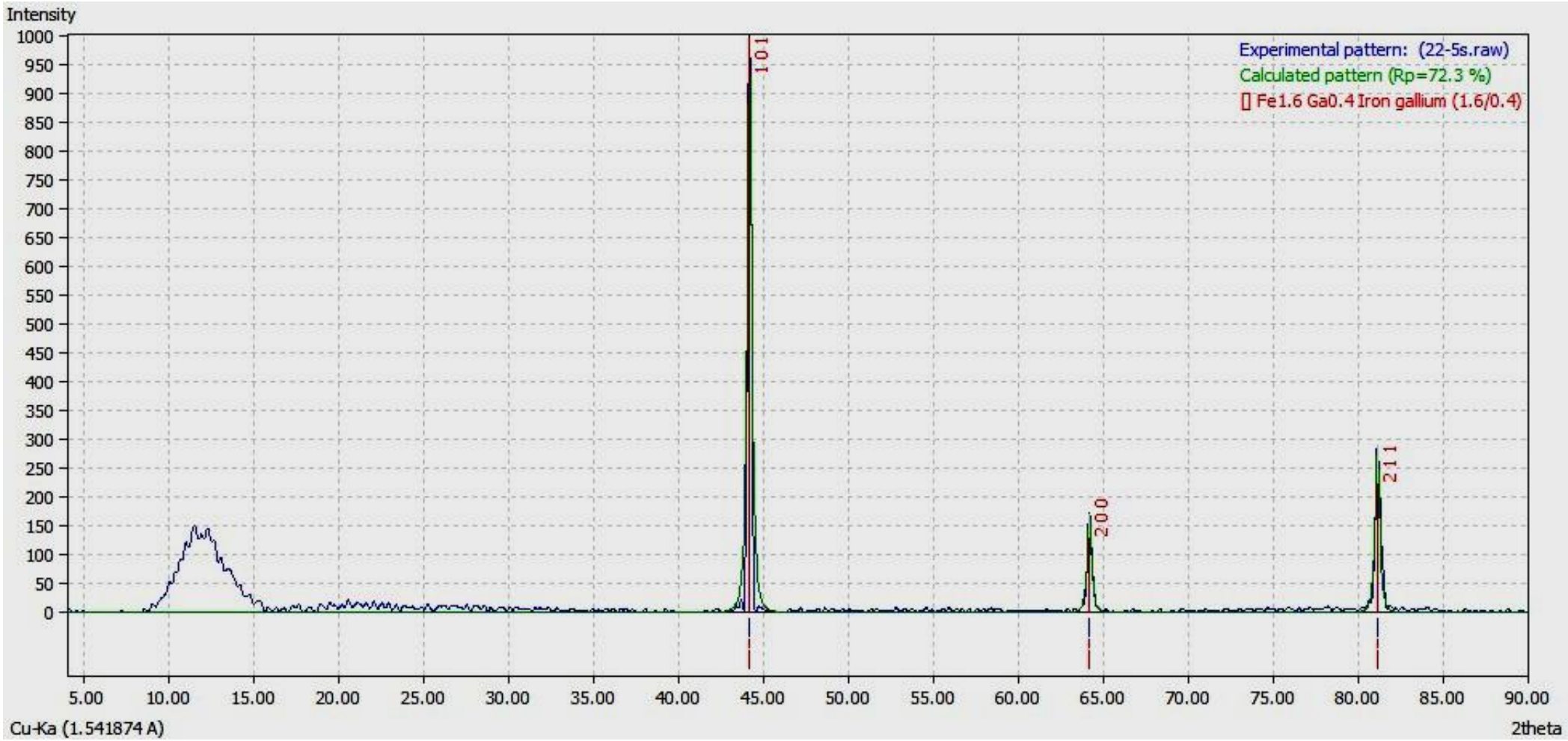

Figure 4.3.2.4 - X-ray scan of Galfenol 22.5 at. % Ga

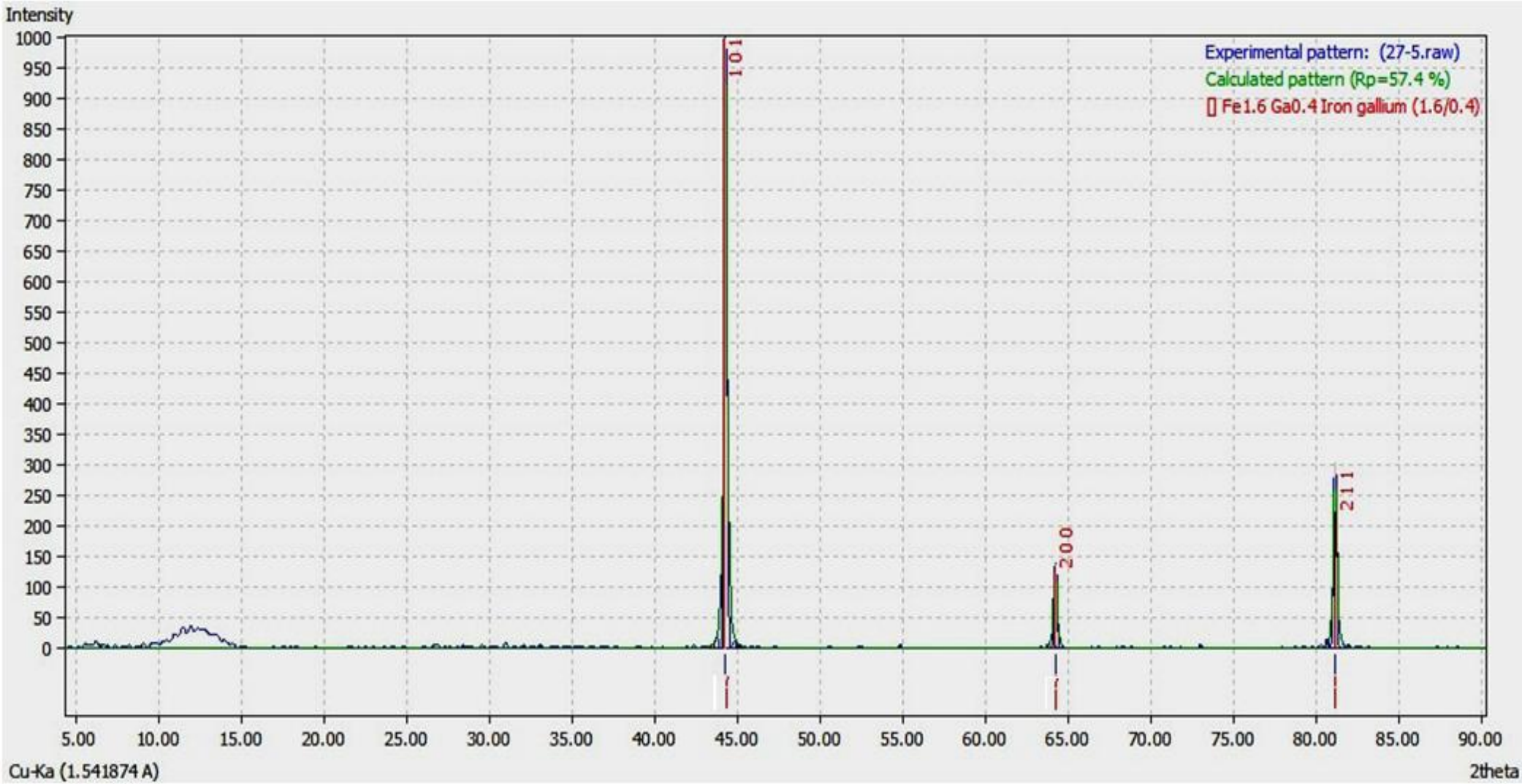

Figure 4.3.2.5 - X-ray scan of Galfenol 27.5 at. % Ga

In order to calculate the lattice parameters for each composition it is usual to index the peak with the highest intensity as this is where the majority of the texture is situated, in this case it is the [110] family of directions. Re-arranging the Bragg equation that was derived earlier and combining it with the equation to calculate lattice parameter, a_0, results in equation 4.3.2.2:

$$d_{hkl} = \frac{\sqrt{h^2+k^2+l^2}}{a_0} \qquad \textbf{(4.3.2.2)}$$

Table 4.3.2.1 simply presents the composition value, the d-spacing used in the calculation and the resulting lattice parameter, a_0. Included in the table is the value for α-Fe which is 0 at. % Ga.

Galfenol Composition at. %	**d-spacing value $d_{[110]}$ (Å)**	**Lattice Parameter a_0 (Å)**	**Volume of Unit Cell V (Å^3)**	**Lattice Parameter a_0 (Å) (Other Studies)**	**Phase(s) Present Within Samples**
0	2.0286*	2.86900*	23.6152*	n/a	bcc
12.8	2.0440	2.89065	24.1538	2.89600 **[3.1.1.1]**	disordered bcc
17.5	2.0492	2.89800	24.3386	2.90010 **[4.2.5.6]**	disordered bcc
19.5	2.0537	2.90451	24.4314	2.90504 **[4.2.5.6]**	disordered bcc
22.5	2.0596	2.91271	24.7111	2.90923 **[4.2.5.6]**	disordered bcc
27.5	2.0672	2.92346	24.9857	2.91734 **[4.2.5.5]**	disordered bcc

Table 4.3.2.1 - Table of compositions at. % Ga, d-spacing and lattice parameter

The results were plotted as such that a graph of composition at. % Ga versus calculated lattice parameter can be seen in figure 4.3.2.6 which shows an almost a linear fit. The black line gives the line of best fit through the points and gives a value of 1.88 x 10^{-3} Å at. %Ga^{-1} or 1.88 x 10^{-4} nm at. %Ga^{-1} which is in very good agreement with Kawamiya **[4.2.5.1]** and Dunlap **[4.2.5.5]** and the neutron diffraction results presented in chapter 4.2.

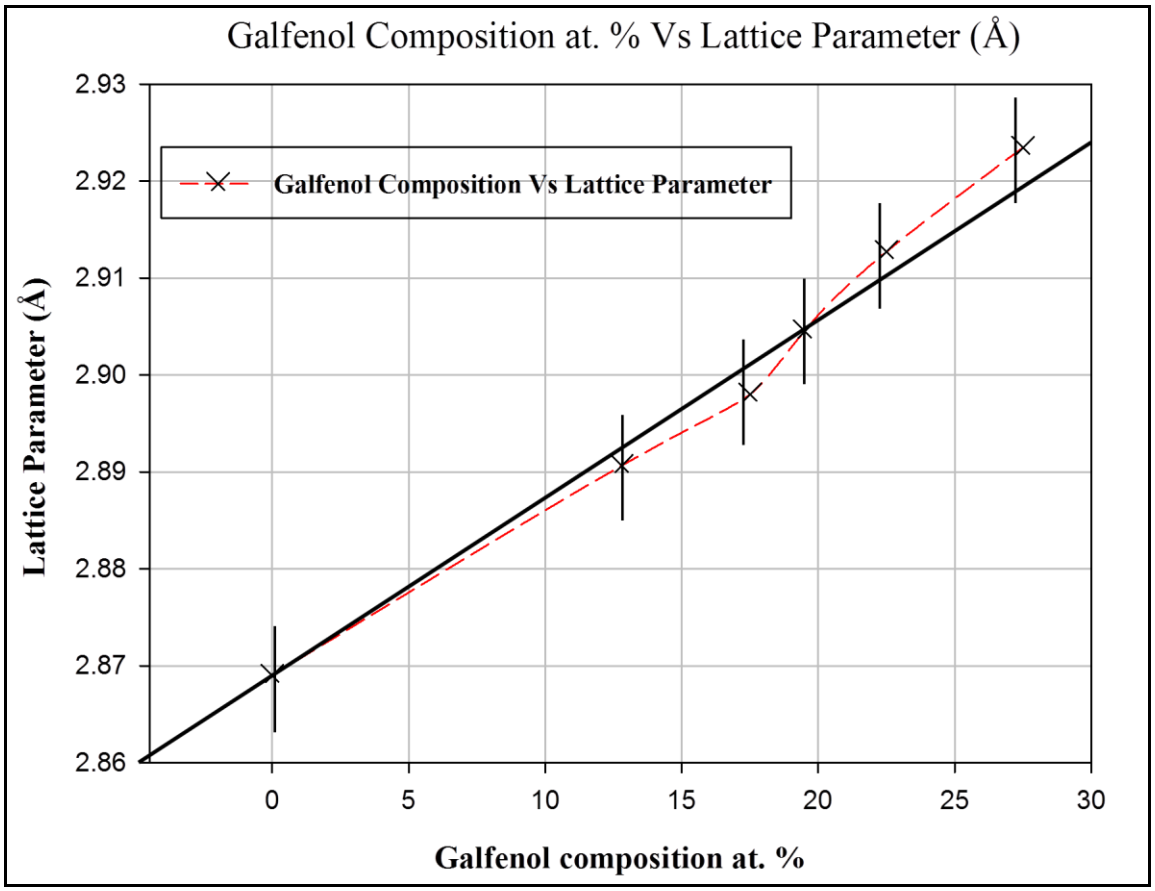

Figure 4.3.2.6 – Galfenol Composition Vs Lattice Parameter. (Actual points are marked with an X complete with error bars. The straight thicker black line is the line of best linear fit.)

Therefore the melt-spinning process is interesting in the fact that the ribbons have enough time to form a polycrystalline solid-solution during cooling i.e. they do not go into an amorphous state. Additionally, the superlattice structure D03 is not formed with rapid solidification. If this type of structure is formed it is not abundant enough to be detected by x-ray diffraction techniques or it must be in such a low concentration that the relative intensity of the peak for the superlattice on these x-ray scans is minimal. The only potential way the D03 phase could be present is if the only D03 texture present is the superlattice equivalent of double the A2 disordered bcc lattice parameter, i.e. the A2 bcc [101] reflection is also the D03 [202] reflection etc which would then result in the peak being in exactly the same place for both structures. Although in the results obtained this is not the case and the lattice parameter results for the bcc phase are in very good agreement with Dunlap et al., Kawamiya and Hume-Rothery **[3.1.1.1, 4.2.5.1, 4.2.5.5].**

As the disordered bcc lattice parameter increases, there is an expectation that if the D03 phase were present, there would be some indication of peak splitting on the scans, but this cannot be seen in these experiments leading to the conclusion that all of these as-spun ribbons are just either in the A2 disordered bcc phase or have concentrations of less than 1% of any other phases.

Annealed and Quenched 19.5 and 27.5 at. % Ga

The annealed and quenched compositions of 19.5 and 27.5 at. % Ga which were heated to 1000°C for 72 hours and then quenched in ice cold water were also tested. The x-ray diffraction scans from these two compositions will now be reviewed, again in a similar manner to all of the as-spun samples.

Firstly, the 19.5 at. % Ga ribbon was analysed using exactly the same criteria as for the as-spun samples, using the same x-ray diffractometer, this scan can be seen in figure 4.3.2.7. Similar to the as-spun sample there seems to be no trace of superlattice peaks but what is interesting is the huge increase in intensity of both the [200] and [211] when compared with the 19.5 at. % Ga as-spun sample which suggests an increase in crystallinity and the subtle peak broadening of the [200] peak from 0.2400 in the as-spun to 0.3200 in the annealed-quenched could suggest that the grain or crystal size is being reduced. Also the preferred orientation of the ribbon has potentially rotated as during the annealing process the Ga atoms have the energy and time to diffuse more succinctly into the lattice; but then are trapped again by the quenching action. The pattern has again been identified as $Fe_{80}Ga_{20}$ as with the as-spun sample of the same composition.

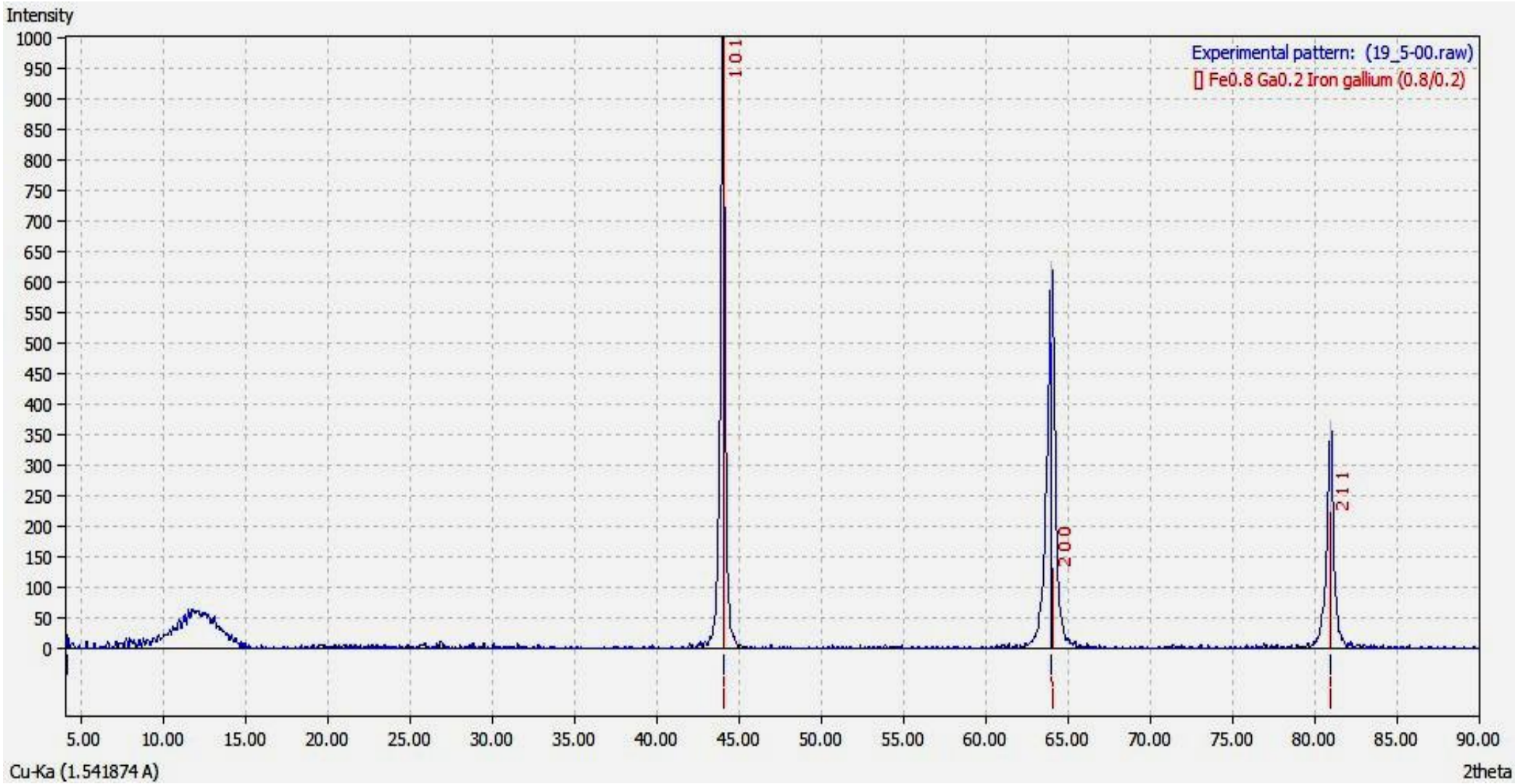

Figure 4.3.2.7 - X-ray scan of Galfenol 19.5 at. % Annealed and Quenched

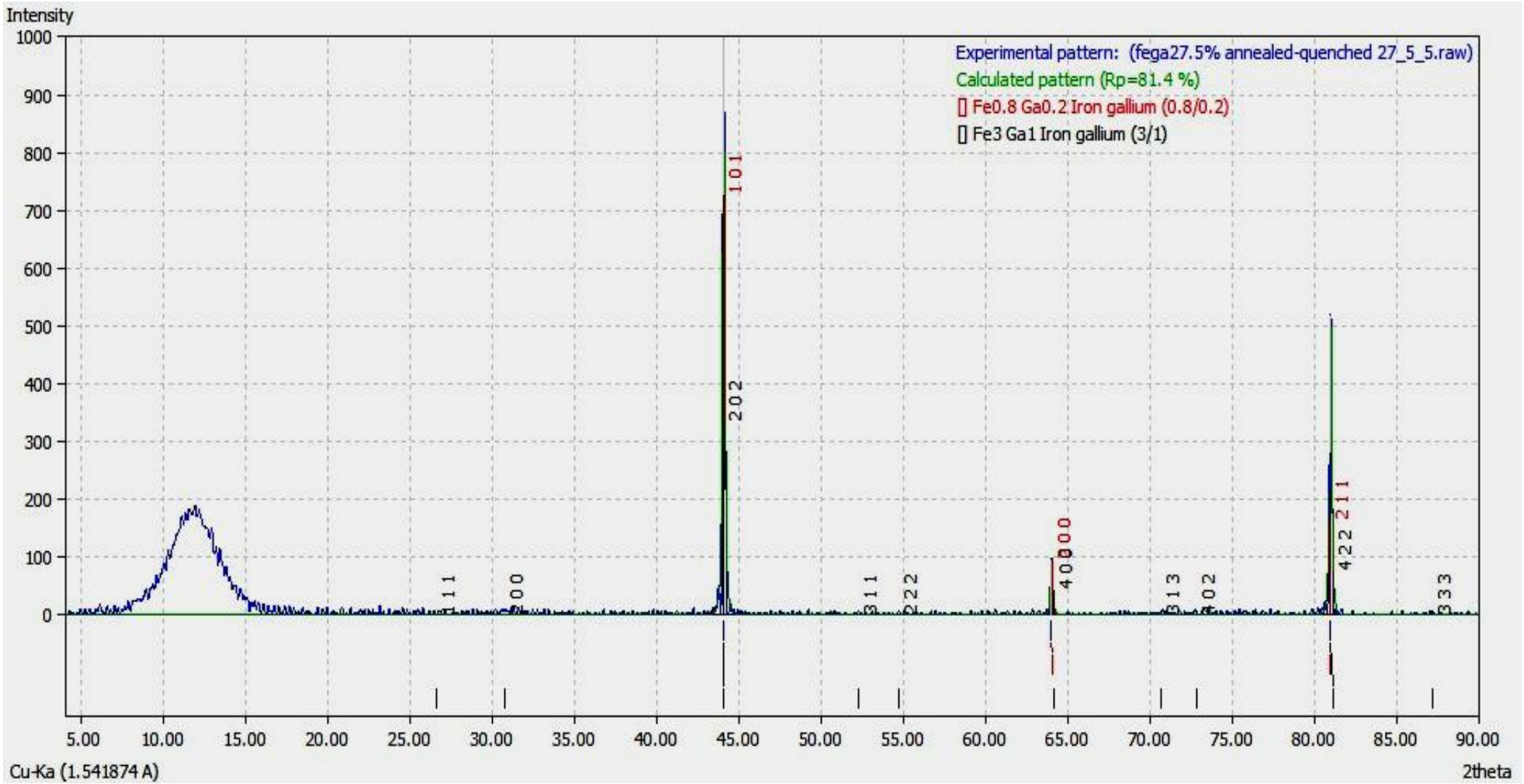

Figure 4.3.2.8 - X-ray scan of Galfenol 27.5 annealed-quenched at. % Ga

Also it should be noted that there has been a small increase in the d-spacing of the main [101] peak which now results in a lattice parameter of 2.9088Å (+~0.15%) which could result from a reduction in the atomic strain in the lattice from the melt-spun state due to the annealing process, which can result in a slight increase in lattice parameter and a small reduction in the crystallite size. **[4.3.2.4]**

Here in figure 4.3.2.8 the pattern is still identified as the $Fe_{80}Ga_{20}$, which is almost identical as mentioned to the $(Fe_4Ga)_{0.4}$ apart from the relative intensities. Here the main noticeable features are that the [200] peak intensity has been substantially reduced as is the [211]. To illustrate where the superlattice D03 peaks should exist, the black miller indices and black check marks at the bottom indicate the specific positions of D03 structure.

A similar result has also occurred in the annealed-quenched sample of the 27.5 at. % Ga, the lattice parameter has ever so slightly increased from 2.92346 Å in the as-spun to 2.92614 Å (~+0.1%). This time though, conversely, the FWHM has actually decreased to 0.2000 indicating sharper and narrower resolution peaks and thus a potential increase in the general overall crystallite size. For completeness, the as-spun plots are also put onto the same graph in order to demonstrate how the peaks have shifted left with increasing Ga content, thus increasing the lattice parameter overall; this can easily be seen in figure 4.3.2.9

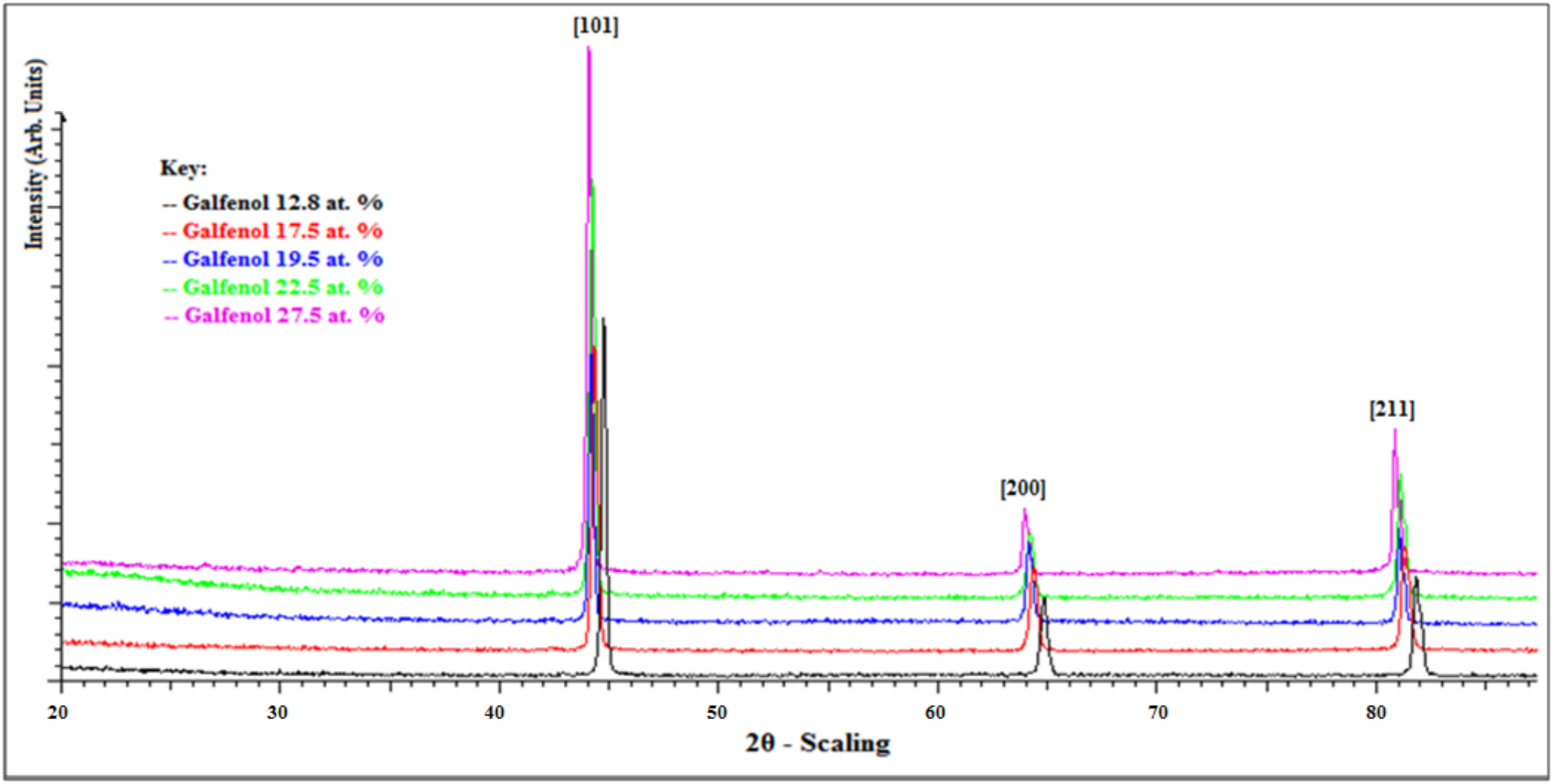

.Figure 4.3.2.9 – Compilation of Galfenol scans for 12.8, 17.5, 19.5, 22.5 and 27.5 at. % Ga As-Spun Ribbons

The reason figure 4.3.2.9 doesn't quite match the earlier figures of the x-ray diffraction data is due to the Crystal Match! software only being able to handle one data set at a time because of the constraints of the fitting procedures. For simplicity each data set has been exported onto the same picture graph so that the comparison between all of the compositions can clearly be observed.

4.4 Chapter 4 References

[4.1.1.1] Gusev A. I.; Nanomaterials, Nanostructures, and Nanotechnologies, Pg 416, Fizmatlit, Moscow. 2007. ISBN:9785922105828

[4.2.1.1] Picture of the Institute Laue-Langevin. http://www.ill.eu/

[4.2.2.1] Schematic of the D2B Instrument. http://www.ill.eu/instruments-support/instruments-groups/instruments/d2b/how-it-works/simulated-experiment/

[4.2.2.2] Description and technical details for the D2B instrument. http://www.ill.eu/instruments-support/instruments-groups/instruments/d2b/characteristics/

[4.2.3.1] Atkins, P.W., Freeman, W.H., Physical Chemistry 7th Edition, Oxford University Press. 2002. ISBN:9780716796787

[4.2.3.2] Bragg Diffraction image: Bragg W.L., The Diffraction of Short Electromagnetic Waves by a Crystal. Proceedings of the Cambridge Philosophical Society **17**: 43–57. 1913.

[4.2.3.3] Image of Reciprocal Lattice and Projection on Ewald Sphere: http://pd.chem.ucl.ac.uk/pdnn/diff1/recip.htm

[4.2.4.1] Lamb, Willis E., Capture of Neutrons by Atoms in a Crystal, Physical Review, vol. 55, Issue 2, pp. 190-197. 1939.

[4.2.4.2] Mössbauer, R. L., Kernresonanzabsorption von Gammastrahlung in Ir^{191}", Naturwissenschaften 45: 538–539, 1958.

[4.2.4.3] Eriksson, O., Svane A., Isomer shifts and hyperfine fields in iron compounds, 1989 J. Phys.: Condens. Matter Vol.1 **1589,** 1989.

[4.2.4.4] Ingalls, R., Isomer Shift of Fe^{57} in Iron, Phys. Rev. **162**, 518. 1967.

[4.2.4.5] Hrynkiewicz, A.Z., Kubisz, J., Kulgawczuk, D.S., Quadrupole splitting of the 14·4 keV gamma line of ^{57}Fe in iron sulphates of the jarosite group, Journal of Inorganic and Nuclear Chemistry, Vol. **27**, Issue 12, Pages 2513-2517, 1965.

[4.2.4.6] DeGrave, E., Vandenberghe, R.E., Dauwe C., ILEEMS: Methodology and applications to iron oxides. Hyperfine Interactions, **161** (1-4): 147-160. 2005.

[4.2.4.7] Vij, D.R., Handbook of Solid State Spectroscopy, Springer Science & Business Media. 2006. ISBN:9780387324975

[4.2.5.1] Kawamiya, N, Adachi, A. Nakamura, Y., Magnetic Properties and Mossbauer Investigations of Fe-Ga Alloys, Journal of the Phys. Soc. Japan, Vol. **33**, No. **5**. 1972.

[4.2.5.2] M.C. Zhang, H.L. Jiang, X.X. Gao, J. Zhu, S.Z. Zhou, Journal of Applied Physics **99** 023903. 2006.

[4.2.5.3] J. Zhang, T. Ma, M. Yan, Physica B **404** 4155-4158. 2009.

[4.2.5.4] A.C. Larson, R.B. Von Dreele, General Structure Analysis System (GSAS), Los Alamos National Laboratory Report LAUR **86**-748. 1994.

[4.2.5.5] Dunlap, R.A, McGraw, J.D., Farrell S.P., Journal of Magnetism and Magnetic Materials **305** 315–320. 2006.

[4.2.5.6] Luo, H.L., Transactions of the Metallurgical Society of AIME, **239** 119. 1967.

[4.2.5.7] X. Zhao, N.J. Mellors, S.H. Kilcoyne, D. Lord, N. Lupu, H., Chiriac, P.F. Henry, Journal of Applied Physics **103** 07B320, 2008.

[4.2.5.8] Rancourt, D.G., Ping, J.Y., Nuclear Instruments and Methods in Physics Research Section B **58** pp85–97. 1991.

[4.2.5.9] Lagarec, K., Rancourt, D.G., Nuclear Instruments and Methods in Physics Research Section B **129** pp266–280. 1997

[4.2.5.10] Blachowski, A., Ruebenbauer, K., Zukrowski J., Przewoznik,J., Journal of Alloys and Compounds **455** pp 47, 2008.

[4.2.5.11] L.R. Newkirk, L.R., Tsuei, C.C., Physical Review B **4** 4046, 1971.

[4.2.6.1] Clark, A.E, Wun-Fogle, M., Restorff, J.B., Lograsso, T.A., Cullen, J.R., IEEE Trans Magn **37** 2678, 2001.

[4.3.2.1] Suortti, P., Ahtee, M., Unonius, L., Voigt function fit of X-ray and neutron powder diffraction profiles *J. Appl. Cryst.* **12**, 365-369, 1979.

[4.3.2.2] Lograsso, T.A., Summers, E.M., Materials Science and Engineering **416** pp240–245, 2006.

[4.3.2.3] Dasarathy C., Hume-Rothery W., The System Iron-Gallium, Proceedings of the Royal Society of London. Series A, Mathematical and Physical Sciences, Vol. **286**, No. **1405**, pp.141-157, 1965.

[4.3.2.4] Bayer, A., Determination of lattice parameters, diffracting crystallite size, and thermal stability in mechanically alloyed Cu-Zn solid solutions, Journal of Materials Engineering and Performance, Springer Link, Vol. **6**, Issue **2**, Pgs 149-152, 1997.

Chapter 5: Scanning Electron Microscopy (SEM) and Energy Dispersive Spectroscopy (EDX) Investigations.

5.1 Scanning Electron Microscopy (SEM) and Energy Dispersive X-Ray Spectroscopy (EDX) Composition Analysis

5.1.1 Theory and Application of SEM and EDX

Scanning electron microscopy is a valuable tool used within science to examine surface morphology of samples using high magnification and high resolution. The system has to be used with the sample chamber under high vacuum in order for the electron beam to be able to reach the samples surface, as in a normal atmosphere i.e. air or other gases, the electrons would be dissipated and deflected by the many other atoms and particles present, also the life of the filament would be short-lived due to rapid oxidisation, if it is not situated within an inert atmosphere.

Usually combinations of vacuums are used here, typically a rotary vane pump, also known as a *roughing* pump coupled with either a diffusion pump or a turbomolecular pump in order to achieve the vacuum required, in this instance a turbomolecular pump was used on the Salford SEM system. The roughing pump is first used to pump the system down to around 10^{-3} mbar, only then can the turbomolecular pump be activated to generate the higher vacuum, both pumps are then run continuously during system operation. A simple schematic of the SEM is shown in figure 5.1.1.1 in which the major components are labelled (the pumps are not shown).

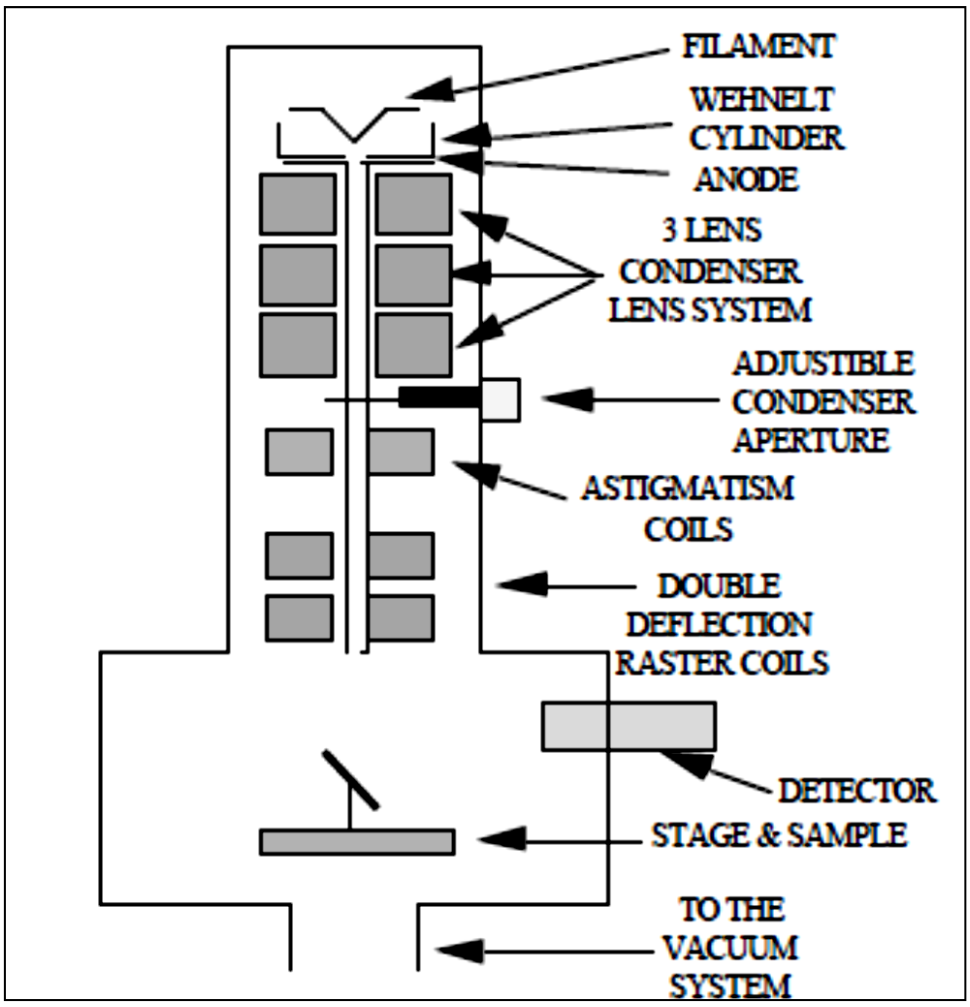

Figure 5.1.1.1 - Schematic of an SEM system [5.1.1.1]

The working pressure of the sample chamber and column is ~10^{-7} mbar. The basis of electron production in this system is known as field-emission and uses a Tungsten tip (W) where the electrons are pulled from the very fine tip by an applied electric field by a high potential on the anode, field emission is sometimes known as cold emission as no current is required through the W tip. Magnetic fields are used to form electron microscope lenses by passing electric current through sets of copper wire coils, these lenses are known as electromagnetic condenser lenses. Most SEM systems use several electromagnetic lenses to reduce the size of the beam's cross-over spot; this allows for a greater control focussing the electron beam. All electromagnetic lenses have spherical aberration which is the inability of the lens to image both the central and peripheral portions of the electron beam at the same focal point and this reduces the overall resolution. The resolution of the final image is limited by the lens with the

worst spherical aberration. As the beam passes through the final condenser lens, two sets of radially opposing magnetic scanning coils control the beam so that it spirals down a central Z-axis which allows it to be manipulated and scanning in both the X and Y directions is possible. The scan pattern is called a *raster pattern* and these final coils are known as raster coils. The raster pattern covers the specimen by starting in the upper left corner and rapidly proceeding to the right, then repeating this by scrolling down one line until the selected area is completely scanned. The Salford system used is a FEI Quanta 250 FEG ESEM and is shown in figure 4.3.1.2 which is situated in the Salford Analytical Services department here shown with the principal users Mr. Geoff Parr and Mr. Joe McMahon. This field emission SEM system has an accelerating voltage for the beam of up to 30 kilovolts and a magnification of up to 10^6. It also has additional electron back scatter detection (EBSD) and energy dispersive x-ray spectrometry detection (EDX).

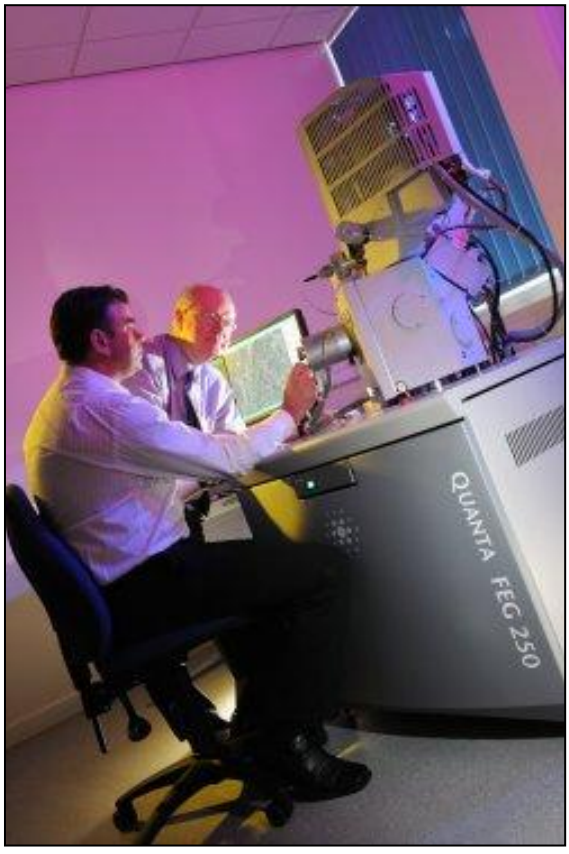

Figure 5.1.1.2 - FEI Quanta 250 FEG ESEM [5.1.1.2]

Principles of SEM and EDX

The SEM system is capable of taking several different sorts of measurements with regards to the samples; sometimes these require additional detection systems in order to interpret the relevant information. The main topics covered here will be for topography and morphology imaging which uses what are called secondary electrons (SE), which are simply low energy electrons resulting from inelastic scattering events with atomic nuclei, backscattered electrons (BSE) which result from elastic collisions from electrons within the material but are of much higher energy than SE, typically these lose less than 1eV. Also energy dispersive x-ray analysis (EDX) which is able to provide elemental compositional analysis by measuring the energies of x-rays which are given off by the sample during Coulomb electron-electron repulsion interaction at the atomic level; also mentioned will be continuum x-ray radiation, known as bremsstrahlung, which is German for *braking radiation*. A simple schematic of these types of interaction can be seen in figure 5.3.1.3

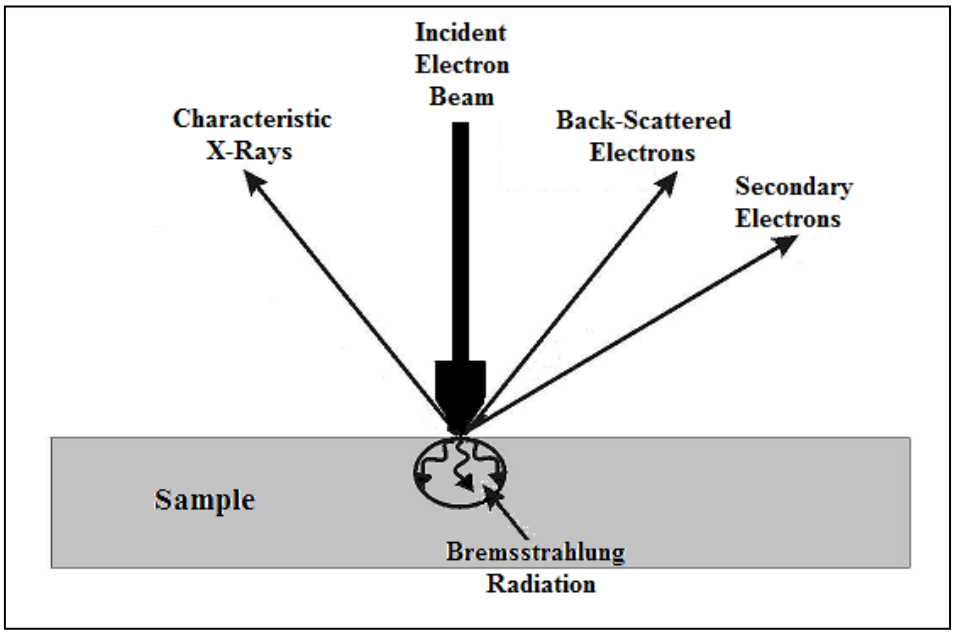

Figure 5.1.1.3 - Schematic of SEM beam and relevant resulting signals

Secondary electrons due to their low energies, typically 5 to 20eV; they are detected using a photomultiplier or scintillator tube where a positive potential of between 100 and 300 volts is

applied to the front of the detector to collect these electrons – around 75% of secondary electrons can usually be collected and the resulting image can now be formed on a screen. Back-scattered electrons lose very little energy when they collide and thus depends strongly upon the atomic number, Z, of the nuclei they are scattered by in the ratio, $\acute{\eta} = N_{backscattered} / N_{incident}$. $\acute{\eta}$ increases with increasing Z meaning that there is what is termed atomic number contrast for BSEs. In the resulting images, areas of high Z number appear brighter than areas of lower Z values. BSEs are usually the result of multiple backscattering events and therefore travel considerable distances before entering the detector which inevitably limits the resolution. **[5.1.1.3]**

The intensity or area of a peak in an EDX spectrum is proportional to the concentration of the corresponding element in the specimen but it must be assumed that the electron beam current is uniform throughout the specimen. Energy dispersive x-ray analysis (EDX) technique is not a surface science technique where the number of x-rays detected is a function of the x-ray energy. Characteristic x-rays (which give discrete quantised energy values) are required to identify the elemental composition of the sample, but bremsstrahlung radiation is of varying wavelengths is also present and is represented by a low intensity yet continuous spectrum of energies on the intensity versus atomic number graph produced by the gradual decrease in energy of the incident electron inside the sample material. The characteristic x-rays are generated by electron-electron collisions inside the atom, where an electron from the incident electron beam collides with an orbiting electron and removes it from the atom. This results in an occupancy state becoming available for a higher level orbiting electron to descend into; as the electron from a higher orbital fills the newly available position into the ground state orbital, it emits a photon of x-ray wavelength corresponding to the change in energy level that it the difference between the energy levels of the transition. This transition corresponds to either K-alpha, L-alpha, K-beta, L-beta etc emission of the x-ray photon. The most common

emission is the K-alpha emission due to the density of electrons near the nucleus being much higher than those in the outer shells. These energy levels are fixed by quantum mechanical rules meaning that it is possible to identify the exact energy or wavelength that results. Each element has slightly different quantised states so that the ratio of intensities of the x-ray photons gives the composition of the material with a resolution of between 150-200 eV **[5.1.1.4].** A schematic of the process is shown in figure 4.3.1.4 which shows the interaction between the incident electron, the target electron and the production of an x-ray photon.

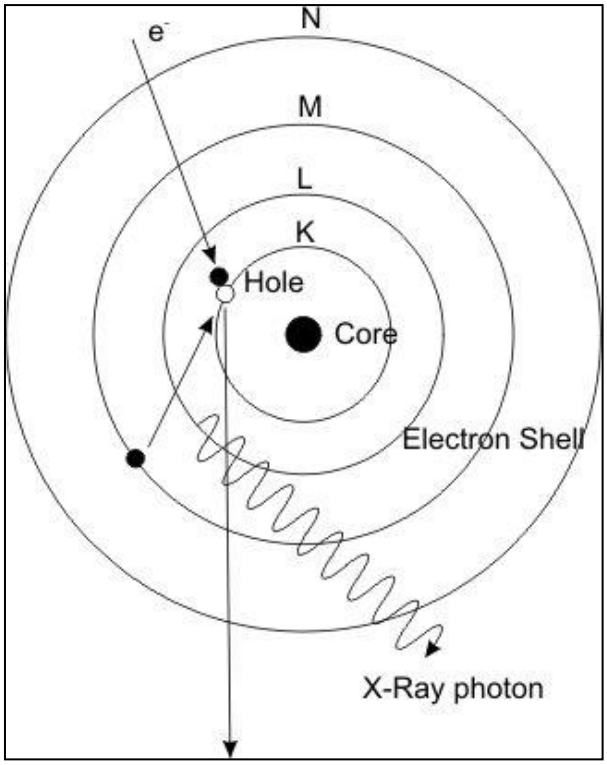

Figure 5.1.1.4 - Schematic of electron-electron interaction and x-ray photon production [5.1.1.3]

The usual accelerating voltage used when applying this method is 5kV as better control is achieved at lower potentials than at the 20 kV used for imaging. Solid state Lithium drifted Silicon (SiLi) detectors are the most prominent in use for this work and are operated at liquid nitrogen temperatures of ~77 Kelvin. When an incoming x-ray strikes the detector, it generates a photoelectron within the Si, the photoelectron travels through the Si and generates electron-hole pairs which in turn produce a current pulse as the electrons and holes are attracted to opposite ends of the detector with the application of a strong electric field. The

size of the current pulse is proportional to the number of electron-hole pairs created. The full x-ray spectrum can be acquired from the sample but it is useful to choose several places on the sample in order to calculate an average spectrum especially if the sample could be inhomogeneous. EDX can identify elements in concentrations as low as 2%. So EDX is also a useful tool of analysing impurities within samples especially oxidisation of metals and alloys.

5.1.2 SEM and EDX Results

The main purpose of using SEM and EDX in this study was to identify the specific compositions of each of the melt-spun ribbon samples The SEM only provides surface information which in this case is very limited in its use, but it does give an accurate value for the thicknesses of the ribbons and how uniform they are along their length, an image of the Galfenol 19.5 at. % Ga ribbon can be seen in figures 5.1.2.1 and 5.1.2.2. As can be seen in these images, the ribbon is approximately 500 micrometers wide and 30 micrometers thick (on average); this was indicative of all of the ribbons produced. The ribbons vary in thickness and are rough on both sides.

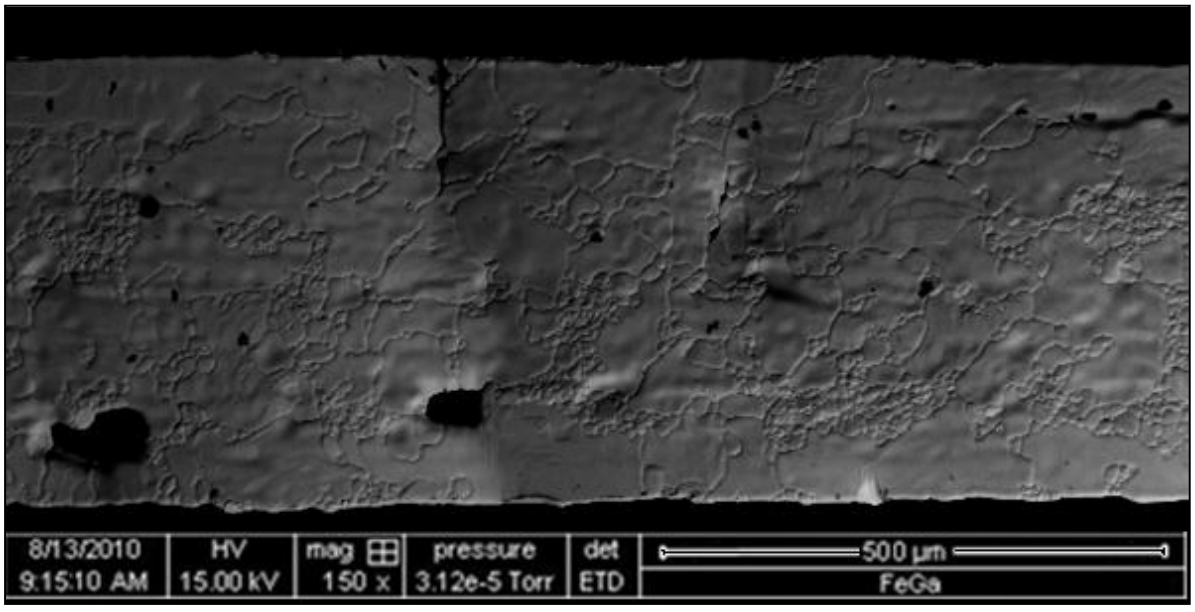

Figure 5.1.2.1 - Topographic image of the Galfenol 19.5% ribbon using the FEI Quanta FEG 250 SEM

It was decided at this time that when performing the future magnetic measurements, it would be much more accurate to use the mass of the ribbon instead of the volume; as the mass could easily be determined using a sensitive balance but to achieve an accurate volume measurement would bring in a variety of complications.

The EDX analysis though is far more useful for this research in the fact that a sample of each ribbon could be taken and then probed five times down its length and then an average composition calculated from the x-ray spectra. These experiments were not carried out until well after the neutron and Mössbauer experiments at the Institute Laue-Langevin and here the focus of the research started to move in the direction of the heavier concentrations of at. % Ga due to the ongoing research being carried out by other institutions and the magnetostrictive properties of the lower percentage Fe-rich concentrations having been conclusively documented in both bulk and thin film samples **[6.1.2.3, 6.1.2.8, 6.2.2.4, 6.3.2.1]** However, EDX analysis was carried out on all compositions of the aforementioned Galfenol ribbons to clarify the average composition in each ribbon sample.

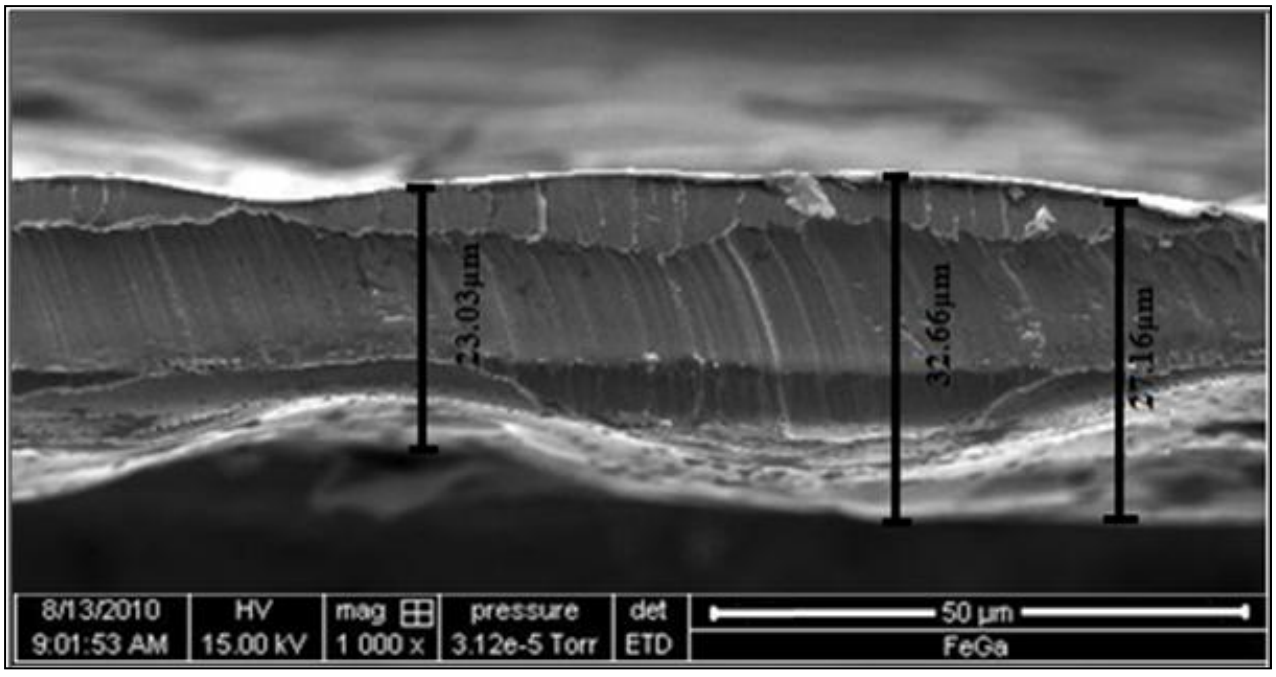

Figure 5.1.2.2 - Thickness view of FeGa 19.5% ribbon indicating non-homogeneity and varying thickness indicated along the length

The following tables 5.1.2.1 to 5.1.2.5 were produced by the EDX system to verify the compositions and an example of the x-ray spectra data is shown in figure 4.3.2.3 for the 19.5 at. % Ga sample.

Sample:	FeGa 15									
Element Normalised										
Measurement	1st		2nd		3rd		4th		5th	
Element	Wt %	At %	Wt %	At %	Wt %	At %	Wt %	At %	Wt %	At %
GaK	15.33	12.67	15.74	13.01	15.48	12.79	15.66	12.94	15.39	12.72
FeK	84.67	87.33	84.26	86.99	84.52	87.21	84.34	87.06	84.61	87.28
Total	100	100	100	100	100	100	100	100	100	100
Average	Wt %	At %								
Ga (Av)	15.52	12.83								
Fe (Av)	84.48	87.17								
Total (Av)	100	100								

Table 5.1.2.1 – EDX Results for Galfenol ribbon 15 at. % Ga

As can be seen here there is a large variation between this predicted composition and the actual composition, it was produced as 15 at. % Ga but has turned out only to be an average of 12.8 at. % Ga. Although this result is consistent throughout the five spot measurements, this now 12.8 at. % Ga sample will not significantly affect the later results. It is thought a mistake has been made here as a 15 wt. % Ga sample equated to a 12.8 at. % sample and this is where the error during production has occurred. The composition is still included in the magnetism results later in this chapter, but for a crystallography aspect, this composition is not really of great interest or importance although it will be included whenever applicable for completeness.

Sample:	FeGa17.5									
Element Normalised										
	1st		2nd		3rd		4th		5th	
Element	Wt %	At %	Wt %	At %	Wt %	At %	Wt %	At %	Wt %	At %
GaK	21.78	18.24	20.45	17.07	21.79	18.25	20.51	17.12	21.41	17.87
FeK	78.22	81.76	79.55	82.93	78.21	81.75	79.49	82.88	78.59	82.13
Total	100	100	100	100						
Average	Wt %	At %								
Ga (Av)	21.12	17.67								
Fe (Av)	78.88	82.33								
Total (Av)	100	100								

Table 5.1.2.2 - EDX for Galfenol ribbon 17.5 at. % Ga

For the 17.5 at. % Ga there is an amount of variation from measurement to measurement (sometimes as high as 1.2 at. % difference), yet overall the average value has equated to 17.67 at. % Ga. The target composition of 17.5 at. % Ga here has been verified to be within the boundary levels accepted (±0.5% at. Ga). This suggests that during the rapid solidification of the melt, there is partial tendency for the Ga atoms to form what could be termed *clusters* within a larger matrix of Fe atoms as described by Ikeda **[6.2.1.2],** thus forming the disordered bcc structure where the Ga atoms just substitute directly for Fe atoms in the structure but seem to have some type of preference to associate with other Ga atoms as either nearest neighbours or next nearest neighbours. Ikeda describes how the quenching effect doesn't allow the Ga atoms enough time during solidification to dilute the lattice evenly thus resulting in the clustering effect of Ga in certain compositions of the Galfenol alloys.

The 19.5 at. % Ga composition shows a more homogenous texture with smaller variations in composition down the length of the ribbon during solidification suggesting that here there are enough Ga atoms to form a more uniform distribution within the ribbon. As this composition is deemed the most magnetostrictive of all of the Galfenol alloys **[5.1.2.1]** it would suggest that here there are elements of short range ordering (SRO) within a much larger disordered bcc matrix where an intrinsic internal strain exists across the entire crystal lattice.

Sample	FeGa 19.5									
EDAX Quantification										
Element Normalised										
	1st		2nd		3rd		4th		5th	
Element	Wt %	At %	Wt %	At %	Wt %	At %	Wt %	At %	Wt %	At %
FeK	77.04	80.87	76.86	80.61	77.1	80.87	77.04	80.79	76.98	80.75
GaK	22.96	19.13	23.16	19.39	23.9	19.13	22.96	19.21	23.02	19.25
Total	100	100	100	100	100	100	100	100	100	100
Average	Wt %	At %								
FeK	77.004	80.77								
GaK	22.996	19.23								
Total	100	100								

Table 5.1.2.3 - EDX Results for Galfenol ribbon 19.5 at. % Ga

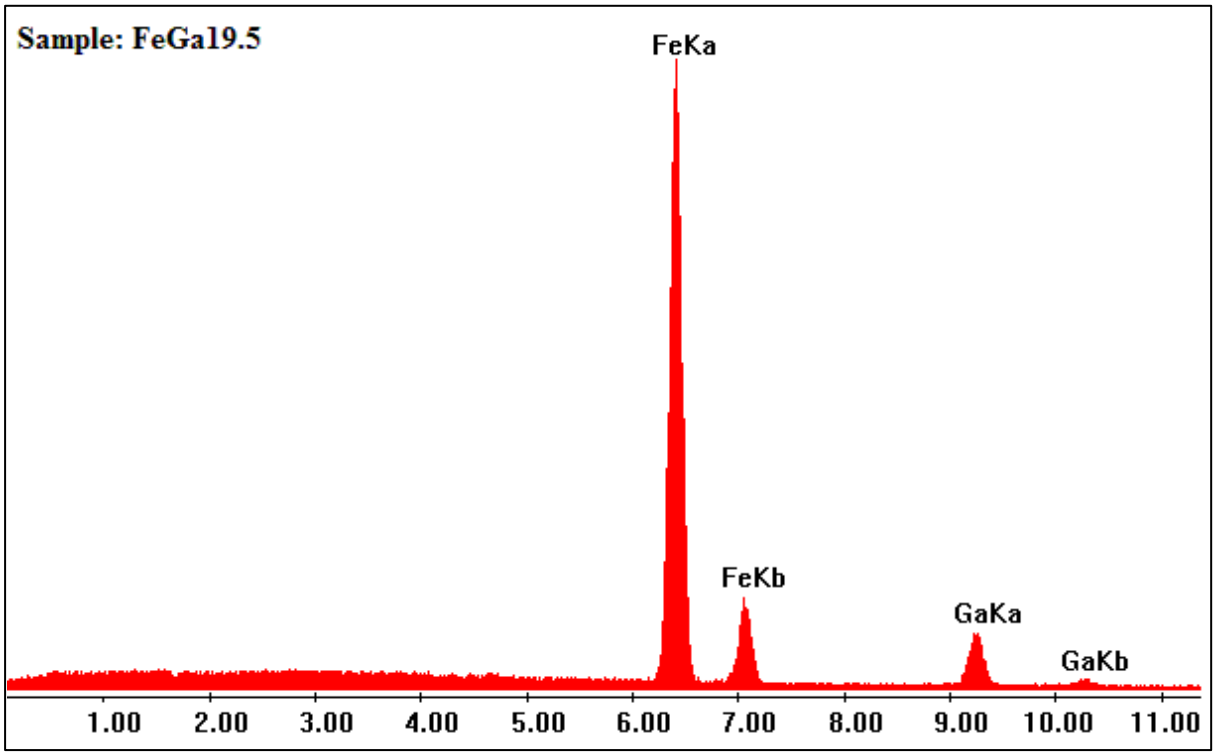

Figure 5.1.2.3 - X-ray spectra graph from the Galfenol 19.5 at. % sample

As in the neutron study performed earlier, there are traces of the DO3 structure within this composition, although there are not enough Ga atoms to form this structure throughout the ribbon, thus the end result is a small amount of DO3 phase present within the A2 disordered bcc lattice.

The 22.5 at. % Ga sample also shows a certain amount of uniformity compared to the 17.5 at. % Ga ribbon, although subtle variations in composition are found along the ribbon length. It is known that with this composition of alloy it can potentially form an array of structures in the phase diagram; yet here it is thought that due to the high cooling rate that these structures are unlikely to form and that the A2 disordered bcc phase still dominates.

Sample:	FeGa22.5									
Element Normalised										
	1st		2nd		3rd		4th		5th	
Element	Wt %	At %	Wt %	At %	Wt %	At %	Wt %	At %	Wt %	At%
GaK	26.67	22.56	27.26	23.08	26.94	22.75	26.81	22.66	26.86	22.71
FeK	73.33	77.44	72.74	76.92	73.06	77.25	73.19	77.34	73.14	77.29
Total	100	100	100	100	100	100	100	100	100	100
Average	Wt %	At %								
Ga (Av)	26.908	22.752								
Fe (Av)	73.092	77.248								
Total	100	100								

Table 5.1.2.4 - EDX Results for Galfenol ribbon 22.5 at. %

Sample:	FeGa27.5									
Element Normalised										
	1st		2nd		3rd		4th		5th	
Element	Wt %	At %	Wt %	At %	Wt %	At %	Wt %	At %	Wt %	At %
GaK	32.13	27.5	31.91	27.279	32.32	27.61	31.89	27.256	32.31	27.61
FeK	67.87	72.5	69.28	72.721	67.68	72.39	68.11	71.744	67.69	72.39
Total	100	100	100	100	100	100	100	100	100	100
	Wt %	At %								
Average										
Ga (Av)	32.112	27.451								
Fe (Av)	67.888	72.549								
Total (Av)	100	100								

Table 5.1.2.5 - EDX Results for Galfenol ribbon 27.5 at. %

The EDX results do not suggest that the formations of clusters of Ga are preferred over a random distribution in the lattice, but that the Ga again substitutes itself within the A2-bcc structure and there is no suggestion of long range order that can be observed from this data. The analysis is completed with the final alloy of Galfenol 27.5 at. % Ga ribbon. It shows a good uniform composition over the length with little variation in Ga content. Again, this composition has been documented to have the potential of forming the more exotic structures associated with the Galfenol alloy. This EDX result does not indicate that anything other than a uniform sample with little or no formation of Ga clusters and an accurate overall at. % Ga content for further testing and assessment.

5.1.3 Discussion of SEM and EDX Results

The main purpose of using the SEM was to visually check the uniformity and thickness of the samples and utilise the EDX for analysing the final composition of the Galfenol alloys. Unfortunately the SEM is of somewhat limited use for the research required here due to it being mainly focussed upon surface imaging and morphology. However, it is useful in the fact that it has provided enough data from the EDX so that it is possible to identify composition and hence suggest the potential crystallographic phases that could be encountered in the other experiments. It should be noted that there could be some sources of error in the EDX results as the internal structure of the ribbon alloys could be considerably different from what is detected on or near the surface. It is for these reasons that the earlier neutron work was carried out and has provided a good basis for further experiments on these alloys.

The main focus now will be to look at magnetic, thermo-magnetic and thermal experiments to establish the fundamental crystal structures that are in the ribbons and the effect of these on the magnetic properties of these alloys.

5.1.4 Chapter 5 References

[5.1.1.1] Dunlap, M., Adagaveg, J., Introduction to the Scanning Electron Microscope, Facility for Advanced Instrumentation, Pg 3. 1997.

[5.1.1.2] Image of the FEI 250 SEM Scanning Electron Microscope: http://www.analytical-services.salford.ac.uk/cms/news/article/?id=5

[5.1.1.3] Electron Microbeam Analysis Laboratory, Scanning Electron Microscopy Manual, 2001.

[5.1.1.4] Titchmarsh, J.M, Comparison of high spatial resolution in EDX and EELS analysis, Ultramicroscopy, Volume **28**, Issues 1–4, Pages 347-351. 1989.

[5.1.2.1] Clark, A.E., Wun-Fogle, M., Restorff, J.B., Lograsso, T.A., Materials Transactions **43** pp881–886. 2002.

Chapter 6: Vibrating Sample Magnetometry (VSM), Differential Scanning Calorimetry (DSC) and X-Ray Diffraction Revisited.

6.1.1 Vibrating Sample Magnetometry

6.1.1.1 Principles of VSM

Vibrating sample magnetometry is one of the most useful tools when examining magnetic materials, especially those that are ferromagnetic by nature. The measurement of sample magnetization is indirect and follows from Lenz's law. If a magnetized sample is moved through a coil of wire, where the sample height is denoted by *z* and time by *t*, the magnitude of the voltage induced is given by equations 6.1.1.1, and equation 6.1.1.2 results by expansion with the chain rule with respect to the z-direction. By substituting in the relevant variables into equation 6.1.1.2, equation 6.1.1.3 is the result. These equations are taken from the Quantum Design VSM manual **[6.1.1.2].**

$$V_{coil} = \frac{d\phi}{dt} \qquad \textbf{(6.1.1.1)}$$

$$V_{coil} = \left(\frac{d\phi}{dz}\right)\left(\frac{dz}{dt}\right) \qquad \textbf{(6.1.1.2)}$$

If the position varies in time with a sinusoidal frequency then equation 6.1.1.3 results:

$$V_{coil} = 2\pi f C m\, A \sin(2\pi f t) \qquad \textbf{(6.1.1.3)}$$

Here *C* is a coupling constant, *f* is the oscillation frequency, *A* is the amplitude of oscillation and *m* is the sample magnetization. The amplitude and frequency are user programmable and known to high accuracy. In this work, A=3mm and f=40Hz.

C is determined by calibration with a Pd pellet as mentioned before. As such, by measuring V_{coil} a highly accurate value of m can be ascertained. When the sample has been mounted to the relevant holder, it is inserted into the VSM and the software briefly takes over and automatically centres the sample at the maximum signal value within the coils; this process is known as the *touchdown* and sometimes a sample must be remounted if it is too near the bottom of the holder due to there being limited headroom within the coilset.

Measurements can proceed in three modes: persistent, driven and sweep which are very briefly described here.

Persistent mode slowly approaches the desired field value and then maintains a steady current to the superconducting coils; this is the most accurate approach but takes vast amounts of time to perform. Driven mode maintains the current in the coil which results in a constant applied field of plus or minus 0.5 Oe; this mode takes the most time as the field is allowed to settle accurately at a pre-determined value, the measurement taken and then the next field value targeted. Sweep mode continuously changes the field at a user-defined rate, usually 0.5 Oe per step and the pick-up coils measure continuously. The continuous sweep mode was an ideal compromise, as it is much faster than persistent mode, yet still maintains a highly accurate reading; this mode was selected as the machine had already been calibrated using this mode. All measurements in this thesis were performed with the magnet in the sweep mode in order to maintain consistent treatment for all of the compositions of Galfenol.

The oscillating sample's dipole field is detected by the pick-up coils, induced due to the applied uniform magnetic field from the large field magnets. In this case a Quantum Design Versalab with additional VSM module was used as seen in figure 6.1.1.2; the sample and coil sets are enclosed within a vacuum chamber which is capable of a large temperature range from 50 up to 1000 Kelvin by either use of a ^{4}He gas compressor for the lower temperature range (50 to 400K) and a special heater sample stick for the high temperature range (300 to

1000K). Depending upon the shape of the sample, whether it is a pellet, a ribbon or a powder, suitable holders such as brass, quartz or plastic can be used. When temperature measurements are performed a more specialist sample holder is used. This is a platinum-rhodium coated ceramic which has several electronic circuits integrated into the coating. The stick itself contains both the heating system and a thermocouple to measure the applied temperature; in conjunction with this, zirconia cement is used to bond the sample to the ceramic stick and this is then wrapped with a thin foil copper shim in order to reduce any thermal losses to the environment. A simple schematic of the VSM is shown in figure 6.1.1.1.

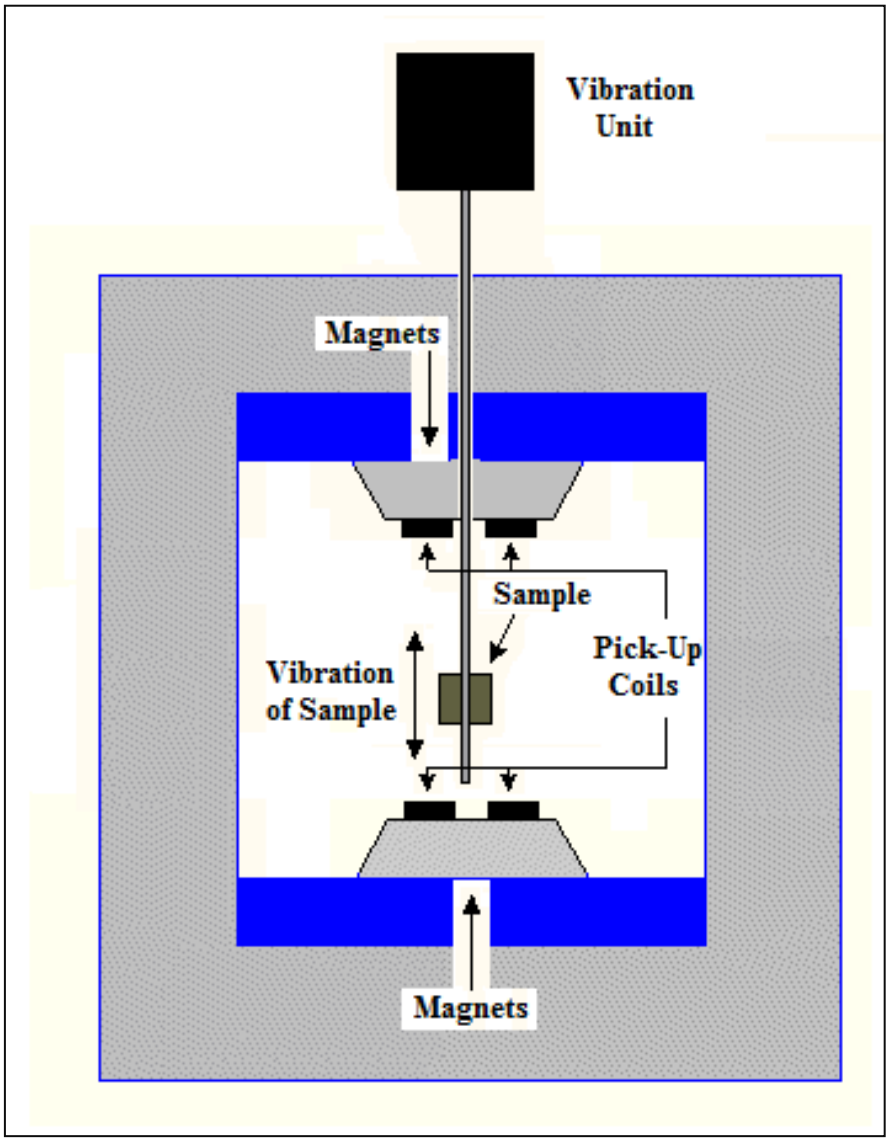

Figure 6.1.1.1 - Simple Schematic of a vertical field VSM

Figure 6.1.1.2 - Quantum Design Versalab with VSM Module stage and ^{4}He compressor [6.1.1.1]

The maximum field produced by the QD supercooled coil-set is 30,000 Oersteds (3 Tesla) in graduations of 0.5 Oe and the system was calibrated using a NIST Palladium sample pellet, giving an accuracy of better than 1 x 10^{-6} Oersteds. The system is fully automated apart from sample orientation which must be altered manually. A dedicated PC controls and monitors the whole system and with the ability to write script programs in Visual Basic, a series of measurements can be set to run whether hysteresis curves or temperature measurements are required.

6.1.2 VSM Measurements and Results

Magnetisation vs. applied field measurements were carried out at room temperature, typically with the temperature chamber set to 295K (~22 Celsius) as the chamber must be between 295K and 305K in order for sample changes to be made; these were all performed using a quartz sample holder and the sample secured using PTFE tape. Firstly a blank quartz holder with PTFE was measured and the resultant data subtracted from the actual measured data in order to remove any background resulting from the quartz and

PTFE. The number of quadrants measured can be set using the various parameters on the software, typically these measurements consisted of 5 quadrants: From zero to maximum positive field, from maximum positive field back to zero, zero to maximum negative field, maximum negative field back to zero and then from zero back to maximum positive field. The field was then reduced to zero using the oscillatory option which allows for the sample to be slowly cycled from the maximum field to maximum negative field and eventually slowly reduced to zero. This ensures that the sample isn't magnetically saturated when it is removed and has as low remanance as possible. A maximum applied field of 30000 Oe (3T) was investigated so that all of the samples would definitely be saturated in both hard and easy directions.

The temperature measurements first used the blank ceramic sample stick with just zirconia cement and copper shim attached in order to be able to remove any residual background from the actual experimental data. A heating rate of 10 $Kmin^{-1}$ was selected and each sample heated up to the maximum temperature of 1000K (~725°C) with a constant applied field of 3000 Oe, so that the material is magnetically saturated. The heating stage was then calibrated using a sample of Ni foil and subsequently checked for accuracy. The heating measurements were only carried out in the easy direction in order to determine the Curie temperature, T_c, for each sample. For the lowest compositions, extrapolation of the data sets was required in order to calculate a value for T_c due to the limitations hot-stage temperature not being high enough to get to the Curie temperature of pure α-Fe of 1043K (770°C). Here figures 6.1.2.1 to 6.1.2.5 present each individual composition for the magnetic hysteresis curve measurement involving both the easy and hard axis; these results will now be discussed.

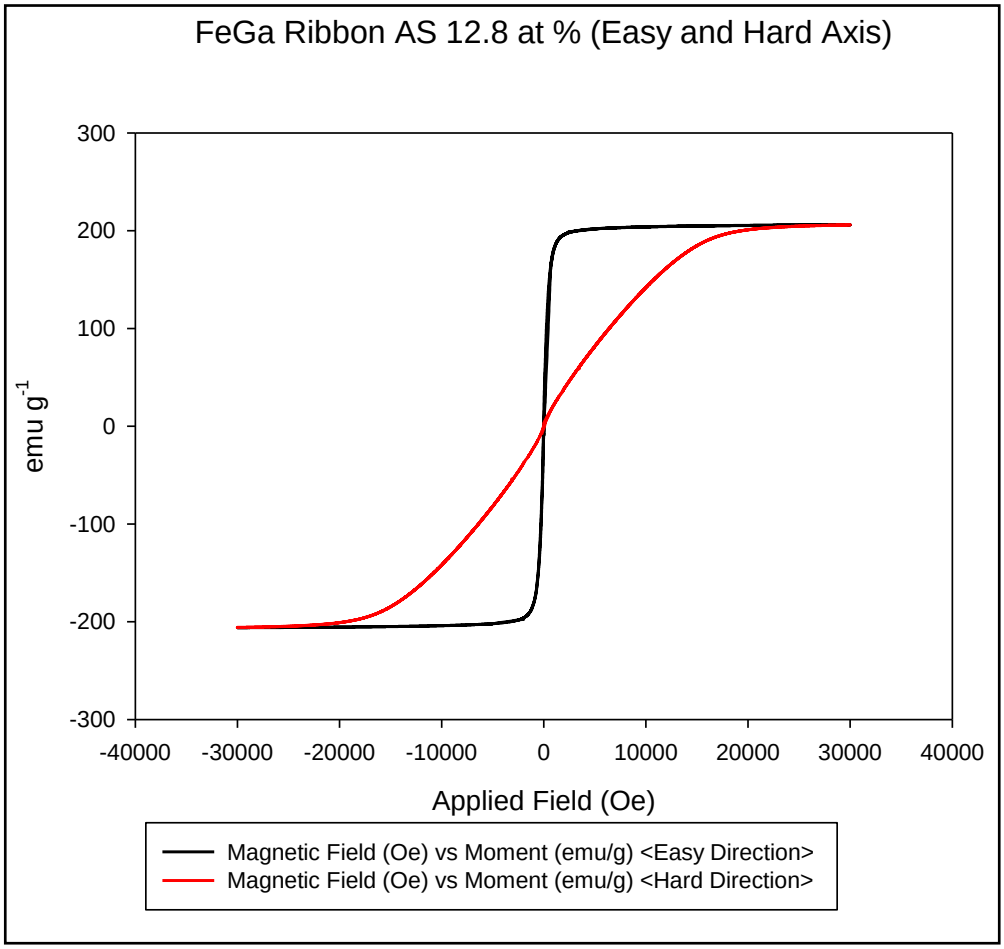

Figure 6.1.2.1 – Magnetic saturation for 12.8 at. % Ga

The 12.8 at. % Ga sample shows a maximum *Ms* value of ~206 emu g^{-1}, with the easy direction saturating at a value of ~2200 Oe, yet the hard direction requires a much greater field to reach saturation, ~22,000 Oe. This is due to the difficulty in magnetising the sample in the hard direction and also the contribution from the much larger demagnetising field opposing the magnetisation caused by the limited thickness of the sample; the many extra free poles cause much greater internal demagnetisation. The sample has a coercivity value, *Hc*, of 19.952 Oe and a remanance, *Mr*, of 1.904 emu g^{-1}, showing that the sample is considered to be very soft magnetically.

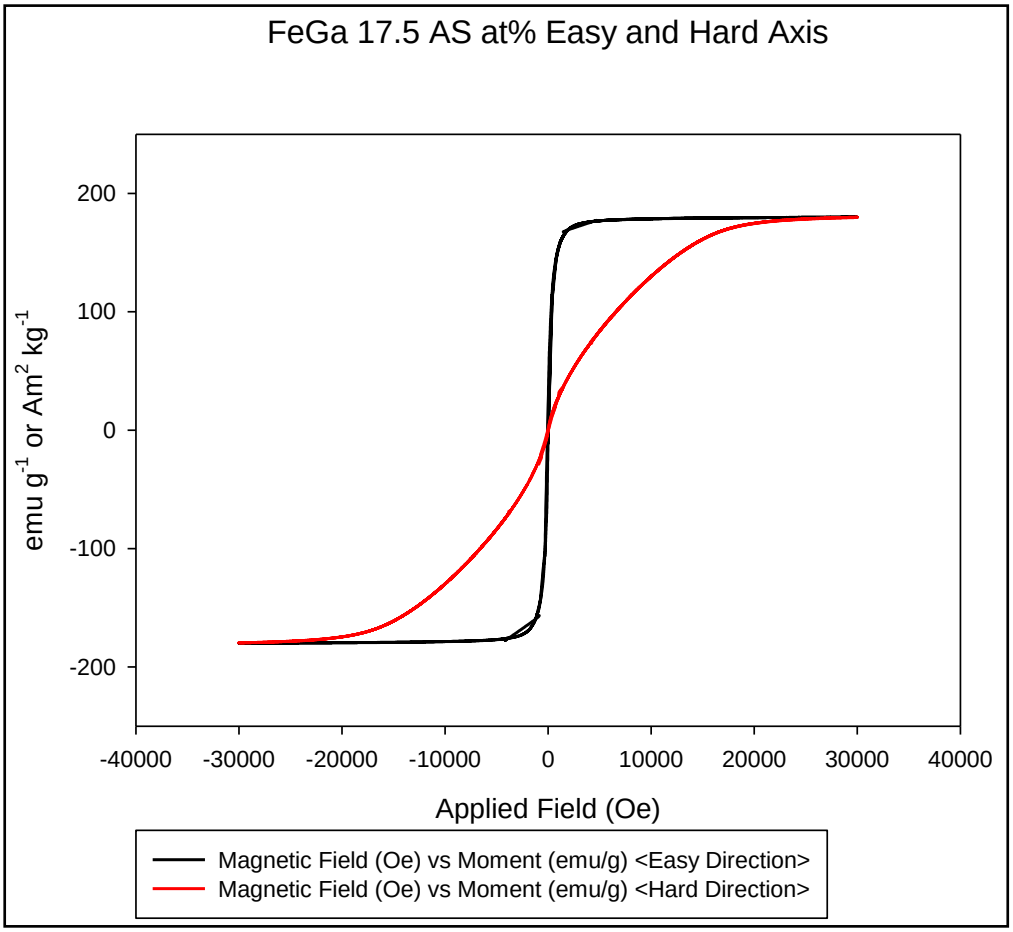

Figure 6.1.2.2 – Magnetic saturation for 17.5 at. % Ga.

The 17.5 at. % Ga was similar in shape to the 12.8 at. % Ga in figure 4.5.2.1, but in this case shows a reduced maximum *Ms* at ~178 emu g^{-1}, *Hc* of 12.078 Oe and *Mr* of 1.391 emu g^{-1}, this is a considerable decrease when compared to the 12.8 at. % Ga sample; yet the material is still magnetically very soft.

Here in figure 6.1.2.3 the 19.5 at. % Ga, the saturation value, *Ms*, has again decreased to 169.5 emu g^{-1}; as is to be expected with the continued addition of non-magnetic atoms into a ferromagnetic lattice, in effect diluting the ferromagnetic material. The coercivity, *Hc* has decreased from the 17.5 at. % Ga sample and is 8.180 Oe and the remanence, *Mr* is 1.152 emu g^{-1} which is also a distinct decrease from the last sample.

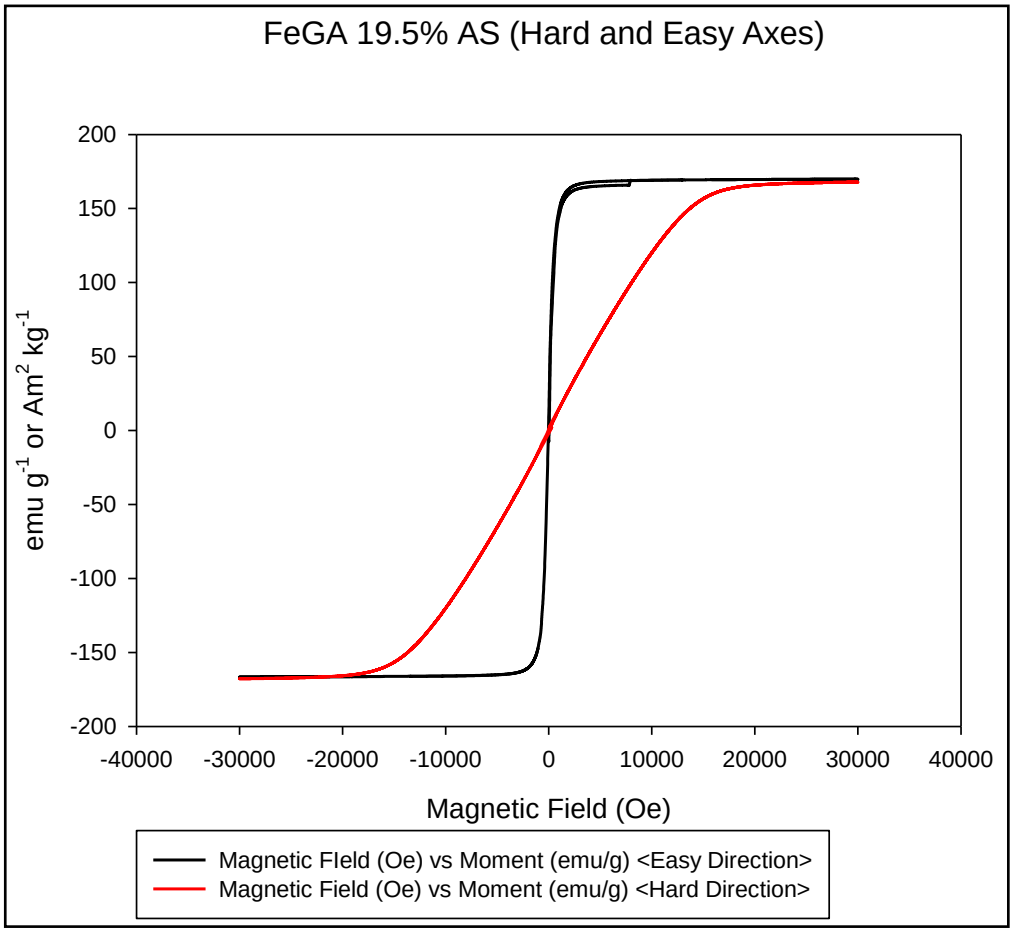

Figure 6.1.2.3 – Magnetic saturation for 19.5 at. % Ga

To complete the compositions figure 6.1.2.5 displays the 27.5 at. % Ga composition which has the lowest *Ms* of all of the compositions at 115 emu g^{-1}. It also shows the lowest coercivity at 0.989 Oe and a very low remanence of 0.280 emu g^{-1}. For completeness figures 6.1.2.5 and 6.1.2.6 show all of the compositions on the same graphs for both easy and hard axes respectively; so they can be compared with each other visually. The saturation value of the 22.5 at. % as can be seen in figure 6.1.2.4 has now dropped significantly from the last sample down to 140 emu g-1, the coercivity approximately the same at 4.882 Oe and the remanence reduced down to 0.722 emu g-1, making this composition extremely soft for a ferromagnetic alloy.

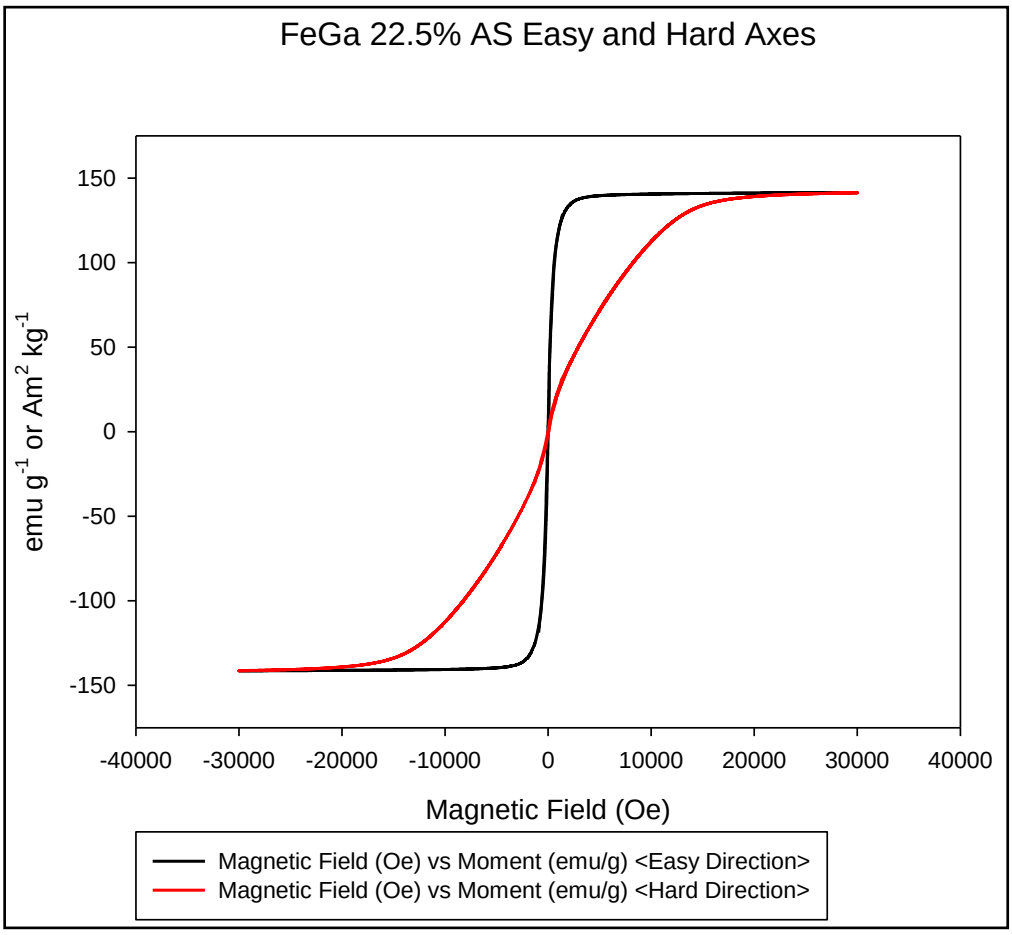

Figure 6.1.2.4 – Magnetic saturation for 22.5 at. % Ga

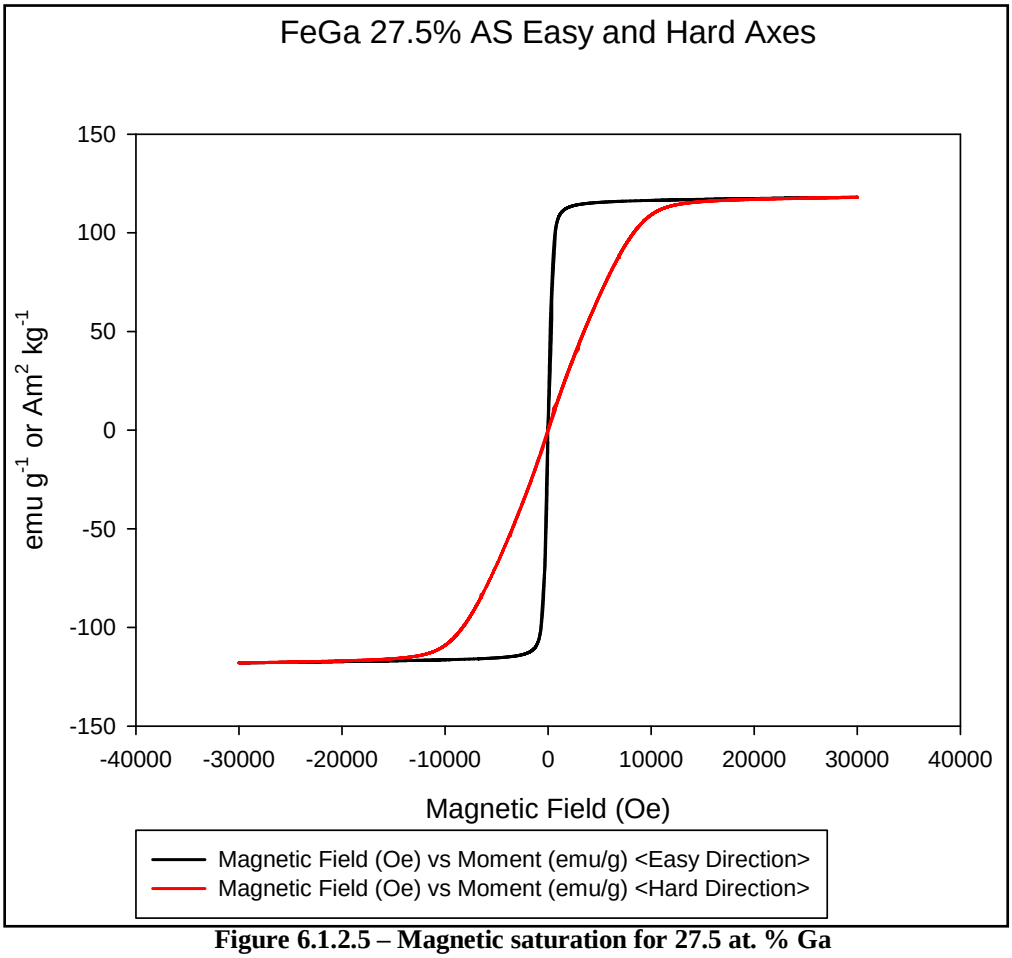

Figure 6.1.2.5 – Magnetic saturation for 27.5 at. % Ga

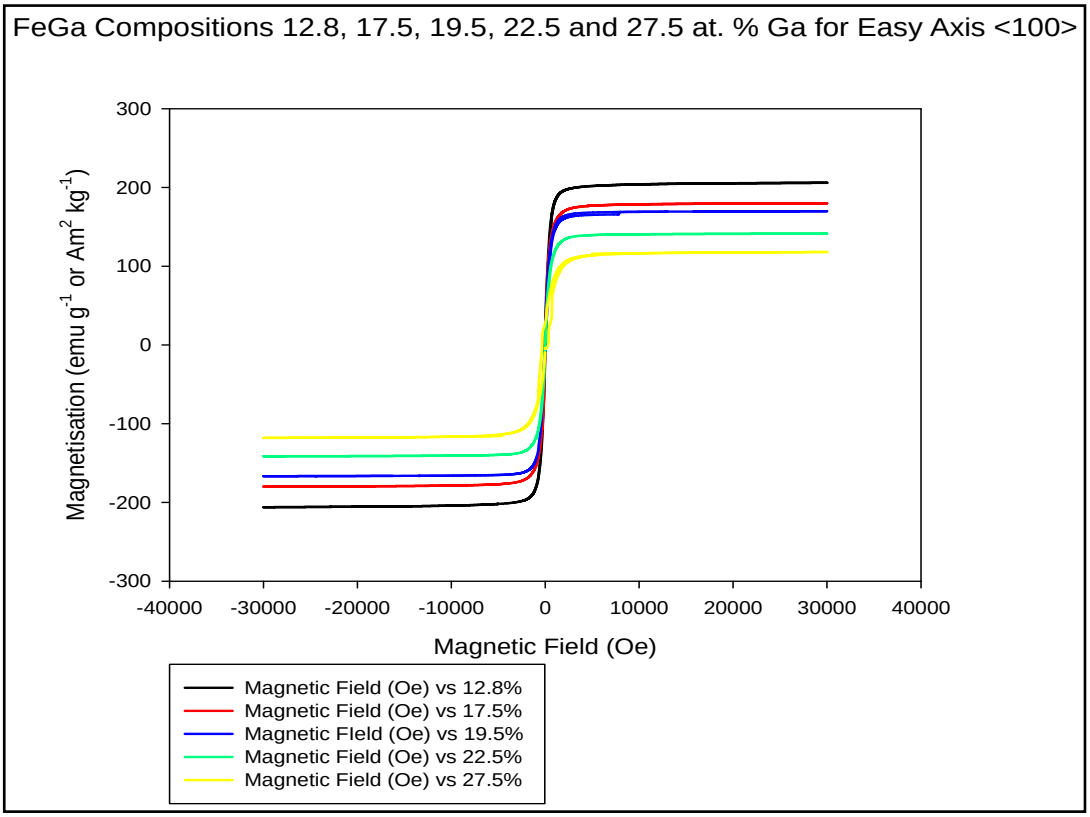

Figure 6.1.2.6 – Magnetic saturation for all compositions in the easy axis

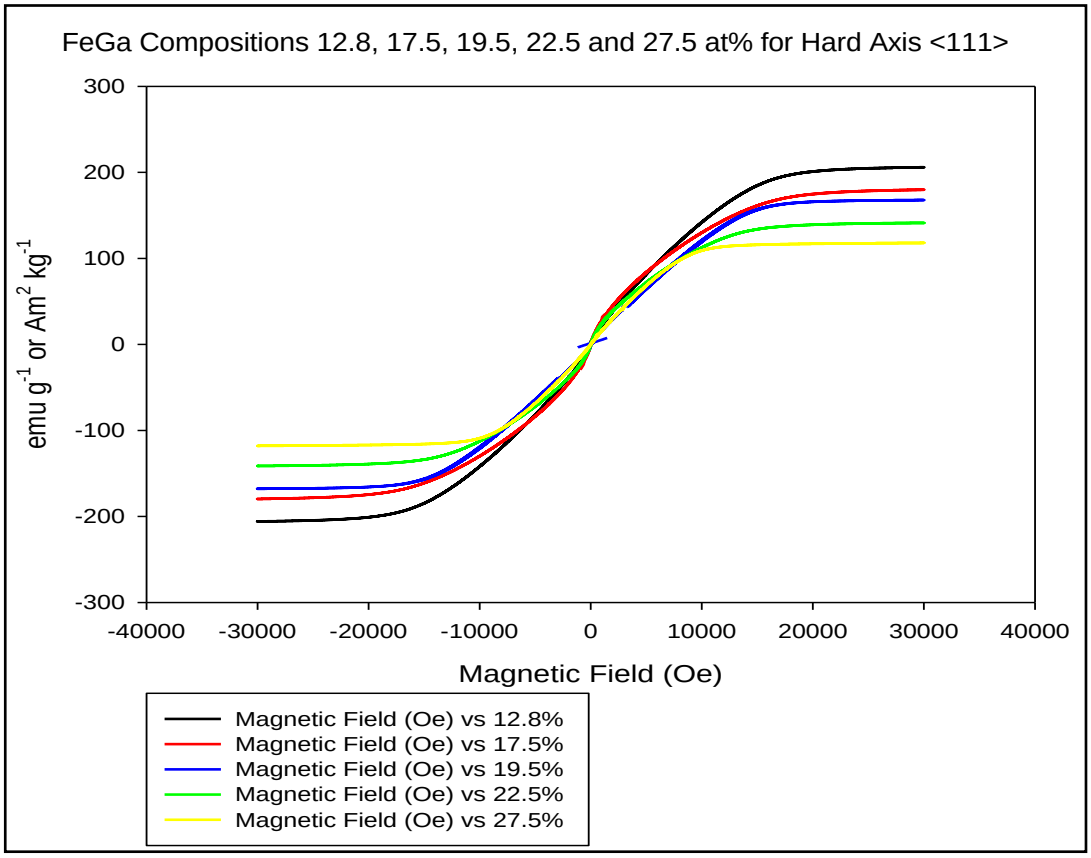

Figure 6.1.2.7 – Magnetic saturation for all compositions in the hard axis

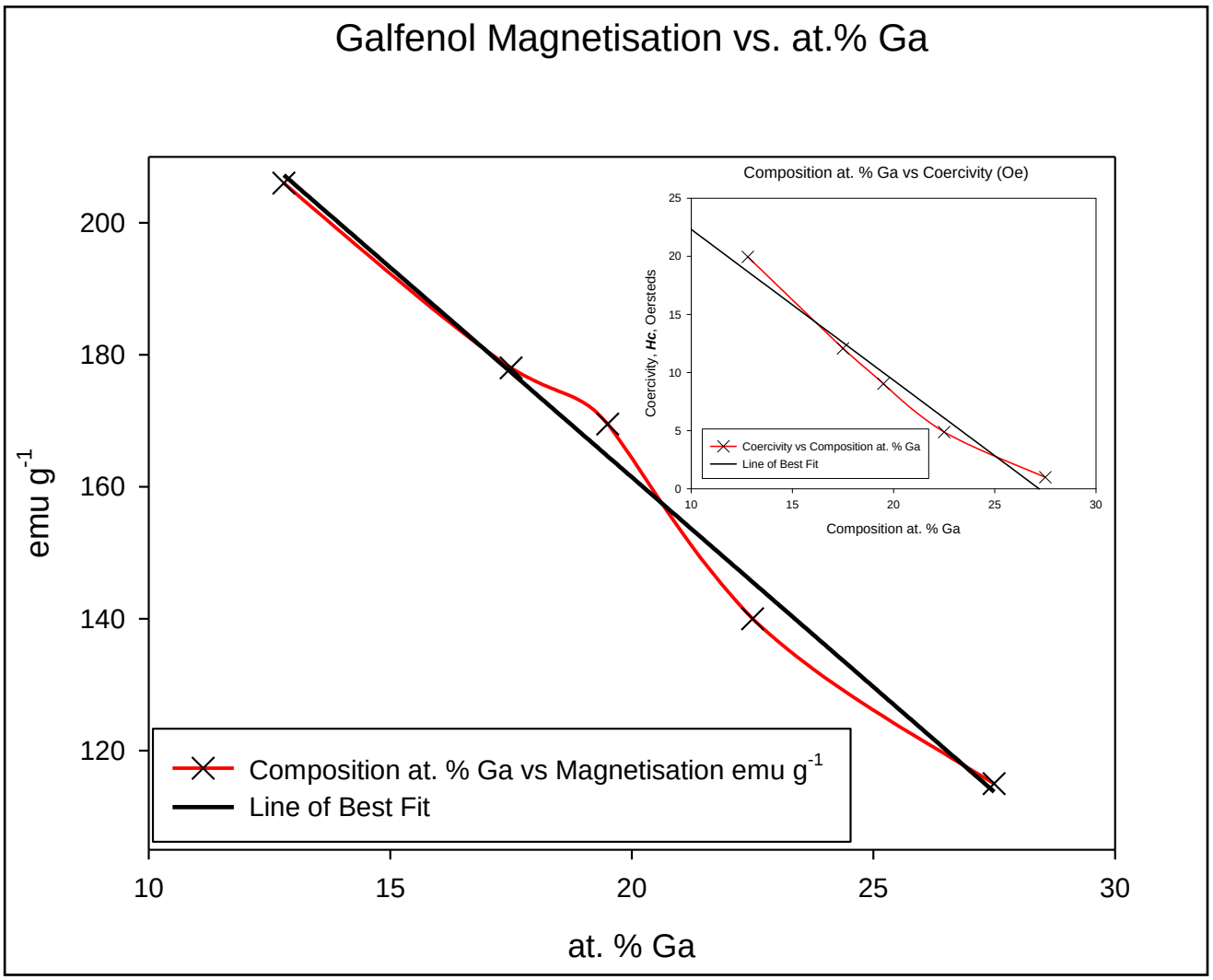

Figure 6.1.2.8 – Magnetisation of Galfenol vs. Composition at. % Ga (Main graph) and Coercivity vs. Composition at. % Ga (Inset) – (Error bars are thinner than the graph lines themselves)

The reduction is magnetisation is approximately linear with Ga addition for the compositions tested; this is similar to the increase in lattice parameter which is also approximately linear as seen in both the neutron and x-ray results. A graph of composition versus magnetisation can be found in figure 6.1.2.8 which visually shows this change in the magnetic parameter. The reduction in magnetisation has been calculated from the line of best fit and gives a value of -6.362 emu g^{-1} at. % Ga^{-1} over the tested composition range 12<x<30 at. % Ga, this is in good agreement with Kawamiya and Zhu for A2 bcc disordered samples **[4.2.5.1, 6.1.2.1].** The two annealed and quenched samples of 19.5 and 27.5 at. % Ga did not show any noticeable difference from the as-spun ribbons of the same compositions and thus are not shown.

Table 6.1.2.1 contains a summary of the relevant magnetic measurements for all the compositions of the Galfenol ribbons.

Ribbon Composition at. % Ga	**Magnetisation M_s (emu g^{-1})**	**Coercivity H_c (Oe)**	**Remanence M_r (emu g^{-1})**	**Density* (g cm^{-3})**	**Bohr Magnetons* ($\mu Fe/\mu B$)**
12.8	**206**	**19.952**	**1.904**	**7.859**	**2.301**
17.5	**178**	**12.078**	**1.391**	**7.955**	**2.254**
19.5	**169.5**	**8.180**	**1.152**	**8.037**	**2.250**
22.5	**140**	**4.882**	**0.722**	**8.002**	**1.895**
27.5	**115**	**0.989**	**0.280**	**7.892**	**1.779**

Table 6.1.2.1 - VSM results for all compositions of melt-spun Galfenol ribbons

*Densities and $\mu Fe/\mu B$ calculated by: Zhu et al, Chin. Phys B, Vol. 20, 7, 077501, 2011.

The decrease in coercivity of the samples changes in an almost linear fashion, as does the remanent magnetisation, which is to be expected with the addition of non-ferrous Ga atoms into a ferrous lattice.

Here are now presented the results for the heating curves generated by the VSM in order to experimentally discover the Curie temperature for each composition of ribbon. The graphs in figures 6.1.2.10 through 6.1.2.13 show the experimental results from the testing of the 12.8, 17.5, 19.5 and 22.5 at. % Ga ribbons and have been averaged over several separate runs for each composition as to remove any anomalous results.

Figure 6.1.2.9 is the heating calibration showing the temperature curve for a thin foil of Ni of 99.99% purity supplied by Testbourne Ltd. The experimental value of 357°C is in good agreement with the standard accepted value of the Curie temperature of Ni which is 354°C **[6.1.2.2].** This result is less than a 1% difference between the experimental and accepted value and therefore the calibration was deemed successful. Each composition of ribbon was orientated in-plane to the field, heated at 10°C min^{-1} and then cooled at the same rate; the field was set to a constant value of 3000 Oersteds (0.3T) whilst the data was collected.

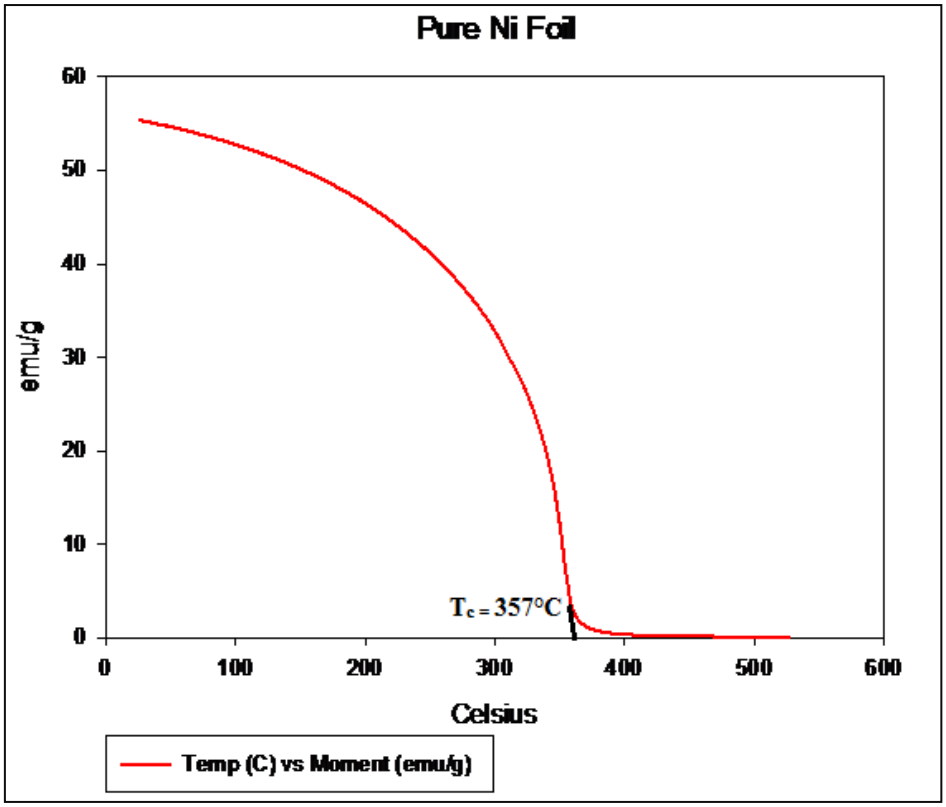

Figure 6.1.2.9 - Curie temperature of pure Ni foil

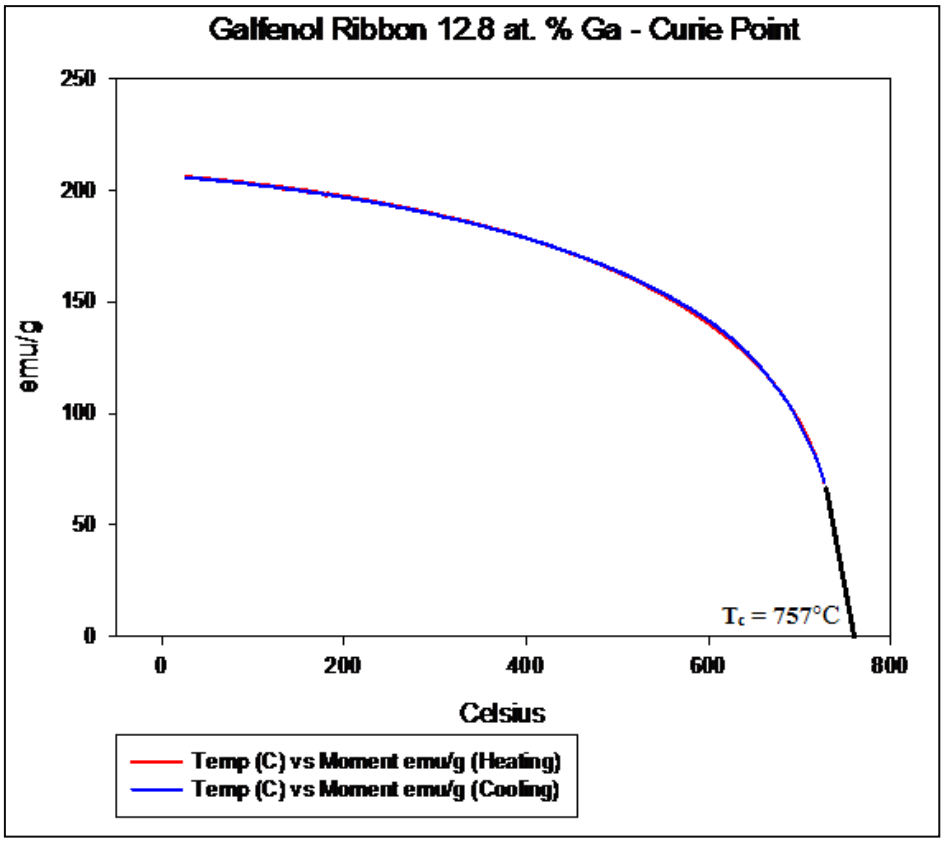

Figure 6.1.2.10 - Curie temperature of Galfenol ribbon 12.8 at. % Ga

The 12.8 at. % ribbon shows a T_c of 757°C and is similar to that of pure α-Fe (770°C) **[6.1.2.2].** It would therefore be expected that as the Ga concentration increases that the corresponding value of Curie temperature will decrease similar to how the saturation magnetisation decreased along with the remanence and coercivity in the hysteresis loops presented earlier.

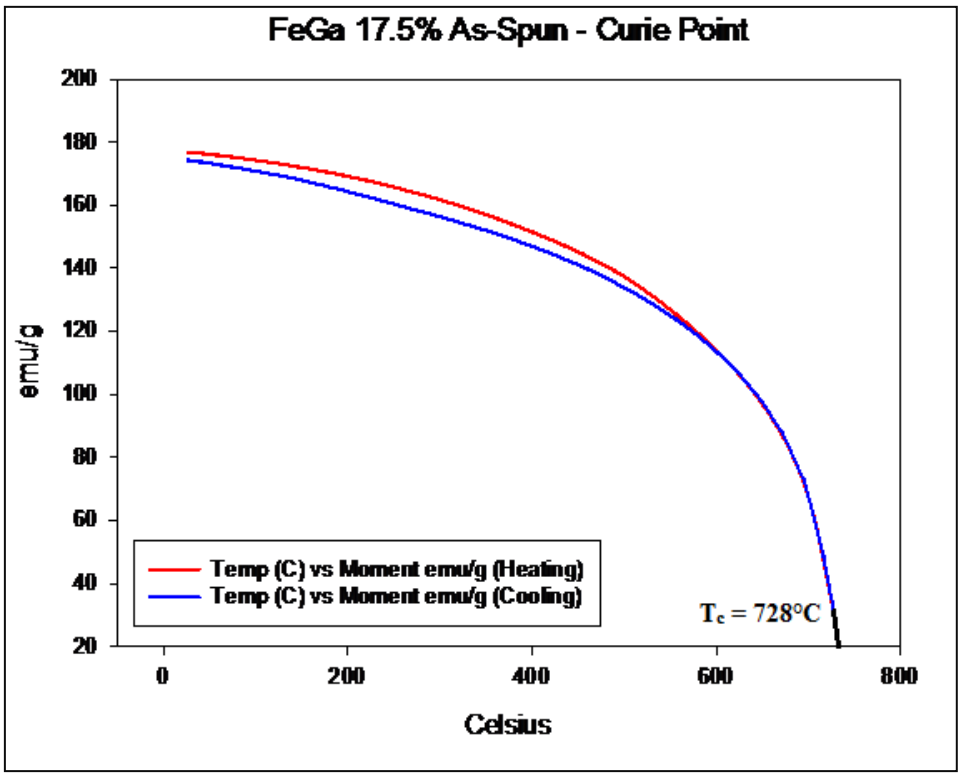

Figure 6.1.2.11 - Curie temperature of Galfenol ribbon 17.5 at. % Ga

The 17.5 and 19.5 at. % ribbons data also had to be extrapolated but not to the same extent as the 12.8 at. %; this was done with the use of a fitting procedure using the Sigmaplot graphical analysis package – the data was only extrapolated so that it would touch the x-axis. The Curie temperatures of 728°C and 718°C are slightly higher than expected as others report bulk samples of Galfenol 20.0 at. % Ga having a Tc ~700°C **[6.1.2.3]** so therefore there could potentially be fundamental differences between bulk single crystal Galfenol and these polycrystalline ribbons.

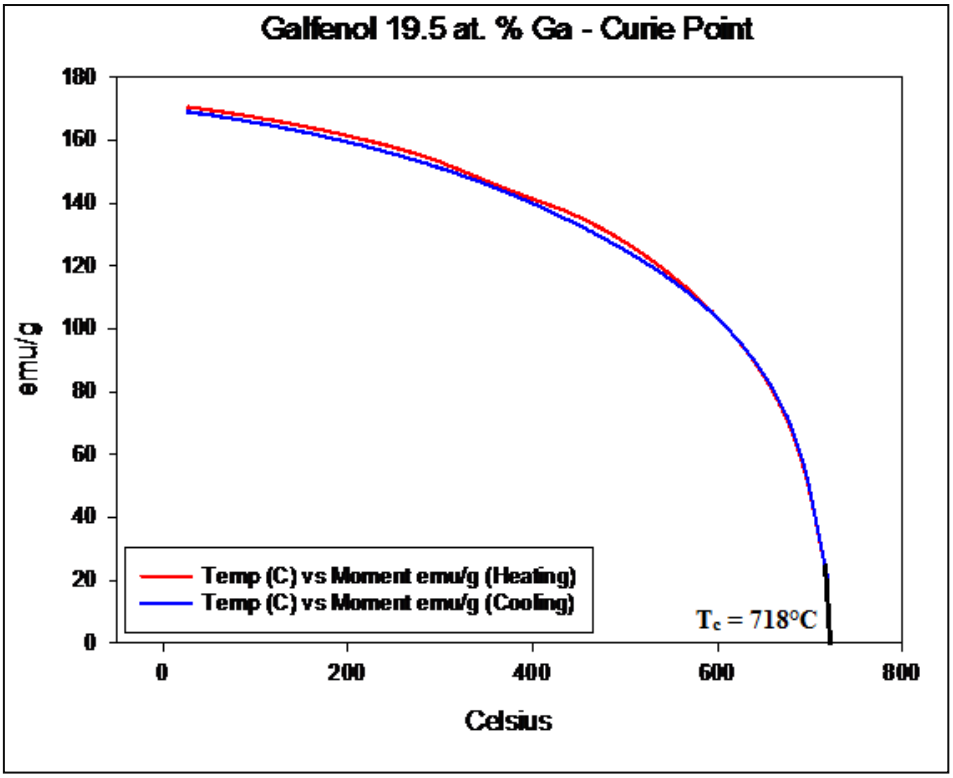

Figure 6.1.2.12 - Curie temperature of Galfenol ribbon 19.5 at. % Ga

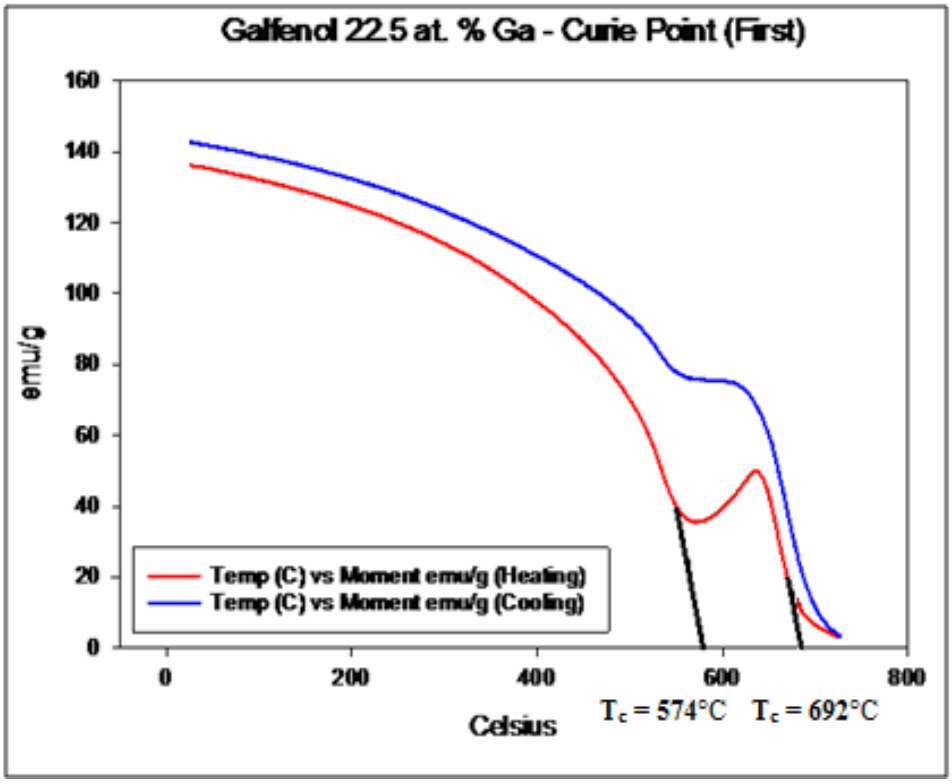

Figure 6.1.2.13 - Curie temperature of Galfenol 22.5 at. % Ga

The results for the 22.5 at. % Ga in figure 6.1.2.13 seemed to bring in an anomaly with this research, as it was not originally predicted. The temperature curves so far have yielded fairly

standard results, but the anomalous curves presented for both heating and cooling were at first were very difficult to explain. At first there was a suggestion of ferrimagnetic behaviour, where it almost seems as though the curve experiences a *compensation temperature*, which is characteristic of ferrimagnetic materials; this is normally reached before the material partially regains a magnetic moment before finally turning paramagnetic. Here that cannot be the case, as there is overwhelming evidence in all of the magnetic testing thus far that all of the Galfenol ribbons are ferromagnetic; so there must be another explanation for this phenomenon. Essentially there are two individual Curie temperatures, where T_c=574°C and T_c=692°C respectively. The higher temperature is the one that is expected due to the previous results, as if we plot the first three results with the 22.5 at. % value as T_c=692°C and expand the linear fit, we have the result in figure 6.1.2.14, where it can be seen that this value seems to fir the correlation of the other data and follows the trend so far. If it is recalled, all of the previous results from the earlier work such as the lattice parameter, magnetisation and coercivity; all of which have had an almost linear fit.

From this it should be possible to predict what the actual Curie point should be for the 27.5 at. % Ga as ~661°C. Firstly though, the first T_c point on figure 6.1.2.13 needs to be investigated. The graph shows a decrease in Curie temperature of -6.7°C per at. % Ga^{-1}.

After 550°C the magnetisation starts to increase again from 38 emu g^{-1} up to 51 emu g^{-1}, which is a substantial change. This increase suggests that there is a structural change or reordering at this temperature, which is in good agreement with the phase diagrams. The diagram does not seem to indicate which phase or mixed phases this is, so it is assumed that the material is of mixed phase. These mixed phases only exist over a narrow temperature range for the 22.5 at. % Ga alloy, as at 660°C the phase diagram indicates that the material should then revert back into the A2 bcc disordered single phase alloy and technically be paramagnetic.

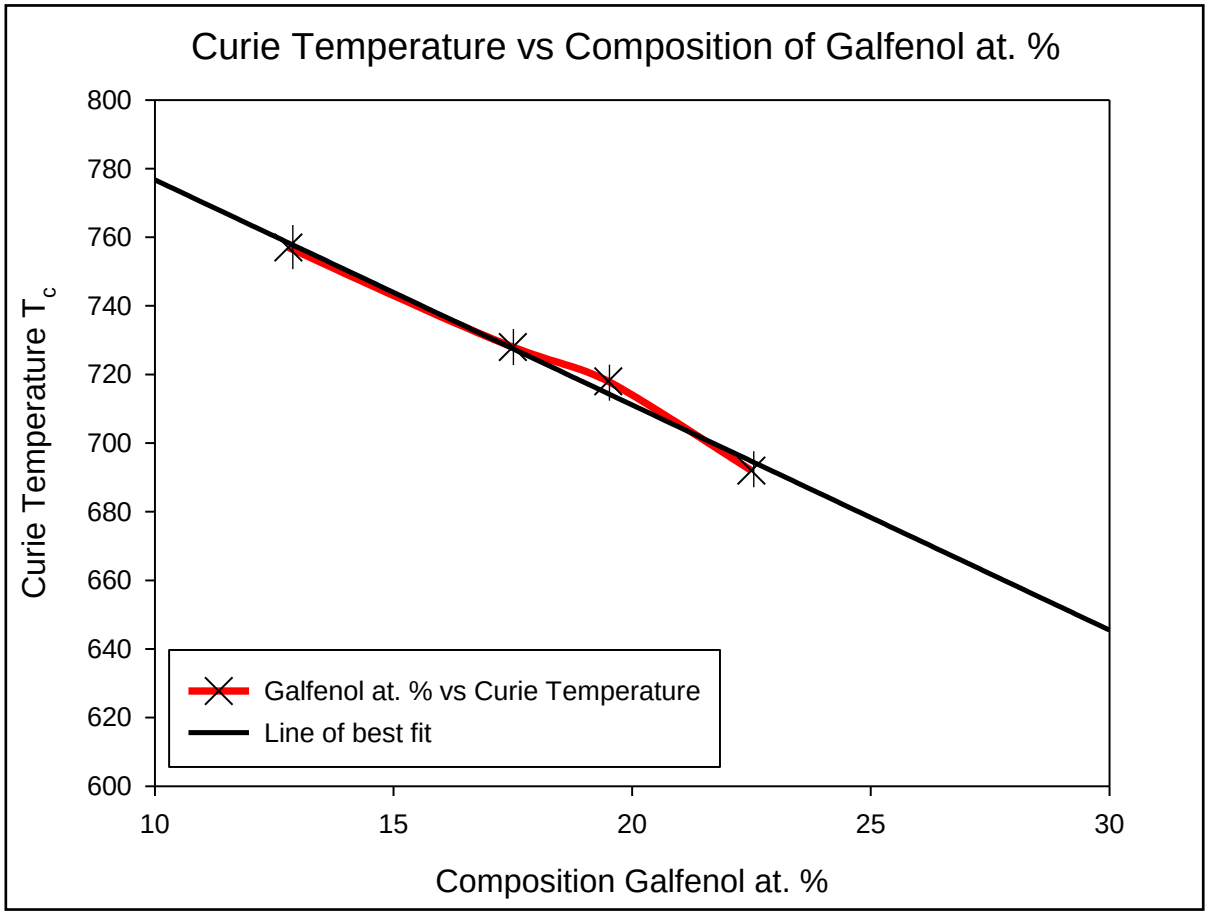

Figure 6.1.2.14 – Curie Temperature versus Galfenol at. % Ga with error bars of ±5°C.

However the ferromagnetic magnetisation does not dissapear until the second T_c, thus suggesting that the metastable phase diagram could potentially be adapted to reflect these findings or that a partial amount of a high-temperature ferromagnetic state remains if the sample has changed to a similar but ordered structure but of ferromagnetic nature such as B2 or L12. This is confirmed during the cooling curve (blue) where in the temperature range of 625°C down to 565°C, there is no change in the magnetisation of the material. Here there has been a partial structural change, potentially from B2 or D03 to A2 which now remains when the temperature gets below 565°C. However, when the temperature eventually cools to room temperature, 25°C, the magnetisation has actually increased overall in the sample by ~4.5%; whether this is indicative of remanent structural changes is still being investigated. In order to compound these results, it was decided to experimentally test the same 22.5 at. % sample over a repeated series of the same heat treatment runs. The results are shown in figure 6.1.2.15 a to d.

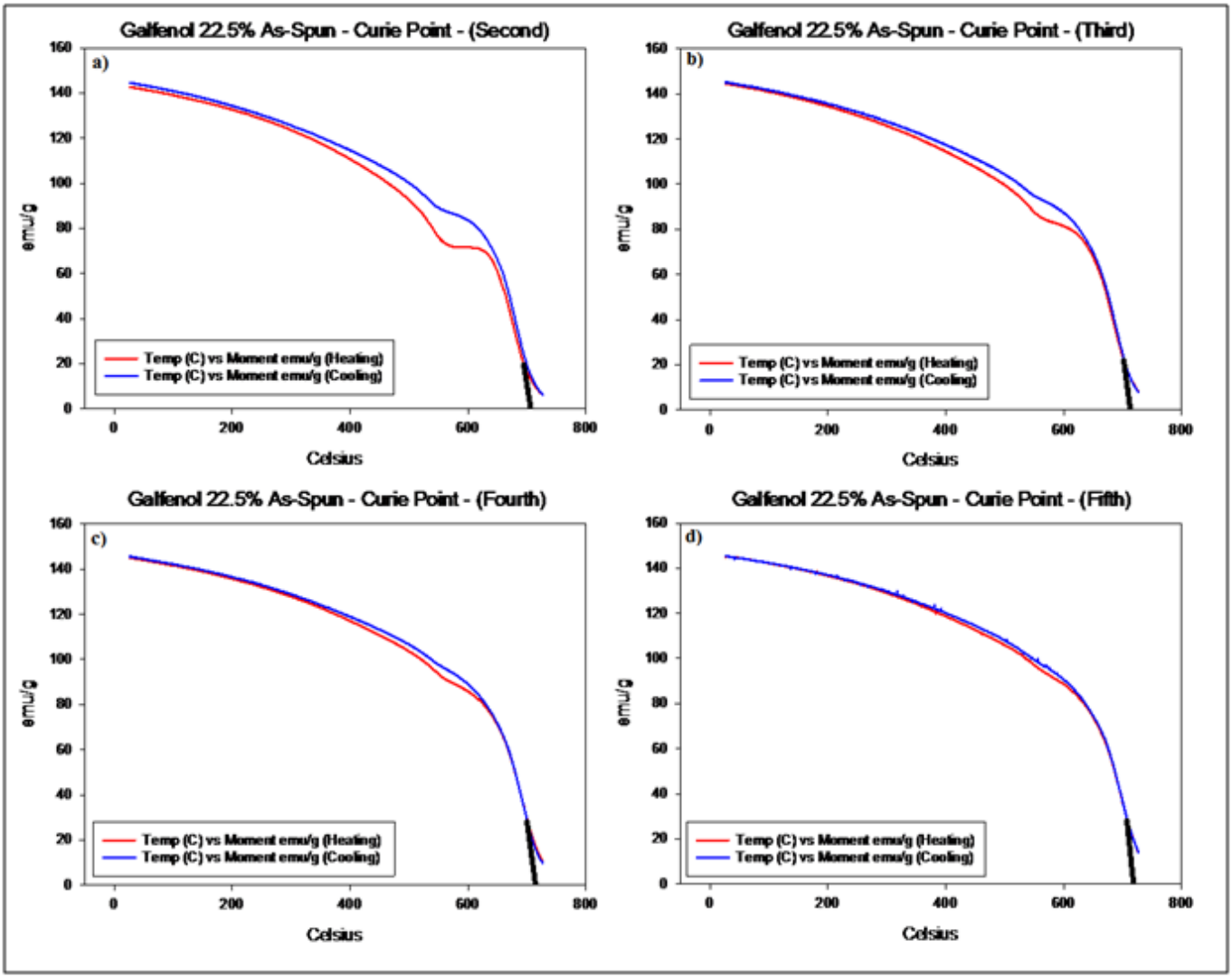

Figure 6.1.2.15 – a) 2nd, b) 3rd, c) 4th and d) 5th temperature runs for the Galfenol 22.5 at. % Ga sample

The gradual reduction is structural hysteresis can be seen quite clearly progressing through the four extra experimental tests. This would seem to indicate that the sample has undergone a partial physical structural transformation until in figure 6.1.2.15 d) it can be seen that the heating and cooling curves are almost identical meaning that no more transformation can now occur and that an equilibrium state has been attained and any structural hysteresis has now becomes neglible. The Curie temperature has increased slightly from the initial first test and has been averaged over the five runs to give a $T_{c(\text{average})}$ of 698°C for this composition of alloy which is at least 20°C greater than previously reported by Kawamiya, Wagini and Okamoto **[4.2.5.1, 6.1.2.4, 6.1.2.5]. I**t should be mentioned that the complete formation of D03 that had been proposed by Okamoto at lower compositions of Galfenol 20.6 at. % Ga is not occurring

here; it is more likely that this is the formation of a mixed phase alloy, as yet undetermined. A mixture of A2, D03, L12 and B2 are all probable, which would be in agreement with Xing and Lograsso **[6.1.2.6]** as their results are similar to those in this work thus far. It is proposed that due to the extremely complex number of phases that can be formed in the 20 to 30 at. % Ga region with temperatures between 580 and 900°C, many metastable phases can potentially coexist and that the relationships between these are currently unclear and further investigations are required with the structural mechanics of the system. It is reported by Dasarathy that some of these phases can only exist in an equilibrium state at high-temperatures and that the final phases formed at room temperature are solely dependent upon the cooling treatment and are usually metastable, hence the need for a metastable phase diagram. **[6.1.2.7]** Also mentioned, is that magnetic annealing at raised temperatures can also affect the magnetic anisotropy of the material as reported by Yoo et al. **[4.2.5.8].** The final composition of 27.5 at. % Ga results are now presented. It was thought that after the relatively unconventional behaviour of the 22.5 at. % that the results were going to be somewhat unpredictable; this proved to be the case and provided novel experimental data which is still under discussion as to how it should be interpreted, although some relevant suggestions and arguments are put forward.

Firstly presented in figure 6.1.5.16 is the first temperature test on the 27.5 at. % Ga. The resulting graph is something extraordinary and has been rarely seen in magnetic measurements. The initial heating curve starts to tend to the first T_c point at ~425°C but then remarkably, fundamentally changes at 450°C and rapidly increases to a maximum magnetisation at 550°C; this maximum is actually 4.3% higher than the initial magnetisation at room temperature.

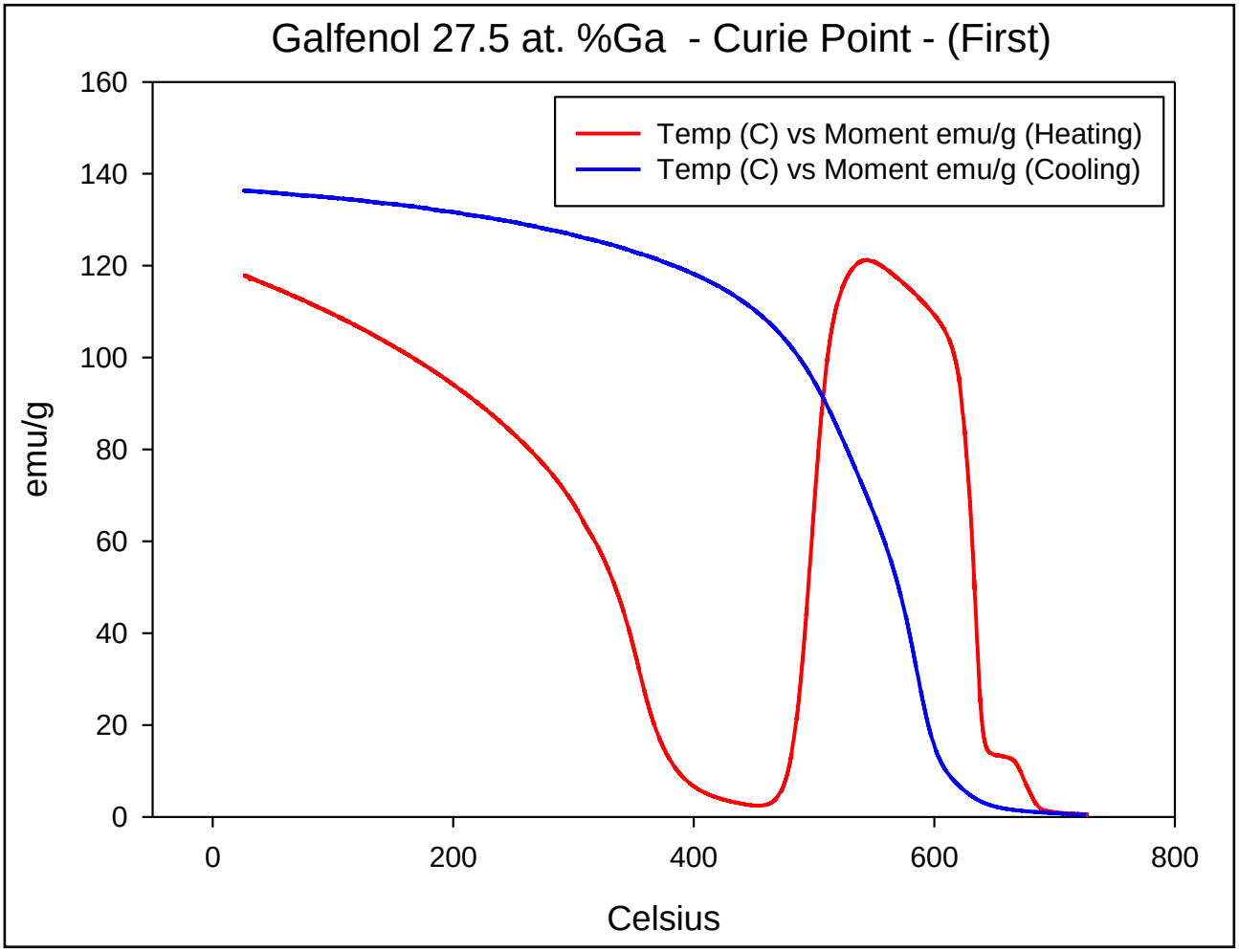

Figure 6.1.5.16 – Curie temperature for Galfenol 27.5 at. % Ga

It is postulated that the material structurally changes from disordered A2 bcc into a mixture of paramagnetic-D03 (Fe3Al-type), L12 (Cu3Au-type) and B2 (CsCl-like) alloys, these forming an ordered bcc-type and an ordered fcc lattice respectively, the ordered fcc lattice having a higher magnetic moment than the bcc lattice hence the increase in magnetisation. This is a large structural and ferromagnetic reconfiguration requiring a large amount of energy and is in good agreement with the work published by Kawamiya **[4.2.5.5]** and the specific phases in partial agreement with those identified by Xing and Lograsso **[6.1.2.6].** In order to clarify this, it would be a suggestion to perform either further neutron or x-ray diffraction work at these elevated temperatures where the relevant information could be ascertained *in-situ*.

The second Curie point this time comes at a temperature of 659°C, which is in good agreement with the earlier prediction that in fact the Curie point also is approximately linear in its behaviour with additional Ga content if the structure remains the same i.e. stays in the bcc structure. Furthermore, following the blue cooling curve back to room temperature it can be seen that the end magnetisation is considerably higher than the starting value, now increased from 116emu g^{-1} up to ~137 emu g^{-1}. This is an increase of ~18%. Again, further experimental testing was performed upon the same sample, with another five runs being undertaken this time; the results are shown in figure 6.1.5.17 a) to e).

It can be seen that these extra tests show some structural hysteresis, so the major fundamental change must have almost completed on the first run. It seems now the sample is stable up until 400°C, where from the magnetic phase diagram it shows that the D03 phase goes paramagnetic, so it has to be deduced that it must be the face centred ordered phase or the A2 disordered phase, or a the transformation into L12 starts to occur and contributes to the magnetisation of the sample when above this temperature. At ~660°C all the phases become paramagnetic. Interestingly on the cooling curve, the magnetisation does not revert back to the same value until the temperature is lower, where the curves overlap once more. This is indicative of a potential order/disorder change between either ordered bcc to disordered bcc or ordered fcc to disordered fcc and is predicted to be a type of structural hysteresis. This transition requires energy to be able to realign the crystal structure and this difference in energy could be represented by the gap in the heating/cooling curves at the temperatures of 580°C (cooling) and 625°C (heating) where the magnetisation of the sample is equal. This would suggest an isothermal structural change at these temperatures where the sample cannot regain its ferromagnetic moment until the structural change has completed.

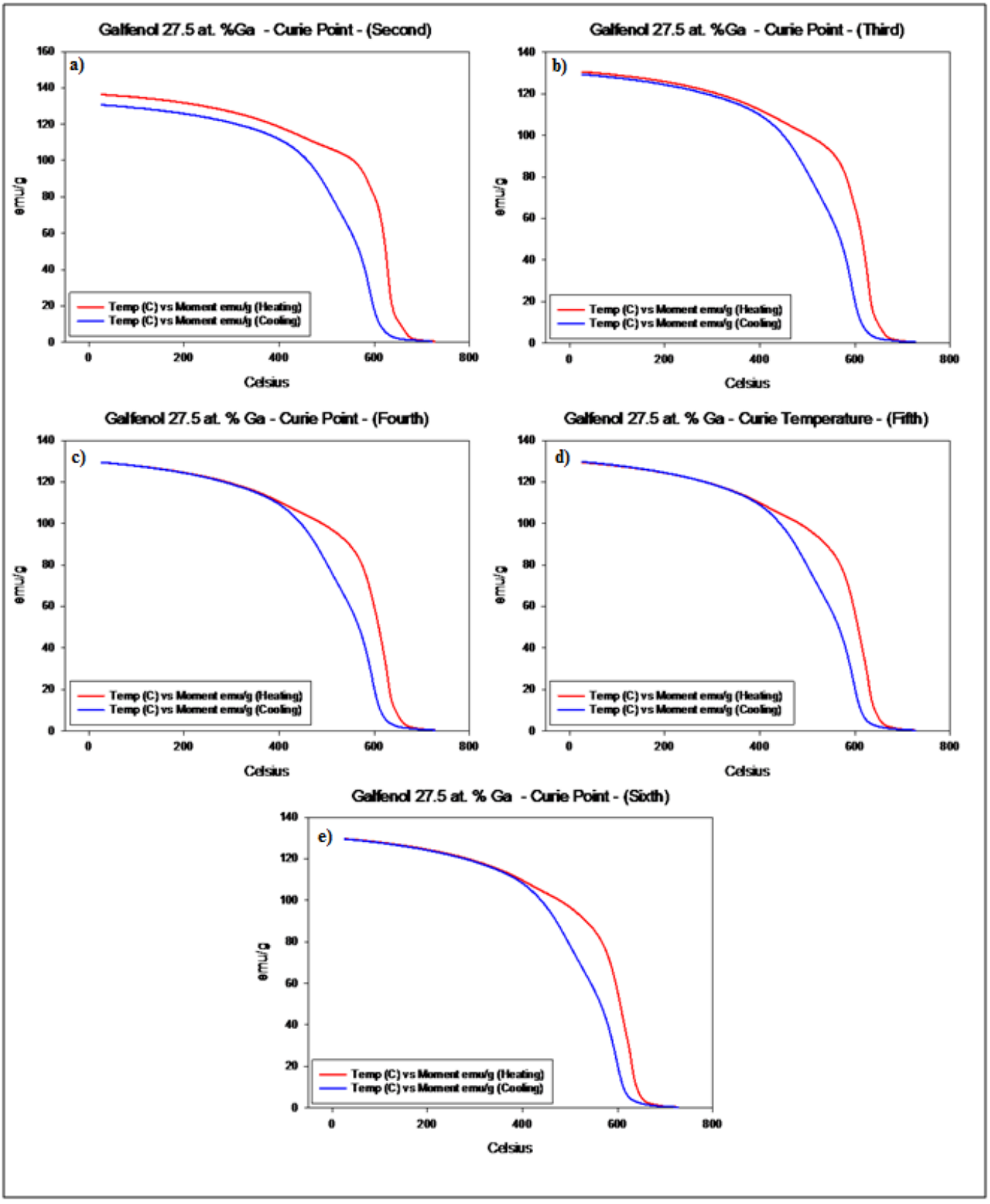

Figure 6.1.5.17 - Curie temperature runs for Galfenol 27.5 at. % a) second, b) third, c) fourth, d) fifth and e) sixth runs respectively.

Unlike the 22.5 at. % Ga, the 27.5 at. % Ga curves do not eventually lie on top of each other, therefore in this composition it is obvious that the first underlying change is irreversible; yet the other more subtle structural changes which subsequently affect the magnetic properties that are observed, are partially reversible and that the temperature plays a crucial role in the transformation of the alloy regarding these transitions. In order to clarify these transitional changes, differential scanning calorimetry (DSC) was employed to confirm these thermo-magnetic and thermo-structural changes.

6.2 Differential Scanning Calorimetry (DSC)

6.2.1 Principles of DSC Measurements

Differential scanning calorimetry (DSC) monitors heat effects associated with fundamental phase transitions and chemical reactions as a function of temperature. In a DSC the difference in heat flow between the sample and a known reference pan, is recorded as a function of temperature. The sample and reference pan are made from an inert material with a high melting point in this case alumina (Al_2O_3). Since the DSC is kept at a constant pressure, the heat flow is equivalent to any enthalpy changes as depicted in equation 6.2.1.1.

$$\left(\frac{dq}{dt}\right)_p = \left(\frac{dH}{dt}\right) \qquad \textbf{(6.2.1.1)}$$

Here *dH/dt* is the heat flow measured in mcal sec^{-1}, therefore the heat flow difference between the sample and the reference is given by expansion of the dH/dt term which results in equation 4.6.1.2:

$$\Delta\left(\frac{dH}{dt}\right) = \left(\frac{dH}{dt}\right)_{sample} - \left(\frac{dH}{dt}\right)_{reference} \qquad \textbf{(6.2.1.2) [6.2.1.1]}$$

The change is heat flow can be either positive or negative, for example in an endothermic process, heat is absorbed by the sample so the heat flow into the sample will be higher than that of the reference, hence, $\Delta dH/dt$ would be positive. Conversely in an exothermic process, such as crystallization, heat flows out from the sample and the $\Delta dH/dt$ term becomes negative. The calorimeter consists of both a sample and reference pan holder which are made of platinum and are situated within the same furnace.

Under each holder is a calibrated thermocouple which allows for accurate temperature measurement from each alumina sample pan. The furnace supplies heat at a pre-selected rate in order to increase the temperature and the difference in the voltage outputs from the two thermocouples is used to calculate $\Delta dH/dt$. A basic schematic diagram of a DSC is shown in Figure 6.2.1.1. A constant flow of oxygen-free nitrogen gas is pumped through the sample chamber inside the furnace to create a dry atmosphere and prevents any oxidisation of the samples, although Argon and Helium can also be used.

The DSC machine used in this work was a Netzsch STA 449 F3 Jupiter with a maximum temperature range of 0°C to 1450°C using a silicon carbide (SiC) furnace which can be seen in figure 6.2.1.2.

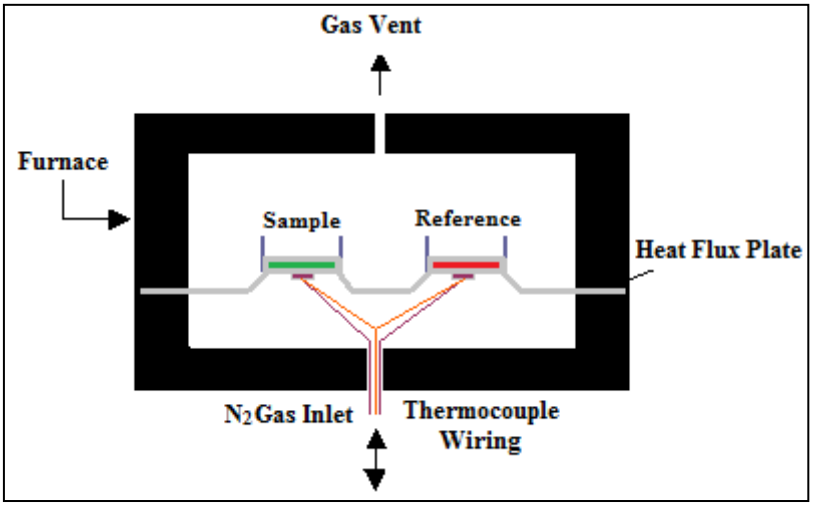

Figure 6.2.1.1 - Simple Schematic of a Differential Scanning Calorimeter (DSC)

Figure 6.2.1.2 - The Netzsch STA 440 F3 Jupiter DSC at Salford

The DSC is calibrated using a series of different high purity metals with various different melting points such as copper (Cu), Tin (Sn), gold (Au), silver (Ag) and zinc (Zn). Before a measurement is taken a background run is performed using the reference pan and the sample pan to be used; this is done in case there are any differences between the two actual pans and this is known as the *correction*. When the measurement is taking place, the correction is automatically subtracted from the measurement data by the Proteus analysis software, which after a small amount of user input, automates the whole measurement process.

6.2.2 DSC Results

The results from the DSC experiments it was decided to concentrate on the 22.5 and 27.5 at. % Ga, this was due to the specific high Ga compositions generating the complex curves in the magnetic results. It is obvious in the magnetic results that there are structural changes happening within these compositions which might be identified with the use of DSC. Each sample selected for analysis was put through a cycle of three individual but consecutive heating runs. The parameters chosen were complimentary to those used on the VSM; the temperature range selected was 300°C to 800°C at a heating rate

of 10 K min^{-1} (the same as the VSM) with a nitrogen flow of 60ml min^{-1}, so that the samples did not oxidise. Presented first in figures 6.2.2.1, 6.2.2.2 and 6.2.2.3 are the results of the first, second and third DSC runs for the 22.5 at. % Ga sample respectively.

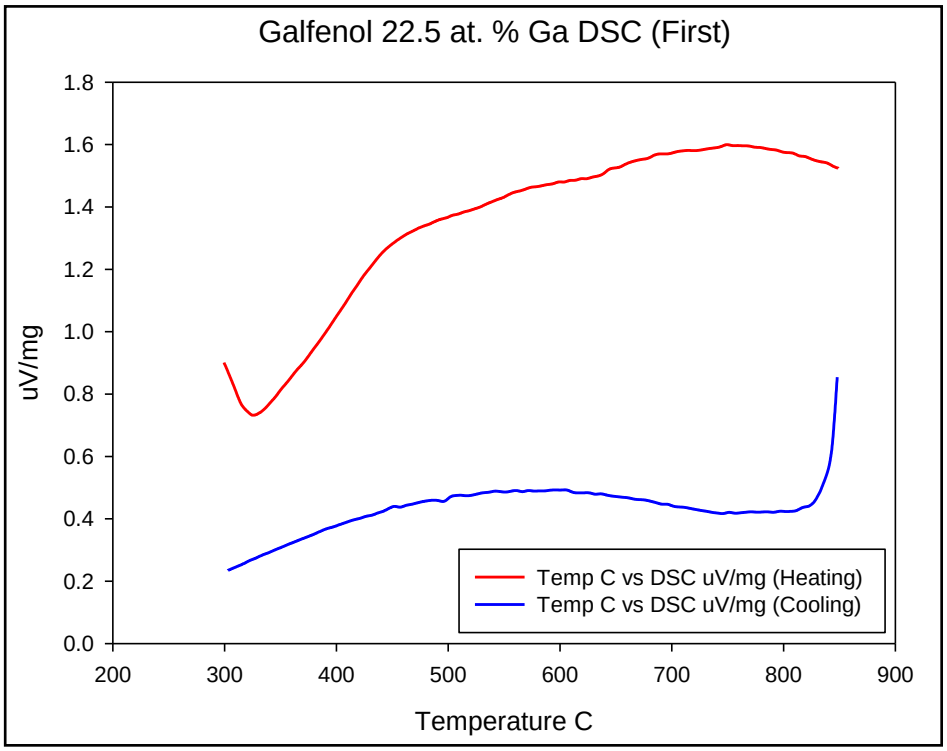

Figure 6.2.2.1 – DSC Curves of Heating and Cooling for Galfenol 22.5 at. % (1)

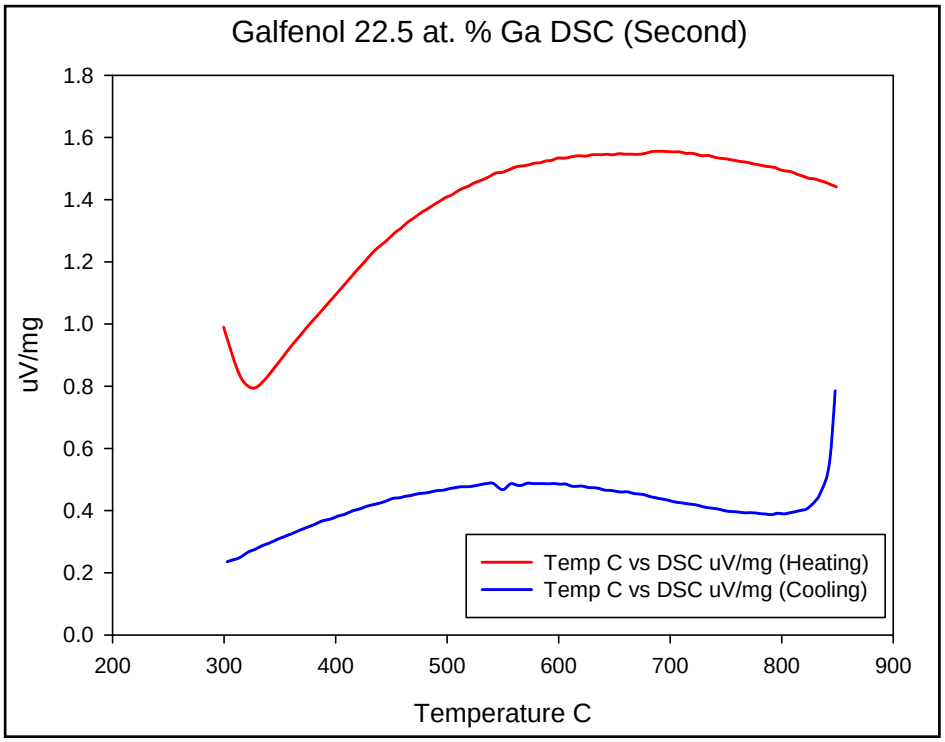

Figure 6.2.2.2 – DSC Curves of Heating and Cooling for Galfenol 22.5 at. % (2)

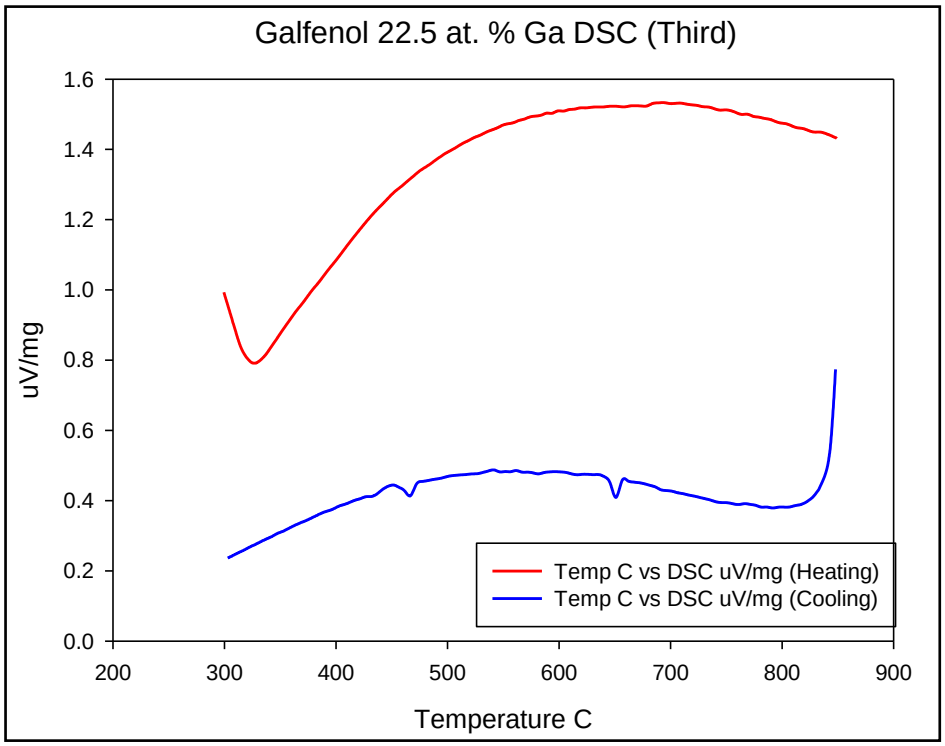

Figure 6.2.2.3 - DSC Curves of Heating and Cooling for Galfenol 22.5 at. % (3)

In general there is not very much that can be ascertained from the 22.5 at. % alloy as the curves don't show very many specific transition points or any that can be readily identified. The heating curves in all three figures show a slow but steady exothermic behaviour, this could relate to a variety of things. Slow exotherms can be indicative of lattice relaxation, as there is a good probability that during the melt-spinning process the alloy would have had an intrinsic internal strain; this could be a sign of the strain being released. It could also indicate a slow disorder to order transformation but usually this would result in a much sharper exothermic peak and it is thought this is not the case here.

In the cooling curves again there are no noticeable sharp peaks, except for in figure 6.2.2.2 at 550°C, where a small endothermic peak appears which could relate to the ferromagnetic Curie temperature of the D03 phase, as this equates well with the magnetic phase diagram. Furthermore in figure 6.2.2.3 there are two endothermic peaks at 650°C and 475°C respectively. The 650°C peak is believed represents the A2 bcc Curie temperature and the renaissance of its ferromagnetism, this explanation also agrees with the magnetic phase

diagram literature, but it could also be attributed to a small structural change as the temperature descends through the FeAl-like region of the equilibrium phase diagram; currently the former reason seems the more rational reason. The peak at 475°C does not seem to correspond to any previous literature and these reasons these anomalies are still under review – it has been suggested it could simply be some structural hysteresis due to the long slow exotherm from the heating curve or it could possibly be attributed to the Curie temperature of the D03 structure, but this has yet to be experimentally confirmed.

The results for the 22.5 at. % Ga composition though does not quite agree with Ikeda et al **[6.2.2.1],** where several transitions were found in the heating curve in a 21.5 at. % Ga as seen in figure 6.2.2.4. This sample was produced by diffusion coupling and then aged at 650°C for 21 days. The cooling curve from this work is in better agreement with Ikeda's work, with the transition at 650°C being a reversible change which they attribute to the D03 back to the A2 phase, thus showing structural hysteresis of the 22.5 at. % Ga.

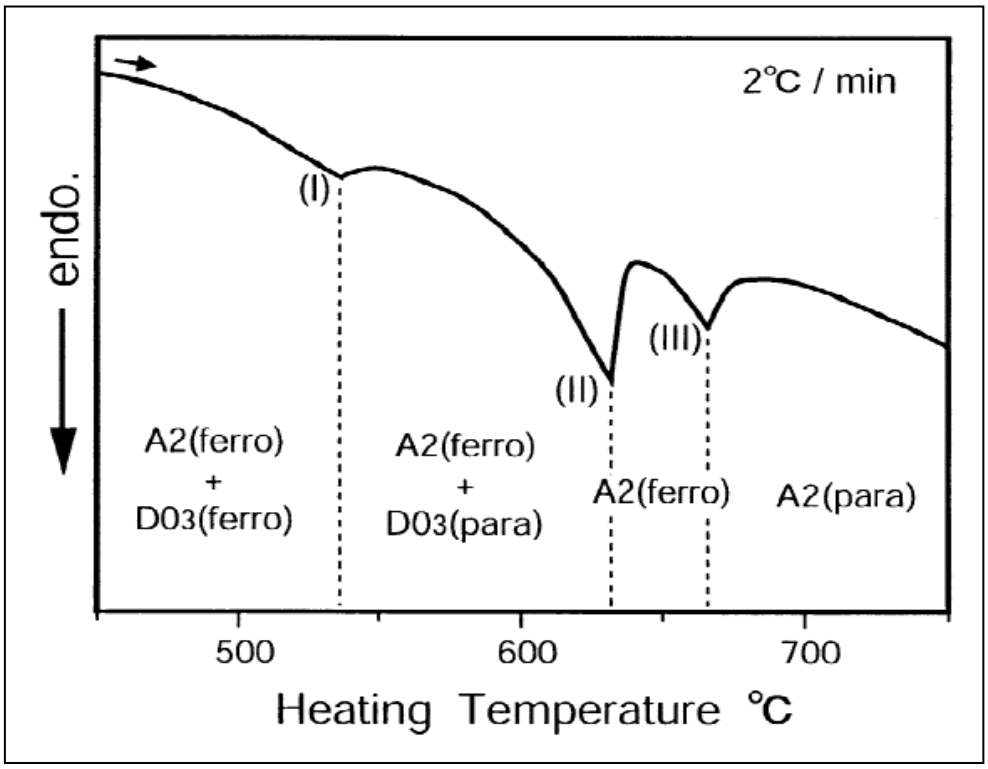

Figure 6.2.2.4 - DSC results for Galfenol 21.5 at. % Ga. [6.2.2.1]

The graphical results for the 27.5 at. % Ga are presented in figures 6.2.2.5 to 6.2.2.7 as the three consecutive heating cooling curves. Here the data is of much greater interest as there are several distinct peaks of interest and the results here are more similar to Ikeda's work, although the structural transitions that Ikeda suggests are debated by this work and ultimately the transitions on the curve do not fit to Ikeda's results. The alternate suggestion here is that there is a partial L12 transition in order to regain magnetisation as shown from the VSM data, although after the initial run, there is just an isothermal type hysteresis; with no change in magnetisation suggesting that this becomes an A2 to D03 change.

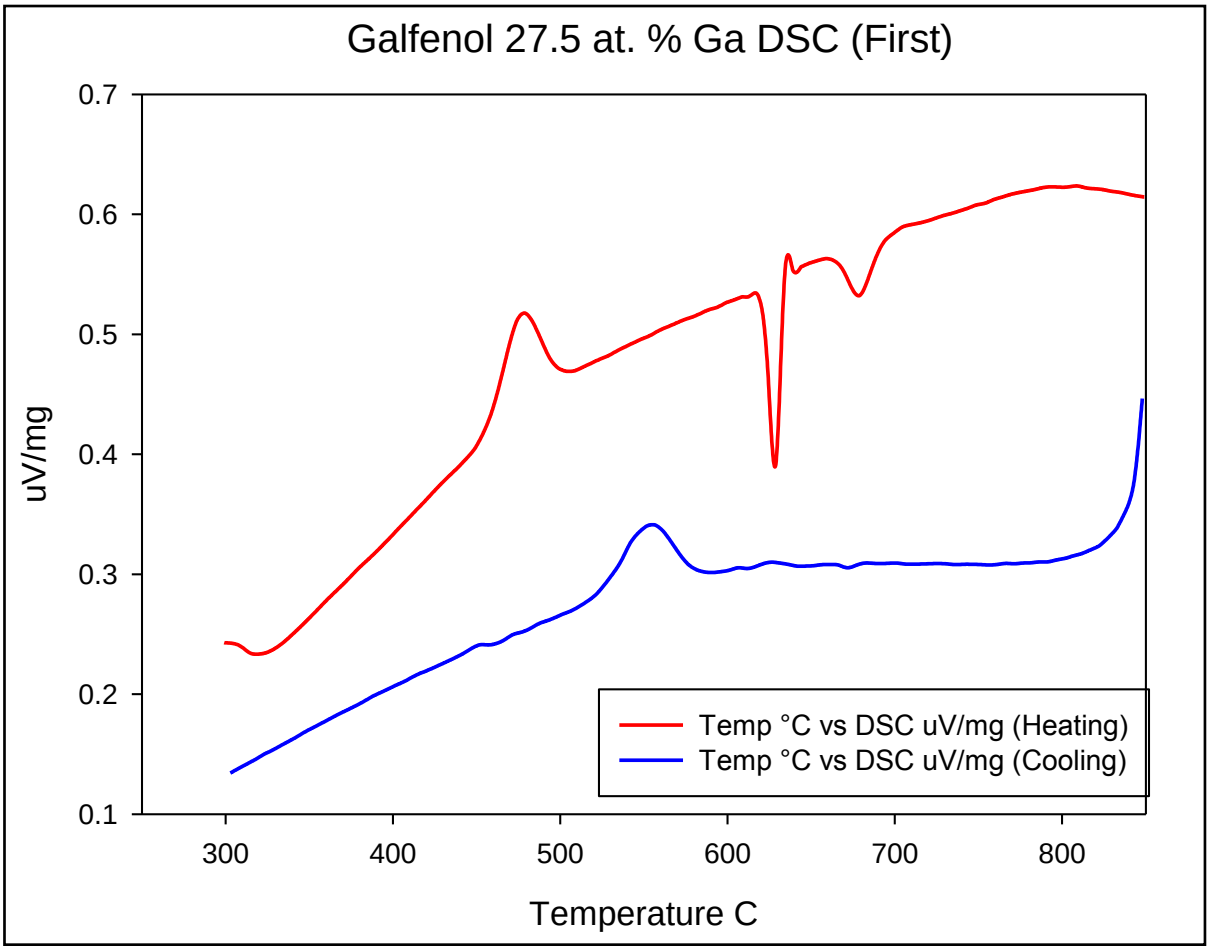

Figure 6.2.2.5 – DSC curves of heating and cooling for Galfenol 27.5 at. Ga (1)

Starting with the heating curve, the first point of interest is that the curve is not dissimilar to that of the 22.5 at. % Ga, as it seems to be following a slow exothermic route as the temperature is increased. The first major peak of interest occurs at an onset temperature of

450°C, with the top of the peak occurring at a slightly higher temperature of 480°C. This peak is exothermic, suggesting that this is a large disorder to order process. According to current literature by Zhu et al **[6.2.2.2],** this is also the temperature that the first magnetic transition appears, but it is unlikely this peak is representing a magnetic transition; it is more likely that this is a structural reordering, in which the A2 disordered phase is converted to ordered bcc B2, hcp D019, bcc D03, fcc L12 or a combination of any of these. Relating back to the phase diagram it is more probable to be an A2 to L12 conversion as at such a low temperature the DO3, B2 and DO19 phases should not exist from an undercooled sample. Although small amounts of D03 have been found in previous as-spun samples this conversion seems too large to indicate that this would be the case. Additionally this assumption agrees somewhat with the neutron diffraction results where the A2 to D03 phase, although small, was detected. This would also agree with Dasarathy and Hume-Rothery who reported that around this temperature the alloy should be a mixed compound of the A2 bcc, D03 and the Cu3Au-type fcc phase, which is now just termed L12 **[6.2.2.3]**

The second peak, as the heating curve is traced, is an extremely sharp endothermic peak which is identified as a structural transition but this time one of order to disorder. According to the current phase diagram, and assuming the material is in a mixed-phase solid solution containing A2, L12 and DO3; this transition should in fact be an fcc L12 to hcp DO19 change whilst maintaining a portion of the DO3 phase if the current literature is to be accepted. This would be in good agreement with the VSM results presented earlier, as it is thought that the ordered DO19 structure is not ferromagnetic, as reported by Sun et al., furthermore Sun suggests that the structural transition is most likely to be A2 + DO3 + DO19 **[6.2.2.4],** whereas according to the data that has been presented in this work, it would appear that the change could possibly be A2 + L12 + D03 to A2 + L12 + DO19, but this is speculative and the final phase formed at the high temperature >690°C is also going to contain ordered B2.

The third peak, also endothermic but not as defined as the previous one, occurs over the temperature range 665°C to 690°C which would be also in agreement with the phase diagram as at 680°C the material should enter the B2 region, in which the material is stable up to 900°C. In the case of the cooling curve, it is somewhat different. There is only one distinct broad peak starting at 580°C and eventually fading at 525°C; this would seem to make some sense with the phase diagram as the DO19/DO3 to A2/L12/DO3 transition is documented to be at 588°C. So it would seem that the majority of the high-temperature phase actually converts back into the mixed, lower temperature phases – confirming the predicted results from the VSM. Furthermore it was suggested within those results that there is a structural hysteresis; which in essence also agrees with the presented VSM data.

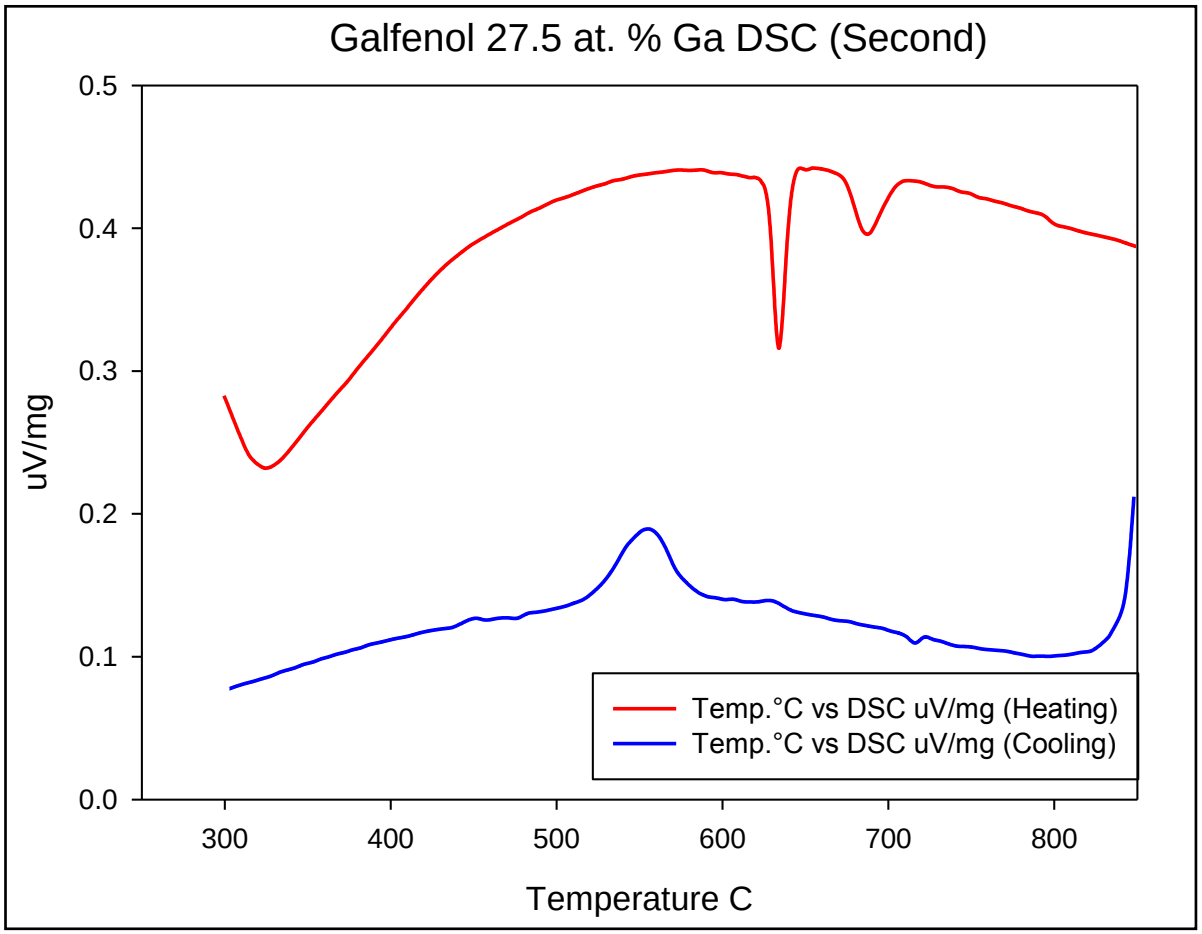

Figure 6.2.2.6 – DSC curves of heating and cooling for Galfenol 27.5 at. Ga (2)

Here in the second curve above, a slightly different result is presented. The first initial peak at the 450°C point has now completely disappeared. This suggests the large transition at this

point is an irreversible one; again in excellent agreement with the VSM results – suggesting that the material is in fact a two-phased mixed alloy after the first heating run, as the much slower cooling rate has allowed the alloy to form a more favourable crystallographic equilibrium state. The two further peaks on the heating curve appear again and the structural hysteresis peak reoccurs on the cooling curve indicating that these other structural changes are indeed reversible and are consistent with the description given before. For completeness the third and final run must also be considered.

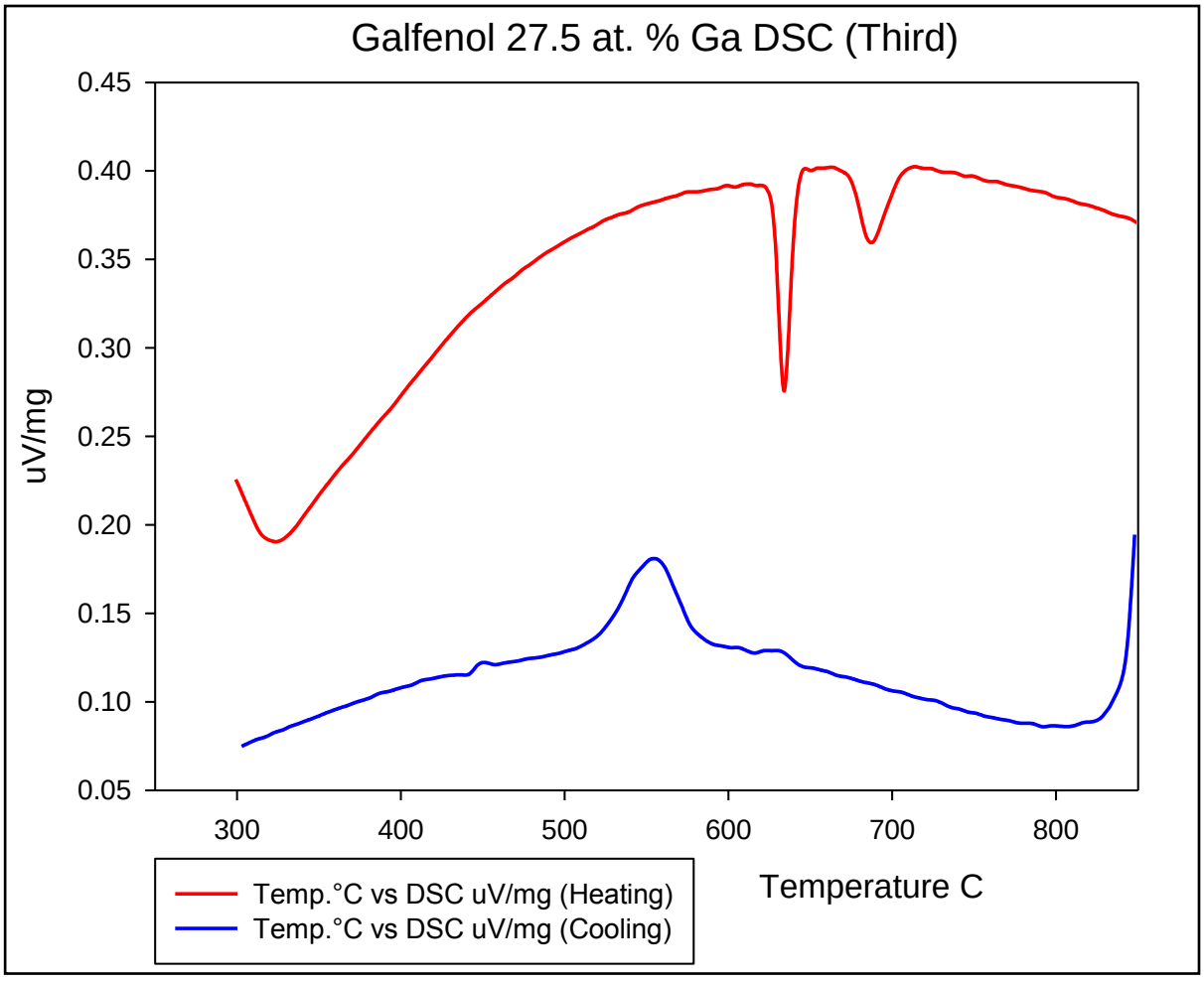

Figure 6.2.2.7 – DSC curves of heating and cooling for Galfenol 27.5 at. Ga (3)

As predicted the third curve essentially repeats the trace of the second curve, thus we assume that the only structural conversions now taking place are all determined by thermal influences and that any crystallographic changes are reversible using this slow heating and cooling rate. There is little documented evidence on what the large exotherm (and magnetic change) is on

both the VSM and the DSC traces. Whatever change is taking place is obviously fundamental as it causes a structural reordering process that rapidly rejuvenates the ferromagnetic moments of the atoms within; increasing the magnetisation past the original magnetisation saturisation point. Thus the phase that has been formed is not only ferromagnetic, but has a higher net magnetic moment than the original structure, indicating that the L12 phase is the primary candidate as earlier thought. Apart from being identified after 21 days of thermal treatment, only Zhao et al and Matsushita et al **[6.2.2.5, 6.2.2.6]** and this work have identified it using thermal treatments of less than 1 day and in the case of this work only around 45 minutes. In order to try to confirm these predictions it was proposed to undertake some further direct analysis comparisons.

6.3 Combining VSM and DSC Results & X-Ray Diffraction Revisited

6.3.1 Presentation and Discussion of Combined VSM and DSC Graphs

To highlight the agreement between the experimental results in both VSM and DSC measurements it was thought the first run results should be plotted together in order to establish if the large structural change relating to the first exotherm on the first DSC trace would coincide with the large magnetic increase on the first VSM graph; this result is shown in figure 6.3.1.1.

As far as is documented no-one previously has directly compared DSC and VSM results simultaneously. Even though the VSM magnetisation heating curve at 300°C shows a reduction of ~50% of its magnetic moment, the DSC signal is increasing quite quickly as an exothermic curve, it is considered that the A2 phase is ordering and forming the D03 phase resulting in what would be a very low Curie temperature. There is a mixed phase structure, where the A2 bcc is being converted quickly to the D03 structure. This would explain the

rapid decrease of magnetisation and is in good agreement with the metastable phase diagram as this suggests the Curie temperature of the D03 phase as 410°C. The VSM curve confirms this postulation. It can clearly be seen that there is direct collaboration between the first large DSC exotherm and the sudden increase in magnetisation on the VSM curve at the ~475°C point; thus the material definitively changes into a ferromagnetic structure.

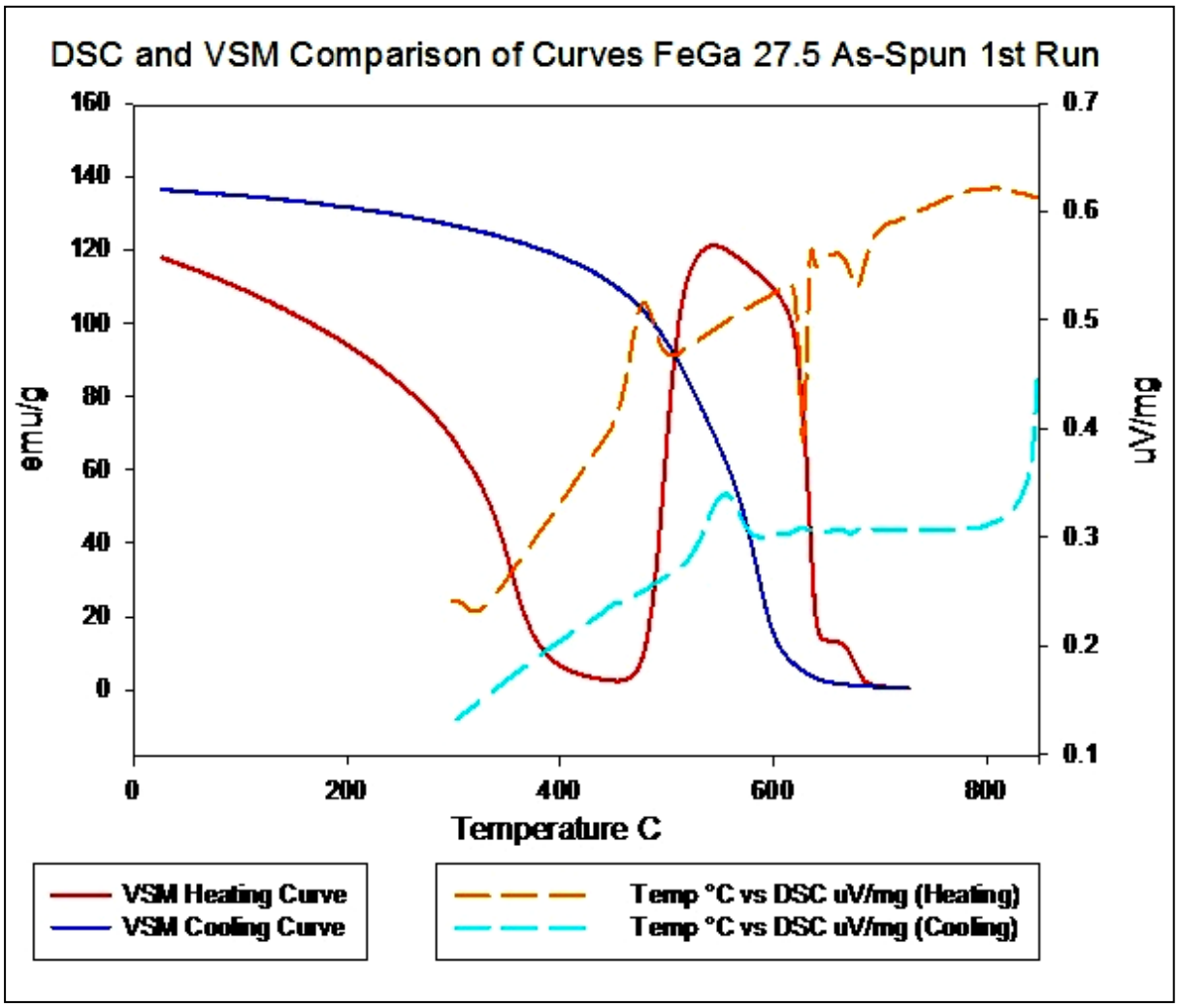

Figure 6.3.1.1 - DSC versus VSM heating and cooling curve (First)

This phase is predicted to be the structural change from A2 + D03 into the fcc L12 phase discovered by Couderg et al. **[6.3.1.1]** with the Fe atoms taking the face-centred positions with the Ga occupying the corner sites. This structure has a larger lattice parameter of 3.670 Å much greater than that of the A2 phase, with a much larger cellular volume of 49.431 $Å^3$ and also a greater magnetic moment, hence the higher saturation magnetisation than at the

outset. The magnetisation starts to decrease again at ~550°C and the structure then changes again at 615°C and the large decrease in magnetisation at 625°C corresponds extremely well to the large endothermic structural change, which is predicted to be the conversion from fcc L12 to hcp DO19, also in agreement with the phase diagram. In order to confirm this, more experimentation is required. The last endothermic change is also in good agreement with the change of phase from the hcp DO19 to the B2 bcc ordered phase, which has the same lattice parameter as the A2 disordered phase. It is inferred that on the first run of the as-spun virgin sample that the series of changes is as follows:

$$A2 \rightarrow A2+D03 \rightarrow L12 \rightarrow L12+D019 \rightarrow D019+B2 \rightarrow B2$$

The VSM cooling curve suggests the magnetisation doesn't start to return until approximately 590°C, this suggests that the structural changes as the material cools are somewhat different. The DSC cooling curve is in partial agreement as it is steadily endothermic until it reaches a temperature of 650°C when there seems to be a small exotherm, which suggests a partial structural change but it would seem not to be the same as the heating curve. The more prominent change occurs at 575°C and this coincidently is where the magnetisation also returns. It is suggested that here there is a different series of changes and as the magnetisation returns at a higher value it is logical to suggest these transitions on cooling:

$$B2 \rightarrow B2+D019 \rightarrow D019+L12 \rightarrow L12+D03 \rightarrow L12+D03+A2.$$

Now a further run is considered, as the material tries to reach some sort of equilibrium as could be seen in the further VSM runs, where there is definitely some structural hysteresis, so the third runs of VSM and DSC is compared in figure 6.3.1.2 to see if the same occurs on both pieces of equipment. As can be observed, on the heating curve the Curie temperature is indicated by the large transition on the DSC curve, this is not indicating a magnetic change, but a structural change peaking at 650°C (onset 625°C) which indicates the change to the

D019 hcp phase; which is reported to be non-magnetic **[6.3.1.2]** and the further change at 690°C corresponds nicely with the equilibrium phase diagram as the structure changes again to B2. In brief here is a simpler series transformation of L12+A2+D03→D019+D03→B2 structural ordering, suggesting it is the L12 fcc that converts to D019 hcp which reflects the correspondence between fcc and hcp structures. The rest of the disordered bcc A2 converts to bcc ordered D03. It can be seen on the cooling curve that the material does not revert back to another phase until 580°C which either suggests large structural hysteresis or the unlikely alternative that upon cooling it reverts directly from B2 to L12+D03+A2 instead of transforming back through the D019 hcp phase. This is in agreement with the analogous transitions in Fe_3Ge as documented by Chen et al. where it is demonstrated that the L12→D019 transformation is observed to be of the order of 300 seconds, but the reverse transition from D019→L12 takes approximately 30 days **[6.3.1.3]**.

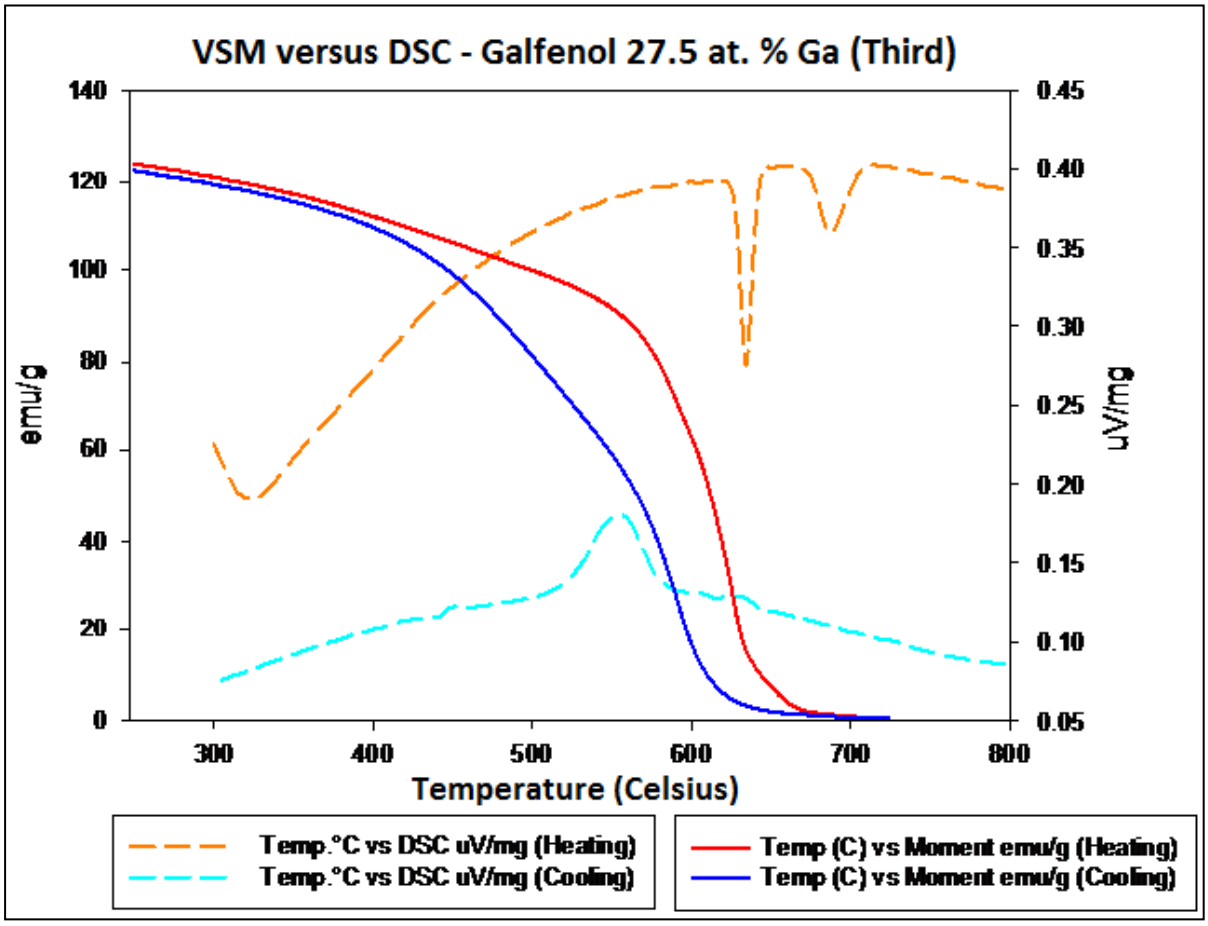

Figure 6.3.1.2 - VSM versus DSC of Galfenol 27.5 at. % Ga (Third)

In order to confirm these predictions, the last of the Galfenol samples of composition 27.5 at. % Ga was subjected to fast annealing and quenching in an ordinary furnace; as no vacuum furnace was available. In order to keep oxidisation to a minimum, the samples were heated at a rate of 60°C min^{-1} to temperatures of 500°C, 650°C and 800°C respectively and annealed for 30 minutes and then the 500°C and 650°C quenched into ice cold water and the 800°C was allowed to slowly cool at a rate of 10°C min^{-1} in the furnace. It was thought that at specific temperatures, due to the minimal thickness of the samples, they would reach thermal equilibrium much sooner and develop some of the more exotic phases that have been predicted by these results.

6.3.2 Annealed and Quenched Ribbons at 500 and 650°C and Slow Furnace Cooled from 800°C

The appearance of the samples of Galfenol had changed slightly during the brief annealing in air and there was some discolouration experienced by each sample. It was thought that this was oxidisation of the material but that it would only be on the surface; so the samples were both analysed at room temperature using the Bruker D8 X-Ray Diffractometer as described previously. The results presented in figures 6.3.2.1 and 6.3.2.2, of the 500°C and 650°C anneal-quench, give an interesting incite on the effects of heat treating this particular composition of Galfenol alloy, also the Crystal Match! generated report is again situated in Appendix III.

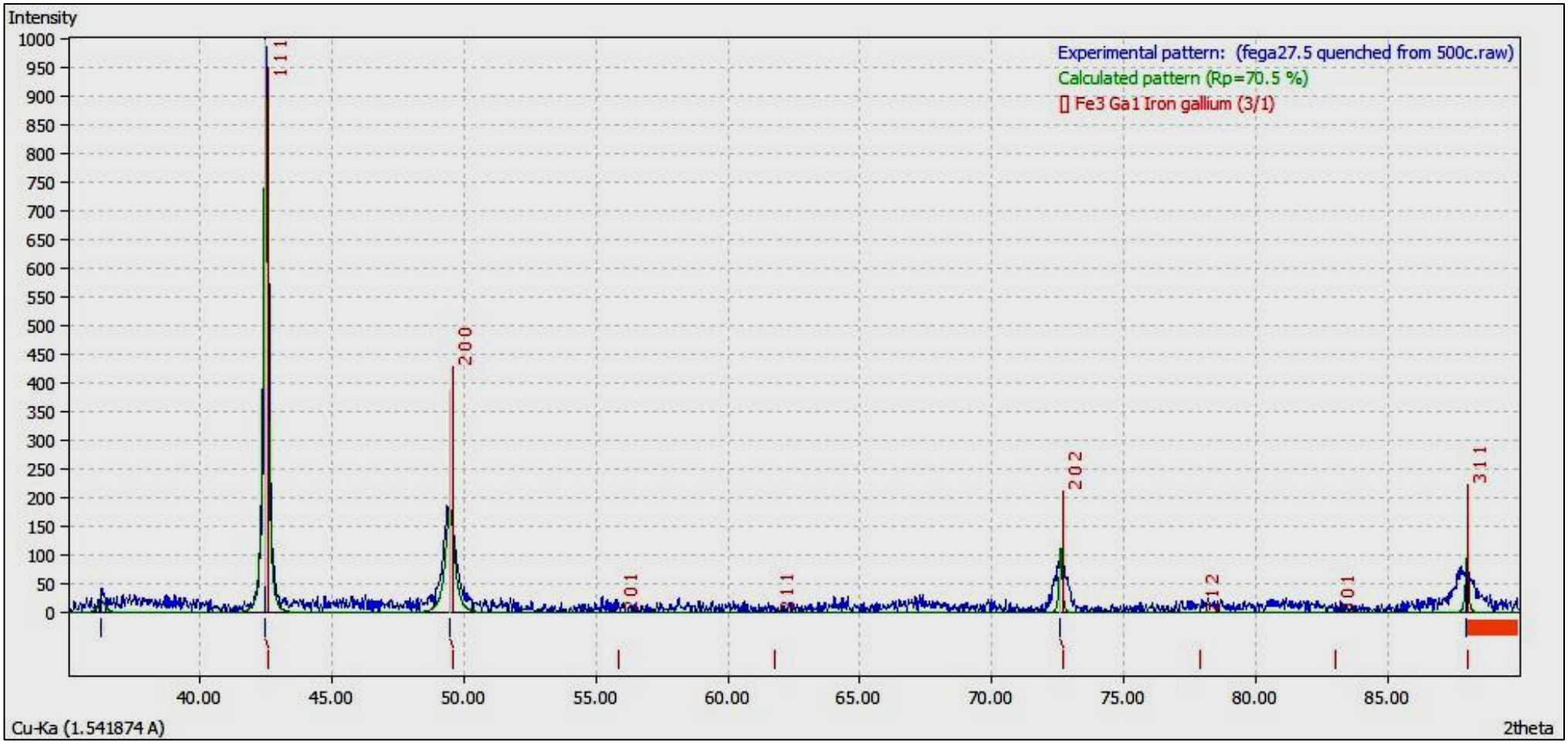

Figure 6.3.2.1 - XRD scan of Galfenol 27.5 at. % Ga after annealing-quenching from 500°C

This pattern suggests that our prediction is correct, as the match is an almost exact peak position fit for the data profile; the best match is the Meissner, Schubert data pattern which is the ordered fcc $AuCu_3$-type or L12 structure. The characteristic peak at 49° is only allowed for the L12 and the 42.7° peak gives the highest intensity which infers a complete transformation into the L12 phase. This agrees with the both the DSC exothermic peak and the VSM magnetic data results for a virgin sample as the main transformation of the sample. Previously this amount of L12 has only been found in Galfenol material after annealing for a month **[6.3.2.1, 6.3.2.2]**. Although it was accepted in the earlier neutron results in chapter 4 that a very small amount of L12 phase potentially existed in the annealed samples. Here though it seems that now the majority phase in the material is the L12 structure. There is no obvious sign of any A2, D019 or D03 structure in the pattern, but there are a number of peaks missing from the L12 diffraction profile which suggests a strong preferred crystallographic orientation. This is considered because the samples in this case were not ground down into a fine powder but left as they were; in small flakes after the annealing process. The interesting conclusion here is that it is possible to form the L12 phase without extensive thermal treatment which has not been reported before and this is reflected by the presented results.

For the 650°C annealing, the prediction was that the result should be one of mixed phase, as it was assumed that even after 30 minutes, not all of the sample would have changed from L12 to D019, D03 or even B2.

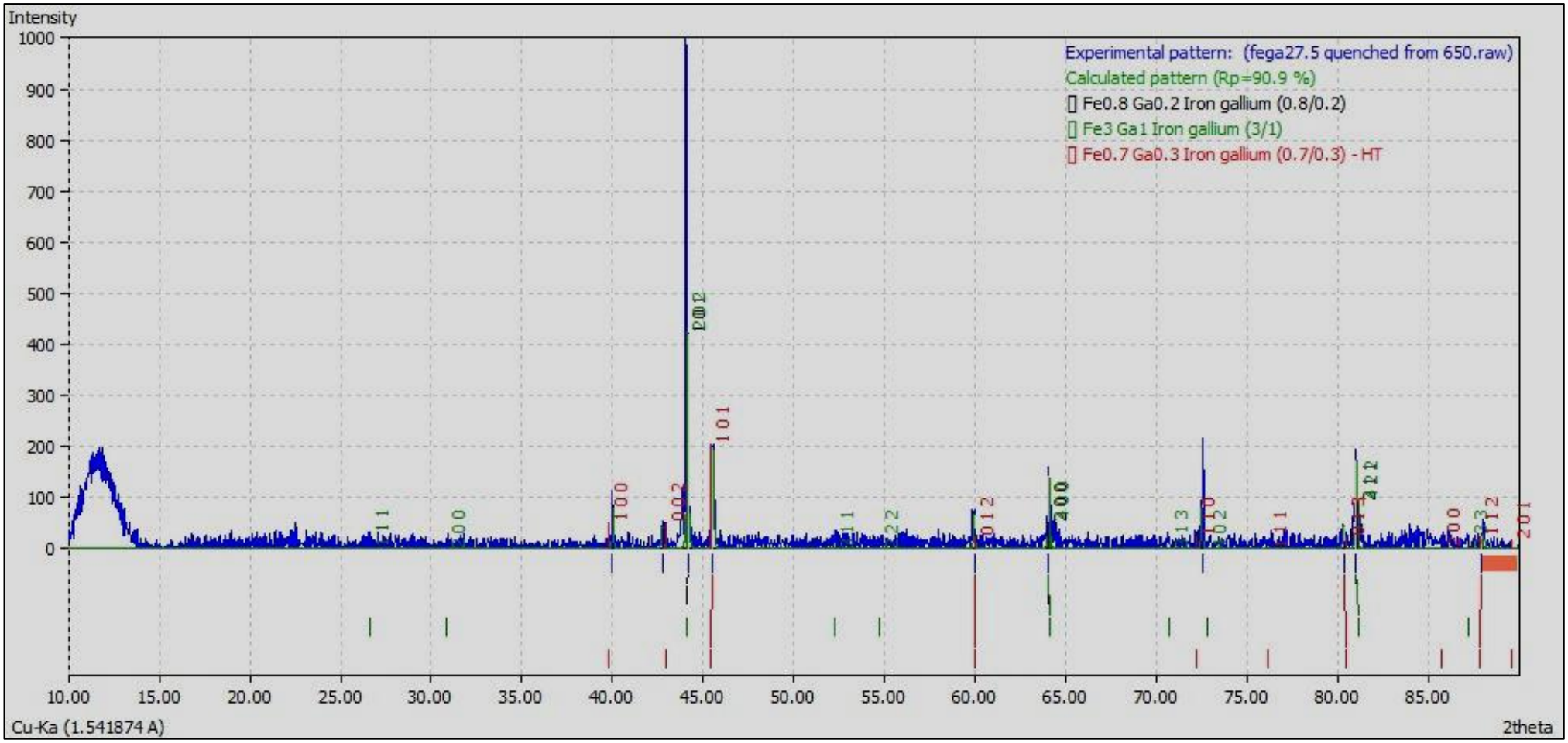

Figure 6.3.2.2 - XRD scan of Galfenol 27.5 at. % Ga after anneal-quenching from 650°C

This result shows an array of structures that can be potentially identified. Here there are still issues in deciphering the differences between the D03 and A2 phases due to the superlattice reflections occurring at the same positions as the A2 reflections. There is no sign of the peak at 2θ=54° which is characteristic of the ordered B2 phase. The Crystal Match! software has determined that the phases present are A2, D03 and D019 in fairly even amounts, 36.61%, 36.68% and 26.56% respectively, but interestingly there is no appearance of the L12 phase, which in the previous sample (500°C) was dominant. The increase in temperature is enough to transform directly from the single L12 phase into a series of phases at 650°C. The hcp D019 phase is identified as $Fe_{0.7}Ga_{0.3}$ - HT on the diffraction pattern, this signifies that this phase is only stable at high temperature and it is definitely present after quenching as the characteristic peaks at 2θ=40° and 45.5° are *only* associated with the hcp structure. It is interesting that upon heating to ~500°C the L12 phase is preferred yet during cooling it seems the A2 and D03 phases are energetically or structurally favourable as earlier suggested. It is clear from these results that simple structural transformations do not occur within the Galfenol 27.5 at. % Ga in the 500°C to 800°C temperature region, but there are a multitude of metastable structural transitions which occur in order to keep the strain in the lattice to a minimum. The thermal energy allows for the Ga atoms to diffuse into the Fe-rich lattice until an equilibrium state is reached. Quenching interrupts this process and results in the material being frozen at whatever state it is currently in.

The furnace-cooled from 800°C sample is presented in figure 6.4.1.3 and the corresponding Crystal Match! report is in Appendix III. It can be observed that during cooling that several crystal structures develop during the slow cooling phase and these were partially predicted with the VSM results.

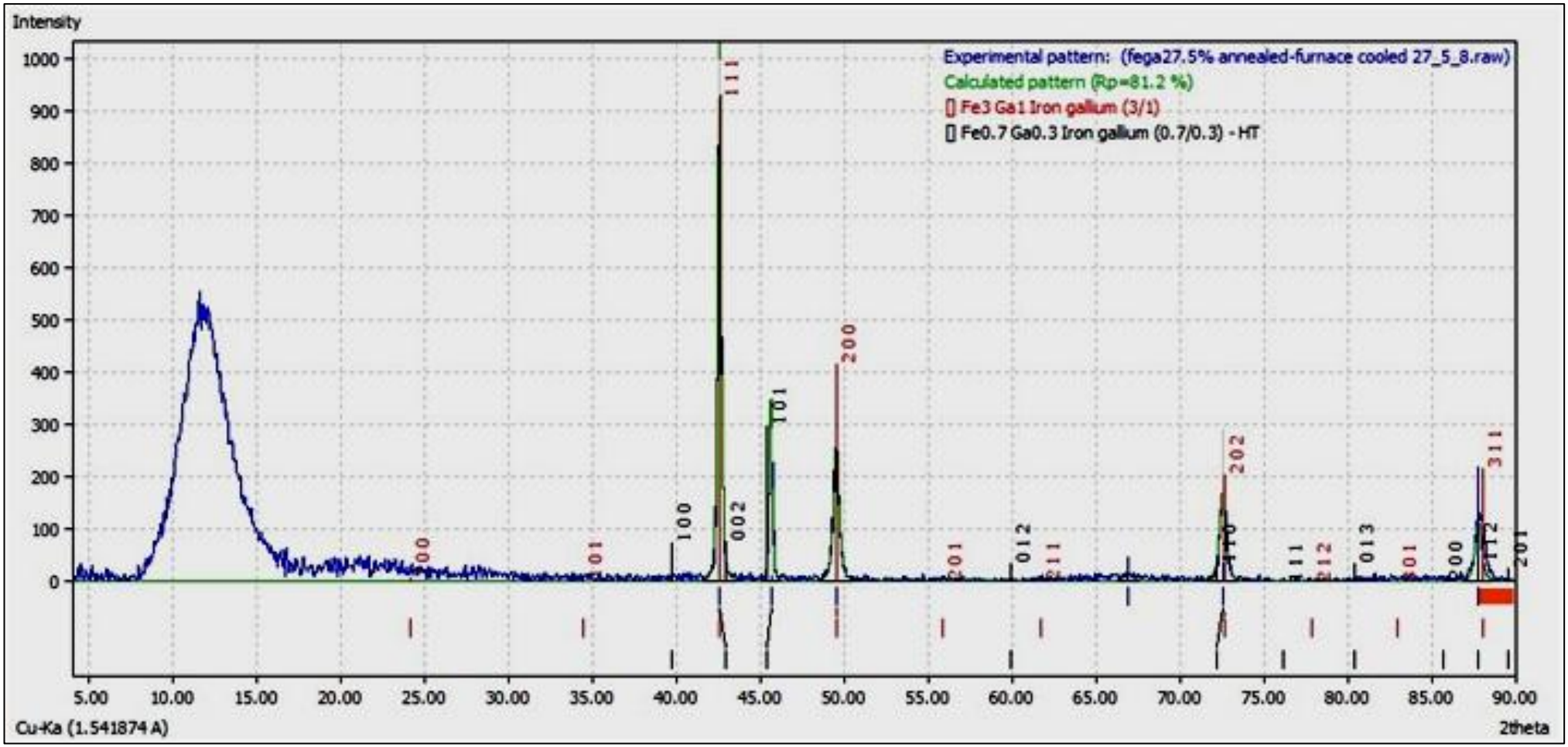

Figure 6.3.2.3 - Galfenol 27.5 at. % Furnace cooled at 10°C min^{-1}

The results are not quite as was predicted, as the material has transformed back to a majority of L12 phase, with the rest being attributed to the D019 hcp phase; this is somewhat unexpected as it was thought that the material would produce some A2 and D03 phase, but this cannot be seen in this work. The D019 phase transforms back to the equivalent fcc L12 phase by quite a large percentage; which is contrary to the transition that occurs in Fe_3Ge as was described earlier. This transformation, although not predicted is not very surprising as the transformation occurs via a slip transformation which is readily seen in Co and no atom diffusion is required as with bcc transformations. The characteristic hcp D019 peak at 39.7° has now disappeared and some of the other peaks are not present. This could again suggest a preferred structural orientation, although again in this experiment the sample was left in ribbon form instead of being powdered and this could also be a contributing factor. Unlike quenching, the slow cooling rate obviously allows for the thermal diffusion into other phases, but at this composition it is found that we just have two. Potentially others exist but in neglible amounts and cannot be detected using XRD. Although this result tends to agree with the equilibrium phase diagram for both heating and cooling, it does not agree with other reports that state the slow cooling process results in mixed D03 and A2 phases.

Table 6.3.2.1 shows the results in a concise format and shows the various lattice parameters calculated from specific peaks in the patterns.

Temperature of Annealing (°C)	**d-spacing $d_{[hkl]}$ (Å)**	**Lattice Parameter a_0 and c (Å)**	**Volume of Unit Cell V (Å^3)**	**Lattice Parameter a_0 (Å)**	**Phase(s) Identified Within Sample.**
500	fcc 2.1251	3.6723	49.5238	3.6704 **[6.3.2.3]**	L12 ordered fcc
650	bcc 2.0596 hcp 2.2527	A2 bcc 2.91271 D03 bcc 5.8152 D019 hcp a_0 = 2.624 c = 4.243	24.7110 196.6500 25.1576	2.90923 5.80824 **[4.2.5.6]** 24.9910 **[6.3.2.4]**	A2 disordered bcc D03 ordered bcc D019 ordered hcp
800	fcc 2.1257 hcp 2.2530	3.6771 a_0 = 2.627 c = 4.242	49.7183 25.1658	3.6704 **[6.3.2.3]** 24.9910 **[6.3.2.3]**	L12 ordered fcc D019 ordered hcp

Table 6.3.2.1 – Overview of lattice parameters and crystal structures after annealing-quenching and annealing-slow cooling treatments.

It is now clear that the specific temperature of the annealing controls the available structural states, which in turn determines the ferromagnetic properties of the sample as has been demonstrated by the results within this chapter. As far as has been reviewed in the literature, the formation of the L12 phase is said to be difficult to form but in this work it has been

demonstrated it is possible with very brief thermal treatment and that even a slow cooling process gives a majority D019→L12 transition with a small retention of the D019 hcp phase.

A brief review and summarisation of the results and discussions is given in chapter 7, with regard to any relevant experiments that could be now performed in order to further enhance the understanding of this complex material system.

6.4 Chapter 6 References

[6.1.1.1] Versalab Brochure, Rev. A0, Quantum Design, USA. http://www.qdusa.com/sitedocs/productBrochures/1300-003.pdf

[6.1.1.2] PPMS VSM Option User Manual, Rev A3. Quantum Design, USA. pp1-2, 2008.

[6.1.2.1] Zhu X-X. et al, A method based on the magnetic moment measurement to identify the structural transition of quenched Fe1-x Gax (x=0.15-0.30) alloys, Chin. Phys. B Vol. **20** No. 7, 077501, 2011.

[6.1.2.2] Buschow, K. H. J. Encyclopedia of materials: science and technology, pp 5021. Elsevier, 2001. ISBN:978008041529

[6.1.2.3] Yong. H., et al, Magnetostriction and structural characterization of Fe-Ga bulk alloy prepared by copper mould casting. Transactions of Nonferrous Metals Society of China, **22**, 2146-2152. 2012.

[6.1.2.4] Wagini, H., Naturforsch. Z., A22 (**1**) **143**, 1967.

[6.1.2.5] Okamoto, H., The Fe-Ga (Iron-Gallium) system, Volume **11**, Issue **6**, pp 576-581. 1990.

[6.1.2.6] Q. Xing, T.A. Lograsso; Phase identification of quenched Fe-25at.% Ga. Scripta Materialia **60** pp373-376, 2009.

[6.1.2.7] Dasarathy, C., Order-Disorder Change in Fe-Ga Alloys, J. Iron Steel Inst. (London), **202**(1), **51**, 1964. (Equi Diagram, Crys Structure; Experimental)

[6.1.2.8] Yoo, J.H, et al., The effect of magnetic field annealing on single crystal iron gallium alloy. J. Appl. Phys. **103**, 07B325, 2008.

[6.2.1.1] Cooper, A., Johnson, C. M., Differential scanning calorimetry. *Methods Mol Biol* **22,** 125-136. 1994.

[6.2.1.2] O. Ikeda, O., R. Kainuma, R., Ohnuma, I., Fukamichi, K. Ishida, K., Phase equilibria and stability of ordered b.c.c. phases in the Fe-rich portion of the Fe–Ga system, Journal of Alloys and Compounds **347** pp198–205, 2002.

[6.2.2.2] Zhu et al, A method based on magnetic moment measurement to identify the structural transition of quenched $Fe_{1-x}Ga_x$ alloys, Chin. Phys B, Vol. **20**, **7**, 077501, 2011.

[6.2.2.3] Dasarathy, C., Order-Disorder Change in Fe-Ga Alloys, J. Iron Steel Inst. (London), **202**(1), **51**, 1964. (Equi Diagram, Crys. Structure; Experimental)

[6.2.2.4] Sun, L., Effect of quenching on magnetostriction and microstructure of melt-spun $Fe_{83}Ga_{17}$ alloy, Journal of Alloys and Compounds, Volume **463**, Issues 1–2, Pages 6–9, 2008.

[6.2.2.5] Zhao, X., Mellors, N.J., Kilcoyne, S.H., Lord, D., Lupu, N., Chiriac, H., Henry, P.F., Journal of Applied Physics **103**, 07B320, 2008.

[6.2.2.6] Matsushita, M., Matsushima, Y., Yasushi, Fumihisa, O., Anomalous structural transformation and magnetism of Fe-Ga alloys, Physica B: Physics of Condensed Matter, Volume **405**, Issue **4**, pp1154-1157

[6.3.1.1] Couderg, J.J., Bras, J., Fagot, M., Study on the Ordered Structure of the Alloy Fe_3Ga, Compt. Rend. B, **272**, pp781–784. 1971.

[6.3.1.2] Hongyan, L., PhD Thesis: Control of the spin relaxation and magnetic anisotropy in Fe_{1-x} Ga_x/ZnSe systems, 2009.

[6.3.1.3] Q.Z., Chen, Ngan, H.W, Duggan, B.J., The L12→D019 transformation in the intermetallics compound Fe_3Ga, Journal of Materials Science, **33**, pp5405-5414, 1998.

[6.3.2.1] Lograsso T.A., Rossa A.R., Schlagela D.L., Clark A.E.,

Wun-Fogled M., Structural transformations in quenched Fe–alloys, Journal of Alloys and Compounds, **350,** 95–101. 2003.

[6.3.2.2] Kawamiya, N., Adachi, A., Nakamura, Y., Magnetic Properties and Mossbauer Investigations of Fe-Ga Alloys, Journal of the Phys. Soc. Japan, Vol. **33**, No. **5**. 1972.

[6.3.2.3] Schubert, K.; Bhan, S.; Burkhardt, W.; Gohle, R.; Meissner, H.G.; Poetzschke, M.; Stolz, E, Einige strukturelle Ergebnisse an metallischen Phasen (5) Naturwissenschaften **47**, (13) p303-p303, 1960.

Chapter 7: Consolidation of Results and Suggestions for Further Work

7.1 Discussion of Results and Comparison with Other Work

The results of the investigation into the Galfenol alloy are interesting and varied. The initial neutron diffraction and Mössbauer investigations (now published) indicate that the alloy, whether just melt-spun or melt-spun then annealed and quenched from 1000°C, show very similar properties to their corresponding composition. It is only in the 19.5 and 22.5 at. % Ga ribbons where any other type of phase could be seen, these being the L12 and D03 respectively. However, in the early x-ray diffraction work, only the A2 phase could be accounted for in all of the compositions; it can only be assumed that due to the difference in structure factors for Fe and Ga that this anomaly has arisen. In neutron diffraction the structure factors differ substantially due to the atomic cross section, where in x-ray diffraction they are very similar due to the similarity with both the Fe and Ga ionic radius.

The Mössbauer results potentially show evidence that the Ga atoms within the ribbons do not necessarily prefer Ga-Ga pairing, but in fact prefer to form nanoclusters in the larger A2 matrix; this was prevalent in the 17.5 at. % Ga ribbons, where this result is in excellent agreement with the EDX data presented for the same ribbon, suggesting a non-homogenous composition with a sporadic clustering of Ga atoms throughout the sample. The observed fraction of L12 phase in the 19.5 at. % Ga sample also suggests that the Ga atoms do prefer each other as neighbours as this phase should only be found at compositions above 25 at. % Ga, but could possibly be formed if the Ga atoms do form these suggested clusters in a more diluted alloy and this also gives credibility to the arguments that Ga atoms form these clusters in a larger A2 disordered matrix.

The EDX study also suggests that for most compositions, the spread of Ga in the melt-spun samples is not entirely random, but due to the speed of the cooling process from the melt; they do not have time to diffuse into their positions of lowest energy. This in turn is identified in the neutron work where the A2 disordered phase is dominant in all of the samples tested. This is also true of the annealed-quenched samples where the temperature of annealing (1000°C) puts all compositions back into the A2 disordered phase and by quenching them rapidly, the A2 phase becomes dominant again; but the neutron study does indicate that in the 19.5 at. % Ga and 22.5 at. % Ga there are small amounts of conversion to other phases.

The initial x-ray diffraction results are somewhat mundane when first examined as they do not seem to provide any more information than the neutron diffraction undertaken earlier. However, the direct identification of the dominant A2 phase confirms the earlier findings and the increase in lattice parameter with increasing Ga content is in very good agreement with not only the neutron work presented here but also with Dunlap and Luo **[7.1.1.1, 7.2.2.2]**. The changes in the peak widths from the melt-spun to the annealed-quenched are of some interest here, as a reduction in crystallite size could potentially mean the formation of smaller domains; thus potentially resulting in an increase in magnetostriction as reported by Lord, Al-Jiboory, James and Kinderlehrer in Terfenol-D samples **[7.1.1.2, 7.1.1.3]**. This could account for the additional magnetostrictive peak in the 27.5 at. % Ga annealed-quenched samples as referenced in chapter 3. No trace of any other phase can be seen in either the melt-spun or annealed-quenched ribbons of the dilute alloys which is contrary to the neutron results presented, this suggests that either the similar structure factors are screening any potential additional phase or that the addition of Ga to Fe is somewhat more complex than first thought.

The magnetic VSM work presented here is in good agreement with many journal articles **[7.1.1.4 – 7.1.1.8]** and is presented to show the linear behaviour of the decrease in saturation

magnetisation with additional Ga content. The Curie temperatures for the A2 bcc phase are also in good agreement with a selection of publications **[7.1.1.9 – 7.1.1.11]**. The interest here lies with the 22.5 at. % and 27.5 at. % Ga samples. This behaviour has only been reported once before by Kawamiya **[7.1.1.10]** in their study of bcc to fcc transitions when taking Curie temperature measurements; although they did not elaborate with their curves or demonstrate the behaviour of the samples during cooling. This transition as is now known to be a direct A2 bcc to L12 fcc structural reordering for both the 22.5 and 27.5 at. % Ga. The 22.5 at. % alloy doesn't have enough Ga addition to allow it to convert any further than a low percentage to the L12 phase, but it is enough to be distinctly noticed on the Curie curve. Some L12 phase does convert back to A2 or otherwise, but a portion remains as the saturation magnetisation is higher by ~6% on returning to room temperature. Over the series of following runs, there is a slow but steady conversion of a certain amount of the alloy into the L12 phase; where eventually the structural hysteresis fades as the equilibrium position is attained. Yet, in the 27.5 at. % Ga sample, the transformation is drastic. As the 27.5 at. % Ga sample is of the near perfect stoichiometry to form the L12 phase; it does so at a critical temperature of 450°C. It seems that this change is partially reversible as the structural hysteresis with this sample does not disappear. The argument is supported by the DSC results for this sample; it is proposed for the 22.5 at. % that the DSC used was not sensitive enough to detect the partial structural transformation on heating, but due to the enormous change in the 27.5 at. % Ga sample the DSC easily detected this transformation. On the first run of the VSM vs. DSC curve it shows that the initial DSC exothermic transform at 450°C occurs only the first time and this peak coincides perfectly with the VSM graph where the increase in magnetic moment is largest and this change must be irreversible. The next two following structural changes (indicated by endotherms) must be reversible, as they occur on every run and the peak on the cooling curve of the DSC data matches the VSM structural hysteresis data, as it can be seen on the VSM graph that the same value of magnetisation exists at two

distinct temperatures, dependent upon whether the material is being heated or cooled. This possibly could be attributed to any structural changes that are influenced by thermal expansion and contraction of the sample in which the result in this work tends to have some relation to the work presented by Matsushita et al **[7.1.1.9]** in their experimentation on Galfenol alloys of compositions 27.5<Ga<37.5 at. % Ga.

It would seem as though the fcc L12 to hcp D019 transition readily occurs but the reversal of this takes more time, similar to the proposals by Paduani et al with the same transition occurring in Fe3Zn. The difference is that the hcp to fcc change takes a much shorter time to occur in Galfenol alloys **[7.1.1.12]**. The final XRD data presented identifies the final phases of the 27.5 at. % Ga samples from the several treatments used from their as-melt-spun state; the final phase of the annealing treatment to 500°C and then quenched is identified as almost 100% L12; which is in good agreement with the relative increase in the overall magnetic moment as the material is transformed. This was not expected due to the reports that the L12 phase only comes into being after long term thermal annealing, but in this work we have demonstrated that this is not necessarily the case.

The sample quenched from 650°C has also given some unreported results. Here the L12 phase has completely transformed but into a mixed phase alloy of D019 and A2, with a possibility of D03, but it seems there are too many D03 peaks missing for it to be present. So part of the material has managed to retain the hcp phase and the remaining proportion has been converted back to an A2 bcc disordered alloy. The direct transition from hcp to bcc is potentially an energetically favourable transition at this temperature or that during the structural change the quenching has the effect of disordering or interrupting the transition taking place resulting in a partial hcp and A2 mixed alloy. This argument makes sense when the last sample to be annealed was taken to a temperature of 800°C and allowed to slowly cool in the furnace. Here the phases found are just the hcp D019 and the fcc L12 which

suggests that quenching destroys the ordering process and induces chaos into the lattice, as opposed to when the material cools slowly the atoms are allowed to thermally diffuse into more ordered structures. By slow cooling to the L12 lattice it would suggest that the Ga would prefer an ordered structure; which is conducive to the magnetostriction. The reasons for the alloy behaving in this manner are not completely understood and more work is required to establish the modes of transport or the slip/shear of the planes within the lattice.

7.2 Suggestions for Further Work to be undertaken

There is much more investigative work to be undertaken on Fe-rich Galfenol alloys before they are fully characterised and understood. Due to the complex and varied structures that can be formed it is necessary to remove as many variables as possible when conducting future experiments. The first proposed study would involve either a synchrotron x-ray or neutron (preferred) diffraction study, carried out slowly on certain compositions of 22.5<Ga<35 at. % of non-magnetically saturated ribbons across a large temperature range of 350°C up to 900°C, these would then be repeated with the application of a magnetic field to saturate the ribbons and the differences established. This would conclude whether or not magnetic annealing plays any role in the structural transformation.

Also transmission electron microscopy work at temperature needs to be carried out in order to develop a better understanding of the localised microstructure and the apparent method of Ga dilution within these alloys established. The major issue concerning further research is that of either performing macroscopic measurements such as neutron diffraction, DSC and VSM which looks at the complete body of the material and in contrast microscopy experiments such as TEM and SEM which either look at very small areas of a sample or only give surface information. Combinatorial experiments, as proved in this work could potentially give further understanding of this complex alloy; but another experimental

technique which has the ability of observing the structural re-ordering in-situ would be of the most practical use.

However, it must be recognised that the sample preparation method, rapid solidification from the melt must always introduce and encourage non-equilibrium conditions and behaviour.

7.3 Accepted Publications and Future Publications

The following publications have arisen from the work in this thesis or the help provided to other researchers regarding investigative work on other magnetic materials.

i) Mellors, N.J., Zhao, X., Simmons, L.M., Quinn, C.J., Kilcoyne, S.H., **A Mossbauer spectroscopy and neutron diffraction study of magnetostrictive, melt-spun Fe–Ga alloy ribbons.** Journal of Magnetism and Magnetic Materials, 324, pp3817–3823, 2012. http://dx.doi.org/10.1016/j.jmmm.2012.06.021

This journal article can be found in full in Appendix V.

ii) Palizdar, M., Comyn, T.P., Ward, M.B., Brown, A.P., Harrington , J.P., Kulkarni, S., Keeney, L., Roy, S., Pemble, M., Whatmore, R., Quinn, C.J., Kilcoyne, S.H., Bell, A.J., **Crystallographic and magnetic identification of secondary phase in orientated Bi5 Fe0.5 Co0.5 Ti3 O15 ceramics.** Journal of Applied Physics, 112, 073919 - 073919-8, 2011. http://dx.doi.org/+10.1063/1.4754562

iii) Quinn, C.J., **Fabrication and Characterisation of Iron-Gallium (FeGa) Thin Films and Melt-Spun Ribbons,** 1st CSE Doctoral School Postgraduate Research Conference, University of Salford, 2010. ISBN:978105732975

iv) Quinn, C.J., Grundy, P.J., Mellors, N.J., **The Crystallographic, Structural and magnetic properties of Fe-rich Galfenol alloy melt-spun ribbons.** (In preparation).

7.4 Chapter 7 References

[7.1.1.1] Dunlap, R.A, McGraw, J.D., Farrell S.P., Journal of Magnetism and Magnetic Materials **305** 315–320. 2006.

[7.1.1.2] Luo, H.L., Transactions of the Metallurgical Society of AIME, **239,** 119, 1967.

[7.1.1.3] James, Richard D. and Kinderlehrer, David, Theory of magnetostriction with applications to $Tb_xDy_{1-x}Fe_2$, Department of Mathematical Sciences. Paper **416**, 1993.

[7.1.1.4] Al-Jiboory, M. and Lord, D.G., Study of the magnetostrictive distortion in single crystal terfenol-D by x-ray diffraction, IEEE Trans. Magnetics **26**, pp. 2583-2585, 1990.

[7.1.1.5] Summers, E.M., Lograsso, T.A., Wun-Fogle, M., Magnetostriction of binary and ternary Fe-Ga alloys, Journal of Materials Science, 42 (**23**), pp9582-9594, 2007.

[7.1.1.6] Clark, E., et al., Extraordinary Magnetoelasticity and lattice softening in bcc Fe-Ga alloys, Journal of Applied Physics, 93 (**10**), pp8621-8623, 2003.

[7.1.1.7] Ikeda, O., Kainuma, R., Ohinuma, I., Fukamichi, K., Ishida, K., Phase equilibria and stability of ordered bcc phases in the Fe-rich portion of the Fe-Ga system, Journal of Alloys and Compounds, **347 (1-2)**, pp198-205, 2002.

[7.1.1.8] Toshiya, T., et al, Characterisation of magnetostrictive Fe-Ga based alloys fabricated by rapid solidification, J. Scripta Materialia, **60 (10)**, pp847-849, 2009.

[7.1.1.9] Matsushita, M., Matsushima, Y., Yasushi, Fumihisa, O., Anomalous structural transformation and magnetism of Fe-Ga alloys, Physica B: Physics of Condensed Matter, Volume **405**, Issue **4**, pp1154-1157

[7.1.1.10] Kawamiya, N, Adachi, A. Nakamura, Y., Magnetic Properties and Mossbauer Investigations of Fe-Ga Alloys, Journal of the Phys. Soc. Japan, Vol. **33**, No. **5,** 1972.

[7.1.1.11] Zhu X-X. et al, A method based on the magnetic moment measurement to identify the structural transition of quenched Fe1-x Gax (x=0.15-0.30) alloys, Chin. Phys. B Vol. **20** No. 7, 077501, 2011.

[7.1.1.12] C. Paduani, C. Bormio-Nunes, Ab initio study of electronic and magnetic properties of the Fe3Zn intermetallic, Physica B: Condensed Matter, Volume **406**, Issue **9**, Pages 1752-1756, 2011.

Appendix I: Galfenol Thin Films.

ApI.1 Fabrication Equipment Overview

The main piece of equipment used for fabrication of films is a high vacuum system which was manufactured by Kurt J. Lesker. It consists of a large central chamber (~0.6 metres diameter) which can hold up to twelve individual substrates and the chamber can also accommodate up to four separate magnetron units. Additionally it has several smaller ports under the chamber so that it is possible to backfill the chamber with up to three different gases – the main one in this case is high-purity argon (99.99999% purity.)

The chamber also has a loading arm linked to a smaller load-lock chamber which is connected to a smaller rotary pump and turbomolecular pump attached; this additional feature maintains the vacuum in the main chamber and the system does not have to be let up to atmospheric pressure when substrates need to be loaded and/or removed from the system.

The main chamber is linked to both a large Edwards' rotary pump and a BOC turbomolecular pump; this enables the chamber to reach a base pressure of 1×10^{-7} mbar. The pressure is monitored by different instruments, an analogue pirani gauge, a cold cathode magnetron and an ion gauge; as these all work at slightly different pressures. It enables the pressure within the chamber to be monitored constantly over a wide range from atmospheric pressure down to the base pressure, it also allows for the pressure to be monitored during the actual sputtering process. The controllers and control systems are similar to most vacuum systems and are located in a rack alongside the main chamber; these consist of two gas controllers, the turbo pump controllers, digital readouts for the pressure gauge monitors, two power amplifiers for powering the magnetron units and a vacuum scan unit for checking what compositions of residual gases or elements are present within the chamber. Figure ApI.1.1.1 shows the main system along with the controllers and monitoring equipment rack.

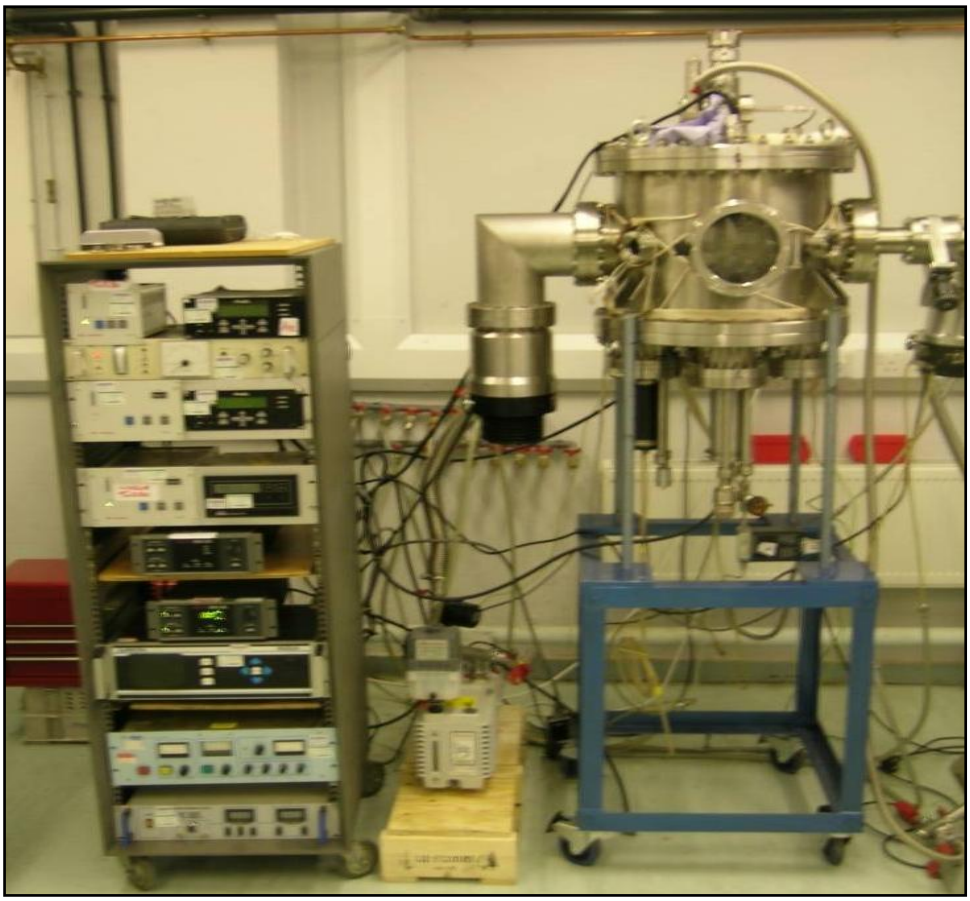

Figure ApI.1.1.1 - Main Vacuum Chamber, Pumps & Controller Units

There are several techniques that can be employed to deposit thin films such as evaporation by resistive heating or electron beam; chemical vapour deposition CVD), radio frequency sputtering (RF) and the chosen method for this research with is unbalanced DC magnetron sputtering (PVD). Physical sputtering is driven by the momentum exchange between the ions and atoms in the material this is due to the collisions between the positive argon ions which are attracted to and then strike the target material. The incident ions set off with a certain amount of kinetic energy which in turn cascade within the target material and when of sufficient energy, release the surface atoms; in this case the material is the bulk FeGa. When such cascades recoil and reach the target surface with energy above the surface binding energy, atoms can then be ejected from the target, secondary electrons are also then ejected and can then potentially also interact with neutral argon atoms to ionise them making them also bombard the target material releasing yet more target atoms; the result is a type of

avalanche effect resulting in a continuous sputtering process; an example of this can be seen in Figure ApI.1.1.2. The average number of atoms ejected from the target per incident ion is called the *sputter yield* and depends on the ion incident angle, the energy of the ion, the mass of the ion and target atoms and the surface binding energy of the atoms comprising the target material **[ApI.1.1.1].**

The permanent magnets which are an integral part of the magnetron are used to provide a magnetic field which traps any charged particles within the field and encourages them to form a spiral flight path towards the target material; in this case the charged particles are predominantly electrons which in turn collide with the Argon atoms making them form positive argon ions which then bombard the target material resulting in the sputtering of the alloy of whose atoms then are ejected towards the substrate.

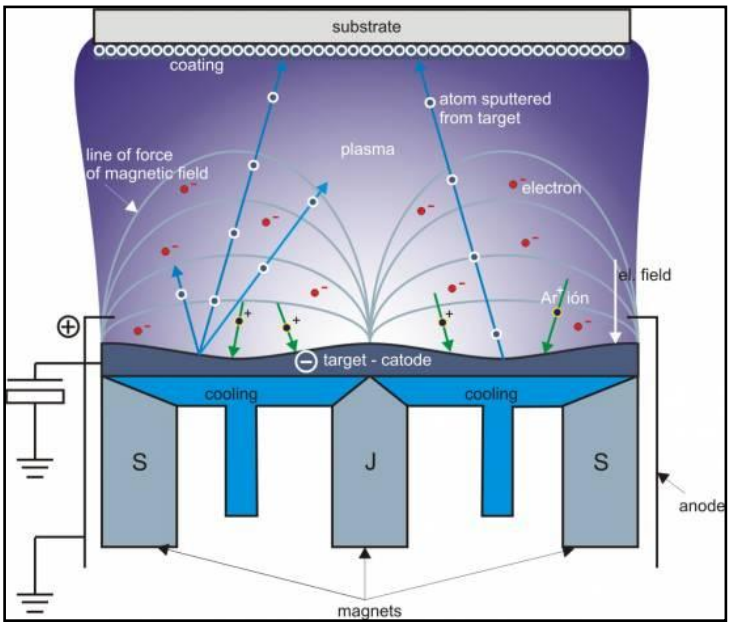

Figure ApI.1.1.2 – Principal of DC Magnetron Sputtering Process [52 – ApI.1.1.2]

It is the high potential difference between anode and cathode with the Argon gas fed into the chamber that causes the formation of this plasma as the gas becomes ionised within the chamber.

The distance that the released atoms will travel can be determined by the mean free path which is given by-:

$$\lambda = \frac{kT}{\sqrt{2}\,\pi P d^2} \qquad \textbf{(ApI.1.1.1)}$$

Where, λ is the mean free path (m), k is the Boltzmann constant (m^2 kg s^{-2} K^{-1}), T is the absolute temperature (K), P is the pressure (Pa), d is the diameter of the gas atoms (m) **[ApI.1.1.3]**

By using the given equation it was calculated that with the sputtering pressure that is being utilised that the mean free path would be ~0.12 metres; the minimum working distance within this particular chamber is 0.10 metres but was augmented to allow for working distances from 0.02m up to 0.12m.

The variety of films that have so far been produced have shown to have uniform thickness with the deposition rate calculated to be ~0.3 nm per second; this is for a sputtering power of 150 Watts with an argon backflow of 5.0 sccm (standard cubic centimetres per minute) and a sputtering height of 0.1 metres. This value however changes for the films grown at oblique angles (>80 degrees) where a shadowing effect takes place. In this instance the film is not flat and uniform but tends to grow into individual structures. The reasons for this behaviour will be discussed later where glancing angle deposition (GLAD) will be described. It is worth mentioning that when sputtering is performed at high angles, the sputtering yield drops by a considerable amount.

The other issue that will be mentioned here is regarding target erosion; this is because of the strong magnetic field that is applied during the sputtering process; the field causes the electrons to follow a semi-circular spiral path around the magnetic field lines, thus giving them a much longer path length before they are absorbed into the target surface; the

disadvantage of this is that the electrons now have a preferred path length into the target when they are trapped by the magnetic field.

This greatly increases the electrons probability of striking and ionising an argon atom, this allows for the same ion density at a much lower pressure than can be used for example in diode or triode sputtering. If the ends of the magnetic field lines are at the cathode then the electrons will continue to traverse both backwards and forwards almost indefinitely.

In DC magnetron sputtering a strong toroidal magnetic field confines the electrons in this way meaning that there is a specific region of the target where the electrons and ions have a much higher probability to strike the target material, this gives rise to a distinct erosion ring known as a 'race-track' in the target material. The main drawback of this is that there can be a large amount of wasted material from the target due to this effect, an example of this is shown in Figure ApI.1.1.3. **[ApI.1.1.4]**

Figure ApI.1.1.3 – Plasma Formed on an FeGa Target

(the inner part of the ring is the point of highest erosion).

As the target is eroded (by the charged ions and scattered electrons) it increases in temperature; therefore the magnetron unit is constantly water cooled to avoid the target overheating and make it less likely to start arc discharging thus prematurely ending the process or potentially damaging the amplification equipment.

ApI.2 Sculptured Thin-Films and Glancing Angle Deposition (GLAD)

Glancing Angle Deposition (GLAD) is a technique invented by Kevin J. Robbie and Michael J. Brett was officially patented in 2001 and then was subsequently improved in 2002. **[ApI.2.1.1]** The method orientates the substrate at oblique angles to the material flux from the sputtering target, the substrate is attached to a stepper motor and controller which allows for the speed and direction of rotation to be varied; this in turn allows for structures of different shapes and orientations to be grown; a schematic of this can be seen in Figure ApI.1.2.1.1.

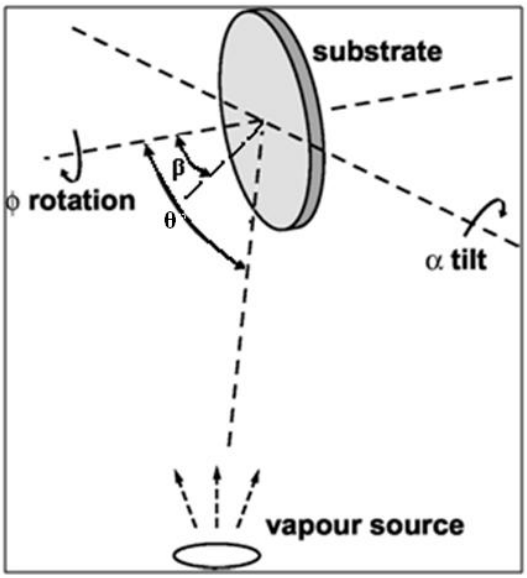

Figure ApI.2.1.1 - Schematic of Glancing Angle Deposition [ApI.2.1.2]

The technique relies upon the 'shadowing effect' which states the greater the angle of tilt, the more porous the film will become; this was experimentally proposed by Tait; then confirmed by Messier et al. **[ApI.2.1.3]** The equation for governing this shadow effect is given by-:

$$\beta = \theta - \arcsin(\frac{1-\cos\theta}{2})$$

Where, β is the column angle and θ is the flux angle.

This equation describes the fixed relationship between the incident flux angle α and the columnar growth angle ***β*** for a fixed set of deposition conditions ~material, temperature, gas composition, pressure and vapour energies**.** Figures ApI.2.1.2 shows the situation more clearly on how the initial nucleation forms the shadowing centres and then how the columnar structures are formed due to the shadowing effect; Figure ApI.2.1.3 indicates a graph of the solid line relationship of the above equation proposed by Tait; the shaded region is the microstructure attainable with the technique described within the capabilities of the GLAD technique.

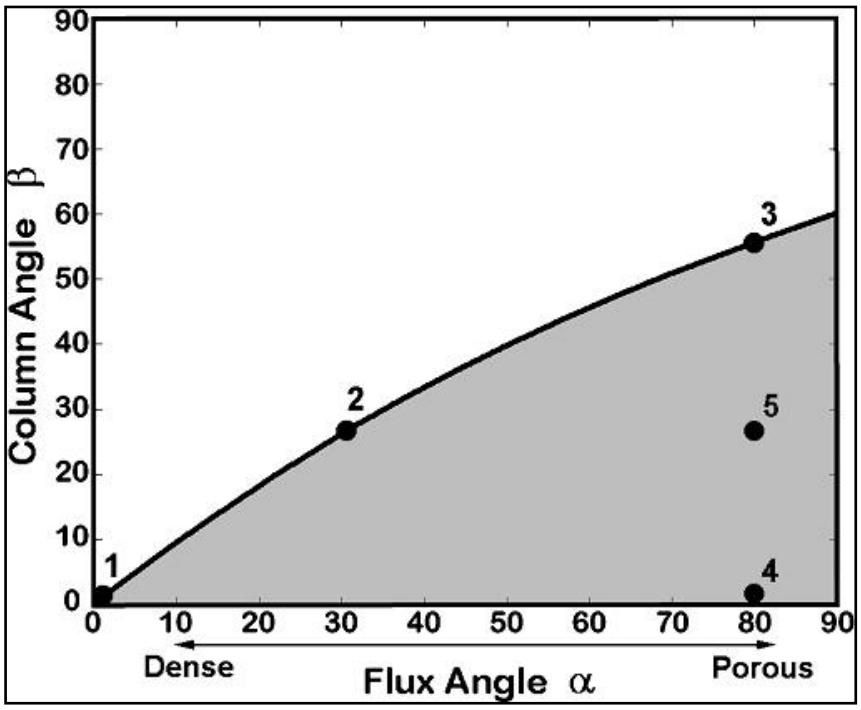

Figure ApI.2.1.2 - Relationship Between Flux Angle and Columnar Growth Angle. [61 – ApI.2.1.4]

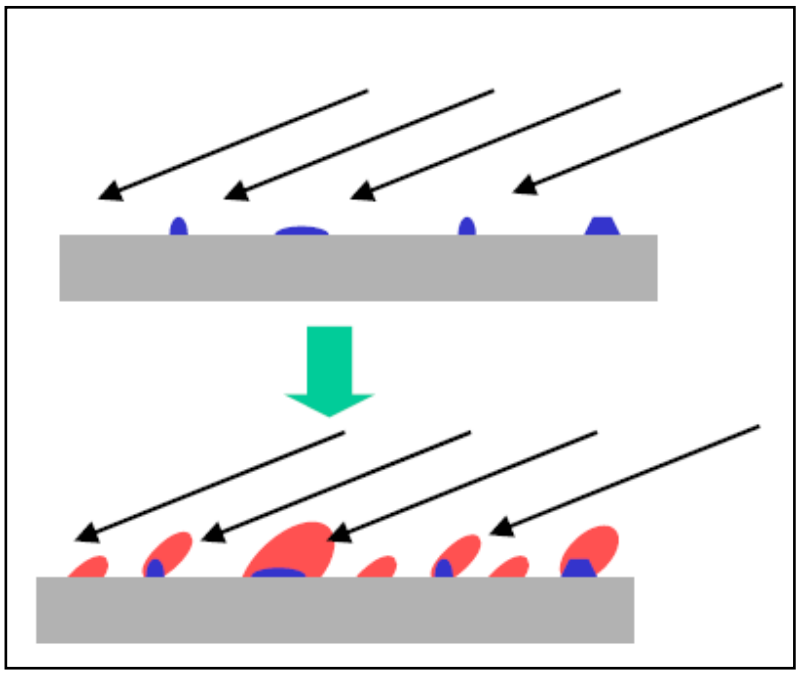

Figure ApI.2.1.3 - Initial Nucleation and Then Growth of Columnar Structures. [60 – ApI.2.1.5]

The main difference between GLAD sputtering and flat film sputtering is the growth rate itself; which in GLAD is much smaller than in standard sputtering, long column type films can take up to several hours to grow using the GLAD technique.

The other main advantage of using GLAD is that pre-seeding of the substrate with nanospheres is not required; although there is no reason why both spin-coating with nanospheres and then employing the GLAD method together is actually perfectly acceptable.

The films fabricated have been a mixture of flat thin films of different thicknesses varying from less than one hundred nanometres up to several thousand nanometres. The sculptured films have been deposited on nanospheres of 500nm diameter which are applied to the substrates using a variety of methods; all of which have their own drawbacks. The spheres reside in an aqueous solution and can be just applied to the substrate at an angle of 15 degrees and the solution left to evaporate or the solution placed on the substrate and rotated quickly (spin-coat) at various speeds from 50 rpm up to 1200 rpm; which was found to give a more

even coverage. In this work the substrates that have been used are made of [001] p-type silicon or glass cover slides.

The 2-axis rotation device consisted of two stepper motors, one to control the substrate angle to the incoming flux and the other to actually rotate the substrate in the plane of the flux.

ApI.3 Scanning Electron Microscopy Analysis

The two images below in figures ApI.3.1.1 and ApI.3.1.2 were taken using a JEOL 6400 scanning electron microscope can be seen showing the nanosphere arrays. It can be observed that in the first image which is taken at 100x magnification that the spheres in this case have tended to form in 'clustered groups' leaving large areas of the silicon uncovered although this wasn't unexpected considering this was accomplished using the 15 degree angle method.

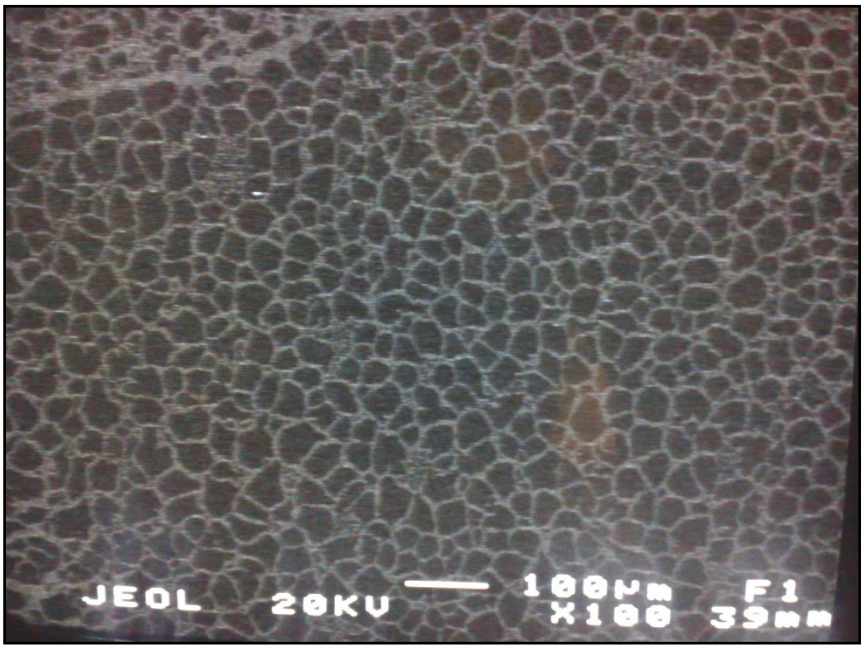

Figure ApI.3.1.1 - 100x Magnification of Nanosphere Coated Silicon Substrate

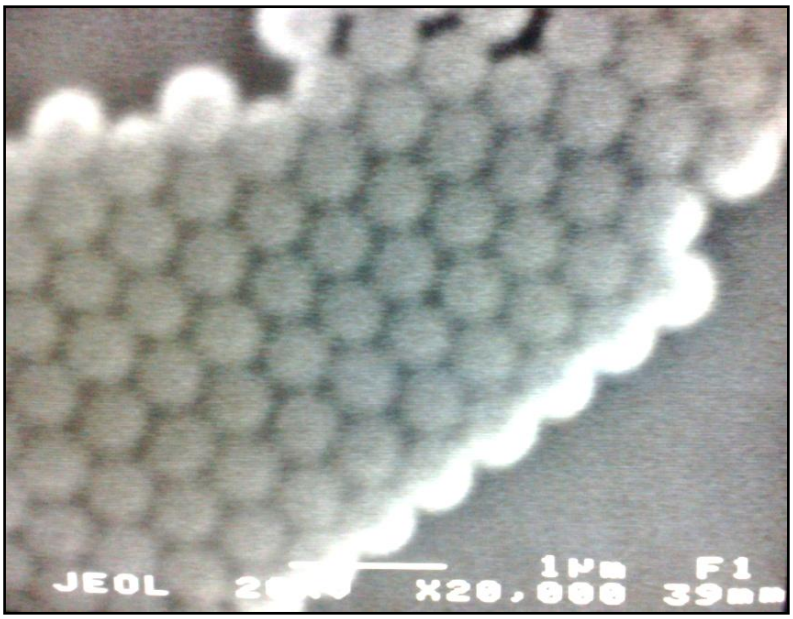

Figure ApI.3.1.2 - 20,000x Magnification of Nanospheres Hexagonal Array

It was thought that at high magnification the packed arrays would be of use to sputter the coated substrate with the Galfenol alloy 20 at. % Ga onto these spheres, this resulted in the image in figure ApI.3.1.3 where it can be seen that in this primary attempt to grow individual Galfenol structures has partially been a success as the growth of the needle like elongation can be seen.

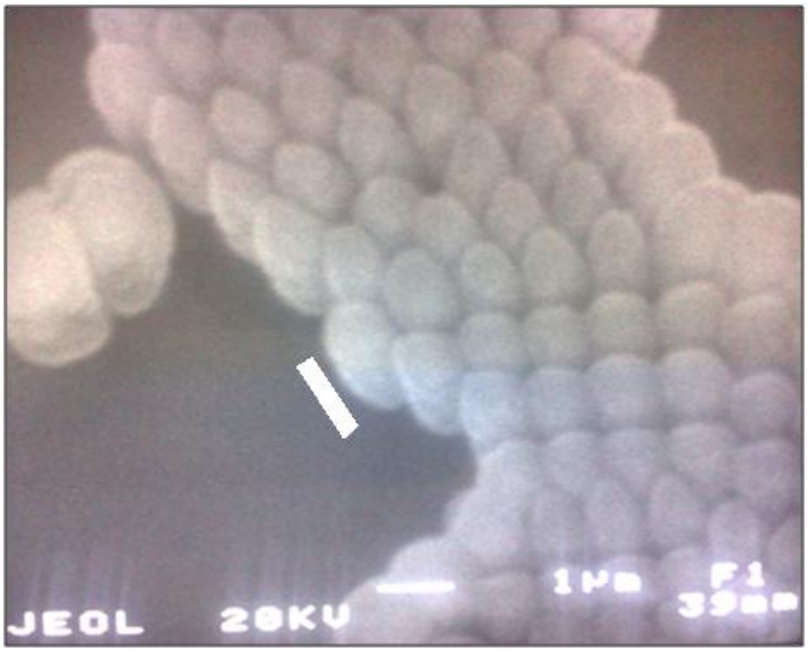

Figure ApI.3.1.3 - Primary Attempt at Growing Nanostructures on Spheres

The growth in height is estimated to be just over 1 micrometre as can be seen on the diagram indicated by the white line next to the column, the line being equivalent to one micrometre in length. It can also be noticed that some of the structures seem to have an unusual random orientation and have grown horizontally rather than vertically especially those to the extreme left and right sides of the image. It is thought this is due to these particular nucleation points being on the barrier or junction between the nanosphere monolayer and the bare silicon substrate. Figure ApI.3.1.4 is a different perspective view of the same substrate. In this example where the nanospheres have not adhered to the silicon, a flat Galfenol film has grown in this area; this is because this film was sputtered directly at an incidence flux angle of zero degrees and the oblique angle method was not used. This however does show though that the possibility of growing close packed nanostructures is possible and with better control methods of nanosphere adhesion even coverage of the substrate could potentially be achieved.

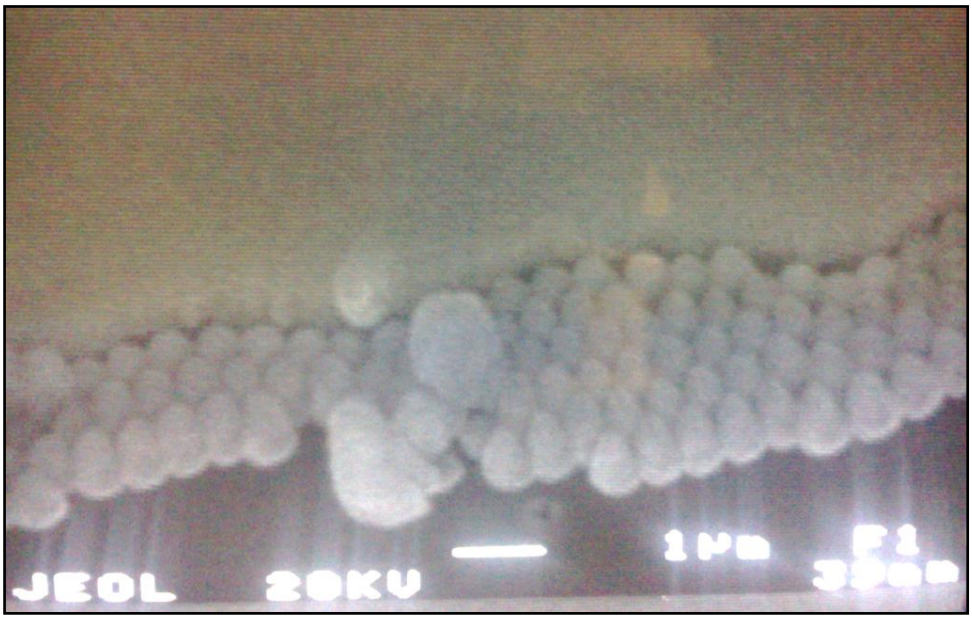

Figure ApI.3.1.4 - Nanostructure Growth alongside Flat Film

Figure ApI.3.1.5 shows the cross-section of a flat film grown onto a glass substrate, the thickness of the film is shown in the figure and an average resulting thickness of ~83nm was

calculated. A simple calculation was used to determine the deposition rate by taking the thickness and dividing by the time of deposition.

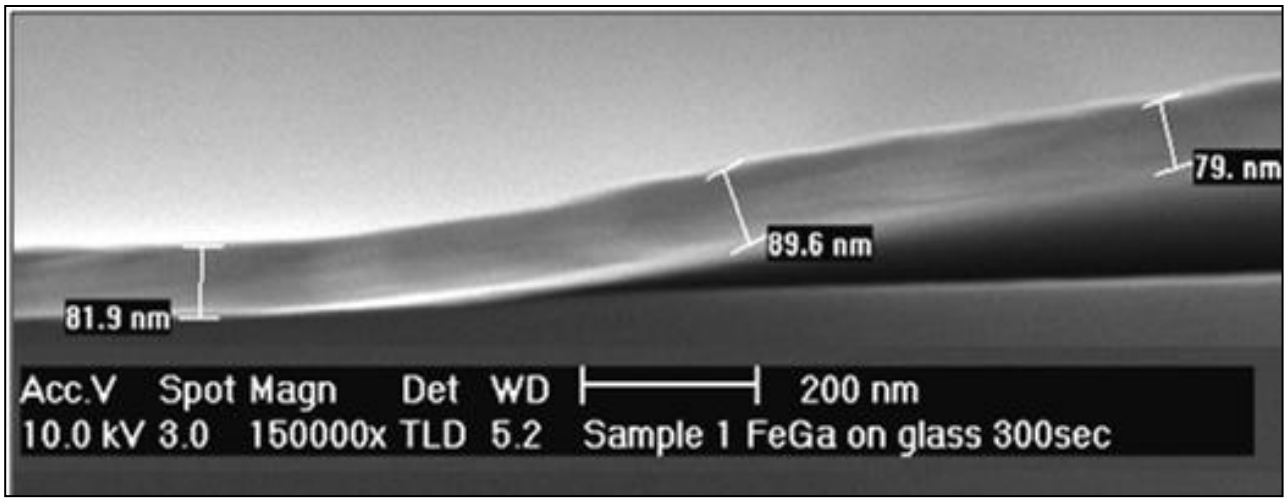

Figure ApI.3.1.5 - Flat film grown on glass substrate

A deposition rate was calculated to be 0.29 nanometres per second (2.9 Angstroms) which is in good agreement with the sputtering yield deposition measurements at a distance of 0.1 metres made by both Chambers and Geller **[ApI.3.1.1]**.

Figure ApI.3.1.6 shows an image of a film grown by GLAD onto a bare Si substrate, thus showing how the shadowing effect manifests itself by not only growing individual structures but also depositing a film simultaneously. It is not quite understood why there are some areas where the structures wish to grow and other areas seem barren, though it would seem likely there is preferential selection for specific areas of the substrate created by the initial nucleation, then the shadowing effect of the rotation starts to control the relative flux rate and hence the allowed growth of each structure.

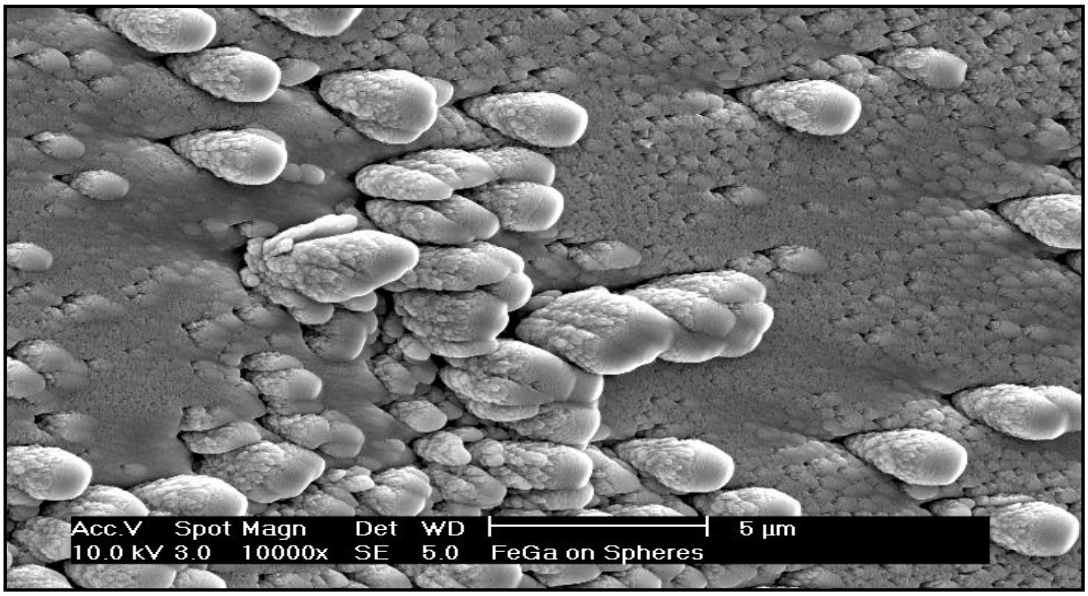

Figure ApI.3.1.7 - Nanostructures grown on bare Si substrate

The method itself turned out to be less scientific than at first thought and behaved more so like a pragmatic process. This can be seen in figure ApI.3.1.8 where again bare Si was used as the substrate and a slightly lower deposition angle selected. This image was taken at 5,000x magnification and the central region displays a long array of nanopillars; the array is approximately 50 micrometres long but only ~3 to 4 micrometres in width, it is thought that each pillar has a height of around 1.5 micrometres. It can also be seen in the rest of the image that other small clumps of material has grown in what seems like a random distribution and it is again thought that the shadowing effect is responsible for this resulting distribution.

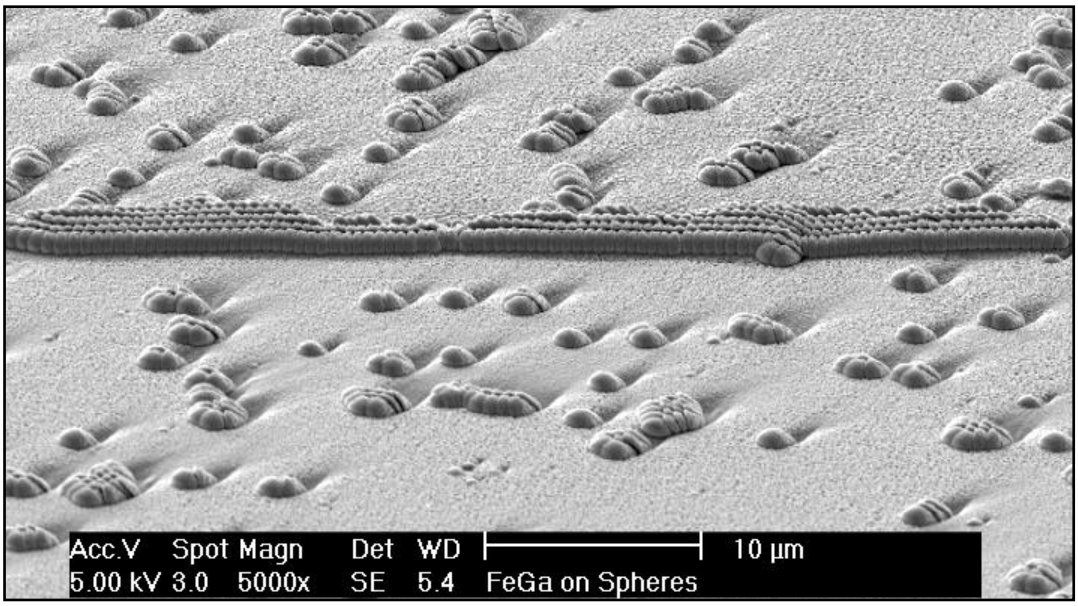

Figure ApI.3.1.8 - Nanopillar array with other randomly distributed structures

ApI.4 Electron Dispersive Microscopy Analysis (EDX)

EDX was used to characterise the thin film samples of both the flat film and the GLAD grown film with some interesting results. A piece of blank Si substrate was firstly measured to be used as a background reduction for the actual film, as the film analysed is only on average 80nm thick and therefore the Si substrate would also be detected. The results are shown in Table ApI.4.1.1.

Sample	FeGa20									
EDAX										
Element Normalised										
	1st		2nd		3rd		4th		5th	
Element	Wt %	At %	Wt %	At %	Wt %	At %	Wt %	At %	Wt %	At %
FeK	76.56	80.31	76.18	79.97	76.03	79.84	76.24	80.02	76.82	80.54
GaK	23.44	19.69	23.82	20.03	23.97	20.16	23.76	19.98	23.18	19.46
Total	100	100	100	100	100	100	100	100	100	100
Average	Wt %	At %								
FeK	76.37	80.14								
GaK	23.63	19.86								
Total	100	100								

Table ApI.4.1.1 - Galfenol thin film 20 at. % Ga

Here the composition of the film matches the target composition very well, though the measurements are more uniform in the middle of the film where it is slightly thicker than at the extreme edges. The composition of the nanostructured film was similar to the earlier results table and thus is not shown. The structures grown on the nanospheres were not tested using EDX as it was thought the polystyrene spheres would throw up anomalous results.

ApI.5 Vibrating Sample Magnetometry Analysis

Due to only having one composition of target material, the magnetic testing is of limited nature but was performed to see if there is any agreement between the ribbons and thin-films. In figure ApI.5.1.1 the hysteresis curves shown for the hard and easy directions are clearly shown, with the sheared curve belonging to the hard axes.

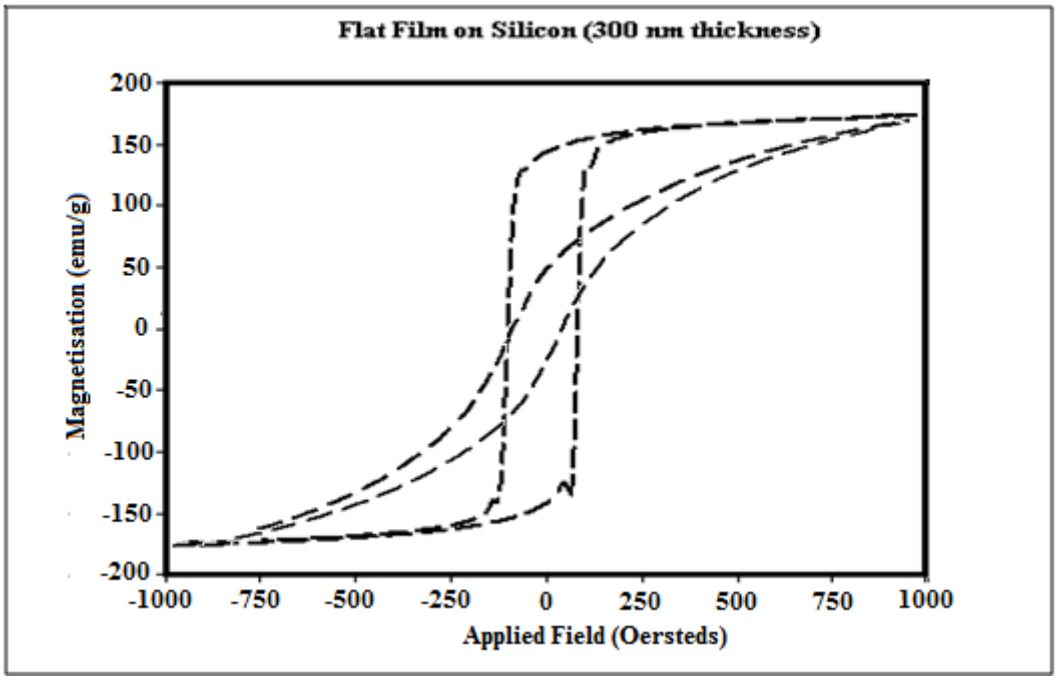

Figure ApI.5.1.1 - VSM Curves for Galfenol thin-film 20 at. % Ga

The saturation magnetisation of 176 emu/g is in good agreement with both the ribbon samples presented in this work and also with Butera et al. in their study of films of 19 at. % Ga **[ApI.5.1.1]**. The one difference is the coercivity and remanence values for the films of ~70 Oersteds and ~151 emu/g respectively for the easy direction and ~45 Oersteds and ~49

emu/g for the hard direction; this is much greater than that of ribbons and bulk samples. It is thought this could partially be attributed to the grain size of the thin film as proposed by Georgieva et al with regard to their research of grain refined Fe films **[ApI.5.1.2]**. The film would therefore better retain the domain orientation after being magnetically saturated until the necessary opposing magnetic field is applied to reverse the domain rotation. In this case, this argument seems to provide a satisfactory explanation.

As the nanostructures were proving difficult to fabricate, more literature research was undertaken and it was found that after discussions with researchers at the Nanosmat-5 conference in France; problems had arisen in the use of Ga as a seed for growing nanowires instead of the more widely used Au. It was found that when using Ga nanodots, the resulting nanowires grew parallel to the substrate instead of perpendicular meaning the nanowires adhered to the substrate rather than arranging themselves as to be harvested in the usual fashion. The concentration of this research to focus upon melt-spun ribbon samples was then made as it was decided that in practical terms the ribbons are much easier to manufacture on a reproducible basis.

ApI.6 Discussion of Results and Suggestions for Further Work

The thin films show good agreement in the magnetic characteristics when compared with the similar research carried out by Butera et al and McClure et al **[ApI.6.1.1, ApI.6.1.2]**.

The technique for growing the structures needs to be reconsidered as at a certain height the film starts to become flat instead of continuing to grow in individual structures as had happened initially, it is thought this happens because of the preferred crystallographic growth anisotropy. Sputtering may not be the way to form the structured films and other methods such as co-evaporation or molecular beam epitaxy should be considered similar to the recent success of forming Ge structures by MBE as performed by Khare et al **[ApI.6.1.3]**.

The scope for research on thin films has predominantly been based on magnetostrictive properties and it is proposed that it would be of fundamental importance to fabricate films with a higher Ga content than has been done so far, for example 20 to 35 at.% Ga, similar to the Galfenol ribbons. It would be interesting to observe whether the results gathered from the melt-spun ribbons performed in this work would be in agreement with thin film samples of a similar composition when given similar magnetic and thermal treatments. It would also be interesting to identify at what thickness of film the remanence and coercivity values become similar to that of both melt-spun and bulk Galfenol samples, suggesting this transformation is a function of film thickness and hence grain size.

ApI.7 Appendix I References

[ApI.1.1.1] Seah, M.P., Clifford, C.A., Green, F.M., Gilmore, I.S., An accurate semi-empirical equation for sputtering yields, I: for argon ions. Surf. Interface Anal., **37**, 444-458, 2005.

[ApI.1.1.2] Schematic Diagram of DC Magnetron Sputtering http://www.umms.sav.sk/data/files/167.jpg, 2009.

[ApI.1.1.3] Geller, J., Veisfeld, N., Ion Sputtering Yield measurements for Sub micrometer Thin Films, JVST 6, 3, Part II, June, 1988

[ApI.1.1.4] Chapman, B.N., Glow Discharge Processes, Wiley, New York 1980. ISBN: 9780471078289

[ApI.2.1.1] Robbie, K., Sit, J.C., and Brett, M.J., Schematic Diagram of Glancing Angle Deposition, Advanced techniques for glancing angle deposition, J. Vac. Sci. Technol. B, Vol. 16, No. 3, 1998.

Sculptured Thin Films and Glancing Angle Deposition, European Cells and Materials Vol. **4**, Suppl. **2**, 2002.

Robbie, K.J., Brett, M.J., US Patent 6206065 B1 for Glancing Angle Deposition Technique 2001 http://www.freepatentsonline.com/6206065.pdf

[ApI.2.1.2] Messier, R., Gehrke, T., Frankel, C., Venugopal, V.C., Otano, W., and Lakhtakia, A., J. Vac. Sci. Technol. A **15**, 2148, 1997.

[ApI.2.1.3] Robbie, K., Sit, J.C., and Brett, M.J., Schematic Diagram of Glancing Angle Deposition, Advanced techniques for glancing angle deposition, J. Vac. Sci. Technol. B, Vol. 16, No. 3, 1998.

[ApI.2.1.4] Robbie, K., Sit, J.C., Brett, M.J., Advanced techniques for glancing angle deposition, J. Vac. Sci. Technol. B, Vol. **16**, No. **3**, 1998.

[ApI.2.1.5] Zhao, Y-P., Yeb, D.X., Wangb, G.C., Lub, T.M., Designing Nanostructures by Glancing Angle Deposition, Proceedings of SPIE Vol. 5219 Nanotubes and Nanowires, SPIE, 2003.

[ApI.5.1.1] Weston, J.L., Butera, A., Lograsso, T.A., Shamsuzzoha, M., Zana, I., Zangari G., Barnard J., Fabrication and characterization of Fe81Ga19 thin films *IEEE Trans. Magn.* **38** 2832–4, 2002.

[ApI.5.1.2] Georgieva, M.T., Telling, N.D., Grundy, P.J., Faunce, C.A., Jones, G.A., 2004, Magnetically soft, high moment grain-refined Fe films: application to magnetic tunnel junctions, Journal of Applied Physics, **96** (5) pp. 2923-2926

[ApI.6.1.1] McClure, A., Li, H., and Idzerda, Y.U., Magnetostrictive effect in single crystal $Fe_{1-x}Ga_x$ thin films, J. Appl. Phys. **107**, 09A924, 2010.

[ApI.6.1.2] Weston, J.L., Butera, A., Lograsso, T.A., Shamsuzzoha, M., Zana, I., Zangari G., Barnard J., Fabrication and characterization of Fe81Ga19 thin films *IEEE Trans. Magn.* **38** 2832–4, 2002.

[ApI.6.1.3] Khare, C., Gerlach, J.W., Höche, T., Buhrmann, B., Leipner, H.S., Rauschenbach, B., Effects of annealing on arrays of Ge nanocolumns formed by glancing angle deposition, Appl. Surf. Sci.258, pp9762-9769, 2012.

Appendix II: ICSD Generated X-Ray Diffraction Patterns

ApII.1 ICSD X-Ray Diffraction Patterns for Galfenol Alloys (using Cu-Kα)

The following generated diffraction patterns of X-ray diffraction data have been produced by the ICSD database for help with the identification of Fe-rich Galfenol alloys. They are presented in historical order from 1960 up to the present day; there are a total of 21 different patterns for the Galfenol phase diagram but here only the patterns with a greater ratio of Fe to Ga are given. These patterns have been used in this work as the reference patterns fitted to the patterns generated by the real x-ray diffraction data; this is in addition to the complete Powder diffraction file-2 (PDF-2) from the International Centre for Diffraction Data (ICDD). The data from these sources provides an indication of the crystal structure, the d-spacing and have been used in the calculation of the lattice parameters of each structure in this work. The relative intensities of the peaks within the diffraction patterns gives an indication of the amount of each phase present in multi-phase structures and these parameters are used by the Crystal Match! software to help quantify the experimental data. The peak data was also indexed manually in order to verify the computer generated fit.

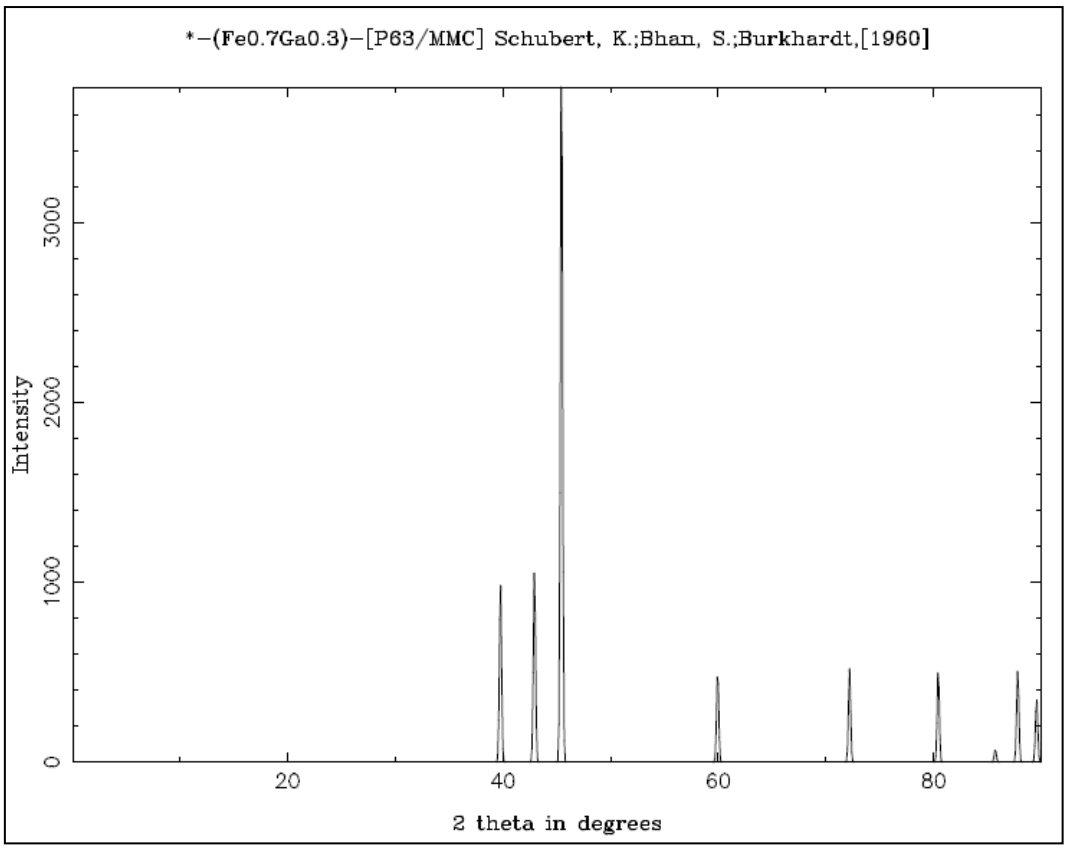

Figure ApII.1.1.1 - Schubert, K., Bhan, S., Burkhardt, S., D019 hcp structure [ApII.1.1.1]

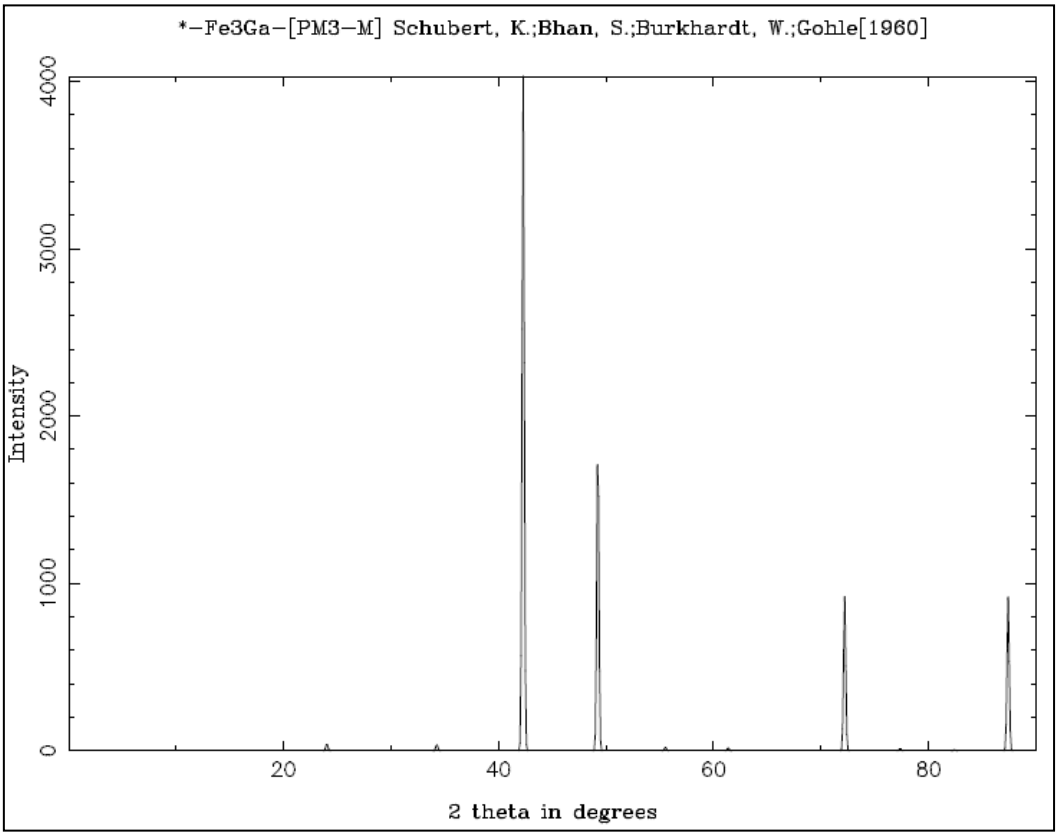

Figure ApII.1.1.2 - Schubert, K., Bhan, S., Burkhardt, S., Gohle, W., Primitive L12-like fcc structure [ApII.1.1.2]

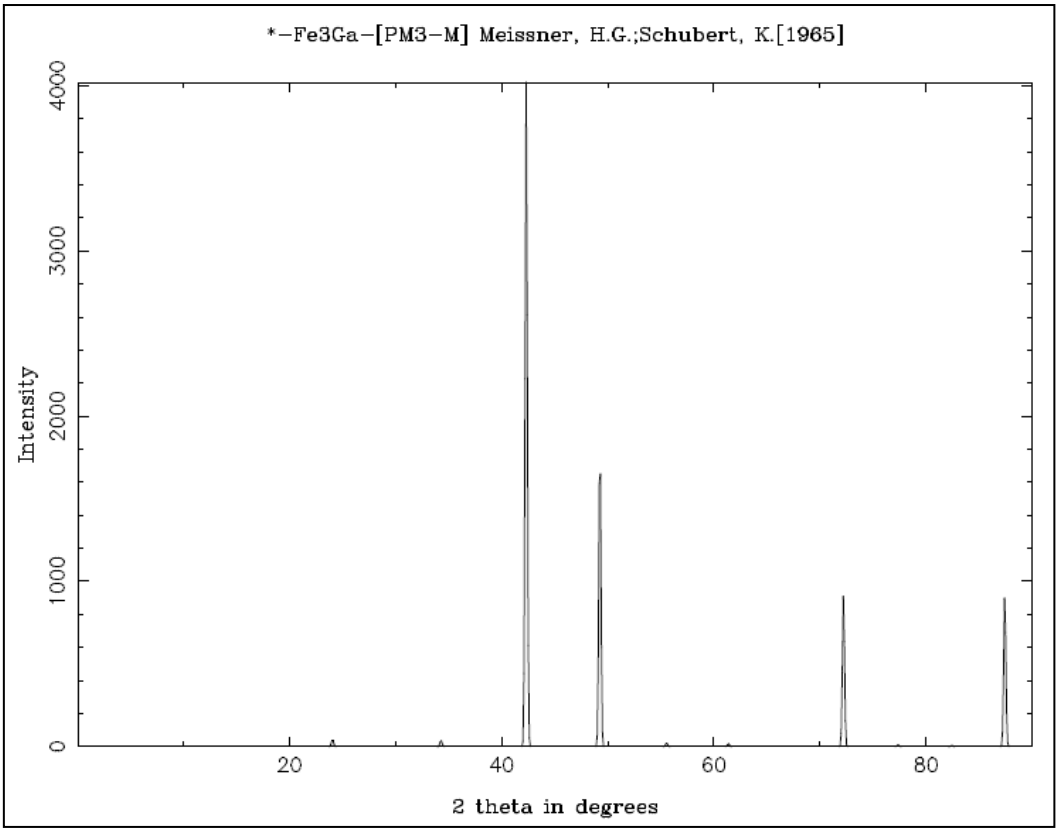

Figure Ap.II.1.1.3 - Meissner, H.G., Schubert, K., Primitive L12-like fcc structure [ApII.1.1.3]

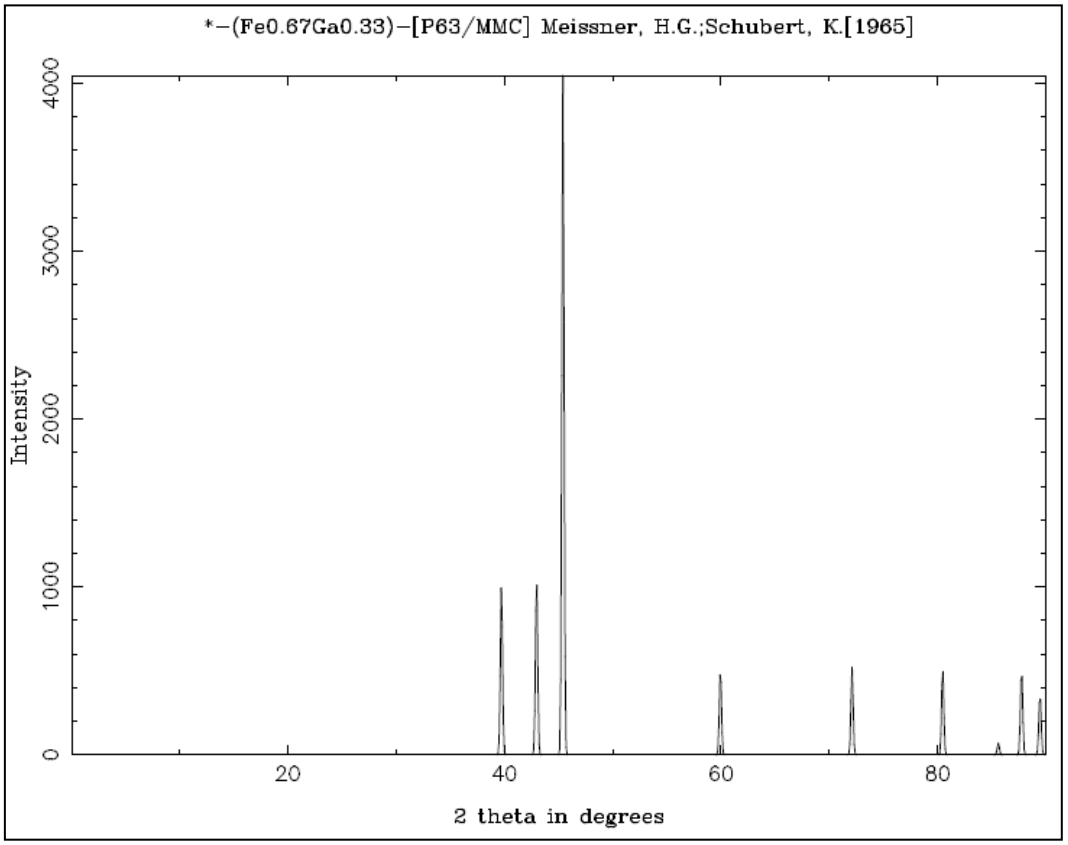

Figure Ap.II.1.1.4 - Meissner, H.G., Schubert, K., D019 hcp structure [ApII.1.1.4]

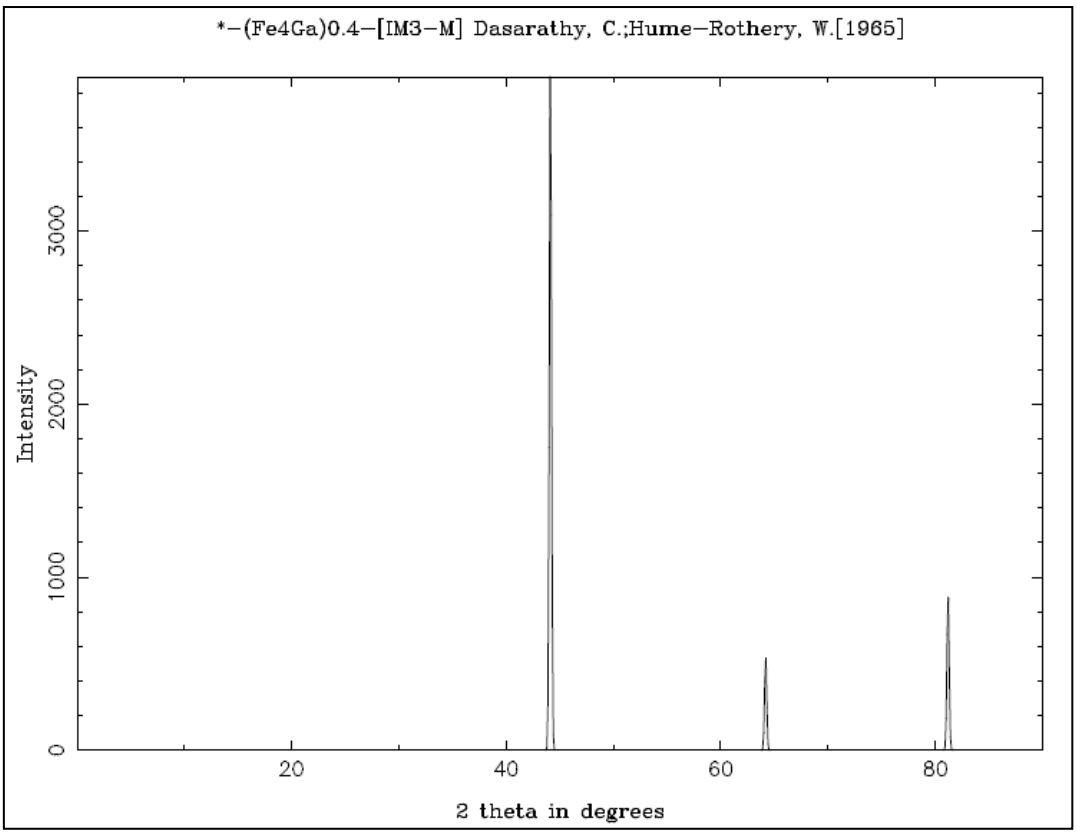

Figure ApII.1.1.5 - Dasarathy, C., Hume-Rothery, W., A2 disordered bcc structure [ApII.1.1.5]

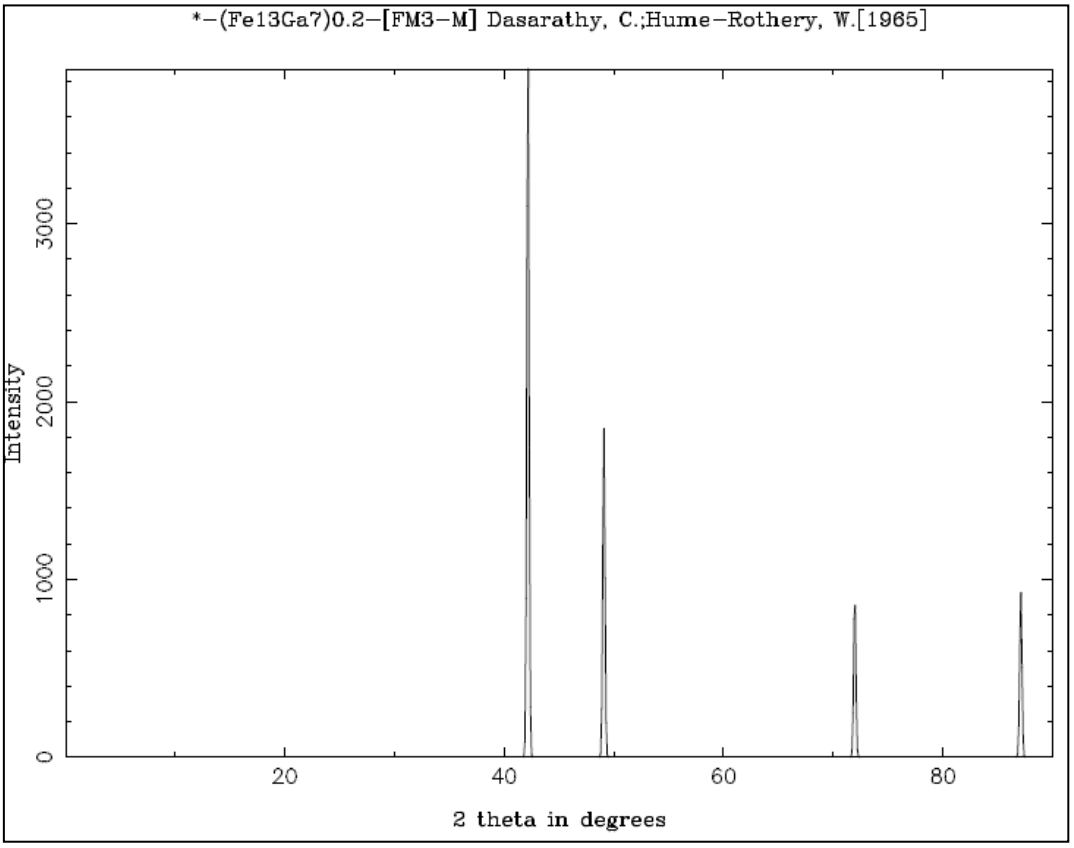

Figure ApII.1.1.6 -Dasarathy, C., Hume-Rothery, W., L12 disordered fcc structure [ApII.1.1.6]

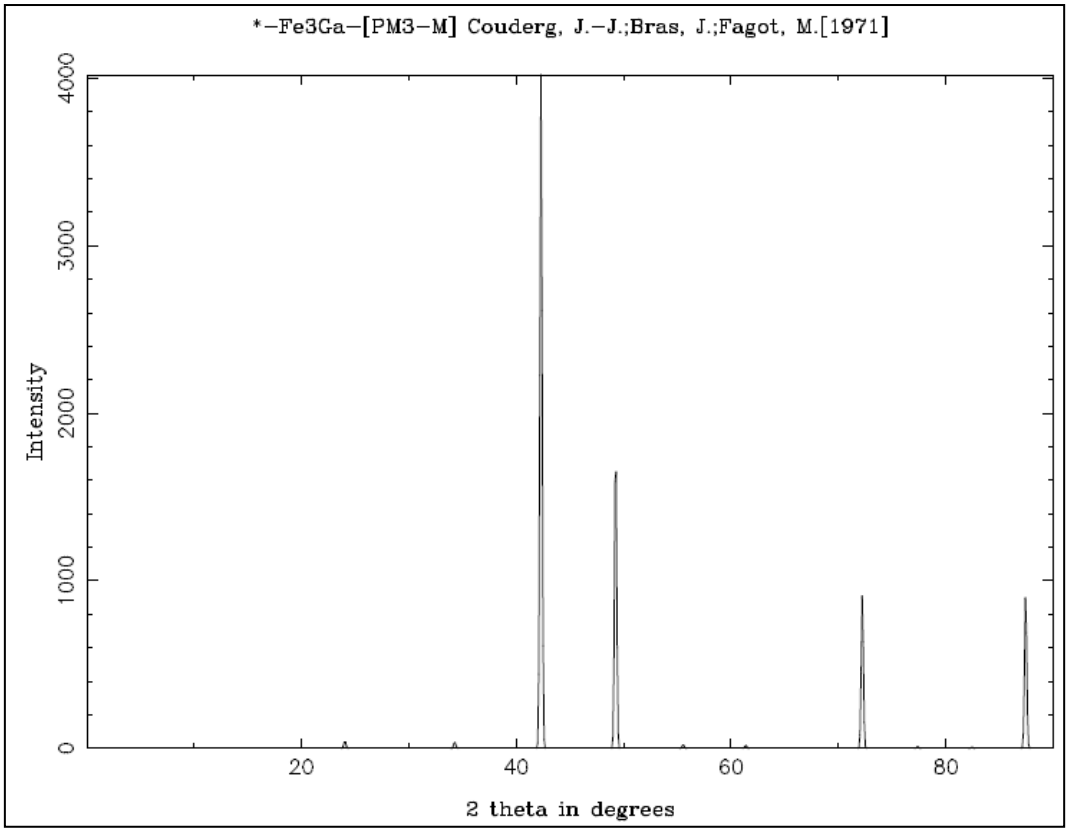

Figure ApII.1.1.7 - Couderg, J-J., Bras, J., Fagot, M., Primitive fcc structure (L12-like) [ApII.1.1.7]

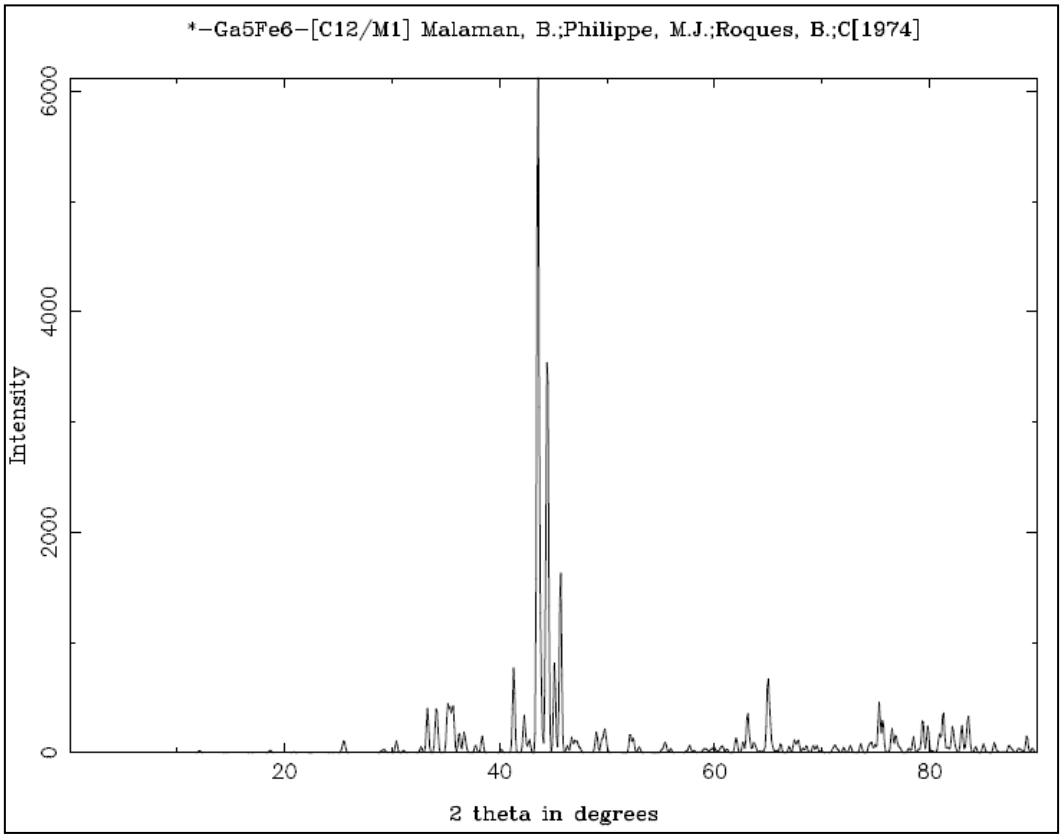

Figure ApII.1.1.8 – Malaman, B., Philppe, M.J., Roques, B., Monoclinic structure of ~45 at. % Ga [ApII.1.1.8]

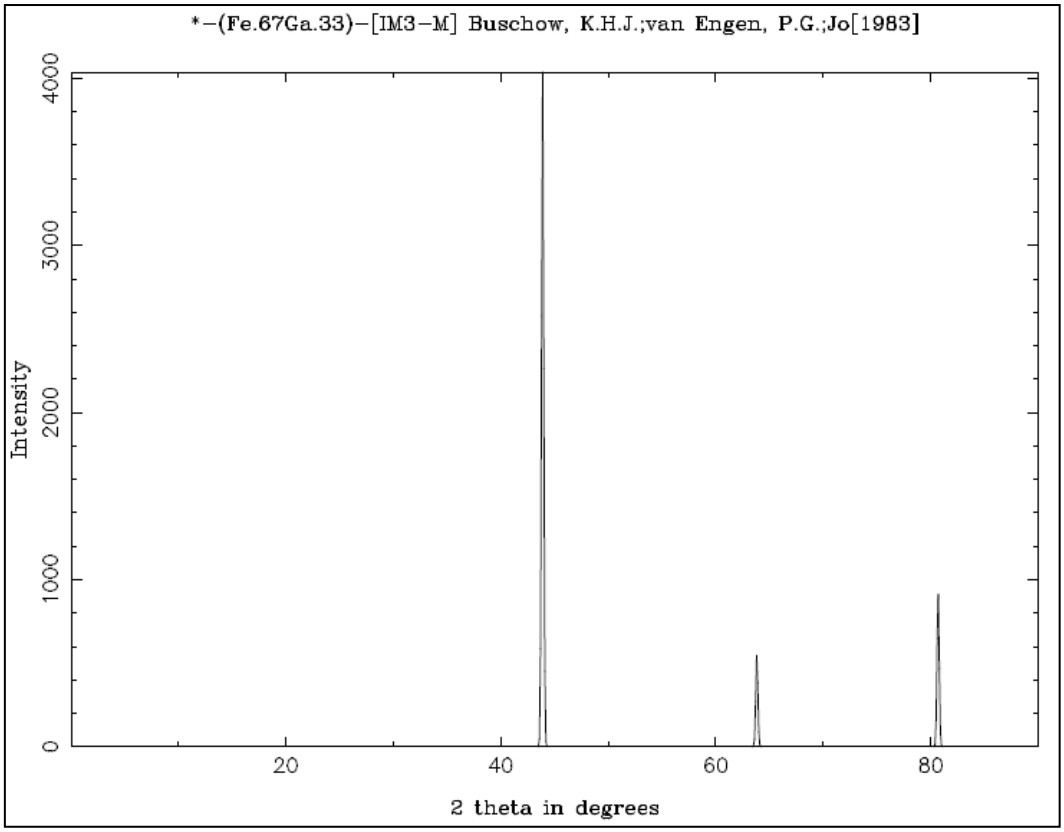

Figure ApII.1.1.9 - Buschow, K.H.J., van Engen, P.G., Jongebreur, R., A2 disordered bcc structure 33.3 at. % Ga [ApII.1.1.9]

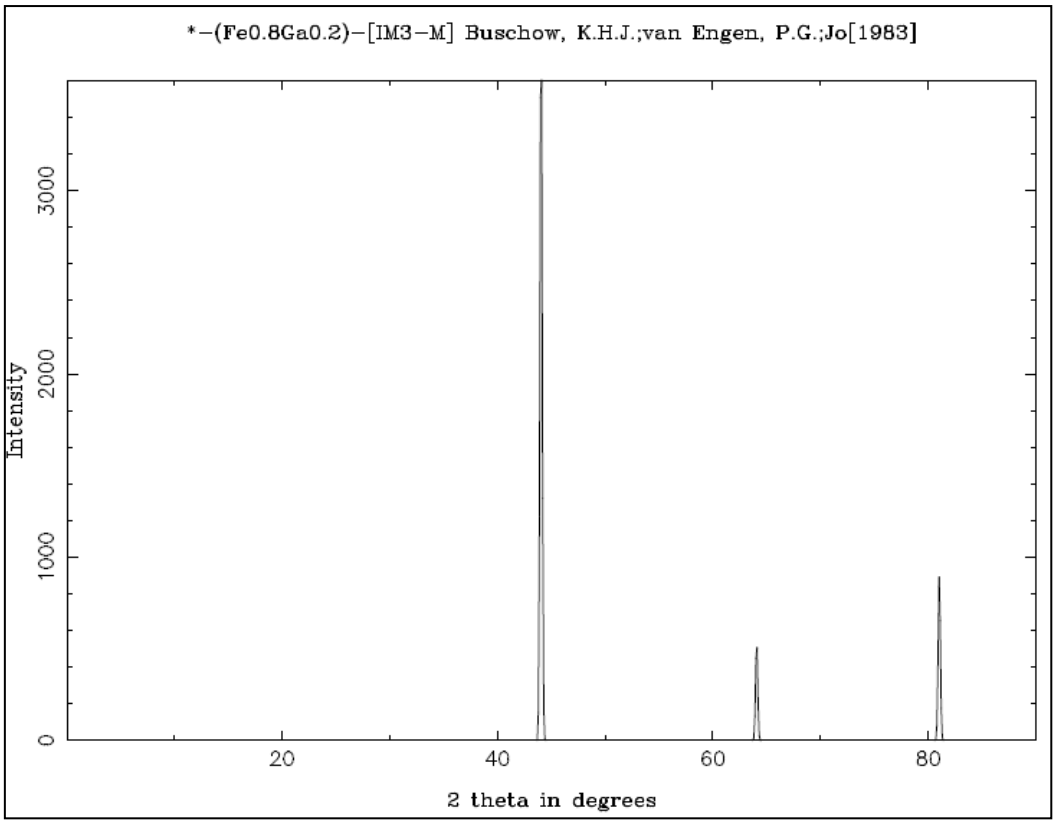

Figure ApII.1.1.10 - Buschow, K.H.J., van Engen, P.G., Jongebreur, R., A2 disordered bcc structure of 20 at. % Ga [ApII.1.1.10]

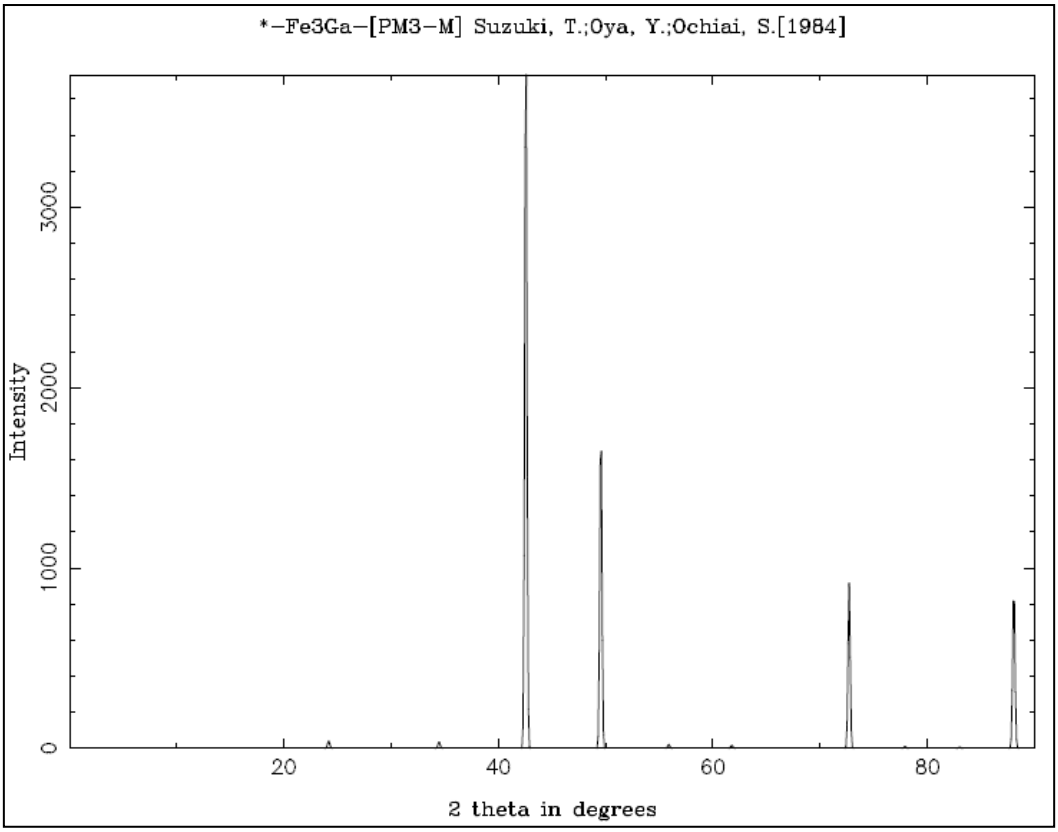

Figure ApII.1.1.11 - Suzuki, T., Oya, Y., Ochia, S., Primitive L12-like fcc structure [ApII.1.1.11]

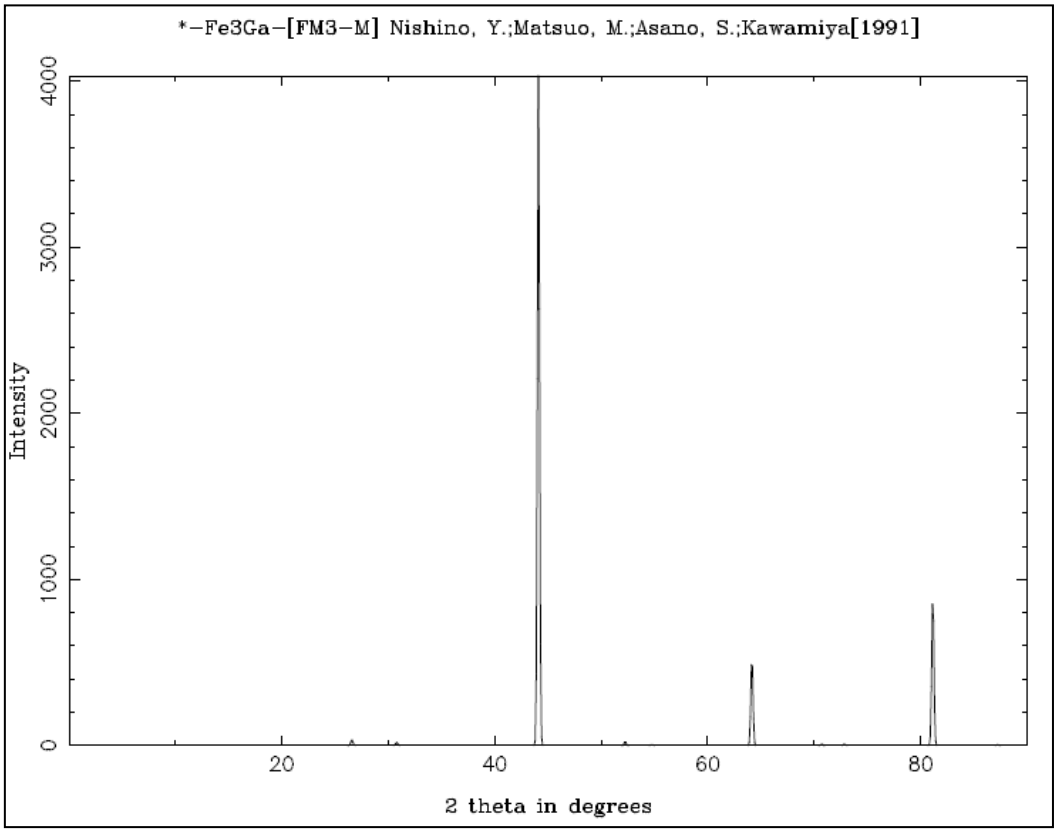

Figure ApII.1.1.12 - Nishino, Y., Matsuo, M., Asano, S., Kawamiya, N., Ordered D03 structure [ApII.1.1.12]

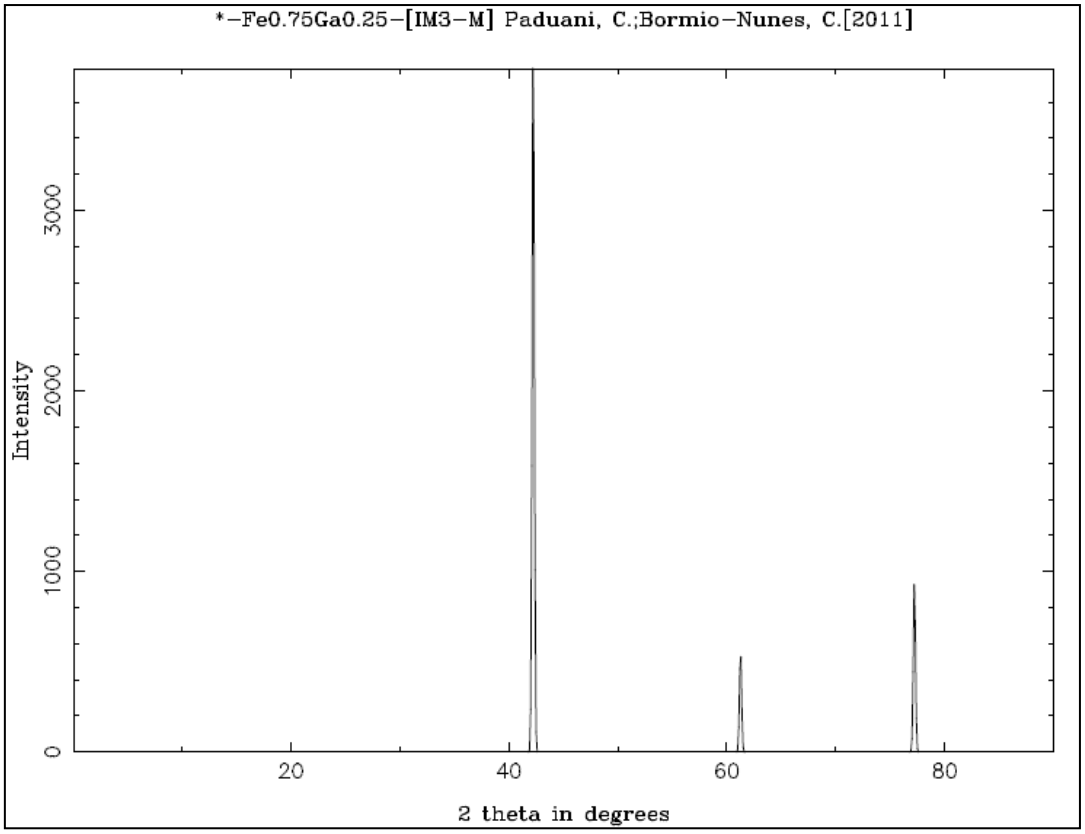

Figure ApII.1.1.13 - Paduani, C., Bormio-Nunes, C., A2 disordered bcc with enlarged unit cell [ApII.1.1.13]

Ap.II.2 Appendix II References

[ApII.1.1.1] Schubert, K.;Bhan, S.;Burkhardt, W.;Gohle, R.;Meissner, H.G.;Poetzschke, M.;Stolz, E., Einige strukturelle Ergebnisse an metallischen Phasen (5), Naturwissenschaften **47**, 303, 1960.

[ApII.1.1.2] Schubert, K.;Bhan, S.;Burkhardt, W.;Gohle, R.;Meissner, H.G.;Poetzschke, M.;Stolz, E., Einige strukturelle Ergebnisse an metallischen Phasen (5), Naturwissenschaften **47**, 303, 1960.

[Ap.1.1.3] Meissner, H.G.;Schubert, K., Zum Aufbau einiger zu T(5)-Ga homologer und quasihomologer Systeme. II. Die Systeme Cr-Ga, Mn-Ga und Fe-Ga sowie einige Bemerkungen zm Aufbau der Systeme V-Sb und V-As, Zeitschrift fuer Metallkunde **56**, 523-530, 1965.

[Ap.1.1.4] Meissner, H.G.;Schubert, K., Zum Aufbau einiger zu T(5)-Ga homologer und quasihomologer Systeme. II. Die Systeme Cr-Ga, Mn-Ga und Fe-Ga sowie einige Bemerkungen zm Aufbau der Systeme V-Sb und V-As, Zeitschrift fuer Metallkunde **56**, 523-530, 1965.

[ApII.1.1.5] Dasarathy, C.;Hume-Rothery, W., The system iron-gallium, Proceedings of the Royal Society of London, Series A Mathematical and Physical Sciences **286**, 141-157, 1965.

[ApII.1.1.6] Dasarathy, C.;Hume-Rothery, W., The system iron-gallium, Proceedings of the Royal Society of London, Series A Mathematical and Physical Sciences **286**, 141-157, 1965.

[ApII.1.1.7] Couderg, J.-J.;Bras, J.;Fagot, M., Etude de la structure ordonee de l'alliage Fe3Ga, Comptes Rendus Hebdomadaires des Seances de l'Academie des Sciences, Serie B **272**, 781-784, 1971.

[ApII.1.1.8] Malaman, B.;Philippe, M.J.;Roques, B.;Courtois, A.;Protas, J., Structures cristallines des phases Fe6 Ge5

et Fe6 Ga5, Acta Crystallographica B **30**, pp2081-2087, 1974.

[ApII.1.1.9] Buschow, K.H.J., van Engen, P.G., Jongebreur, R., Magneto-optical properties of metallic ferromagnetic materials, Journal of Magnetism and Magnetic Materials, Volume **38**, Issue **1**, Pages 1-22, 1983.

[ApII.1.1.10] Buschow, K.H.J., van Engen, P.G., Jongebreur, R., Magneto-optical properties of metallic ferromagnetic materials, Journal of Magnetism and Magnetic Materials, Volume **38**, Issue **1**, Pages 1-22, 1983.

[ApII.1.1.11] Suzuki, T.;Oya, Y.;Ochiai, S., The mechanical behaviour of nonstoichiometric compounds Ni3Si, Ni3Ge, and Ni3Ga, Golden Book of Phase Transitions, Wroclaw **1**, pp1-123, 2002 & Metallurgical Transactions A: Physical Metallurgy and Materials Science **15**, 173-181, 1984.

[ApII.1.1.12] Nishino, Y., Matsuo, M., Asano, S., Kawamiya, N., Stability of the DO3 phase in $(Fe_{1-x}M_x)3Ga$ (M; 3d transition metals), Scripta Metallurgica et Materialia, Volume **25**, Issue **10**, pp2291-2296, 1991.

[ApII.1.1.13] Paduani, C.;Bormio-Nunes, C., Ab initio study of electronic and magnetic properties of the Fe3Zn intermetallic, Physica B: Condensed Matter **406**, pp1752-1756, 2011.

Appendix III: Crystal Match! Generated Reports for Galfenol 12.8, 17.5, 19.5, 22.5 and 27.5 at. % Ga

ApIII.1 Crystal Match Report for 12.8 at. % Ga

##

Match! Phase Analysis Report

##

Licensee: Christopher Quinn

Sample : FeGa 12.8%

********** Sample Data **********

File name : 12.8.raw

File path : C:\XRD

Data collected: 09/23/10

Data range : 4.000° to 90.000°

No. of points : 2151

Step size : 0.040

Alpha2 subtr.?: Yes

Backgr.subtr.?: Yes

Data smoothed?: Yes

Radiation : Cu-Ka

Wavelength : 1.541874 A

********** Matched Phases**********

Phase A: Iron gallium (1.6/0.4)

Formula sum : Fe1.6 Ga0.4

Entry number : 99-500-0014

FoM : 0.813896

No. of peaks : 4

Peaks in range : 3

Peaks matched : 3

Int. scale fct : 1.00

Quant. (weight %): 100.00

********** Other Candidates **********

Name	Formula	Entry No.	FoM
Iron gallium (3/1)	Fe3 Ga1	99-500-000	0.697540
Fe	Fe	99-500-0000	0.770131

********** Search-Match**********

Settings:

Profile data used? : Yes

Automatic zeropoint adaptation? : Yes

Minimum figure-of-merit (FoM) : 0.685

Parameter/influence 2theta : 0.50

Parameter/influence intensities : 0.50

Parameter multiple/single phase(s): 0.50

********** Peak List**********

Wavelength used for calculation of 2theta values: lambda = 1.541874 A

d[A]	2theta[°]	Int.	FWHM	Matched
2.0440	44.3175	1000.00	0.3200	Yes
1.4458	64.4492	220.18	0.3200	Yes
1.1812	81.4853	270.88	0.3200	Yes

********** Copyright **********

********** **********

ApIII.2 Crystal Match Report for 17.5 at. % Ga

##

Match! Phase Analysis Report

##

Licensee: Christopher Quinn

Sample : FeGa 17.5

********** Sample Data**********

File name : 17-5.raw

File path : c:\XRD

Data collected: 09/23/10

Data range : 4.000° to 90.000°

No. of points : 2151

Step size : 0.040

Alpha2 subtr.?: Yes

Backgr.subtr.?: Yes

Data smoothed?: Yes

Radiation : Cu-Ka

Wavelength : 1.541874 A

********** Matched Phases**********

Phase A: Iron gallium (1.6/0.4)

Formula sum : Fe1.6 Ga0.4

Entry number : 99-500-0014

FoM : 0.819128

No. of peaks : 5

Peaks in range : 3

Peaks matched : 3

Int. scale fct : 1.00

Quant. (weight %): 100.00

********** Candidates**********

Name	Formula	Entry No.	FoM
Iron gallium (3/1)	Fe3 Ga1	99-500-000	0.743502
Iron gallium (0.8/0.2)	Fe0.8 Ga0.2	99-500-000	0.652844

********** Search-Match**********

Settings:

Profile data used? : Yes

Automatic zeropoint adaptation? : Yes

Minimum figure-of-merit (FoM) : 0.60

Parameter/influence 2theta : 0.50

Parameter/influence intensities : 0.50

Parameter multiple/single phase(s): 0.50

********** Peak List**********

Wavelength used for calculation of 2theta values: lambda = 1.541874 A

d[A]	2theta[°]	Int.	FWHM	Matched
2.0492	44.2991	1000.00	0.3200	Yes
1.4472	64.3783	272.80	0.3200	Yes
1.1828	81.3574	330.35	0.3200	Yes

********** Copyright**********

ApIII.3 Crystal Match Report for 19.5 at. % Ga

##

Match! Phase Analysis Report

##

********** Sample Data**********

File name : 19-5m-2.raw

File path : c:\XRD

Data collected: 09/26/10

Data range : 4.000° to 90.000°

No. of points : 2151

Step size : 0.040

Alpha2 subtr.?: Yes

Backgr.subtr.?: Yes

Data smoothed?: Yes

Radiation : Cu-Ka

Wavelength : 1.541874 A

********** Matched Phases**********

Phase A: Iron gallium (0.8/0.2)

Formula sum : Fe0.8 Ga0.2

Entry number : 99-500-000

FoM : 0.811555

No. of peaks : 4

Peaks in range : 3

Peaks matched : 3

Int. scale fct : 1.00

Quant. (weight %): 100.00

********** Candidates**********

Name	Formula	Entry No.	FoM
Iron gallium (3/1)	Fe3 Ga1	99-500-000	0.724854
Iron gallium (1.6/0.4)	Fe1.6 Ga0.4	99-500-0014	0.645713

********** Search-Match**********

Settings:

Profile data used? : Yes

Automatic zeropoint adaptation? : Yes

Minimum figure-of-merit (FoM) : 0.60

Parameter/influence 2theta : 0.50

Parameter/influence intensities : 0.50

Parameter multiple/single phase(s): 0.50

********** Peak List**********

Wavelength used for calculation of 2theta values: lambda = 1.541874 A

d[A]	2theta[°]	Int.	FWHM	Matched
2.0537	44.1405	1000.00	0.2400	Yes
1.4513	64.1742	316.28	0.2400	Yes
1.1857	81.1108	329.93	0.2400	Yes

********** Copyright**********

ApIII.4 Crystal Match Report for 22.5 at. % Ga

##

Match! Phase Analysis Report

##

Licensee: Christopher Quinn

Sample : FeGa 22.5

********** Sample Data**********

File name : 22-5s.raw

File path : c:\XRD

Data collected: 09/24/10

Data range : 4.000° to 90.000°

No. of points : 2151

Step size : 0.040

Alpha2 subtr.?: Yes

Backgr.subtr.?: Yes

Data smoothed?: Yes

Radiation : Cu-Ka

Wavelength : 1.541874 A

********** Matched Phases**********

Phase A: Iron gallium (1.6/0.4)

Formula sum : Fe1.6 Ga0.4

Entry number : 99-500-0014

FoM : 0.840545

No. of peaks : 4

Peaks in range : 3

Peaks matched : 3

Int. scale fct : 1.00

Quant. (weight %): 100.00

********** Candidates**********

Name	Formula	Entry No.	FoM
Iron gallium (3/1)	Fe3 Ga1	99-500-000	0.740960
Iron gallium (0.8/0.2)	Fe0.8 Ga0.2	99-500-000	0.682089

********** Search-Match**********

Settings:

Profile data used? : Yes

Automatic zeropoint adaptation? : Yes

Minimum figure-of-merit (FoM) : 0.60

Parameter/influence 2theta : 0.50

Parameter/influence intensities : 0.50

Parameter multiple/single phase(s): 0.50

********** Peak List**********

Wavelength used for calculation of 2theta values: lambda = 1.541874 A

d[A]	2theta[°]	Int.	FWHM	Matched
2.0596	44.1902	1000.00	0.3200	Yes
1.4584	64.2049	173.80	0.3200	Yes
1.1883	81.1614	291.24	0.3200	Yes

********** Copyright**********

ApIII.5 Crystal Match Report for 27.5 at. % Ga

##

Match! Phase Analysis Report

##

Licensee: Christopher Quinn

Sample : FeGa 27.5

********** Sample Data**********

File name : 27-5.raw

File path : c:\XRD

Data collected: 09/23/10

Data range : 4.250° to 90.250°

No. of points : 2151

Step size : 0.040

Alpha2 subtr.?: Yes

Backgr.subtr.?: Yes

Data smoothed?: Yes

2theta corr. : 0.25000

Radiation : Cu-Ka

Wavelength : 1.541874 A

********** Matched Phases**********

Phase A: Iron gallium (1.6/0.4)

Formula sum : Fe1.6 Ga0.4

Entry number : 99-500-0014

FoM : 0.798619

No. of peaks : 5

Peaks in range : 4

Peaks matched : 3

Int. scale fct : 1.00

Quant. (weight %): 100.00

********** Candidates**********

Name	Formula	Entry No.	FoM
Iron gallium (3/1)	Fe3 Ga1	99-500-000	0.700205
Iron gallium (0.8/0.2)	Fe0.8 Ga0.2	99-500-000	0.661459

********** Search-Match**********

Settings:

Profile data used? : Yes

Automatic zeropoint adaptation? : Yes

Minimum figure-of-merit (FoM) : 0.60

Parameter/influence 2theta : 0.50

Parameter/influence intensities : 0.50

Parameter multiple/single phase(s): 0.50

********** Peak List **********

Wavelength used for calculation of 2theta values: lambda = 1.541874 A

d[A]	2theta[°]	Int.	FWHM	Matched
2.0465	44.2600	1000.00	0.2400	Yes
1.4671	64.2164	141.00	0.2400	Yes
1.1925	81.1528	305.65	0.2400	Yes

********** Copyright**********

ApIII.6 Crystal Match Report for 19.5 at. % Ga (1000°C Annealed-Quenched)

##

Match! Phase Analysis Report

##

Licensee: Christopher Quinn

Sample : FeGa ref:19.5AQ

********** Sample Data**********

File name : 19_5-AQ.raw

File path : c:\XRD

Data collected: 07/28/10

Data range : 4.000° to 90.000°

No. of points : 4301

Step size : 0.040

Alpha2 subtr.?: Yes

Backgr.subtr.?: Yes

Data smoothed?: Yes

Radiation : Cu-Ka

Wavelength : 1.541874 A

********** Matched Phases**********

Phase A: Iron gallium (0.8/0.2)

Formula sum : Fe0.8 Ga0.2

Entry number : 99-500-000

FoM : 0.780504

No. of peaks : 4

Peaks in range : 3

Peaks matched : 3

Int. scale fct : 1.00

Quant. (weight %): 100.00

********** Candidates**********

Name	Formula	Entry No.	FoM
Iron gallium (3/1)	Fe3 Ga1	99-500-000	0.701586
Iron gallium (1.6/0.4)	Fe1.6 Ga0.4	99-500-0014	0.621191

********** Search-Match**********

Settings:

Profile data used? : Yes

Automatic zeropoint adaptation? : Yes

Minimum figure-of-merit (FoM) : 0.60

Parameter/influence 2theta : 0.50

Parameter/influence intensities : 0.50

Parameter multiple/single phase(s): 0.50

********** Peak List**********

Wavelength used for calculation of 2theta values: lambda = 1.541874 A

d[A]	2theta[°]	Int.	FWHM	Matched
2.0568	44.0273	1000.00	0.3200	Yes
1.4543	64.0237	634.88	0.3200	Yes
1.1872	80.9863	375.27	0.3200	Yes

**********Copyright**********

ApIII.7 Crystal Match Report for 27.5 at. % Ga (1000°C Annealed-Quenched)

##

Match! Phase Analysis Report

##

Licensee: Christopher Quinn

Sample : FeGa 27.5 (5)

********** Sample Data**********

File name : fega27.5% annealed-quenched 27_5_5.raw

File path : c:\XRD

Data collected: 10/21/10

Data range : 3.990° to 90.990°

No. of points : 4301

Step size : 0.040

Alpha2 subtr.?: Yes

Backgr.subtr.?: Yes

Data smoothed?: Yes

2theta corr. : -0.01000

Radiation : Cu-Ka

Wavelength : 1.541874 A

********** Matched Phases**********

Phase A: Iron gallium (0.8/0.2)

Formula sum : Fe0.8 Ga0.2

Entry number : 99-500-000

FoM : 0.794178

No. of peaks : 4

Peaks in range : 3

Peaks matched : 3

Int. scale fct : 1.00

Quant. (weight %): 100.00

********** Candidates**********

Name	Formula	Entry No.	FoM
Iron gallium (3/1)	Fe3 Ga1	99-500-000	0.661750

********** Search-Match**********

Settings:

Profile data used? : Yes

Automatic zeropoint adaptation? : Yes

Minimum figure-of-merit (FoM) : 0.60

Parameter/influence 2theta : 0.50

Parameter/influence intensities : 0.50

Parameter multiple/single phase(s): 0.50

********** Peak List**********

Wavelength used for calculation of 2theta values: lambda = 1.541874 A

d[A]	2theta[°]	Int.	FWHM	Matched
2.0691	43.793	1000.00	0.2000	Yes
1.4543	64.0261	100.51	0.2000	Yes
1.1869	81.0125	525.45	0.2000	Yes

********** Copyright**********

ApIII.8 Crystal Match Report for 27.5 at. % Ga (500°C) Annealed-Quenched)

##

Match! Phase Analysis Report

##

Licensee: Christopher Quinn

Sample : FeGa 27.5 AQ (heated to 500°C water quenched)

********** Sample Data**********

File name : fega27.5 quenched from 500c.raw

File path : c:\XRD

Data collected: 04/25/12

Data range : 35.000° to 89.998°

No. of points : 6009

Step size : 0.005

Alpha2 subtr.?: Yes

Backgr.subtr.?: Yes

Data smoothed?: Yes

Radiation : Cu-Ka

Wavelength : 1.541874 A

********** Matched Phases**********

Phase A: Iron gallium (3/1)

Formula sum : Fe3 Ga1

Entry number : 99-500-0011

FoM : 0.956433

No. of peaks : 15

Peaks in range : 7

Peaks matched : 4

Int. scale fct : 0.95

Quant. (weight %): 100.00

********** Search-Match**********

Settings:

Profile data used? : Yes

Automatic zeropoint adaptation? : Yes

Minimum figure-of-merit (FoM) : 0.60

Parameter/influence 2theta : 1.00

Parameter/influence intensities : 0.00

Parameter multiple/single phase(s): 0.00

********** Peak List**********

Wavelength used for calculation of 2theta values: lambda = 1.541874 A

d[A]	2theta[°]	Int.	FWHM	Matched
2.4770	36.2678	42.15	0.3845	No
2.1282	42.4769	1000.00	0.1990	Yes
1.8425	49.4686	390.54	0.3845	Yes
1.3021	72.6109	80.25	0.1282	Yes
1.1098	88.0055	68.54	0.1282	Yes

********** Copyright **********

ApIII.9 Crystal Match Report for 27.5 at. % Ga (650°C) Annealed-Quenched)

##

Match! Phase Analysis Report

##

Licensee: Christopher Quinn

Sample : FeGa 27.5 Annealed-Quenched 650oC

********** Sample Data**********

File name : fega27.5 quenched from 650.raw

File path : c:\XRD

Data collected: 05/08/12

Data range : 9.980° to 89.978°

No. of points : 8740

Step size : 0.005

Alpha2 subtr.?: Yes

Backgr.subtr.?: Yes

Data smoothed?: Yes

2theta corr. : -0.02000

Radiation : Cu-Ka

Wavelength : 1.541874 A

********** Matched Phases**********

Phase A: Iron gallium (0.8/0.2)

Formula sum : Fe0.8 Ga0.2

Entry number : 99-500-000

FoM : 0.846350

No. of peaks : 4

Peaks in range : 3

Peaks matched : 3

Int. scale fct : 0.42

Quant. (weight %): 36.61

Phase B: Iron gallium (3/1)

Formula sum : Fe3 Ga1

Entry number : 99-500-000

FoM : 0.757399

No. of peaks : 14

Peaks in range : 6

Peaks matched : 3

Int. scale fct : 0.43

Quant. (weight %): 36.83

Phase C: Iron gallium (0.7/0.3) - HT

Formula sum : Fe0.7 Ga0.3

Entry number : 99-500-000

FoM : 0.648948

No. of peaks : 13

Peaks in range : 7

Peaks matched : 4

Int. scale fct : 0.21

Quant. (weight %): 26.56

********** Candidates**********

Name	Formula	Entry No.	FoM
Gallium iron (5/6)	Fe6 Ga5	99-500-0021	0.746149
Iron gallium (1/3)	Fe1 Ga3	99-500-0019	0.692931
Iron gallium (1/3)	Fe1 Ga3	99-500-0016	0.692002
Gallium iron (4/3)	Fe3 Ga4	99-500-0020	0.662704

********** Search-Match**********

Settings:

Profile data used? : Yes

Automatic zeropoint adaptation? : Yes

Minimum figure-of-merit (FoM) : 0.60

Parameter/influence 2theta : 0.50

Parameter/influence intensities : 0.50

Parameter multiple/single phase(s): 0.50

********** Peak List**********

Wavelength used for calculation of 2theta values: lambda = 1.541874 A

d[A]	2theta[°]	Int.	FWHM	Matched
2.2534	40.0120	82.18	0.0915	Yes
2.1160	42.7342	43.33	0.0915	Yes
2.0518	44.1392	421.11	0.0915	Yes
1.9917	45.5442	201.15	0.0915	Yes
1.5431	59.9455	68.06	0.0915	Yes
1.4533	64.0727	144.62	0.0915	Yes
1.3037	72.5027	81.18	0.0915	Yes
1.1954	80.3181	45.16	0.0915	Yes
1.1868	81.0206	175.11	0.0915	Yes
1.1102	87.9578	25.78	0.0915	Yes

********** Copyright**********

ApIII.10 Crystal Match Report for 27.5 at. % Ga (800°C) (Annealed-Furnace-Cooled)

##

Match! Phase Analysis Report

##

Licensee: Christopher Quinn

Sample : FeGa 27.5 Annealed to 800C and Furnace-Cooled

********** Sample Data**********

File name : fega27.5% annealed 800-furnace cooled 27_5_8.raw

File path : c:\XRD

Data collected: 18/08/12

Data range : 4.000° to 90.000°

No. of points : 4301

Step size : 0.020

Alpha2 subtr.?: Yes

Backgr.subtr.?: Yes

Data smoothed?: Yes

Radiation : Cu-Ka

Wavelength : 1.541874 A

********** Matched Phases**********

Phase A: Iron gallium (3/1)

Formula sum : Fe3 Ga1

Entry number : 99-500-0011

FoM : 0.928532

No. of peaks : 15

Peaks in range : 10

Peaks matched : 4

Int. scale fct : 0.93

Quant. (weight %): 73.90

Phase B: Iron gallium (0.7/0.3) - HT

Formula sum : Fe0.7 Ga0.3

Entry number : 99-500-000

FoM : 0.843092

No. of peaks : 13

Peaks in range : 10

Peaks matched : 4

Int. scale fct : 0.30

Quant. (weight %): 26.10

********** Candidates**********

Name	Formula	Entry No.	FoM
Iron gallium (3/1)	Fe3 Ga1	99-500-0013	0.809696
Iron gallium (3/1)	Fe3 Ga1	99-500-0010	0.809696
Iron gallium (3/1)	Fe3 Ga1	99-500-0012	0.809693

********** Search-Match**********

Settings:

Profile data used? : Yes

Automatic zeropoint adaptation? : Yes

Minimum figure-of-merit (FoM) : 0.60

Parameter/influence 2theta : 0.50

Parameter/influence intensities : 0.50

Parameter multiple/single phase(s): 0.60

********** Peak List**********

Wavelength used for calculation of 2theta values: lambda = 1.541874 A

d[A]	2theta[°]	Int.	FWHM	Matched
2.1237	42.5707	1000.00	0.2240	Yes
1.9881	45.6326	296.58	0.1956	Yes
1.8397	49.5499	416.71	0.3714	Yes
1.3977	66.9501	49.26	0.7200	No
1.3031	72.5435	295.76	0.4127	Yes
1.1118	87.8048	222.05	0.4404	Yes

Appendix IV: Magnetic Units Conversion Table

TABLE 1. Conversion factors for Magnetic Quantities

Magnetic Term	Symbol	SI Unit	CGS Unit	Conversion Factor
Magnetic induction	B	tesla (T)	gauss (G)	1 T = 10^4 G
Magnetic field	H	A m^{-1}	oersted (Oe)	1 A m^{-1} = $4\pi \times 10^{-3}$ Oe
Magnetization	M	A m^{-1}	emu cm^{-3}	1 A m^{-1} = 10^{-3} emu cm^{-3}
Magnetic polarization	J	T	G	1 T = $10^4/4\pi$ emu cm^{-3}
Magnetic moment	m	A m^2	emu = G cm^3	1 A m^2 = 10^3 emu
Magnetic moment per unit mass	σ	A m^2 kg^{-1}	emu g^{-1}	1 A m^2 kg^{-1} = 1 emu g^{-1}
Volume magnetic susceptibility (κ=M/H)	κ	dimensionless	dimensionless	1(SI) = $1/4\pi$ (cgs)
Mass magnetic susceptibility ($\chi=\kappa/\rho$)	χ	m^3 kg^{-1}	emu Oe^{-1} g^{-1}	1 m^3 kg^{-1} = $10^3/4\pi$ emu Oe^{-1} g^{-1}
Molar magnetic susceptibility ($\chi_m=\chi M^*$)	χ_m	m^3 mol^{-1}	emu Oe^{-1} g^{-1} mol^{-1}	1 m^3 mol^{-1} = $10^6/4\pi$ emu $Oe^{-1}g^{-1}$ mol^{-1}
Magnetic permeability (μ=B/H)	μ	H m^{-1}	G Oe^{-1}	1 H m^{-1} = $10^7/4\pi$ G Oe^{-1}
Magnetic flux	Φ	Weber (Wb)	maxwell (Mx)	1 Wb = 10^8 Mx
Magnetic scalar potential; Magnetomotive force	ϕ	A	gilbert	1 A = $4\pi/10$ gilbert
Magnetic vector potential	A	Wb m^{-1}	emu = G cm	1 Wb m^{-1} = 10^6 emu
Magnetic pole strength	p	A m	emu = G cm^2	1 A m = 10 emu
Demagnetizing factor	N	dimensionless	dimensionless	1(SI) = 4π (cgs)
Magnetostriction constant	λ	dimensionless	dimensionless	1(SI) = 1(cgs)
Anisotropy constant Magnetostatic energy Energy product	K, K_1, K_u E_m $(BH)_{max}$	J m^{-3}	erg cm^{-3}	1 J m^{-3} = 10 erg cm^{-3}

A=ampere: H=Henry=Newton/Ampere: M^*=molecular weight: Tesla=Weber/m^2: ρ=density (1 kg/m^3=10^3 g/cm^3). Volume magnetic susceptibility in cgs units is sometimes given as emu cm^{-3} Oe^{-1} or G/Oe, both are dimensionless. Mass magnetic susceptibility in cgs units is sometimes given as emu g^{-1}, emu g^{-1} oe^{-1}, emu $g^{-1}G^{-1}$, G cm^3 g^{-1}, or cm^3 g^{-1}. The csg unit gamma $\gamma = 10^{-5}$ G = 10^{-9} T = 1 nanotesla (nT). The SI units are based on the Sommerfeld convention which gives the unit of magnetic moment as A m^2. The Kennelly convention gives the unit of magnetic moment as Wb m.

Table ApIV.1.1.1 - Magnetic Units Conversion Table [ApIV.1.1.1]

Appendix IV References

[ApIV.1.1.1] Crangle, J., The Magnetic Properties of Solids, Hodder-Arnold, 1977. ISBN:9780713125733

Appendix V: Published Journal Paper.

Journal of Magnetism and Magnetic Materials 324 (2012) 3817–3823

Contents lists available at SciVerse ScienceDirect

Journal of Magnetism and Magnetic Materials

journal homepage: www.elsevier.com/locate/jmmm

A Mössbauer spectroscopy and neutron diffraction study of magnetostrictive, melt-spun Fe–Ga alloy ribbons

N.J. Mellors [a], X. Zhao [b], L.M. Simmons [a], C.J. Quinn [a], S.H. Kilcoyne [c,*]

[a] Materials and Physics Research Centre, College of Science and Technology, University of Salford, Salford M5 4WT, UK
[b] Manchester Materials Science Centre, University of Manchester, Manchester M13 9PL, UK
[c] School of Applied Sciences, University of Huddersfield, Queensgate, Huddersfield HD1 3DH, UK

ARTICLE INFO

Article history:
Received 27 March 2012
Received in revised form
7 June 2012
Available online 28 June 2012

Keywords:
Melt spun FeGa alloy
Magnetostrictive alloy
Mössbauer spectroscopy
Neutron diffraction
Short-range order
Ferromagnetism

ABSTRACT

Ribbons of $Fe_{100-x}Ga_x$ ($x=15$, 17.5, 19.5 and 22.5) were prepared by rapid solidification from the melt. ^{57}Fe Mössbauer spectroscopy and high resolution neutron diffraction have revealed that $Fe_{100-x}Ga_x$ alloys with $x=15$ and 17.5 have the disordered bcc (A2) structure even after annealing, but the alloy with $x=19.5$ developed the short-range ordered DO_3 phase when annealed. The $x=22.5$ alloys showed mainly DO_3 phase with a fraction of bcc phase. A fraction of the bcc phase transformed into DO_3 phase and the long-range ordering of DO_3 phase was improved after annealing. ^{57}Fe Mössbauer spectra showed no observable $L1_2$ phase in any samples even though less than 1% volume of $L1_2$ phases has been found in the annealed samples by neutron diffraction. The additional absorption at hyperfine field of 25 T in $x=22.5$ samples was regarded as a result of imperfect DO_3 structure, rather than $L1_2$ phase.

1. Introduction

The iron–gallium alloy system $Fe_{100-x}Ga_x$ has attracted a great deal of attention over the last few years as a promising magnetostrictive material for sensor or actuator applications. The alloys exhibit superior magnetostrictive properties at low field, negligible magnetic hysteresis, high mechanical strength, and good ductility, and are of low cost [1–3]. Although the exact nature of this magnetostrictive behaviour is still to be understood, recent studies have suggested that there is a close correlation between the structure of these alloys and their resulting magnetostrictive performance [4–6]. Therefore in order to understand the origin of the magnetostrictive effect in Fe–Ga alloys, knowledge of both the phase constitutions and the short range ordering within these phases is required.

According to widely accepted literature, equilibrium and metastable phase diagrams suggest three possible phases in the $Fe_{100-x}Ga_x$ ($15<x\leq 30$) alloys. In the equilibrium phase diagram of bulk FeGa alloys, a disordered body-centred cubic (bcc) α-Fe (A2) phase, an ordered bcc (DO_3) phase and an ordered face-centred cubic (fcc) phase ($L1_2$) can exist [7], whilst the metastable phase diagram of single crystal samples indicates the possibility of the disordered A2 phase with Ga distributed at random, a B2 simple cubic structure with Fe or Ga occupying the centre position of the bcc structure randomly and the DO_3 phase, where the Ga occupies alternate centre positions [8]. Rapid cooling of $Fe_{100-x}Ga_x$ crystals with $18<x<21$ results in an alloy entirely in the A2 phase [9]. However, the phase formation after slow cooling is open to debate: Lograsso et al. established that bulk $Fe_{100-x}Ga_x$ alloys with $18<x<21$ and cooled at a rate of 2 °C/min exhibited a two-phase mixture of A2 and DO_3 [5] and a similar result was noted by Zhang et al. in $Fe_{81}Ga_{19}$ ribbons cooled at 1.29 °C/min [10]. However, in the same paper [10] a cooling rate in the range 0.43–0.26 °C/min was reported to result in the precipitation of an fcc phase into the A2 matrix. Such a result has also been noted by Zhao et al. in $Fe_{80.5}Ga_{19.5}$ ribbons slow cooled from 1000 °C [11].

Early work on FeGa crystals suggested that the local short-range ordering of the Ga atoms along <100> directions in rapidly quenched $Fe_{100-x}Ga_x$ bcc alloys near $x=19$ is responsible for the increase in magnetostriction and that the formation of the ordered DO_3 phase in annealed alloys or in those with higher Ga content results in a decrease in magnetostriction [1,12]. However, an alternative suggestion was put forward by Khachaturyan that magnetostriction in melt spun ribbons is a result of the reorientation of DO_3 precipitates in the bcc A2 matrix when an external field is applied [13].

Experimental confirmation of these hypotheses still remains a challenge [5,14] particularly as the phase diagram and the magnetostrictive behaviour of the alloys are strongly dependent on the form of the alloy (bulk, single crystal, thin film, melt spun

* Corresponding author. Tel.: +44 1484 472499.
E-mail address: s.h.kilcoyne@hud.ac.uk (S.H. Kilcoyne).

0304-8853/$ - see front matter © 2012 Elsevier B.V. All rights reserved.
http://dx.doi.org/10.1016/j.jmmm.2012.06.021

ribbon, etc.). It is difficult to confirm the $D0_3$ ordering in Fe–Ga alloys using standard diffraction techniques because, with the exception of the satellite peaks corresponding to the ordered superlattice structure, many of the peaks corresponding to both $D0_3$ and A2 phases overlap. In addition, the similarity in the atomic scattering factors of Fe and Ga in this system results in extremely weak superlattice reflections, making identification almost impossible using X-ray diffraction. High resolution neutron diffraction might be expected to give more informative results since the difference between the neutron scattering factors of Fe and Ga atoms is more pronounced and almost constant with the change of scanning angles [15]. The value of this technique in structural analysis has been proven to be significant [11]. Mössbauer spectroscopy, in contrast, is sensitive to short-range order, and is capable of distinguishing between ordered and disordered atomic structures. There is much experimental literature dating from the early 1970s reporting the use of ^{57}Fe Mössbauer spectroscopy for the investigation of Fe–Ga alloys [16–18]. However, in more recent studies of Fe–Ga alloys the benefit of using Mössbauer spectroscopy in the investigation of Ga–Ga pairing in the $D0_3$ phase of $Fe_{100-x}Ga_x$ alloys has been highlighted [19].

The formation of Ga–Ga clusters in FeGa alloys and the effect of these clusters on the alloys' magnetostrictive properties have been the subject of much debate. The presence of Ga clusters was proposed by Hall in 1957 as a possible explanation of the existence of strain in highly magnetostrictive FeGa alloys in the disordered A2 phase [20]. In 2004, Lui et al. [21] suggested that the magnetostriction in $Fe_{85}Ga_{15}$ ribbons was a result of the formation of Ga clusters within the ribbons, while Dunlap et al. [19] suggested that rapidly quenched samples of $Fe_{91.7}Ga_{8.3}$ showed a small amount of Ga–Ga pairing which increased significantly as the Ga concentration increase to ~20 at%. However, more recently Pascarelli et al. [22] have stated that their EXAFS and XANES studies show that Ga clustering does not occur in their melt spun $Fe_{80}Ga_{20}$ alloys. Instead they propose an approximately random substitution of Ga on Fe sites which introduces local strain, and hence the magnetostrictive behaviour observed in their ribbons. They also have evidence of strain inducing local defects in the form of second shell Ga–Ga pairs, and claim that their work supports the total energy calculations of Cullen et al. [23] that show that the large magnetostriction seen in these alloys is due to this strain. Clearly more work needs to be carried out in this area to resolve this dichotomy.

In the present work the extent to which the disordered bcc phase can be retained at room temperature by melt spinning and how this phase contributes to an increase of magnetostriction are explored using a combination of neutron diffraction and Mössbauer spectroscopy.

2. Experimental methods

Ingots of $Fe_{100-x}Ga_x$ with $x=15$, 17.5, 19.5 and 22.5 were prepared by co-melting the appropriate amounts of high purity (>99.9%) constituent elements in an argon arc furnace. The ingots were turned and re-melted multiple times to ensure homogeneity. Ribbon samples were produced by melting 3 g of ingot with an induction coil in a partial argon atmosphere and ejecting the melt onto the surface of a rapidly rotating copper wheel. The peripheral speed of the wheel was approximately 35 m s^{-1}. The orifice diameter of the quartz crucible was approximately 0.5 mm. The resulting polycrystalline ribbons were typically 30 μm thick, 5 mm wide and of lengths varying between 10 and 100 mm. A fraction of the ribbons were sealed in a quartz tube under approximately one atmosphere of argon, heated at 1000 °C for 1 h and then cooled slowly to room temperature.

Neutron diffraction experiments were carried out on both as-quenched and annealed ribbons on the D2B diffractometer, at the ILL Grenoble, France [24]. Approximately 2 g of ribbons were packed into vanadium cans and diffraction patterns were collected from 0° to 158° at ambient temperature by using the high-resolution mode with a scanning step size of 0.05°. Room-temperature ^{57}Fe Mössbauer effect spectra were collected in transmission geometry using a Rh^{57}Co source and a Wissel System Mössbauer spectrometer operating in the sinusoidal mode, with the γ-ray perpendicular to the ribbon plane. All spectra were referenced to a room-temperature α-Fe pattern. The intrinsic spectrometer line width is approximately 0.10 mm s^{-1} (FWHM). Details of the fitting procedures used for spectral analysis are described in Section 3.2.

3. Results

3.1. Neutron diffraction

The neutron diffraction patterns from both as-quenched and annealed ribbons are shown in Fig. 1. The six strong diffraction peaks can be easily identified as arising from the bcc A2 structure or the corresponding reflections from the $D0_3$ structure. Diffraction patterns from the ribbons with $x=19.5$ and 22.5 are emphasised in Fig. 2, in which the portion between $2\theta=20°$ and 110° has been enlarged and shows the existence of small additional peaks in the pattern. One group belongs to the vanadium can used in the

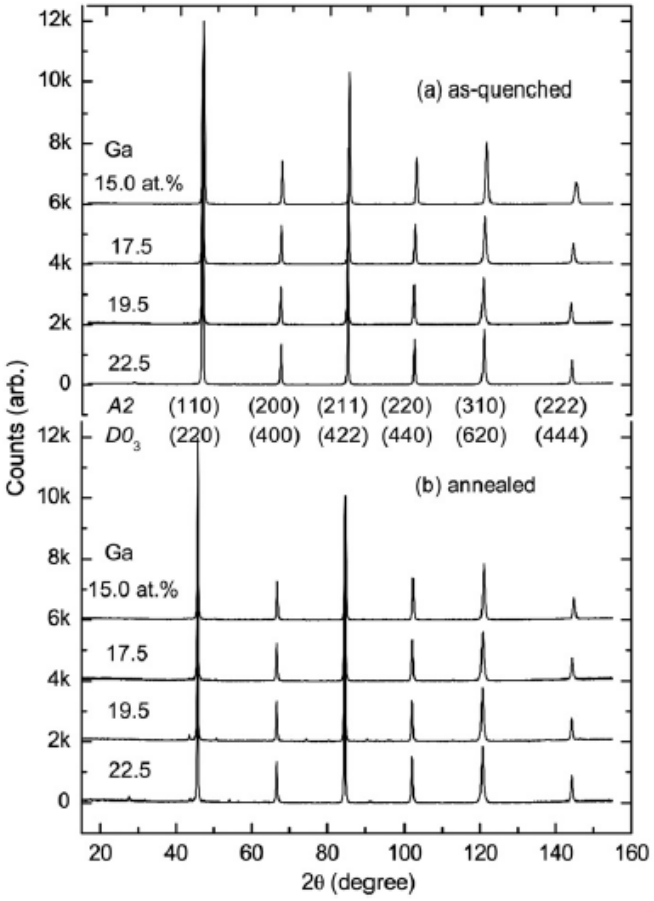

Fig. 1. Room temperature neutron diffraction patterns of as-quenched and annealed $Fe_{100-x}Ga_x$ ribbons with $x=15$, 17.5, 19.5, and 22.5.

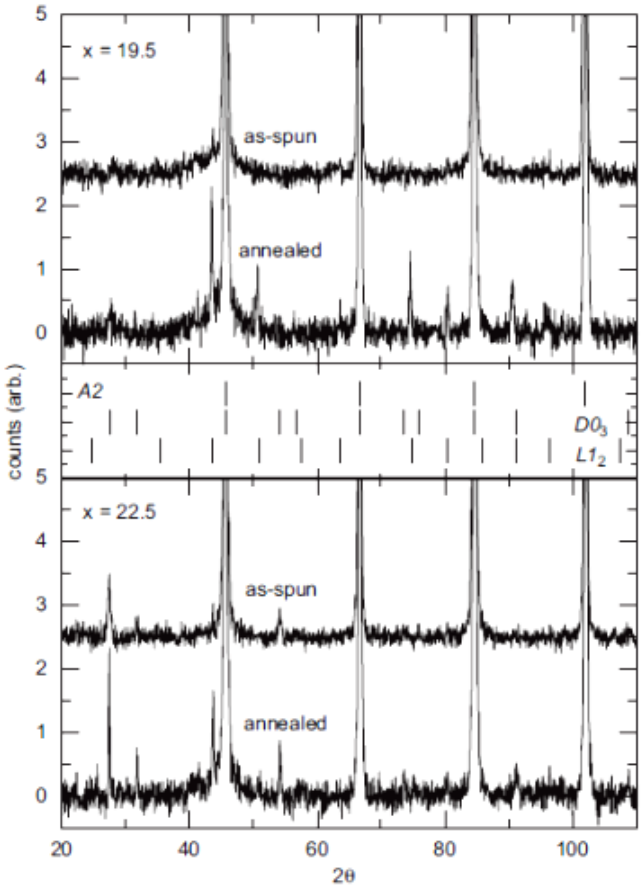

Fig. 2. Expanded room temperature neutron diffraction pattern of as-quenched and annealed $x=19.5$ and $x=22.5$ $Fe_{100-x}Ga_x$ alloy ribbons. Tick marks for the A2, $D0_3$ and $L1_2$ phases are shown in the central panel.

experiment. Vanadium is bcc with $a=3.0297$ Å, and gives rise to diffraction peaks on the left of the A2 peaks. One such peak is clearly seen at $2\theta\sim41^\circ$ in all the patterns.

Additional reflections were observed in the patterns from both the annealed and the as quenched ribbons, and are particularly obvious in the $x=19.5$ pattern. These new peaks have been indexed and are associated with a Fe_3Ga $L1_2$ phase. This was unexpected, as it is generally believed that the $L1_2$ phase is very difficult to form and we have not observed this phase in annealed FeGa bulk samples with a similar composition (unpublished results). It is clear that a significant volume of the $D0_3$ phase has not formed in the $x=19.5$ ribbon as no obvious Bragg peaks from $D0_3$ can be seen even in the low intensity part of the diffraction pattern. This suggests a structural transformation from A2 to $L1_2$, rather than from $D0_3$ to $L1_2$ during the annealing process. When the Ga content is increased to 22.5 at%, extra reflections arising from the ordered Fe_3Ga $D0_3$ structure are observed. There is some agreement between these results and those of Zhang et al. [25,26]. In their work melt spun ribbons of $Fe_{100-x}Ga_x$ with $x=17$ and 19 exhibit the distorted bcc (A2) structure. This phase remains in the $x=19$ sample after annealing but is accompanied by the $D0_3$ phase when the $x=17$ sample is annealed, a result which is not seen in this work.

The lattice parameters for all eight samples were determined using the diffraction fitting software package GSAS [27]. There is good agreement between these lattice parameters and those determined by Dunlap et al. [19], where ribbons of $Fe_{100-x}Ga_x$ with $x=8.3$, 17.9, 20.5 and 23.3 were also shown to form in the A2 structure when quenched. The results of this work together with the results of Dunlap et al. [19] and Luo [28] are shown in Fig. 3, where it can be seen that in all three systems the lattice parameter increases approximately linearly as the Ga concentration increases at a rate of 1.9×10^{-4} nm/at%.

A more detailed discussion of the neutron diffraction data is given in an earlier paper by Zhao et al. [11], but to summarise: the high-resolution neutron diffraction spectra shown in Figs. 1 and 2 indicate that only diffraction peaks arising from the disordered bcc A2 phase are present in as-quenched $x=15$, 17.5 and 19.5 ribbons, without any trace of satellite or split peaks. Post-annealing $L1_2$ reflections appeared, and are most prominent in the $x=19.5$ alloy. In contrast, the as-quenched $x=22.5$ ribbons contain traces of both the A2 and $D0_3$ phases, furthermore, upon annealing it is noted that that fractions of the A2 phase are transformed into the $D0_3$ phase.

3.2. Mössbauer spectroscopy

Room-temperature ^{57}Fe Mössbauer spectra of both as-quenched and annealed ribbons are shown in Fig. 4. It is apparent that all samples are ferromagnetically ordered at room temperature as six line spectra are observed for all compositions. However there are some variations in the form of the magnetic order. The spectra from ribbons with $x=15$, and 17.5 exhibit only broadened sextets while the spectra from $x=19.5$ samples start to show additional, sharper features. The $x=22.5$ spectra are noticeably different from those of alloys with lower Ga content, showing several resolvable sextets that suggest some structural changes and a much greater degree of local ordering as the Ga content has increased (Fig. 5). Rancourt and Ping [29] and Lagarec and Rancourt [30] have shown that it is appropriate to model Mössbauer spectra from such materials as a combination of Gaussian-distributed Lorentzian sextets. Each sextet was described using an isomer shift δ, a mean hyperfine field value $<H>$, a width, σ_H, and an area A. The quadrupole shift was assumed to be zero in all cases. The relative areas of the six spectral peaks were constrained to be $3{:}y{:}1{:}1{:}y{:}3$ where y was determined during the fit.

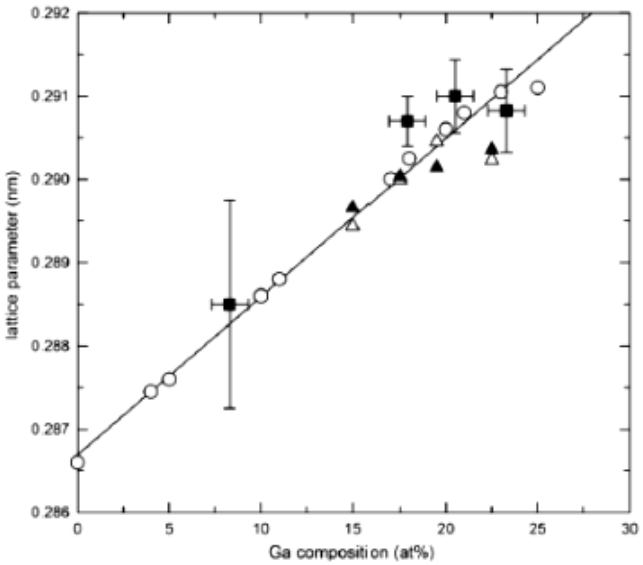

Fig. 3. Room temperature lattice parameter of the bcc phase as a function of Ga content. The values are taken from Luo (◯) [23], Dunlap et al. (■) [19] and this work (▲△).

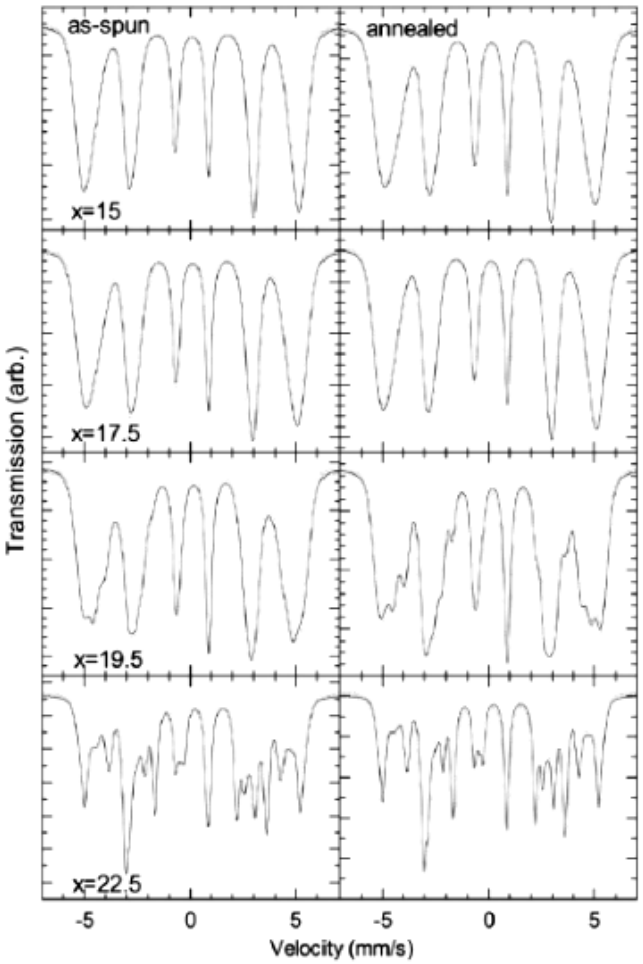

Fig. 4. Room-temperature ^{57}Fe Mössbauer spectra of $Fe_{100-x}Ga_x$ ribbons. Circles represent experimental data, the solid lines going through circles are the best fit.

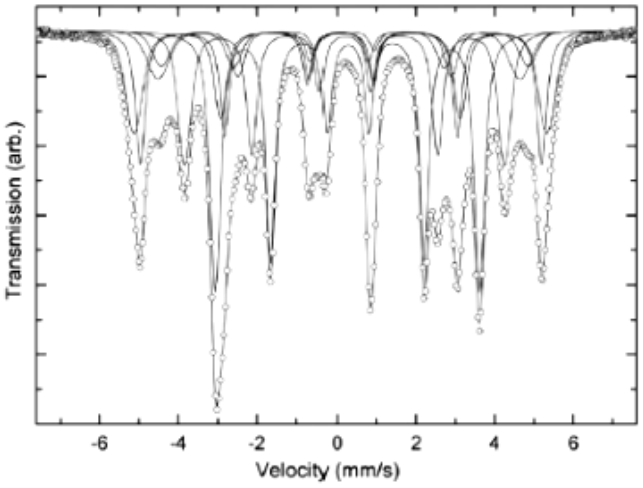

Fig. 5. Room-temperature ^{57}Fe Mössbauer spectra of as-spun $x=22.5$ ribbons. Circles represent experimental data, the solid lines going through circles are the best fit. The individual sub-spectra are shown as thin solid lines.

The spectra from both the annealed and the quenched ribbons with $x=15$ and 17.5 were best fitted using two sextets, and the resulting hyperfine field distributions are illustrated in Fig. 6. The

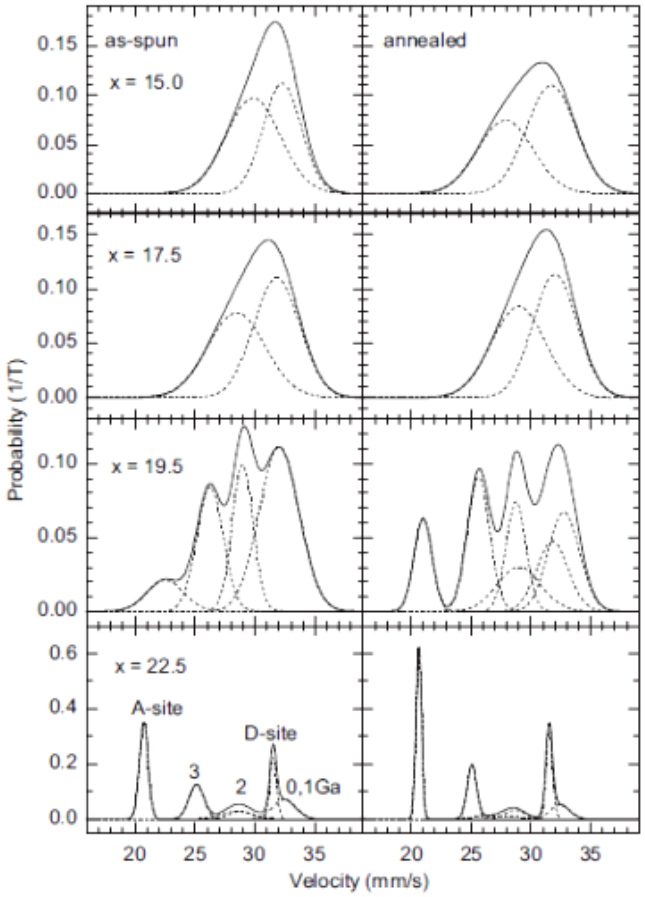

Fig. 6. Room-temperature Fe hyperfine field distributions in $Fe_{100-x}Ga_x$ ribbons The distributions for the individual spectral components are shown by the broken lines and the total distribution is shown by the solid line.

mean values of the hyperfine fields decrease with the increase of Ga content. Annealing has little effect on the hyperfine field in these samples, except to reduce the hyperfine fields of the $x=15$ sample slightly. The spectra from the $x=19.5$ ribbons show more features than observed in the spectra from ribbons with $x=15$ and 17.5. In order to model these additional features four sextets are needed to fit the as-quenched spectrum, while the spectrum from the annealed $x=19.5$ ribbon is best fitted with six sites. The parameters for the best fits for spectra from ribbons with $x=15$, 17.5 and 19.5 are shown in Table 1. For $x\leq 20$ the variation in mean hyperfine field value is approximately linear with Ga composition decreasing at a rate of 0.18 T/at%.

There have been several Mössbauer studies on FeGa alloys. For example Conversion Electron Mössbauer Spectroscopy (CEMS) was used to study thin film samples of $Fe_{100-x}Ga_x$ with $10\leq x\leq 35$ [31,32]. Blachowski et al. [33] have carried out a Mössbauer study of $Fe_{100-x}Ga_x$ ingots with $10\leq x\leq 29$. However as the structural examinations have shown, the phase-composition diagrams vary for different forms of the alloys and therefore it is really useful to compare the results of this study only with the results obtained from studies of rapidly quenched material. Newkirk and Tsuei [16] examined quenched $Fe_{100-x}Ga_x$ foils ~35 μm thick. For $0\leq x\leq 20$ the samples gave broad six line Mössbauer spectra, while the sample with $x=25$ gave a spectrum with sharper lines arising from several distinct magnetic sites. Similarly Dunlap et al.'s study of melt spun $Fe_{100-x}Ga_x$ ribbons showed broad six line Mössbauer spectra from samples with $8.3\leq x\leq 20$, which were best fitted with a distribution of

Table 1
^{57}Fe Mössbauer effect parameters for the sites obtained from the fits to the spectra from the ribbons with $x=15$, 17.5 and 19.5 as described in the text. The velocity scale is referenced to the α-Fe spectrum at room-temperature.

Site	$<H>$ (T)	σ_H (T)	δ (mm s^{-1})	A (%)	Site	$<H>$ (T)	σ_H (T)	δ (mm s^{-1})	A (%)
$x=15$ *as-spun*					$x=15$ *annealed*				
1	32.26	1.59	0.04	44.6	1	31.71	2.07	0.09	56.96
2	29.83	2.28	0.13	55.4	2	27.87	2.30	0.16	43.04
$x=17.5$ *as-spun*					$x=17.5$ *annealed*				
1	31.80	1.94	0.07	53.2	1	32.03	1.85	0.07	52.5
2	28.45	2.39	0.16	46.8	2	28.99	2.27	0.15	47.5
$x=19.5$ *as-spun*					$x=19.5$ *annealed*				
1	31.80	1.94	0.07	53.2	1	32.03	1.85	0.07	52.5
2	28.45	2.39	0.16	46.8	2	28.99	2.27	0.15	47.5
3	31.80	1.94	0.07	53.2	3	32.03	1.85	0.07	52.5
4	28.45	2.39	0.16	46.8	4	28.99	2.27	0.15	47.5
					5	32.03	1.85	0.07	52.5
					6	28.99	2.27	0.15	47.5

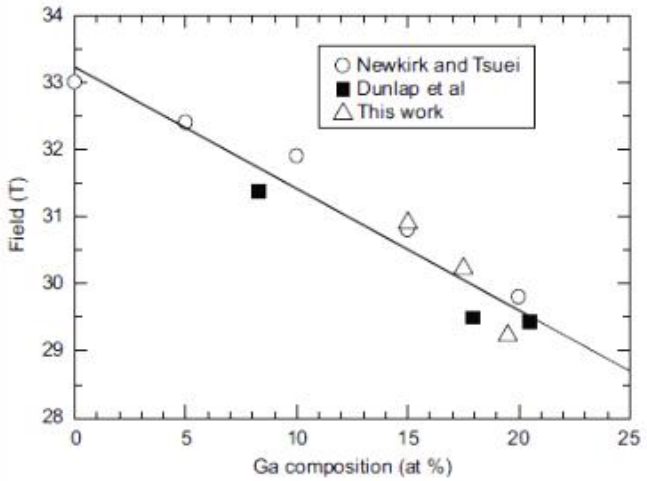

Fig. 7. Mean hyperfine fields calculated from room temperature spectra of quenched samples with $x=15$, 17.5 and 19.5. The plot includes results from Newkirk and Tsuei (○) [16], Dunlap et al. (■) [19] and the present work (△).

hyperfine fields. When x was increased to 23.5 the spectrum became much sharper, showing three clearly resolved sextets. In both these studies the spectra were comparable to those obtained in this work from the as-quenched samples (displayed on the left hand side of Fig. 4). Neither Newkirk and Tsuei nor Dunlap et al. examined annealed alloys.

These results of the fits to the Mössbauer spectra from ribbons with $15 \le x \le 19.5$ are shown in Fig. 7, where the agreement of this work with the results of Newkirk and Tsuei [16] and Dunlap et al. [19] can be observed.

Visual inspection of the resolvable absorption peaks in the spectrum of as-spun $x=22.5$ ribbon suggests the presence of at least four distinct sites; however, in practice six distinct sites are needed to obtain a good fit to this spectrum. The final fit is shown in Fig. 5, with the resulting hyperfine field distribution in Fig. 6. The mean hyperfine parameters for the six sites are summarised in Table 2. The values of y (not shown) from the fit to this spectrum are greater than 2, suggesting the existence of a small amount of in-plane magnetic texture. It should be noted that this is in complete contrast to the results of Dunlap et al. [19], where the spectra from as-quenched samples with $8.3 \le x \le 23.3$ could be fitted with $1.95 \le y \le 2.09$, indicating that there is no evidence for magnetic texture in their samples.

4. Discussion

For a random distribution of Ga on the bcc Fe lattice, assuming a binomial distribution and that the eight nearest neighbours have the nominal composition, we expect the probability, $P(n)$, of Fe sites with n Ga nearest neighbour to be

$$P(n) = \frac{8!}{n!(8-n)!}\left(\frac{x}{100}\right)^n\left(1-\frac{x}{100}\right)^{8-n} \quad (1)$$

For the $x=15$ and 17.5 samples, the probability of Fe sites with 0 or 1 Ga nearest neighbours is calculated to be 0.66 and 0.58 respectively. However, it is found that the relative area of the sites at higher field is 45% and 53%, respectively, which is less than the calculated value. This seems to indicate that the distribution of Ga in the bcc phase is not entirely random and that Ga prefers sites with a high number of Ga nearest neighbours. Initially this phenomenon was regarded as evidence of the enhancement of Ga–Ga pairing [19]. However, the assumption above completely neglects the fact that the central atom must be an Fe atom. When taking the central Fe atom and the eight nearest neighbours as a whole and assuming its Ga content is x, the Ga content in the nearest neighbours should be $9x/8$, instead of x. With this new Ga content and Eq. (1), the probability of sites with 0 or 1 Ga atom is 0.60 and 0.51 for $x=15$ and 17.5 ribbons respectively, which is closer to the observed value.

At least four sextets were needed to fit the spectrum from the as-quenched $x=19.5$ ribbon, corresponding to the sites with 0 or 1 Ga nearest neighbour, and 2, 3, and 4 Ga nearest neighbours, respectively. The resulting hyperfine field distributions are shown in Fig. 6. The mean hyperfine fields and isomer shifts change approximately linearly with the number of Ga neighbours. The probabilities calculated from Eq. (1) are 0.52, 0.29, 0.14 and 0.04 for the four sites mentioned above. The relative areas of sites at 32.0, 29.0, 26.2 and 22.5 T are 46.7, 21.9, 23.3 and 8.2% respectively. Again this seems to indicate that the distribution of Ga in the A2 phase in these ribbons is not entirely random but that Ga prefers Ga nearest neighbours. However, the calculated probability of the site with two Ga nearest neighbours is higher than the observed 21.9%, suggesting no improvement in the Ga–Ga pairing although the disordered bcc Fe–Ga alloys of this composition demonstrate the highest magnetostriction. In contrast, the relative area of the site with four Ga nearest neighbours is double that predicted, indicating the formation of high Ga content clusters or even the short-range ordered $D0_3$ precipitates in the bcc A2 matrix. It is possible these $D0_3$ precipitates might be responsible for the increase in magnetostriction of high Ga content Fe–Ga alloys, as predicted in [14].

The absorptions in the Mössbauer spectrum from the annealed ribbon with $x=19.5$ occur at the hyperfine fields similar to those observed in the $x=22.5$ spectrum. All three spectra were best fitted using six sextets. In the $x=19.5$ ribbon the absorption at around 21 T is well separated from other peaks, and is believed to be attributed to Fe sites with four Ga nearest neighbours, similar to the A-sites of $D0_3$, indicating the formation of $D0_3$ phase after annealing treatment. However, the broader distribution of this site suggests that the formed $D0_3$ phase is probably only short-range ordered. This is confirmed by its neutron diffraction pattern, where no obvious superlattice diffractions from $D0_3$ phase can be found. The relative area of this site fitted from the spectrum is 12%, which corresponds to a $D0_3$ volume of approximately 18% in this sample when assuming that the number of A-sites is twice that of D-sites.

In the spectrum from the as-quenched $x=22.5$ ribbon the two sites with hyperfine fields of 20.7 and 31.5 T and narrow field distributions correspond well to the values of the $D0_3$ phase reported by others [17,19], with room-temperature Fe hyperfine

Table 2
^{57}Fe Mössbauer effect parameters for the sites obtained from the fits to the spectra of ribbons with $x=22.5$ as described in the text. The velocity scale is referenced to the α-Fe spectrum at room-temperature.

$x=22.5$ as-spun						$x=22.5$ annealed					
Site	$<H>$ (T)	σ_H (T)	δ (mm s^{-1})	A (%)	Description	Site	$<H>$ (T)	σ_H (T)	δ (mm s^{-1})	A (%)	Description
1	32.42	0.94	0.10	16.9	<6 Ga NNN	1	32.43	0.79	0.09	10.4	<6 Ga NNN
2	31.51	0.27	0.11	15.4	DO_3 D-site	2	31.55	0.28	0.11	22.5	DO_3 D-site
3	28.78	1.00	0.21	7	2 Ga NN	3	28.66	0.85	0.15	7.03	2 Ga NN
4	28.42	1.36	0.06	9.2	2 Ga NN	4	27.14	1.59	0.00	5.3	2 Ga NN
5	25.10	0.62	0.21	19.3	3 Ga NN	5	25.09	0.38	0.21	18.6	3 Ga NN
6	20.70	0.36	0.28	32.1	DO_3 A-site	6	20.65	0.23	0.28	36.1	DO_3 A-site

field values of 20.5 and 31.2 T for the DO_3 phase and 26.9 T for the $L1_2$ phase in Fe_3Ga samples [17], and 20.69 and 31.44 T for the DO_3 phase and 25.30 T for the $L1_2$ phase in $x=23.3$ samples [19]. The two fields for the DO_3 structure correspond to the so-called A-sites with four Fe and four Ga nearest neighbours and six Fe next nearest neighbours (NNN), and D-sites with eight Fe nearest neighbours and six Ga next nearest neighbours. We believe that the reasonable agreement of the hyperfine fields for those samples, suggests a conventional Ga–Ga pairing along $<110>$ directions which occurs in the DO_3 structure. However, the site with a hyperfine field of 25.08 T is expected to be a Fe site similar to A-sites of DO_3 but with only three Ga and five Fe nearest neighbours, rather than $L1_2$ site as suggested previously [19]. It is reported that the Fe_3Ga $L1_2$ phase has one hyperfine field at 26.9 T with two quadrupole shifts [16]. In the present work, there is no need to introduce quadrupole shifts to obtain a better fit, suggesting no observable $L1_2$ absorptions in the samples. However, despite the fact that neutron diffraction patterns show no $L1_2$ phase in the as-quenched ribbons, they do reveal a trace of $L1_2$ phases in the annealed samples, most notably in the $x=19.5$ ribbons although the volume of such a phase is estimated to be less than 1%, which is not discernable in the Mössbauer spectra. In contrast, the relative area of absorption with a hyperfine field of 25.08 T is around 19%.

The two sites with a hyperfine field of around 28.6 T are considered as Fe sites with two Ga and six Fe nearest neighbours; the difference in the isomer shift value might indicate a difference in the Ga pair arrangement, either along the $<100>$, $<110>$ or $<111>$ directions. The site with a hyperfine field of 32.45 T has an isomer shift value identical to that of DO_3 D-sites, suggesting that this site is similar to D-sites but with fewer Ga atoms as its next nearest neighbours. As the absorption area is much larger than the site with two Ga nearest neighbours, it is very likely the absorption with a hyperfine field of 32.45 T has a contribution from the site having one Ga nearest neighbour, as the sites with 0 or 1 Ga nearest neighbours in disordered bcc phase are believed to have similar hyperfine fields [16]. The occurrence of sites with hyperfine fields around 28.6 T and 32.45 T indicates the existence of disordered bcc Fe–Ga phase in this sample.

Comparing the hyperfine field distributions of the $x=22.5$ ribbons pre- and post-annealing treatment (lower section of Fig. 6), one can see that the hyperfine field distributions of A-sites and D-sites of annealed samples become narrower, suggesting an improvement of chemical ordering in the DO_3 phase, and that the corresponding probabilities are also higher than those of as-quenched ribbons while the probabilities of bcc sites mentioned above become lower. The probability increases from 32.1% to 36.1% for A-sites, and 15.4% to 22.5% for D-sites. This is consistent with neutron diffraction results, where the integrated intensities of DO_3 superlattice peaks at $2\theta \sim 27.5^\circ$ and 57.2°, normalised to the (220) peak, increases from 2.14% and 0.82% to 2.40% and 1.07% respectively after annealing, with an uncertainty of $\pm 0.05\%$. The increases in both the peak intensities of neutron diffraction and the relative areas of Mössbauer spectrum indicate an increase in the volume of DO_3 phase after annealing, which in turn confirms that there may be an A2 phase in the as-quenched ribbons and a transformation from an A2 phase into DO_3 phase after annealing.

5. Conclusions

^{57}Fe Mössbauer spectroscopy and neutron diffraction have been used to study as quenched and annealed samples of melt spun $Fe_{100-x}Ga_x$ alloys. Neutron diffraction has shown that ribbons with $x=15$ and 17.5 have the disordered bcc (A2) structure both before and after annealing, but ribbons with $x=19.5$, which has the A2 structure initially, develops short-range ordered DO_3 phase upon annealing. The ribbons with $x=22.5$ show mainly DO_3 phase with a fraction of bcc phase; moreover, some of the bcc phase transforms into DO_3 phase and the long-range ordering of DO_3 phase was improved after annealing.

Room temperature Mossbauer spectroscopy has shown that all samples are ferromagnetically ordered. At low Ga concentrations there is a distribution of hyperfine fields in the samples, centred around ~29 T and ~32 T for both the as spun and annealed ribbons. However, as the Ga concentration is increased beyond ~19 at% there is a much greater degree of local order in the material with four distinct Fe sites in the $x=19.5$ as-quenched ribbons and six distinct Fe sites in the $x=19.5$ annealed ribbons and in both the $x=22.5$ as-quenched and annealed ribbons.

These results also demonstrate the suitability of ^{57}Fe Mössbauer spectroscopy for studying the formation of DO_3 ordering that cannot be observed by conventional diffraction techniques due to either insufficiently long range ordering or, as in the Fe–Ga system, because of the closeness of the elements' atomic scattering factors. Mössbauer spectroscopy together with neutron diffraction can build a detailed knowledge of the structural properties of these alloys and help correlate this structural information to changes in the magnetostriction and help understand the causes underlying the formation of a large magnetostriction.

Acknowledgements

This work was generated in the context of the MESEMA project, funded under the 6th Framework Programme of the European Community under Contract no. AST3-CT-2003-502915. Dr. N. Lupu and Professor H. Chiriac from the National Institute of Research and Development for Technical Physics, Romania, are gratefully acknowledged for their help with the sample preparation.

References

[1] J.R. Cullen, A.E. Clarke, M. Wun-Fogle, J.B. Restorff, T.A. Lograsso, Journal of Magnetism and Magnetic Materials 226–230 (2001) 948–949.
[2] R.A. Kellogg, A.B. Flatau, A.E. Clark, M. Wun-Fogle, T.A. Lograsso, Journal of Applied Physics 91 (2002) 7821–7823.
[3] A.E. Clark, M. Wun-Fogle, J.B. Restorff, T.A. Lograsso, Materials Transactions 43 (2002) 881–886.
[4] A.E. Clark, K.B. Hatherway, M. Wun-Fogle, J.B. Restorff, T.A. Lograsso, V.M. Keppens, G. Perculescu, Journal of Applied Physics 91 (2003) 8621–8623.
[5] T.A. Lograsso, E.M. Summers, Materials Science and Engineering 416 (2006) 240–245.
[6] J. Zhang, T. Ma, M. Yan, Physica B 404 (2009) 4155–4158.
[7] O. Ikeda, R. Kainuma, I. Ohnuma, K. Fukamichi, K. Ishida, Journal of Alloys and Compounds 347 (2002) 198–205.
[8] Y. Du, M. Huang, S. Chang, D.L. Schlagel, T.A. Lograsso, R.J. McQueeney, Physical Review B 81 (2010) 054432 1–054432 9.
[9] H. Cao, F.M. Bai, J.F. Li, D.D. Viehland, T.A. Lograsso, P.M. Gehring, Journal of Alloys and Compounds 465 (2008) 244–249.
[10] J. Zhang, T. Ma, M. Yan, Journal of Magnetism and Magnetic Materials 322 (2010) 2882–2887.
[11] X. Zhao, N.J. Mellors, S.H. Kilcoyne, D. Lord, N. Lupu, H. Chiriac, P.F. Henry, Journal of Applied Physics 103 (2008) 07B320.
[12] C. Li, J. Liu, Z. Wang, C. Jiang, Journal of Magnetism and Magnetic Materials 324 (2012) 1177–1181.
[13] A.G. Khachaturyan, D.D. Viehland, Metallurgical and Materials Transactions 38A (2007) 2308–2316.
[14] T.A. Lograsso, A.R. Ross, D.L. Schlagel, A.E. Clarke, M. Wun-Fogle, Journal of Alloys and Compounds 350 (2003) 92–101.
[15] G.E. Bacon, Neutron Diffraction, third ed., Clarendon Press, Oxford, UK, 1975.
[16] L.R. Newkirk, C.C. Tsuei, Physical Review B 4 (1971) 4046.
[17] N. Kawamiya, K. Adachi, Y. Nakamura, Journal of the Physical Society of Japan 33 (1972) 1318–1327.
[18] G.K. Wertheim, V. Jaccarino, J.H. Wernick, D.N.E. Buchanan, Physical Review Letters 12 (1964) 24–27.
[19] R.A. Dunlap, J.D. McGraw, S.P. Farrell, Journal of Magnetism and Magnetic Materials 305 (2006) 315–320.
[20] R.C. Hall, Journal of Applied Physics 28 (1957) 707.
[21] G.D. Lui, L.B. Liu, Z.H. Liu, M. Zhang, J.L. Chen, J.Q. Li, G.H. Wu, Y.X. Li, J.P. Qu, T.S. Chin, Applied Physics Letters 84 (2004) 2124–2126.
[22] S. Pascarelli, M.P. Ruffoni, R. Sato Turtelli, F. Kubel, R. Grössinger, Physical Review B 77 (2008) 184406.
[23] J. Cullen, P. Zhao, M. Wuttig, Journal of Applied Physics 101 (2007) 123922.
[24] D2B High resolution two axis diffractometer 〈www.ill.eu/instruments-support/instruments-groups/instruments/d2b/〉, 2012.
[25] M.C. Zhang, H.L. Jiang, X.X. Gao, J. Zhu, S.Z. Zhou, Journal of Applied Physics 99 (2006) 023903.
[26] J. Zhang, T. Ma, M. Yan, Physica B 404 (2009) 4155.
[27] A.C. Larson, R.B. Von Dreele, General Structure Analysis System (GSAS), Los Alamos National Laboratory Report LAUR (1994) 86-748.
[28] H.L. Luo, Transactions of the Metallurgical Society of AIME 239 (1967) 119.
[29] D.G. Rancourt, J.Y. Ping, Nuclear Instruments and Methods in Physics Research Section B 58 (1991) 85–97.
[30] K. Lagarec, D.G. Rancourt, Nuclear Instruments and Methods in Physics Research Section B 129 (1997) 266–280.
[31] A. Javed, N.A. Morley, T. Szumiata, M.R.J. Gibbs, Applied Surface Science 257 (2011) 5977–5983.
[32] T. Szumiata, K. Brzozka, M. Gawronski, B. Gorka, A. Javed, N.A. Morley, M.R.J. Gibbs., Acta Physica Polonica A 119 (2011) 21.
[33] A. Blachowski, K. Ruebenbauer, J. Zukrowski, J. Przewoznik, Journal of Alloys and Compounds 455 (2008) 47.